Luminescent Ruthenium on Gold Nanoparticles; Novel DNA Probes for Cancer Theranostics

By

Patrícia Alexandra Madeira Gírio

A thesis submitted to the University of Birmingham for the degree of
DOCTOR OF PHILOSOPHY

School of Chemistry
College of Engineering and Physical Sciences
University of Birmingham
December 2023

Abstract

Ruthenium (II) polypyridyl complexes have been extensively investigated for cancer research as imaging probes or as therapeutic drug due to their photothermal stability, large stoke shifts, relatively long lifetimes, and potential anticancer activity. To overcome issues of solubility and delivery, gold nanoparticles (AuNPs) have emerged as nano carriers due to their relative chemical inertness, large surface area with possibilities of functionalisation as well as their unique multimodal imaging properties due to their surface plasmon resonance and electron density. Three ruthenium (II) complexes carrying DNA intercalating groups (RuPhenL1, RuPhenL2 and RuDppzL2) were successfully attached onto the surface of 13 nm and 25 nm gold nanoparticles. Luminescence studies of Au.RuPhenL1 and Au.RuPhenL2 revealed enhancement of the ruthenium luminescence lifetime upon attachment to gold nanoparticles by considering the type of ancillary ligands around the metal in combination with the type of surfactant used to stabilise the AuNPs. Furthermore, the negatively charged Au.RuPhenL2 and Au.RuDppzL2 conjugates demonstrated to have a high binding affinity with DNA, with binding constants comparable to known intercalators (Ka= 10^6 M^{-1}). Unsurprisingly, Au.RuDppzL2 had the strongest interaction with DNA. For the first time, the interaction of the Au.RuPhenL2 and Au.RuDppzL2 conjugates is visualised by Transmission Electron Microscopy (TEM) and Energy Dispersed X-ray Spectroscopy (EDX). Intercalation and electrostatic interactions with an uncoiling of DNA, are the suggested modes of binding between AuNP.Ru conjugates and DNA. The luminescent nanoparticles (Au.RuPhenL1, Au.RuPhenL2 and Au.RuDppzL2) accumulated in the cytoplasm and in the nucleus of A549 cells just after 4 hours incubation. The larger 25 nm AuNPs showed higher cellular uptake than the 13 nm ones for Au.RuPhenL1 and Au.RuPhenL2. However, in the case of Au.RuDppzL2 there was high uptake for both 13 nm and 25 nm sized nanoparticles. All the AuNP.Ru conjugates showed phototoxicity in the nanomolar range for A549 cells upon visible light irradiation at 535 nm, whereas no toxicity was found in the dark. Overall, novel AuNP.Ru conjugates demonstrated promising results as DNA probes for imaging and as pro-drugs for photodynamic therapy for an effective theranostics strategy against cancer.

Acknowledgments

Firstly, I would like to express my sincere gratitude to my supervisors Prof. Zoe Pikramenou and Prof. Mike Hannon for their continued guidance and support during this project. I would also like to thank Prof. Nik Hodges and Prof. Isolda Romero Canelon for the opportunity to learn from them and work in their labs. Without them, none of my biological experiments would have been possible. I would also like to acknowledge the Engineering and Physical Science Research Council (EPSRC) for their funding and the directors of the CDT programme Physical Sciences for health, Prof Mike Hannon and Prof Rob Neiley for all the support, especially during my first year in the UK.

During the three years of this project, I have had the opportunity to work and learn from so many amazing and knowledgeable people, without whom this work would have not been possible. Firstly, I would like to thank our collaborators Prof. Gilles Gasser and Maria Dalla Pozza, from Chimie ParisTech, PSL University, France. I would also like to thank to all the technical staff from University of Birmingham, in particular Dr. Ludwig Schneider and Dr. Theresa Morris for the training in TEM, EDX and for all their patience demonstrated when I had endless samples to analyse. To Dr. Alessandro di Maio for the confocal microscopy training and kindness. To Dr. Chris Williams and Dr. Cécile Le Duff for the help and support with my challenging MS and NMR samples as well as always being there for a sometimes very needed friendly chat. And finally, to Trevor Hardy for the everyday support, never letting the lab fall apart.

I would like to thank all the members of the ZP and MH group past and present, you've made my PhD experience so much more memorable. In particular, a huge thank you to Elena for being such an amazing colleague and housemate, and for being able to still be my friend even after going through a PhD and a lockdown with me. To Asier, my Iberian compatriot, thank you for always being there for me with a joke ready, and for our lovely fancy dates. Those always made my days! To Maria for being not only a very knowledgeable postdoc but also one of the kindest and strongest persons I know. To Grace, for always making me laugh with her mannerisms and northern expressions and for inspiring me every day to go to the gym after I hear about her running competitions, to Joe for being such a kind-hearted person and a great colleague and finally to Menisha and Jamie for being such great mentors. Thank you to Hugo, James and Cat from the MH group for all the kindness and help with the DNA work. A big thank you to George and Alex Quy for making the office so much more fun and always having interesting conversations. Finally, a huge thank you to all my friends in Birmingham and Lisbon, in particular: Jack, Sam, Montse, Chiara, Matt, Cam, Inês, Rita, Patecas and Duarte.

A very special thanks to Laurence for all the support, positivity and for always believing in me, even when I did not.

Por fim, o maior agradecimento do mundo vai para a minha família, em especial à minha mãe, ao meu pai e ao meu mano por todo o apoio incondicional. Mesmo estando longe, sempre ouviram as minhas frustrações e celebraram as minhas vitórias. Obrigada por acreditarem em mim e me inspirarem a ser a mulher que sou hoje.

Table of Contents

List of Abbreviations

^{13}C NMR	Carbon nuclear magnetic resonance
^{1}H NMR	Hydrogen nuclear magnetic resonance
^{31}P NMR	Phosphorus nuclear magnetic resonance
ATP	Adenosine triphosphate
AuNP	Gold nanoparticles
bpy	2,2'-bipyridine
CD	Circular dichroism
CH_3CN	Acetonitrile
COSY	Correlation spectroscopy
CTC	Circulating tumour cells
ctDNA	calf thymus deoxyribonucleic acid
DLS	Dynamic Light Scattering
DMSO	Dimethyl Sulfoxide
DNA	Deoxyribonucleic acid
dppz	Dipyrido[3,2-a:2',3'-c]phenazine
EDC	1-ethyl-3-(-3-dimethylaminopropyl) carbodiimide
EDTA	Ethylenediamine tetraacetic acid
EDX	Energy dispersive x-ray
FDA	Food and drug administration
HMBC	Heteronuclear multiple bond correlation spectroscopy
HOMO	Highest occupied molecular orbital
HSQC	Heteronuclear single quantum correlation spectroscopy
IC	Internal Conversion
ICP-MS	Inductively Coupled plasma Mass Spectrometry
IR	Infrared Spectroscopy
ISC	Intersystem Crossing
K_n	Rate of radiative decay
K_{nr}	Rate of non-radiative decay
LC	Ligand centre transfer
LD	Linear dichroism
LUMO	Lowest unoccupied molecular orbital
MC	Metal centre transfer
MeOH	Methanol
MLCT	Metal to ligand charge transfer
mRNA	messenger ribonucleic acid
MS	Mass spectrometry
nm	nanometres
ns	Nanoseconds
NSCLC	Non-small cell carcinoma
ϕ	Luminescence quantum yield
PACT	Photoactivation Therapy
PCR	Polymerase Chain Reaction

PDI	Polydispersity index
PDT	Photodynamic Therapy
PEG	Polyethylene glycol
phen	1,10-phenanthroline
PS	Photosensitiser
PTT	Photothermal Therapy
ROS	Reactive oxygen species
Ru	Ruthenium
SCLC	Small cell carcinoma
SPR	Surface plasmon resonance
STEM	Scanning transmission electron microscopy
TEM	Transmission electron microscopy
TFA	Trifluoroacetic acid
TNF-α	Tumour necrosis factor alpha
UV	Ultraviolet
Vis	Visible
ε	Molar absorptivity
ζ- potential	Zeta potential
λmax	Wavelength with maximum intensity
τ	Luminescence lifetime

1. Introduction

1.1 Lung Cancer

Lung cancer is the leading cause of cancer-related deaths worldwide, with the highest mortality rates among both men and women.[1] Lung cancer begins with mutations in lung cells (to form abnormal cells) that grow in an uncontrolled way, forming a tumour. Lung cancer is often broken down into two main groups: non-small cell carcinoma (NSCLC) and small cell carcinoma (SCLC) (Figure 1.1).[2] SCLC is usually caused by smoking tobacco and represents less than 20 % of worldwide lung cancer cases. It typically starts in the bronchi before rapidly spreading to other parts of the body. NSCLC represents the majority of lung cancer diagnoses, and it usually grows at a very slow rate with little to no symptoms until the advanced stages.[3] There are three main types of NSCLC: adenocarcinoma, the most common type, which can be found in the outer region of the lung; Squamous cell lung, usually linked to tobacco smoking, which is usually found in the centre of the lung; and Large cell undifferentiated carcinoma, which can begin in any part of the lung and usually spreads very quickly.[3]

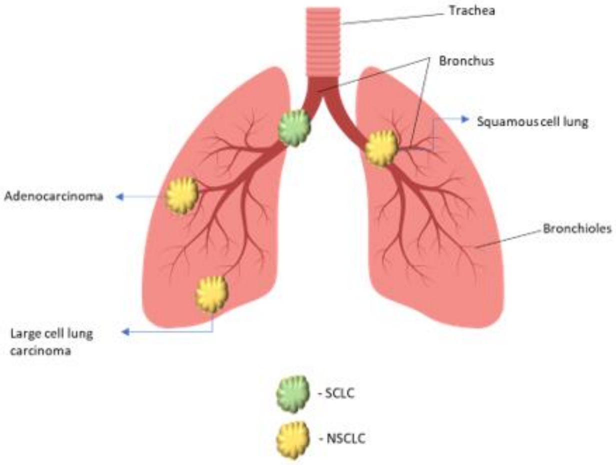

Figure 1.1- Schematic representation of the regions where different types of lung cancer start.

The treatment of lung cancer, as for most cancers, depends on the stage of the disease and the type of cancer.[2] Usually, the treatment for SCLC is immediate chemotherapy and radiation due to the fast spread of the disease, helping at least a quarter of patients to enter in remission.[4] However, this type of cancer is still very likely to spread to other parts of the body. Due to the slower rate of spread of NSCLC cancers, early-stage diagnosis often retains the option of surgery to remove the tumour. However, only 25 % of people receive an early diagnosis.[3] In later stages, chemotherapy is the most common treatment option.[4] However, in 2020 there were still over a million deaths worldwide due to lung cancer, the main reason being that lung cancer is often diagnosed at a late stage, when the tumour has spread to other parts of the body, leading to very limited treatment options.[1] This mortality rate will increase if no other viable treatments are found, and therefore it is crucial to continue investigating new ways to tackle this disease, especially if combined with an early diagnosis to avoid metastasis.

1.2 Ruthenium (II) complexes in cancer research

Since the introduction of cisplatin (figure 1.2-A) as chemotherapeutic drug for cancer, metal complexes have been extensively explored in this field, especially platinum-based drugs.[5] However, reports on the severe side effects of platinum-based drugs are increasing, so researchers have turned their attention to other metals.[5] Today, ruthenium is one of the most studied metals for cancer research.[6-8] Ruthenium has three main oxidation states: Ru (IV) is unstable and so unsuitable for antitumor effects investigation. Ru (III) complexes have good stability and can usually be administered as inert complexes and be reduced to Ru (II) for a therapeutic effect.[6] Ru (II) complexes are the most widely studied due to their ability to mimic iron and therefore easily binds to human serum transferrin, which is highly expressed in tumour cells, exhibits low toxicity for healthy cells and has the ability to coordinate with multidentate ligands, conferring characteristic properties to the metal complex.[9, 10] Ruthenium (II) polypyridyl complexes exhibit photothermal stability, large Stokes shifts and considerably long luminescence lifetimes.[11] Such properties make these complexes exciting candidates for cancer research, biological imaging[11-13] and therapeutics[11, 14, 15] but also for other applications such as redox catalysis[16, 17] and solar cells[18]. Beyond excellent photophysical properties, some of these ruthenium (II) complexes have shown selective toxicity against cancer cells by cell division inhibition[19] and interaction with DNA[20, 21]. Therefore, ruthenium (II) complexes are expected to become a new generation of clinical metal antitumour drugs.

Two of the first ruthenium (II) complexes to reach clinical trials were NAMI-A and KP1019 (Figure 1.2-B and C). However, after reaching phase II, the complexes were discovered to cause severe side effects and to have poor water solubility.[6, 22-24] More recently, the photosensitizer TLD-1433, has emerged as promising example of a ruthenium (II) complex in cancer research (Figure 1.2-D). This complex has a powerful therapeutic efficacy for bladder cancer, using photodynamic therapy, and it is currently in phase II clinical trials.[25]

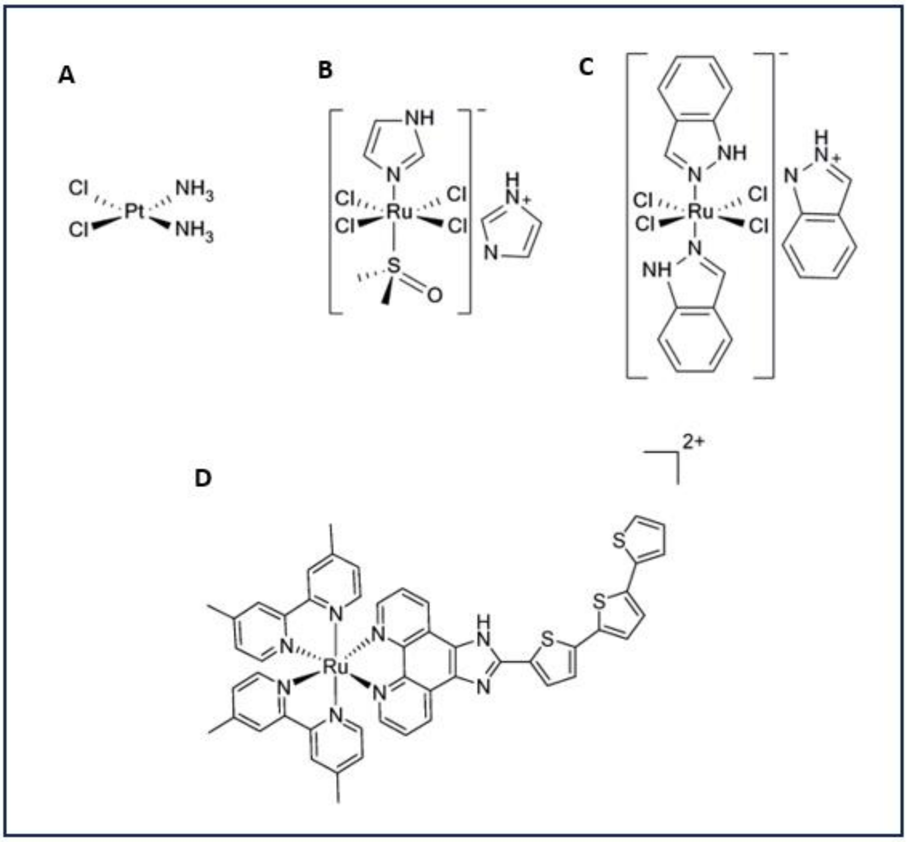

Figure 1.2- Chemical structures of metal complexes that reached clinical trials, (A) Cisplatin, (B), NAMI-A, (C) KP1019, (D) TLD1433.

1.2.1 Ruthenium (II) complexes' mode of action

Ruthenium (II) complexes have different cellular targets and multiple mechanisms of antitumour efficacy. Some ruthenium (II) complexes were found to induce cell cycle arrest and apoptosis, while others can bind to DNA and interfere with its replication and transcription. A ruthenium (II) complex bearing two 1,10-phenanthroline ligands and a plant derived analgesic (xanthoxylic) was studied on human hepatocellular carcinoma HepG2 cells.[26] This complex showed to have cytotoxic effect and induce apoptosis in spheroids and *in vivo*, revealing an intercalation with DNA followed by its synthesis inhibition and a cell cycle arrest in the S-phase of HepG2 cells. Another ruthenium-based strategy currently used to tackle cancer cells is the targeting of G-quadruplex (G4) structures composed of guanosine residues, since G4 motifs are often found in the promoter regions of cancer related genes. McQuaid and co-workers showed that a ruthenium (II) complex, Λ-$[Ru(phen)_2(qdppz)]^{2+}$, (phen= 1,10-phenanthroline and qdppz= 12,17-dihydronaphtho[2,3-h]dipyrido[3,2-a:2′,3′-c]phenazine-12,17-dione) displayed enantiospecific G-quadruplex binding, inhibiting DNA replication.[27] By interacting with G-quadruplex structures, ruthenium (II) complexes are expected to prevent the recognition and elongation of telomerase, towards telomere, hence unprotecting the chromosomes. Furthermore, Liao and co-workers demonstrated that a family of ruthenium (II) complexes (Figure 1.3) showed inhibition towards telomerase by stabilising the G4 structure.[28] These complexes, were also found to inhibit topoisomerase. These enzymes are known to control DNA replication and transcription and are overexpressed in cancer cells, thus, designing a ruthenium (II) complex that can both inhibit telomerase and topoisomerase in cancer cells is a very powerful therapeutic strategy, producing strong apoptosis in tumour cells.

Figure 1.3- Structures of ruthenium (II) complexes that stabilise the G4 structure and inhibit topoisomerase, obtained from[28].

Producing new drugs that can target DNA produce cell responses that induce tumour cell apoptosis, such as a cell cycle arrest, DNA replication inhibition, mutagenic activity and RNA synthesis reduction.[29] Therefore, DNA interactions of antitumor ruthenium (II) complexes are of a great interest and have been intensively explored in the recent years.[30] However, typically ruthenium (II) complexes accumulate more in the organelles of the cytoplasm of cells, than in the nucleus.[31] Thus, studies targeting the mitochondria have also emerged, which have shown ruthenium (II) complexes can decrease the membrane mitochondria potential, leading to its disfunction or activate mitochondrial apoptosis pathways.[32, 33] One of the most common strategies to utilize mitochondria as a strategy to tackle cancer cells is the generation of reactive oxygen species (ROS).[34] ROS are a group of molecules that derive from molecular oxygen and are usually formed by redox reactions or electronic excitation from oxidative metabolisms within the cells.[35] Mitochondria are the primary source of ROS due to their role in ATP production, in which molecular oxygen is reduced to water.[36] Due to the presence of high levels of molecular oxygen in the mitochondria, intrinsic ROS species, like hydrogen peroxide, are locally generated by enzymes such as NADPH oxidases.[35] Low levels of hydrogen peroxide are not harmful for cells. However, higher levels can lead to oxidative stress, inflammation and later on to cell death.[35] Organic hydroperoxides are another type of ROS generated from fatty acids and sterols which are also implicated in cell death. In cancer research, the most common type of ROS used to tackle tumour cells is singlet molecular oxygen ($^1O_2$) which is an electronically excited form of molecular oxygen that is generated by tissues exposed to light.[37] $^1O_2$ can interact with biomolecules, generating their oxidative modification and consequently leading to cell death.[37] Therefore, ruthenium (II) complexes' ability to produce $^1O_2$ upon visible light activation has recently been studied (mechanism details will be explained later in this Chapter-section 1.2.2.1). Han and co-workers, showed that three ruthenium (II) complexes (Figure 1.4-A) can induce apoptosis of A549 cells by enhancing the ROS levels, leading to a decrease of the membrane potential of mitochondria. In particular, compound 3 that presents 1,10-phenanthroline ligands, has been demonstrated to activate cell responses that lead to cell death through apoptosis.[38] Moreover, if the ruthenium (II) complexes can have a combinatory effect involving DNA damage, ROS generation and cell cycle arrest, this would produce a powerful response in tackling cancer cells (Figure 1.4-B).[33]

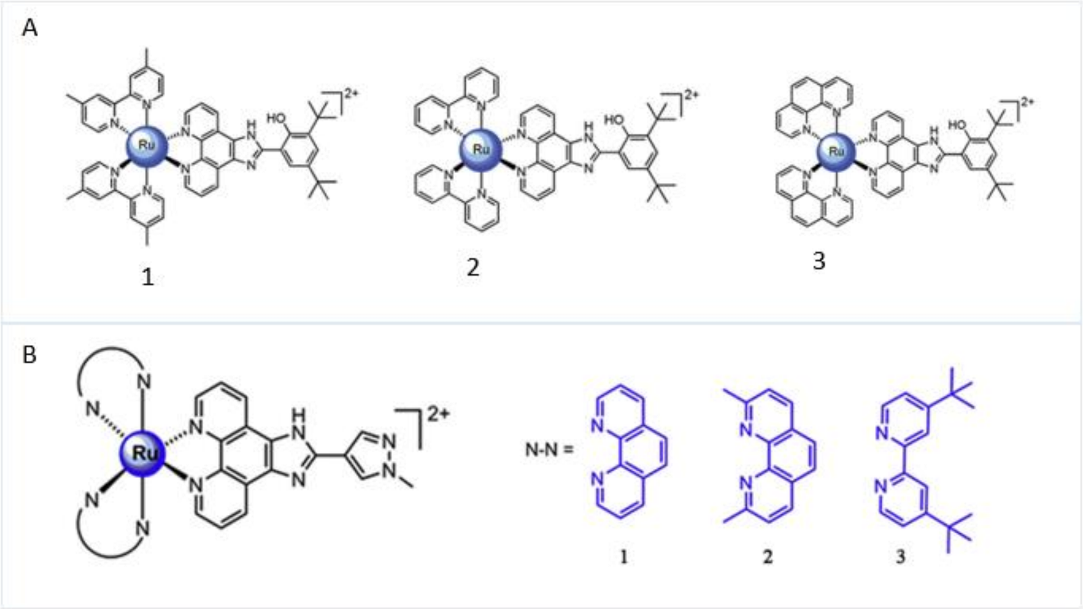

Figure 1.4. (A)- Structures of ruthenium (II) complexes 1, 2 and 3 that demonstrated reduction of membrane mitochondria potential and enhance ROS production, obtained from[38], (B)- Structures of ruthenium (II) complexes that showed DNA damage, ROS production and cell cycle arrest, obtained from[33].

Lysosomes[39], endoplasmic reticulum[40], and cell membranes[41] are also organelles where ruthenium (II) complexes can accumulate and so induce cytotoxicity to tumour cells. Qiu and co-workers, proposed a novel strategy with five different fluorinated ruthenium (II) complexes as photosensitisers to target both mitochondria and the cell membrane of cancer cells (Figure 1.5).[42] These ruthenium (II) complexes offered a two-photon photodynamic therapy, inducing apoptosis of tumour cells under visible light irradiation, in deeper tissues with less damage to healthy cells.

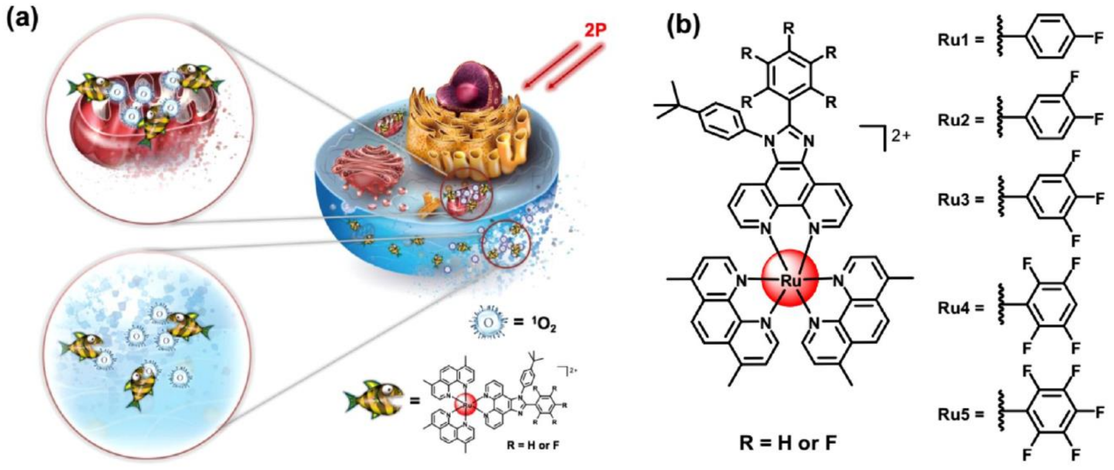

Figure 1.5- Schematic illustration of ruthenium (II) complexes ablating the cytomembrane and mitochondria by two photon laser irradiation, obtained from[42].

Martin and co-workers synthesised a dinuclear ruthenium (II) complex conjugated with a peptide that allows mitochondrial penetration (Figure 1.6).[43] This probe was specifically localised in the mitochondria after 2 hours of incubation in Hela cells. Moreover, this dinuclear ruthenium (II) complex can monitor oxygen changes within the cell by measuring its luminescence lifetime in the presence of Antimycin A. Antimycin A is a cellular respiration inhibitor that causes an increase in oxygen production, leading to a decrease in ATP production and an increase in production of reactive oxygen species that are toxic for the cells. Then, the ruthenium (II) complex rapidly responded to an oxygen level change by decreasing from 525 ns to 228 ns on its luminescence lifetime after 100 minutes (Figure 1.7). This decrease in lifetime was concluded to be due to a quenching mechanism from ROS formation. Overall, this study revealed that a dinuclear ruthenium (II) complex can be used as a probe for mitochondrial targeting and imaging but also revealed an ability to monitor a disease progression, by responding to oxygen levels inside the cell.

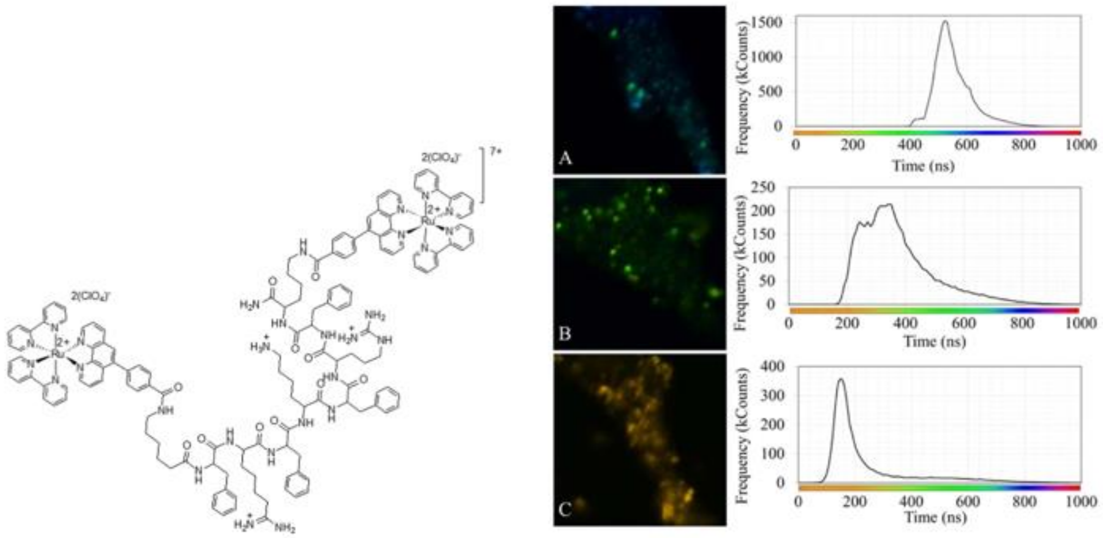

Figure 1.6. (L) Schematic illustration of the structure of the dinuclear Ruthenium (II) complex and (R) Luminescence lifetimes distributions in Hela cells after incubating with the dinuclear ruthenium (II) probe (A), after addition of Antimycin A for 10 minutes (B) and for 100 minutes (C), obtained from[43].

Importantly, most of the studies in the literature have shown that the ruthenium (II) complexes evaluated are effective against platinum resistant tumours, demonstrating the advantages of using this metal for cancer research.[44-46] However, the main limitations involves the solubility of the ruthenium (II) complexes in cellular media and its intracellular delivery. Thus, novel systems need to be addressed to overcome such issues.

1.2.2 The photophysics behind ruthenium's imaging and therapy

Ruthenium (II) complexes typically have a broad absorption in the blue region (λ_{max}= 450 nm) of the visible spectrum due to the excitation of the singlet metal to ligand charge transfer (^{1}MLCT) band (Figure 1.7). When this band is excited, fast intersystem crossing (ISC) followed by vibrational relaxation leads to population of the lowest triplet excited level, ^{3}MLCT state. This state is highly energetic and unstable, so must undergo rapid decay to the ground state via emission of light and non-radiative decay (heat). The large Stoke shifts characteristic of these complexes allows none of the emitting light to be reabsorbed leading to a more efficient process. The relaxation to the ground state from a ^{3}MLCT (spin forbidden transition), usually provides relatively long lifetimes (> 100 ns in aerated water) for these types of complexes.[47-49] Therefore, photothermal stability, large stokes shifts and reasonably long lifetimes makes ruthenium (II) polypyridyl complexes exciting candidates for use as probes and tracers for sub-cellular structure localisation or for detection of biomolecules in the microenvironment of the tumour.

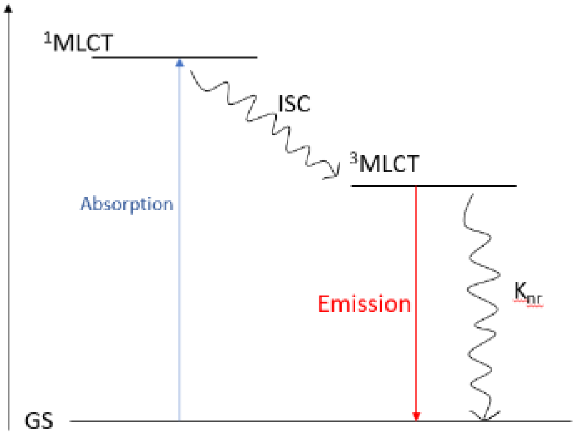

Figure 1.7- General schematic of Jablonsky diagram for the complex Ru(bpy$_3$)Cl$_2$.

1.2.2.1 Using light as treatment strategies

Nowadays, there are three main areas of cancer research related to light activation: Photodynamic therapy (PDT), Photoactivated Chemotherapy (PACT) and Photothermal Therapy (PTT). PDT is a process that involves a photosensitizer (PS) which is non-toxic in the dark, but upon irradiation at a specific wavelength, is excited to the singlet state, followed by an intersystem crossing (ISC) process to the most stable excited triplet state (Figure 1.8). This excited triplet state can then decay by phosphorescence or influence the biological environment by two different pathways, type I or type II. Type I involves the transfer of an electron or proton to or from the photosensitizer to form radicals that can generate ROS. In a type II mechanism, the photosensitizer triplet excited state transfers its energy to molecular oxygen producing singlet oxygen species.[50]

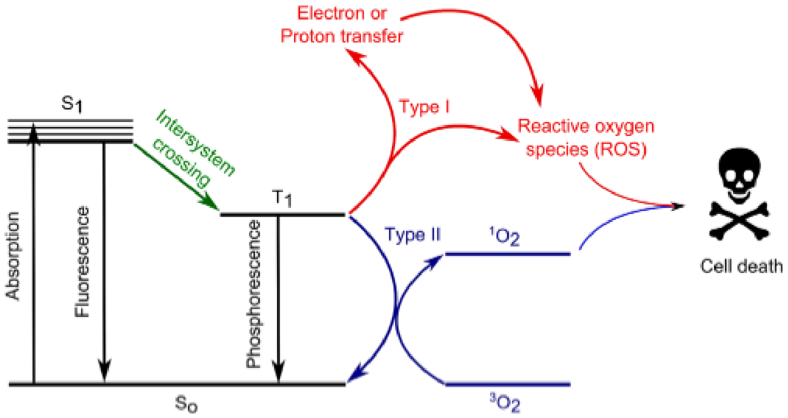

Figure 1.8- Mechanism of action of Photodynamic therapy (PDT), obtained from[50].

Most photosensitisers approved in clinic are derivatives of porphyrins, which have major drawbacks such as photobleaching, poor water solubility, lack of cancer cells selectivity and slow clearance from the body causing photosensitivity.[51] So, in an attempt to tackle the current disadvantages of known photosensitisers, ruthenium (II) polypyridyl complexes have been studied due to their high water solubility compared to porphyrins, large Stokes shifts, multiphoton excitation, and the ability to produce $^1O_2$ species, which is ideal for PDT type II. Moreover, most of the ruthenium (II) complexes are chemically and photochemically stable, and display little or no photobleaching in contrast to porphyrins derivatives.[50, 52] As previously described, a ruthenium (II) complex (TLD-1433) is nowadays in phase II clinical trials for a type II PDT treatment of bladder cancer.[53] This complex can be activated with green light (520 nm to 540 nm) generating $^1O_2$ to the bladder tumour. The difference of toxicity between dark and light has two orders of magnitude. Besides it demonstrates a very quick clearance *in vivo,* in which 24 hours after administrating the drug, the concentration was in the nM range. TLD-1433 does not show effects of skin photosensitivity, which is one of the side effects of the photosensitisers currently in the market.[54, 55]

Due to its promising efficacy, current literature is rich in PDT studies using ruthenium (II) complexes.[8, 56-58] PACT, however, is a recent field and therefore there is a lack of studies in this area.[59] PACT entails an irreversible photochemical reaction that leads to the formation of a new complex toxic to the cells. Ruthenium (II) complexes have very promising results for PACT due to their excited state nature.[60] Light irradiation of inert d^6 Ru(II) complexes generates an excited triplet metal to ligand state (^{3}MLCT) as stated above. However, the triplet metal state (^{3}MC) for these compounds has a very similar energy to ^{3}MLCT, allowing rapid interconversion between the ^{3}MLCT and this highly dissociative character state (^{3}MC) (Figure 1.9). This results in a ligand exchange between the photoactivable ligand and solvent molecules. This ligand is then released inside the tumour and becomes toxic for the cells.[61]

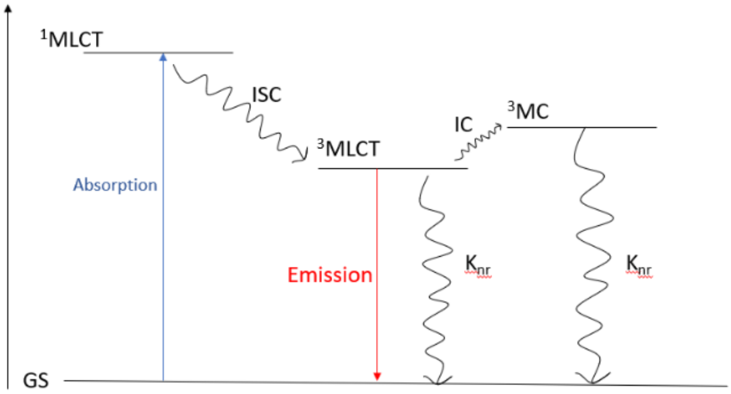

Figure 1.9- Mechanism of action of Photoactivated Chemotherapy (PACT), demonstrated by Jablonsky diagram.

An ideal photosensitiser for light therapy should be nontoxic in the dark, stable in a biological media, and soluble under physiological conditions, while the wavelength of activation should ideally lie within the therapeutic window and have relatively high efficiency of the photochemical process.[62, 63] Moreover, a photosensitiser should be independent of oxygen levels. Several tumours can be found in tissues that lack of oxygen (hypoxic tumours). In these cases, PDT efficacy can be limited.[64] Moreover, although PACT is an exciting strategy that has gained a lot of attention in the last few years, there is no example of a PACT compound currently in clinical trials.[65] The combination of a PDT and a PACT therapy can be a powerful strategy since it combines ROS production with a toxic compound formed upon irradiation on the tumour cells. Thus, studies on this synergetic effect have started to emerge, in which, the groups Turro and Bonnet have been extensively studying the combination effect between PDT and

PACT.[66-71] The dual-active compound $[Ru(bpy)(dppn)(CH_3CN)_2]^{2+}$ showed a $^1O_2$ production and photoinduced ligand exchange from CH_3CN to water molecules, which exhibited a potent toxicity of 2.5 fold more potent than its precursors.[72] Later, another ruthenium (II) complex with the same ligand dppn but also containing a peptide that inhibits enzymes leading to cell death (Figure 1.10), was shown to be a promising dual agent by undergoing ligand exchange and release the protein, but also by producing $^1O_2$ to kill tumour cells.[73] Moreover, after light irradiation, the complex can damage DNA demonstrating a three-way therapeutic system to tackle Hela cells.

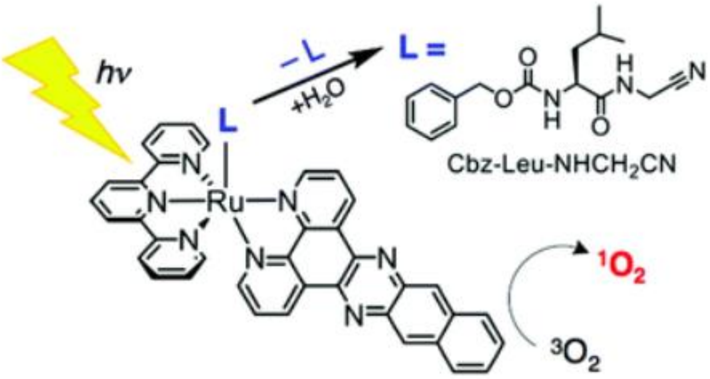

Figure 1.10- Schematic representation of a ruthenium (II) complex dual phototoxicity by singlet oxygen species formation and release of a protein that inhibits enzymes, leading to cell death, obtained from[73].

1.2.2.2 Using DNA as treatment strategies

In addition to light therapy, one of the most studied strategies for cancer therapy is the induction of DNA damage through interaction with small molecules. B form is the most common DNA conformation found within the cells. Although less common, A and Z forms are also other conformations that DNA can adopt under certain specific conditions and can be identified as a left-handed double helix (A-form) or a left-handed helix with a zig-zag pattern on the phosphate bone (Z-form).[74] Due to being the most common form in nature, scientists have been extensively studying B-form DNA, to allow an efficient interaction between DNA and small molecules.[75, 76] B-form DNA is represented by two polynucleotide chains that coil around each other to form a right-handed double helix. The two chains are oriented in opposite directions, and they hold together by nucleobases that point towards the centre of the helix. Complementary nucleobases bind to each other by hydrogen bonds (cytosine (C)- guanine (G) and thymine (T) - adenosine (A)). These hydrogen bonds provide enough stability to hold the DNA in a double helix structure. DNA has a structural framework of alternating deoxyribose sugars and phosphate groups forming a linear chain that runs along the length of each DNA strand. This negatively charged backbone provides structural support and flexibility to the helix, allowing the nucleobases to be in the centre of the helix where they can interact with each other. The π-π stack between the nucleobases provides a twisting of the strands which allows the presence of the minor and major grove on the DNA double helix. By having different sizes, the accessibility to each groove is also different and it depends very much on its position and the moleculare structure.[77]

There are two types of interactions with DNA: irreversible and reversible. Irreversible interaction refers to the formation of a covalent or coordination bond between the small molecule and the DNA and usually implicates inhibition of DNA transcription or replication followed by cell death.[78] A very well-known example of this mode of action is cisplatin, where it binds to guanine sites of DNA.[79] Reversible interactions can be from external electrostatic interactions (Figure 1.11- A), groove binding (Figure 1.11- B), external self-aggregation (Figure 1.11- C), or intercalation (Figure 1.11- D).[80] External electrostatic interactions originates from positively charged molecules that interact with the negatively charged phosphate backbone. The groove binding typically occurs when a molecule has the right size and flexibility to be able to lay in one of the grooves and interact with DNA by electrostatic interactions, Van der Waals forces and hydrogen bonds. Usually, these molecules have aromatic rings that allow them to rotate around the bonds and adapt to the DNA shape. External self-aggregation happens when a molecule, usually aromatic planar species, stacks in the external part of the double helix forming huge aggregates. Finally, intercalation is a stacking interaction upon the insertion of an aromatic planar species between the base pairs of DNA. This interaction comes from π-π stacking but also with Van der Waals forces and hydrophobic interactions. Intercalation can force DNA to change configuration from B-form to A-form and cause helix unwinding. Although these structural changes are not always harmful or toxic to DNA, several intercalators can be used as anticancer agents, antibiotics or antifungals.[78, 80, 81]

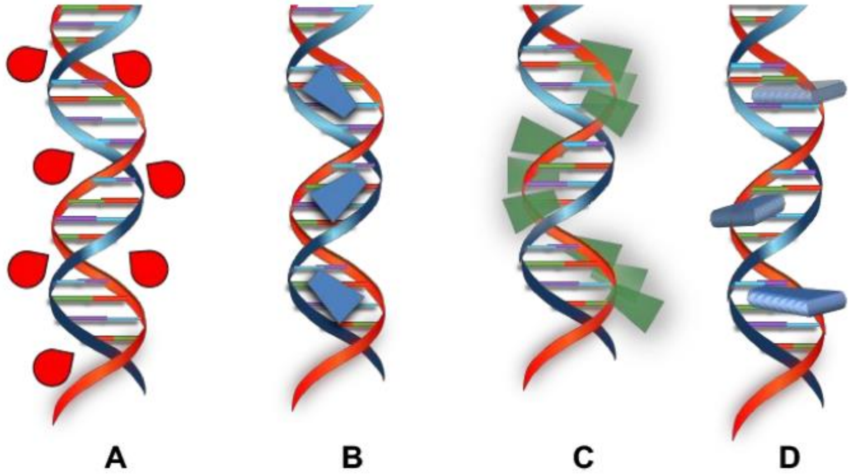

Figure 1.11- Schematic representation of the main reversible interactions, A- external interaction, B- interaction in the grooves, C- external self-aggregation, D- intercalation, obtained from[80].

Ruthenium (II) complexes have been extensively studied for their interaction with DNA.[82] These complexes exhibit octahedral geometry with a ruthenium (II) complex atom in the centre surrounded by three aromatic bidentate and planar ligands. Overall, these complexes interact noncovalently to DNA by electrostatic, Van der Walls forces and/or π-π stacking by intercalating their rigid planar aromatic ligands between DNA base pairs.[83] When ruthenium (II) complexes interact with DNA, they can perturb the electronic properties of the intercalator allowing monitoring this interaction by absorption spectroscopic studies. It is generally agreed that a hypochromic effect (decrease in absorption intensity) in the UV-Visible spectrum upon DNA binding is due to intercalation and a strong π-π stacking between the aromatic planar ligand of the ruthenium (II) complex and DNA base pairs.[84] When an intercalator interacts with the DNA base pairs, the π* orbital of the intercalative ligand can couple with π orbital of the base pairs, leading to a decrease in π- π* transition energy, resulting in a red shift in the intra ligand (IL) band visible on UV-Vis spectroscopy.[85, 86] Emission spectroscopy is also a very useful tool to analyse DNA interactions with ruthenium (II) complexes. When ruthenium (II) complexes bind to DNA, they reduce the accessibility to water molecules, avoiding its luminescence quenching. Therefore, the emission intensity of ruthenium (II) complexes tends to increase upon interaction with DNA.[87] Besides these two common techniques to analyse the interaction between ruthenium (II) complexes and DNA there are others methods that are equally important, such as linear and circular dichroism, viscosity, thermal denaturation and displacement studies. Linear and circular dichroism are also spectroscopic techniques used for analysis of DNA interaction. Linear dichroism (LD) measures the absorption of linearly polarised light and can give information on the orientation and conformation of a molecule.[88] LD usually uses two beams, one parallel and another perpendicular to the flow, so that the molecules that are not oriented in each direction are not going to be detected. DNA helix can be oriented so that the base pairs are perpendicular to the helix axis, leading to a negative LD spectrum (Figure 1.12). If the molecule is oriented parallel to the flow then the LD spectrum would be positive.[89] When a ruthenium (II) complex is added to the oriented DNA solution, it is only possible to observe it if it binds to DNA, i.e, if binding occurs in the same orientation.[90] Therefore, if the ruthenium (II) complex is an intercalator between the base pairs, then it will be oriented perpendicular to flow, producing a negative signal, whereas if it is a grove binding the signal will be positive. In contrary to LD, where the electromagnetic waves oscillate on a single plane, in circular dichroism (CD) two electromagnetic wave plans are at 90° degrees phase difference, rotating as the light beam propagates. The absorption of left and right-handed circularly polarised light by chiral molecules is different, giving them different CD spectra.[88] The CD spectrum can be very useful to detect conformational changes of DNA upon addition of another molecules, such as a ruthenium (II) complex. Although the base pairs of DNA are not chiral, the backbone of this structure is. The chirality of the sugar groups induces a CD signal in the π-π* transition of the base pairs and therefore each different DNA conformation has a different CD spectrum.[91] Very often both LD and CD techniques complement each other to demonstrate an interaction between a ruthenium (II) complex and DNA.[92]

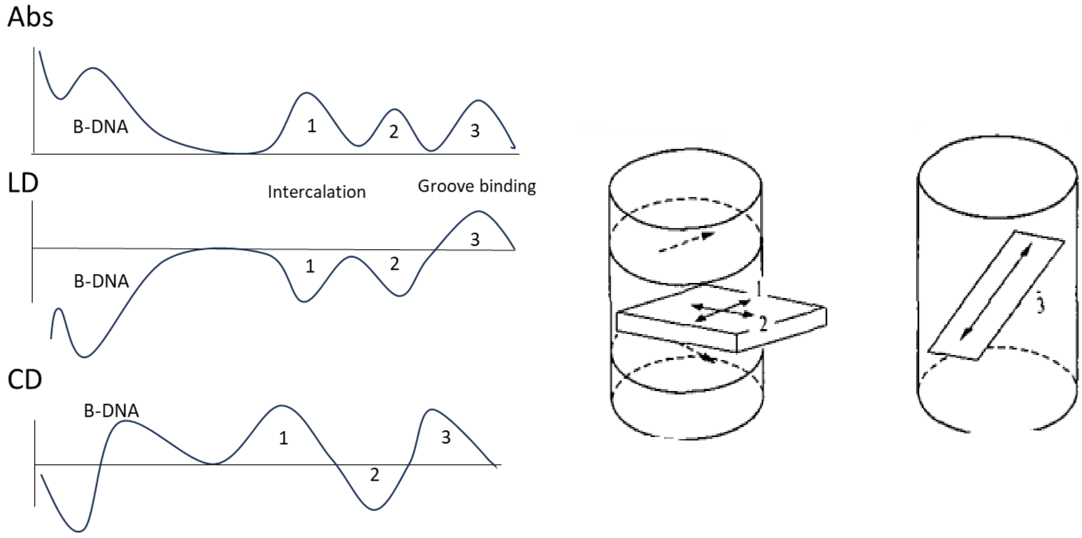

Figure 1.12- Schematic representation of an LD and CD spectra in comparison with an absorption spectrum when a B-form DNA interacts with an intercalator (1,2) or a groove binder (3). Intercalators are oriented perpendicular to the flow and groove binders are usually with a 45° angle to the helix axis, adapted from[88, 89].

Viscosity is defined as a resistance to a liquid flow.[93] When an intercalator bind to DNA between the base pairs, there is an increase in the DNA length and therefore an increase in DNA solution viscosity.[94, 95] On the other hand, if the ruthenium (II) complex binds to one of the grooves with no intercalation process, typically there will be no variation in DNA viscosity because the DNA length would not change.[96] When a ruthenium (II) complex binds by partial intercalation, usually the DNA would bend, leading to a decrease in DNA length and viscosity.[96] Therefore, measuring the viscosity of a DNA solution before and after ruthenium (II) interaction, can be a good indication to the type of binding involved between these two molecules.

Thermal denaturation can be defined as the temperature needed to make the double strand DNA to dissociate into single strands. This effect usually leads to an hyperchromic effect (increase in absorption intensity) visible on the DNA bases' absorption band (λ_{max} = 260 nm). It is well known that the temperature where half of the total base pairs is unbonded (T_m) considerably increases in the presence of an intercalator, leading to an easy identification of an intercalation process.[97-99] Displacements studies are usually carried out with DNA and ethidium bromide. This well-known DNA intercalator significantly increases its fluorescence upon DNA binding and therefore it is a very used dye for DNA detection.[100] To understand if the ruthenium (II) complex is a DNA intercalator, a competitive spectroscopic study can be performed, where the concentration of DNA and ethidium bromide is kept constant, but the concentration of the ruthenium (II) complex gradually increases. If upon the addition of the ruthenium (II) complex, a decrease on ethidium bromide fluorescence is observed than it means that the ruthenium (II) complex is displacing the ethidium bromide and intercalating between the DNA base pairs.[101]

1.3 Nanomaterials

Nanotechnology emerged in the 1980´s and since then, nanomaterials have been used in several applications such as environment, agriculture, biotechnology and biomedical sciences.[102-104] Nanotechnology produces nanoparticles (NPs) of various types at a nanoscale level (1- 100 nm).[103] Nanoparticles (NPs) can have different shapes such as nanorods[105], nanostars[106], nanowires[107], nanofibers[108] and quantum dots[109], which can be made of gold[110], silver[111], platinum[112], palladium[113], silica[114], carbon[115], a wide range of polymers[116] and many others. NPs have different size-dependent features, due to their very small size but large surface area. This allows the functionalisation of the nanoparticles' surface with molecules of interest, creating a strong benefit in nanotherapeutics research, since nano sized particles can be functionalized with molecules to their surface such as antibodies, DNA fragments, nucleic acids, and other biological moieties.[117] Consequently, NPs can easily accumulate inside the cells, due to their specific targeting and fast uptake. Due to a high surface area, nanoparticles have the potential to have high loading of compounds attached to their surface, and therefore, enable the delivery of larger quantities of drugs to the cells, than a typical molecular drug in solution. This has let to, NPs be extensively researched for use in cancer imaging and therapy (Figure 1.13).[118-120]

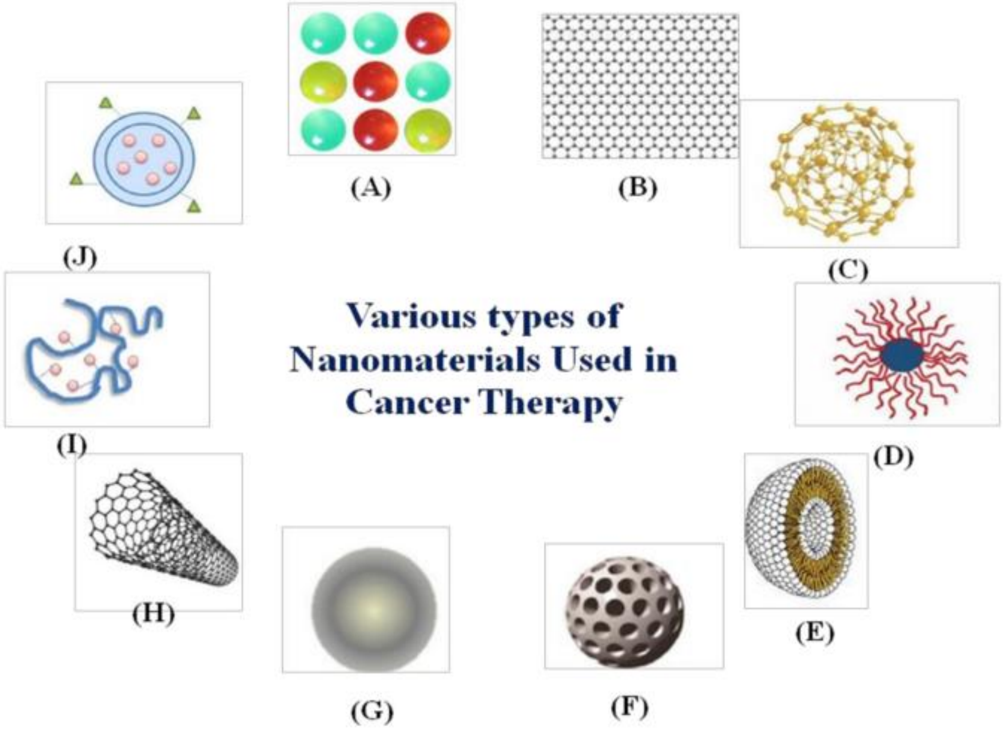

Figure 1.13- Types of nanomaterials researched for cancer therapy: A- quantum dots, B- graphene, C- gold nanoparticles, D- polymeric micelles, E- liposomes, F- silica nanoparticles, G- magnetic nanoparticles, H- carbon nanotubes, I- polymer-drug conjugates, J- polymeric nanoparticles, obtained from[118].

The first nanomaterial approved by the Food and Drug administration (FDA) was a delivery system based on liposomes for the cancer drug doxorubicin in 1995.[121] Since then, the quantity of research focussing on NPs as delivery systems has significantly increased.[122] Until now, more than 90 nano drug delivery systems have been approved.[123] The latest nanomedicine formulations approved by the FDA, in 2021, were Comirnaty and mRNA-1273, vaccines of mRNA-containing lipid nanoparticles for SARS-CoV-2 virus.[124-126] However, for the purpose of cancer treatment the last nanomedicine approved and marketed was in 2019, for metastatic breast cancer using paclitaxel (an approved anticancer drug) formulated as albumin bound nanoparticles.[127] Paclitaxel targets microtubules inducing apoptosis of cancer cells by mitotic arrest. However, this drug is associated with several side effects associated with the vehicles used to improve the solubility of the drug. Using an albumin nanoparticle carrier not only improved the solubility of the drug but also minimised the side effects, producing a good safety profile for cancer treatments.[128]

Despite the advances nanotechnology has brought to cancer treatments, mostly liposomes, polymers and protein-based nanoparticles have been approved. Nonetheless, various others, including inorganic nanoparticles, have generated significant attention due to their unique and promising characteristics; offering the possibility not only of treatment but also of an early diagnosis. For instance, gold nanoparticles have been extensively studied for biomedical applications, hinting to a promising future in nanomedicine.[129]

1.3.1 Gold nanoparticles

Gold nanoparticles (AuNPs) are nanomaterials made of gold. AuNPs have been prepared in various shapes such as spheres, rods, stars, wires and cages. These nanomaterials have been intensively explored for biosensors, diagnostics, and therapeutics in cancer but also bacteria resistance, due to their exciting properties.[130] AuNPs have high chemical and physical stability as well as high biocompatibility, ease synthesis, characterisation, and functionalisation with a wide range of molecules, and their unique optical properties due to their surface plasmons.[103, 131-133] Plasmons are oscillations of free electrons in metals at a defined frequency. In a nanoparticle, these oscillations create a localised electric field around the nanoparticle, called a resonance (Figure 1.14). When the frequency of incident visible light matches the frequency in which the electrons oscillate collectively (plasmon resonance), the AuNPs absorb that light very efficiently, leading to scattering peaks and spectral absorption. The absorption of light by the AuNPs is therefore very dependent on the shape and size of the nanoparticles, which can be identified by UV-Vis spectroscopy. Thus, when the shape or size of the AuNPs changes, the electrical field density of the surface of the nanoparticles will change, and the surface plasmon resonance (SPR) of the AuNPs will change. Thus, the UV-Vis λ_{max} will shift.[130, 134, 135] Moreover, the SPR of AuNPs offer the possibility of multimodal imaging such as dark field microscopy[136], due to the light scattering properties, but also photoacoustic imaging[137] and electron microscopy[138] due to the highly dense electronic structure and their high absorption in the visible and near infrared region.

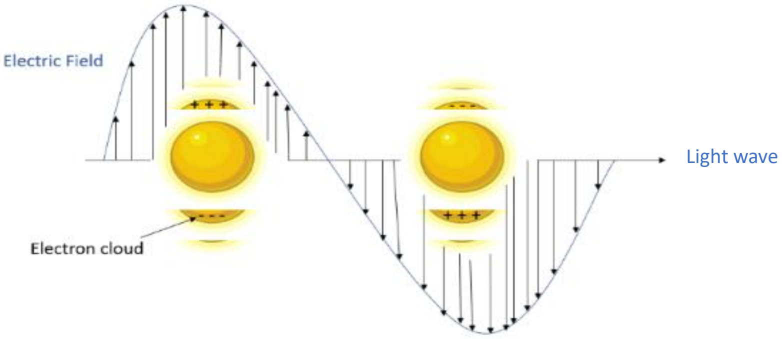

Figure 1.14- Illustration of localised surface plasmon resonance (SPR) in a gold nanoparticle.

1.3.2 Gold nanoparticles for cancer theranostics

Due to their large surface to volume ratio, facile functionalisation, surface plasmon properties and low cost, AuNPs have been tested as biomarkers for cancer diagnosis.[139]

For example, AuNPs can detect circulating tumour cells (CTC). CTCs are responsible for tumour metastasis, but they also can be found in early stages of cancer and therefore, their early detection is of primary important.[140] Functionalising AuNPs with antibodies or aptamers that specifically target CTCs in the bloodstream is one of the strategies used in the current literature.[141] By attaching up to 95 aptamers to AuNPs an enhanced capability of molecular recognition was observed leading to an increase from 49 % to 92% of CTC's detection (Figure 1.15).[142] Besides CTCs, AuNP-based strategies have also demonstrated detection enhancement for circulating nucleic acids and vesicles in the blood, excluding healthy blood cells.[141]

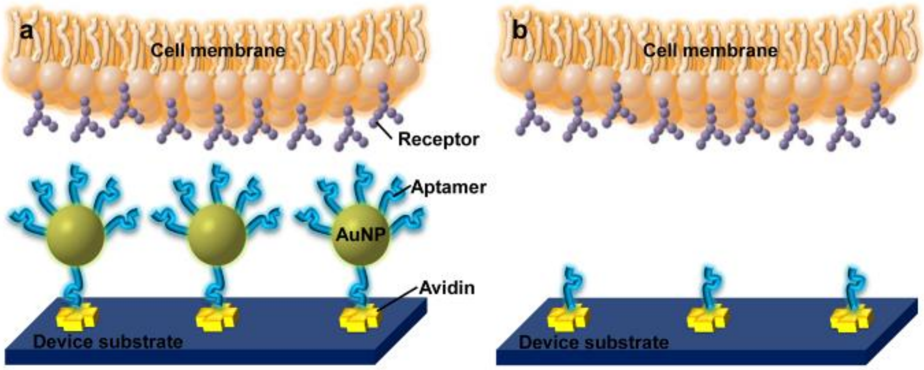

Figure 1.15- Schematic illustration of enhanced cell capture using AuNP-aptamer (a) versus a poorer detection with only aptamers (b), obtained from[142].

Proteases are implicated in a wide range of diseases, such as cancer, so monitoring proteases activity can be a useful biomarker in cancer diagnosis. Common tools to monitor proteases activity includes the use of fluorescence, mass spectrometry and MRI.[143] However, recently a AuNP-based strategy showed promising results *in vivo* for colorectal cancer. A nano sensor was made by functionalising gold clusters with a large protein carrier that binds to biotin (Neutravidin) and a protease-cleavable peptide linker.[144] This nano sensor was made so that it disassembles with high levels of proteases such as MMP9 (Figure 1.16). After cleavage, the gold clusters are efficiently filtered through the kidneys and can be detected in the urine by a colorimetric assay. This strategy showed that this novel system can be used as a sensor for colorectal tumour, however it requires further investigation to determine if it can be extended to other types of cancer or disease .[144]

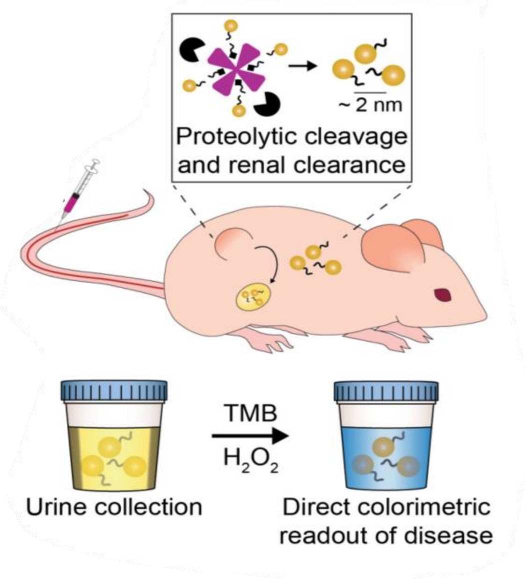

Figure 1.16- Schematic demonstration of gold nano sensors for the detection of high levels of protease MMP9, obtained from[144].

AuNPs have been shown to be able to detect genetic mutations in tumours[145] and even volatile organic compounds (VOCs)[146] which are produced through the metabolism of cancer cells. Moreover, AuNPs are strong contrast imaging agents due to their absorption coefficient larger than organic dyes, optimal tissue penetration with no photobleaching.[147] Thus, AuNPs can be used to track STEM cells *in vivo* by photoacoustic imaging with high spatial and temporal resolution.[148] In this study, gold nanorods were coated with silica, to shift the plasmon resonance peak to 910 nm, then coated with a ROS sensitive near infrared dye IR775c and doxorubicin (an anticancer drug known to intercalate with DNA and produce ROS species). The nano system was able to track cells viability for 10 days and monitor cell death caused by doxorubicin (Figure 1.17).

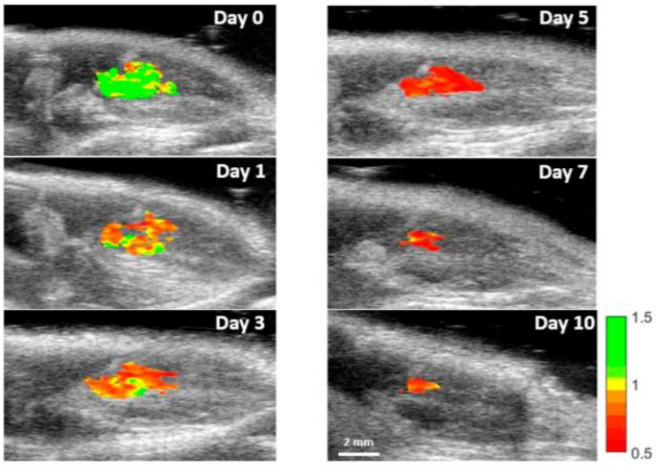

Figure 1.17- Overtime photoacoustic images at 795 and 920 nm of labelled STEM cells with the nano system, showing a cell viability decrease due to the addition of doxorubicin, obtained from[148].

Besides photoacoustic imaging, AuNPs have been used as contrast agents for several other imaging techniques such as magnetic resonance imaging, computed tomography and photothermal imaging showing that AuNPs are a good option for long term imaging due to their biocompatibility, low toxicity and relatively long tumour retention.[149-151] Improving imaging techniques to allow early diagnosis of cancer is crucial to successfully tackling tumour cells. However, combining a system that allows for early imaging of a tumour with therapy has been the goal of cancer research. In general, chemotherapeutic drugs can have solubility and biocompatible issues, fail in tumour targeting or even enhance drug efflux in resistant tumour cells. Therefore, AuNPs can be designed such that there is an increase in drug loading to maximise the therapy efficacy and utilise the visible and near-infrared response to eliminate drug resistance limitations. It has been shown in the literature that after making sure that the gold nanostars were accumulated in lung cancer cells, the drug mitoxantrone that was loaded in the surface of the nanostars, by electrostatic interactions, was released by laser irradiation and therefore effectively killed the tumour cells.[152] In a different study, it was shown that by coating AuNPs with the anticancer drug, drug delivery around tumour cells and cellular uptake increased 6.5 fold rather than just using the drug by itself.[153] Even without drug release, it is possible to kill cancer cells by using gold nano systems. AuNPs can be used as nano carriers of photosensitisers for photodynamic therapy (PDT) and therefore produce ROS species that allow cancerous cells apoptosis.[154] Moreover, it has been shown that the fact that the photosensitisers are attached to AuNPs, enhances the ROS production due to its high localised plasmonic field.[155, 156] The SPR effect can lead to the generation of high energy electrons upon light irradiation that can participate in redox reactions and contribute to the ROS production of the photosensitiser. Moreover, AuNPs themselves can generate ROS. It has been demonstrated that AuNPs can catalyse the decomposition of hydrogen peroxide into hydroxyl radicals and oxygen, which induces cell death mechanisms.[157-159] It is important to note that although this ability can be beneficial for photodynamic therapy, it can also raise questions related to the toxicity of AuNPs. Therefore, it is important to bear this in mind during the design of an efficient gold nano system against cancer.

1.3.3. Gold nanoparticles in clinical studies

Despite the promising results of AuNPs systems in nanomedicine, few of them have reached clinical trials. This is assumed to be due to the direction of AuNPs research being directed at a materials level, enhancing the nanomaterial properties rather than focusing on what is clinically relevant.[160] Therefore, the only AuNPs that have reached clinical trials have had very simple formulations, making them easy to scale-up production and predict the *in vivo* behaviour. Moreover, there are studies that show gold accumulation in the liver and spleen, leading to incomplete excretion and toxicity concerns.[160, 161] However, with this in mind there is one case of AuNPs that is currently in phase II of clinical trials for cancer therapy, showing that AuNPs have exciting properties that cannot be matched by other formulations, and therefore reaching the market is a possibility.[162] CYT-6091 is a PEGylated AuNP functionalised with recombinant human tumour necrosis factor alpha (TNF-α). This is a protein produced by the immune system and is involved in several processes such as inflammation, immune response and apoptosis, and so it can be a key factor against the formation and progression of tumours. However, since TNF-α is a very important inflammatory mediator widely expressed in several cells, high levels of this protein can have the opposite effect, contributing to the promotion of tumour growth by creating a pro-inflammatory microenvironment.[163] Therefore, TNF-α must be administered with strict control over quantity limits and biodistribution.[164] Through the use of AuNPs, it is possible to control the amount of TNF-α as well as stablish an efficient targeted delivery system for tumours that are not able to be surgically isolated (Figure 1.18). Using AuNPs allowed an easy functionalisation of the protein TNF-α to the surface of the nanoparticles, due to a strong thiol bond between the gold and the protein.

Moreover, the PEGylated AuNPs injected into solid tumours, increased the TNF-α circulation within the body. The results from phase I showed the safe delivery of TNF-α to tumour cells, even after administrating triple the usual dose of TNF-α. The AuNPs-TNF system was demonstrated to disrupt blood vessels in tumour sites allowing chemotherapeutics to penetrate and kill cancer cells.[164] Aside from cancer therapy, there are AuNPs formulations that are active in phase I clinical trials for autoimmune disorder type 1 diabetes, a vaccine against dengue fever and COVID-19.[160]

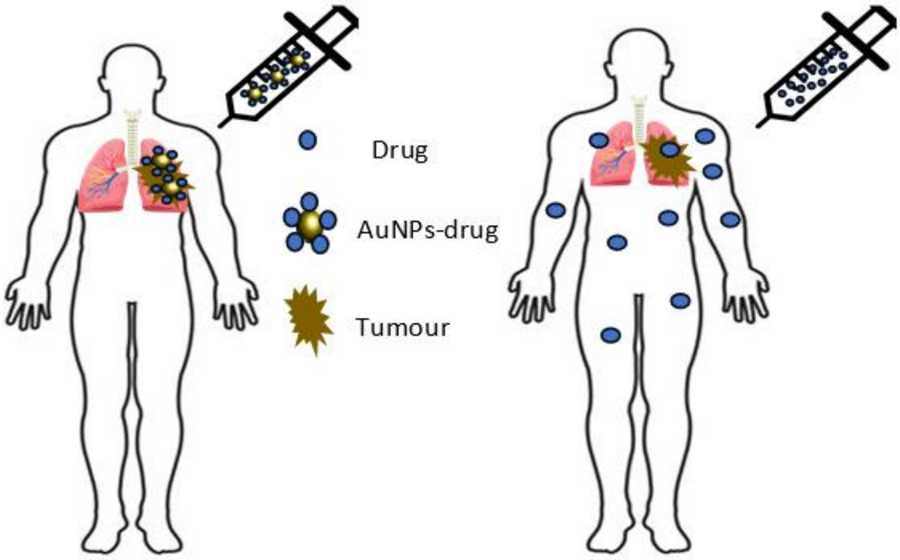

Figure 1.18- Schematic representation of drug distribution in a human body after administration of a AuNP-drug formulation (left) or only the drug by itself (right).

1.4 Gold nanoparticles and ruthenium (II) complexes for cancer theranostics

Given the remarkable properties of both AuNPs and ruthenium (II) complexes, it is evident that their combination can serve as a powerful theranostics strategy in cancer research. In early studies, focus on conjugating ruthenium (II) complexes to AuNPs was for use as a coating and stabilisation agent for the study of the photophysical properties of the complexes.[165] Later, it was understood that this nano luminescent system can be used for cell imaging using techniques such as confocal microscopy to detect a ruthenium luminescence signal and transmission electron microscopy to detect AuNPs. Zhang and co-workers, made a $RuNH_2$ complex and conjugated through the amine to the AuNPs to be used as a two-photon luminescence sensor.[166] On addition of a thiolate amino acid (Cys and Hcy), there is displacement of the ruthenium (II) complex by the amino acid, on the surface of the AuNPs. The liberated ruthenium (II) complex then, exhibits a strong two-photon signal that can be detected in live cells and mouse tissues with a penetration depth up to 170 µm (Figure 1.19).[166]

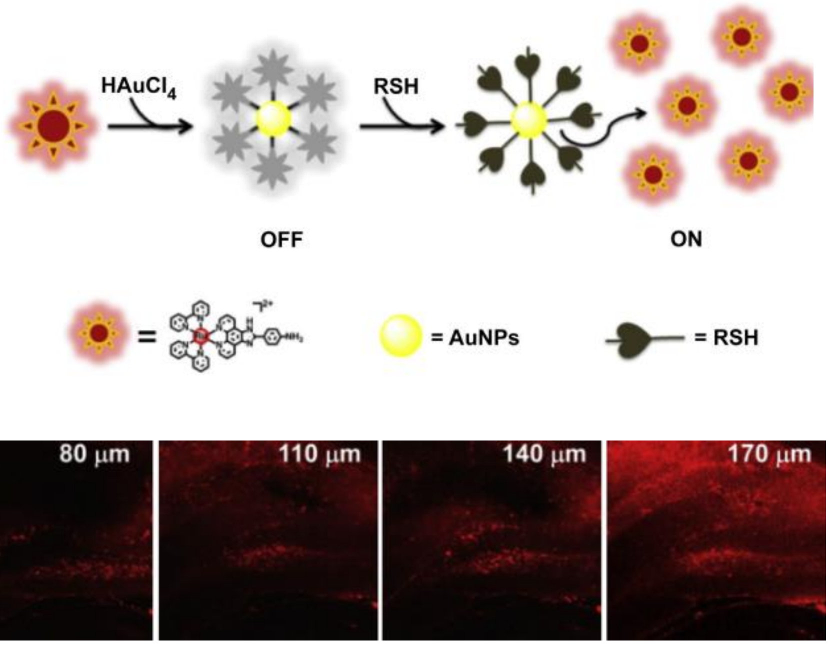

Figure 1.19- Schematic representation of the $AuNP.RuNH_2$ nano system and the detection of the ruthenium signal by two-photon microscope in different penetration depths of a rat slice, figures obtained from[166].

Later, the same group realised that by conjugating two-photon luminescence ruthenium (II) complexes, it would be advantageous not only for imaging but also to tackle cancer cells through photothermal therapy.[167] Photothermal therapy (PTT) is a therapeutic strategy that converts light energy into heat. Tumour cells do not resist heat well, and therefore increasing the temperature of the tumour site allows the triggering of cell death mechanisms.[168] In this study, three different ruthenium (II) complexes were conjugated to AuNPs, demonstrating that AuNP.Ru2 had the highest two-photon luminescence. So, the PTT effect of AuNP.Ru2 was investigated, which demonstrated the ability of real time imaging of the tumour and an *in vivo* tumour ablation through PTT after specific irradiation of the tumour tissue with 808 nm light (Figure 1.20).

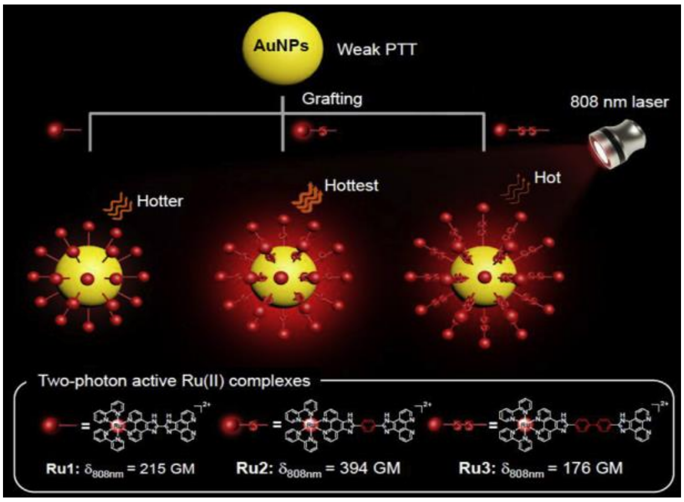

Figure 1.20- Schematic representation of the three different ruthenium (II) complexes in study attached to AuNPs and demonstration of the two-photon luminescence and PTT efficiency of the three nano systems, obtained from[167].

Recently, AuNP.Ru nano conjugates have been applied as stabilising agents for collagen *in vitro*, attributed to their ability to generate $^1O_2$ through photo crosslinking.[169] Additionally, they have been employed to address the limitations of Ru(II) arene complexes in cancer research, aiming to enhance their performance.[170] Half sandwich Ru(II) arene complexes have shown their anticancer properties.[171, 172] However, most of these complexes have two big limitations; the solubility in physiological media and the short half-life during blood circulation. To overcome these drawbacks, these complexes can be attached to AuNPs, to increase their solubility and cytotoxicity against colorectal adenocarcinoma compared to the complex on its own. However, localisation of the AuNPs inside the cells and an apoptosis mechanism is needed in this study to evaluate the performance of AuNP-Ru(II) arene conjugates. [170]

The remarkable progress in the conjugation of AuNP with ruthenium (II) complexes for biomedical applications, specifically in cancer research, suggests the potential of these nano systems to progress to clinical trials. However, as the utilisation of these nano systems is still relatively recent, there is a lack of research on this topic. In order to fill the prerequisites essential for a formulation to reach clinical trials, it is crucial to continue the investigation in depth and acquire an extensive understanding of these nano systems' behaviour.

1.5 Thesis Outline

In this work, AuNPs conjugated with three different luminescent ruthenium (II) complexes were designed, synthesised, and characterised. Using the appropriate distance from the metal complex to the gold and an appropriate surfactant, AuNP.Ru conjugates can enhance the luminescence lifetime of the ruthenium (II) complexes. The novel AuNPs-Ru conjugates showed the ability of live cell imaging of A549 cancer cells and their accumulation in the cytoplasm and nucleus of the cells after 4- and 12-hours incubation. AuNP.Ru conjugates bound strongly to DNA by intercalation and electrostatic interaction, revealing a possible DNA uncoiling effect. Additionally, AuNP.Ru showed promising PDT effect by revealing phototoxicity in the nanomolar range upon irradiation with a 535 nm visible green light and no toxicity in the dark.

Chapter 2 explains the photophysical study of two of the complexes synthesised (RuPhenL1 and RuPhenL2), their attachment to two different sizes (13 nm and 25 nm) AuNPs and their characterisation. It also demonstrates the importance of surfactants on the surface of AuNPs and their influence on the ruthenium luminescence signal, in which different types or lengths of surfactant can increase or decrease the luminescence lifetime of the ruthenium (II) complexes when attached to AuNPs.

Chapter 3 evidence the photophysical study of the third luminescence ruthenium (II) complex (RuDppzL2) and its attachment to AuNPs. In this chapter, an investigation of the interaction between AuNP.Ru and DNA is carried out. To the best of our current knowledge, this is the first time that the interaction between AuNP.Ru and DNA can be visualised by microscopy, in which a possible uncoiling of the double helix of DNA to two single strands upon AuNP.Ru binding is visible. This interaction is then further investigated, where intercalation and electrostatic interactions are the two suggested modes of binding between DNA and AuNP-Ru.

Chapter 4 shows the visualisation of the AuNP.Ru conjugates in A549 cells by confocal and electron microscopy, demonstrating accumulation in both the cytoplasm and nucleus of the cells. 25 nm size AuNPs revealed a higher cellular uptake than 13 nm

AuNPs. However, the results also showed that higher lipophilicity of the ruthenium (II) complexes improved the uptake, even in 13 nm AuNPs. The phototoxicity of AuNP.Ru conjugates was evaluated in the dark and after irradiation with visible green light at 535 nm, revealing no toxicity in the dark in A549 cells but a significant drop in cell viability upon light irradiation, demonstrating a promising PDT effect.

Each research chapter contains a brief literature review to introduce the context discussed, followed by discussion of results and conclusions. Afterwards, there is an experimental section and appendices detailing additional data. To finish, a general conclusion and future work is presented.

2. Effect of surface coating on ruthenium gold nanoparticles luminescence properties

2.1 Introduction

2.1.1 Luminescence properties of Ruthenium (II) complexes

The combined luminescence and cytotoxic properties of ruthenium (II) complexes make them promising candidates for biomedical applications. The luminescence properties of the complexes depend on the ligand field strength, ligand intrinsic properties and oxidation states of the metal.[173] Therefore, the type of ancillary ligand around the metal centre plays a very important role on tunning the overall properties of the complex. One of the first and therefore most studied complexes, $Ru(bpy)_3Cl_{2,}$(bpy= 2,2'-bipyridine) was found to be of relevant interest because of its photochemical stability, relatively high luminescence in aqueous solution (4 % quantum yield and 360 ns of luminescence lifetime) and good water solubility.[48] Nevertheless, it was discovered early on that $Ru(phen)_3Cl_2$, (phen= 1,10-phenanthroline) had higher luminescence lifetimes and quantum yields than $Ru(bpy)_3Cl_2$ (8 % quantum yield and 450 ns of luminescence lifetime in aqueous solution).[48, 174, 175] The complex $Ru(phen)_3Cl_2$, although structurally analogous has a characteristic blue shift in absorption and emission, when compared with $Ru(bpy)_3Cl_2$.[48] It is assumed that this is due to the incorporation of the bridgehead carbon into the 1,10-phenanthroline structure causing some rigidity to the ligand. This causes destabilization and an increase on energy of the π_L* orbital and therefore a bigger gap between HOMO and LUMO. This increase in the HOMO-LUMO gap leads to a likelihood decrease for non-radiative decay processes which causes an increase of quantum yield.[176-178] Fluorescence quantum yield is defined as a measure of emission efficiency of radiative photons upon excitation by light; that is, the ratio of the number of photons emitted to the number of photons absorbed. This can be showed as a relationship between the rate of radiative decay (k) and the total decay rate (eq.1)

$$\phi = \frac{k}{k + k_{nr}} \qquad (1)$$

The luminescence lifetime is defined as the inverse of the total decay rate. (eq.2) The total decay rate includes radiative decay (k) such as fluorescence or phosphorescence and nonradiative decay (k_{nr}) which involves dissipation of energy by heat or vibrations, or energy transfer decay.

$$\tau = \frac{1}{k + k_{nr}} \qquad (2)$$

Therefore, the relationship between quantum yield and lifetime can be expressed as

$$\phi = \frac{k_{\tau}}{(1 + k_{nr\tau})} \qquad (3)$$

The lifetime of a molecule is related to the probability of undergoing radiative and nonradiative decay pathways. If a molecule has long lifetimes, this does not mean that the radiative decay is long, in fact it could mean that the nonradiative decay is longer than the radiative decay. The quantum yield is influenced by the competition between radiative and nonradiative decay. If the molecule undergoes extensive nonradiative decay, that means there are fewer photons emitted compared to the number of photons absorbed and therefore, the quantum yield will decrease.[179-181] An increase in luminescence lifetimes and quantum yields could make a difference when used for biomedical applications such as imaging in cells. From that reason, the ligand 1,10-phenantroline was chosen for the two complexes studied in this chapter.

2.1.2 Influence of surface coating on gold nanoparticles

Gold nanoparticles (AuNPs) due to their unique chemical and physical properties have potential for medical applications. Their small size carries a big advantage since it makes it possible to cross multiple biological barriers and be internalised into cells and specific organelles of the cells, that otherwise would be very hard to reach and penetrate.[182] Peckys and co-workers have showed, using scanning transmission electron microscopy (STEM), that 30 nm gold citrate nanoparticles could be internalised by live kidney cell type and bound to membrane of vesicles.[183] More recently, Katoozi and co-workers studied the uptake of cetyltrimethylammonium bromide (CTAB) coated gold nanoparticles and quantified the number of particles inside the cells by dark-field microscopy and reflectance confocal.[184] Furthermore, studies have showed internalisation of PEG coated gold nanoparticles into cells by using techniques such as induced coupled plasma mass spectrometry (ICP-MS)[185, 186], transmission electron microscopy (TEM)[187] or even confocal microscopy, in reflection mode, can be very efficient[188]. However, if a fluorophore is attached to AuNPs, luminescence imaging also becomes a reality. Due to the high electron density on the surface of AuNPs and the presence of a fluorophore, multimodal imaging is possible, making it a big advantage of these systems in relation to the traditional molecular probes used for biological imaging.[187] To attach fluorophores to gold nanoparticles usually is necessary to include anchoring groups, such as carboxylic acids[189], disulfides[190], sulfonates[191]. However, thiols are by far the most studied molecules due to their high binding affinity with gold and long-term stability.[192, 193]

Ruthenium (II) complexes, due to the photophysical properties, are good candidates as luminescent probes on the surface of the gold nanoparticles. Within the Pikramenou group, ruthenium (II) complexes attached to AuNPs have been explored due to its easy functionalisation to the surface of AuNPs and good photostability.[194-198] Rogers, Claire and co-workers synthesised 13 and 100 nm gold nanoparticles coated with a ruthenium (II) complex analogous with $Ru(bpy)_3Cl_2$ but with an aliphatic chain ending in a thiol group, and managed to image single particles in flow with the same emission than the ruthenium (II) complex in solution. Moreover, the 100 nm AuNPs were found inside of the nucleus using luminescence and electron microscopy.[196] More recently, a similar ruthenium (II) complex coated in 13 nm gold nanoparticles was quantified, within cells, not only by ICP-MS, which is the standard technique to quantify AuNPs, but also by the binary image produced by the greyscale of confocal microscopy images (Figure 2.1). The number of particles inside the cells was quantified for both techniques and there was a clear correlation, revealing a multi modal pathway to quantify particles inside cells.[194]

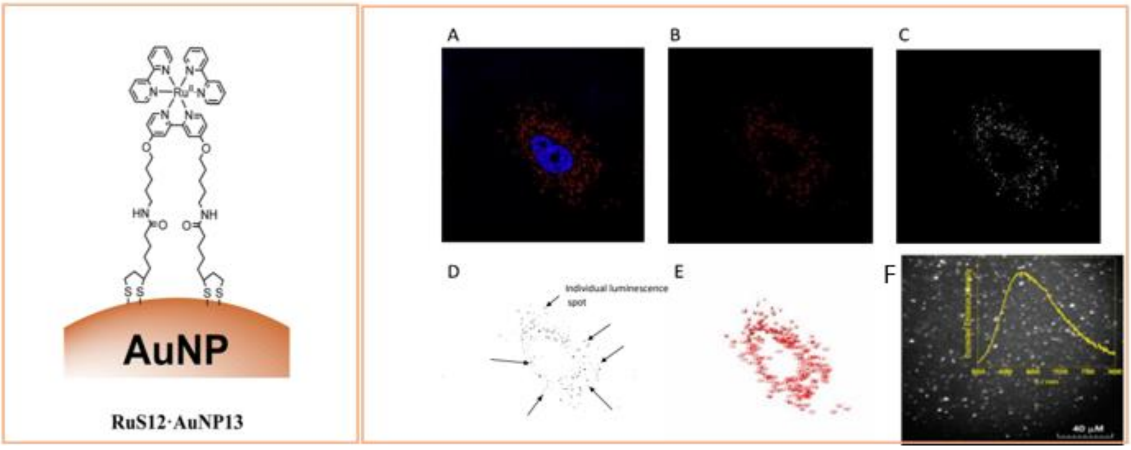

Figure 2.1- (L) structure of RuS12 complex functionalised in AuNPs with 13 nm size. (R) a) confocal image acquired of a single cell with gold nanoparticles visualised through Ru signal (red channel), b) conversion of a) to greyscale, c) Thresholding of the greyscale image in ImageJ to binary image to visualise single luminescence spots, d) and e) the binary image is analysed in ImageJ to calculate the number of features and thus the number of particles. F- Luminescence image and emission spectrum of a solution of gold nanoparticles 100 nm in flow imaged using epiluminescence microscopy. Emission spectrum shows that the particles possess the luminescence properties of the ruthenium (II) complex with the characteristic ^{3}MLCT centred at 640 nm. Scale bar- 40μM. Adapted from[194].

Although, the coating of AuNPs with fluorophores are very advantageous for imaging and quantification, there are still limitations. It has been reported previously that the attachment of fluorophores to the gold nanoparticles can quench the fluorescent signal. This quenching is induced by short distances from the fluorophore to the gold due to the strong electromagnetic field generated at the surface of the gold.[199, 200] This “near-field” has showed that if an organic fluorophore is within 5 nm to the surface of the gold, then its close enough to the excited electrons to be donated from the fluorophore to the gold.[201] However, if the fluorophore is distant enough from the surface of the gold particle by attaching long linkers to it, this effect is not observed, and in some cases the fluorescence can even be enhanced.[195] Osborne and co-workers studied coated gold nanoparticles, 13, 50 and 100 nm, with ruthenium bipyridine complexes with different size linkers to the gold (Figure 2.2). This study showed an increase on luminescence lifetime compared to the free complex, of 20% for the shortest distance and an enhancement of 70% for the longest distance between the ruthenium (II) complex and the gold surface. The longest linker complex also showed an increase of quantum yield in relation to the free complex showing that this increase is due to a radiative decay and a decrease of non-radiative decay. However, it is noted that this luminescence enhancement was only possible due to the presence of a surfactant attached to the gold particles.[195]

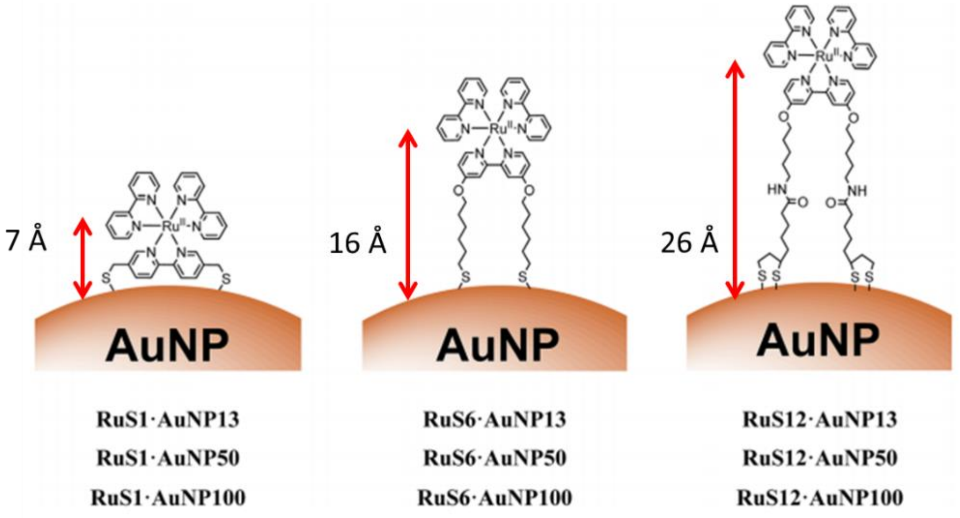

Figure 2.2- Schematic illustration of RuS1, RuS6 and RuS12 distances to the gold when functionalised into AuNPs, adapted from[195].

Studies have showed that even with optimal distances from the gold, the luminescence signal of the ruthenium (II) complexes is quenched when attached to the AuNPs. Kedem and co-workers showed that at different distances of 3 nm and 20 nm from the gold, $Ru(bpy_3)Cl_2$ showed a weak luminescence in both cases, thus the luminescence intensity was not only dependent on distance between probe and gold surface.[202] Several studies have used this ruthenium quenching signal as an advantage to create bio sensors.[12] Nonetheless, if the aim is to image the AuNPs in cells, this signal quenching effect can be disadvantageous.[203]

2.1.3 The role of surfactants in gold nanoparticles

The attachment of surfactants to AuNPs is widely used to prevent aggregation and thus helping the conjugation to other ligands.[204] Aggregation occurs when the nanoparticles tightly bond and clump together, making it difficult to break by mechanical forces. Aggregated nanoparticles are influenced by several factors such as temperature, pH or cationic molecules addition, leading to a colour change, larger size particles, reduction on UV-Vis absorbance and a red shift in the SPR band attributed to the coupling of the plasmon resonances of the particles.[205-207] Although the latter effect be advantageous for imaging, the colloidal stability is poor and therefore difficult to tune the nanoparticles size.[208] Moreover, aggregation could influence the AuNPs ability to interact or enter cells, leading to an inefficient imaging strategy.[209, 210] Albanese and Chan were one of the first studying the effect of AuNPs aggregates *in vitro*.[211] By coating different sizes AuNPs with transferrin and analysing uptake in three different cell lines, they realised that not only the AuNPs immediately aggregated in cell media, but also hindered cell uptake. They realise with this study that predicting a cell’s response to a heterogeneous size particles samples can be very challenging since it depends on several factors such as expression of target receptor, endocytosis mechanism and cell phenotype (Figure 2.3).

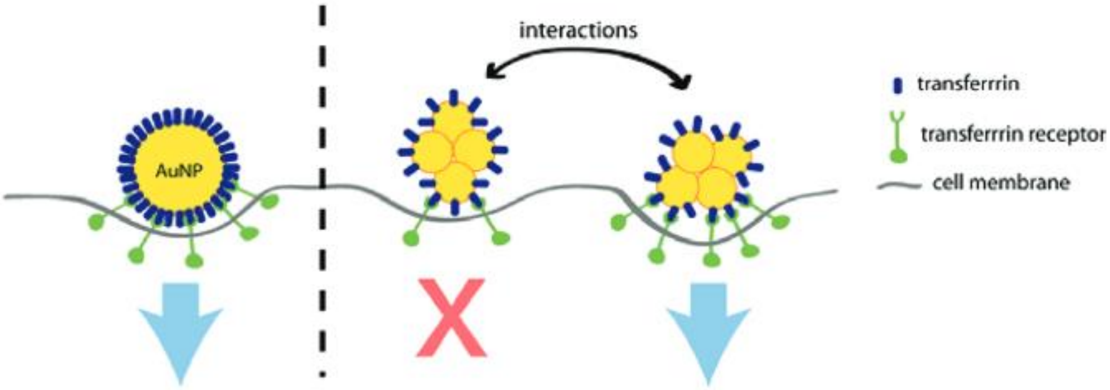

Figure 2.3- Scheme comparing 30 nm AuNPs uptake of a single particles and aggregates showing that when the aggregate's tip interacts with the cell membrane there is not enough free energy produced by ligand-receptor binding to promote the uptake, adapted from[211].

To gain some control on gold nanoparticles self-assembly, the functionalisation of AuNPs with small molecules or polymers is a crucial step.[212] Polyethylene glycol (PEG) anchored with thiol groups is one of the most common surfactants used on AuNPs. PEGylation, creates a "corona" (layer that is spontaneously formed around the NP), so AuNPs are not recognised by the immune system. Moreover, PEG is commercially available, inexpensive, and approved by the FDA.[213] David and co-workers compared 30 nm citrate capped AuNPs with functionalised PEG-thiol AuNPs and demonstrated that, contrary to citrate-AuNPs, the functionalised nanoparticles with PEG-thiol can undergo cellular uptake without aggregation.[214] Wang and co-workers found that cyclised PEG on the surface of AuNP can enhance dispersion stability of the nanoparticles due to an increase of steric repulsions, when compared with linear PEG, reducing aggregation even through freezing, lyophilization or heating (Figure 2.4).[215]

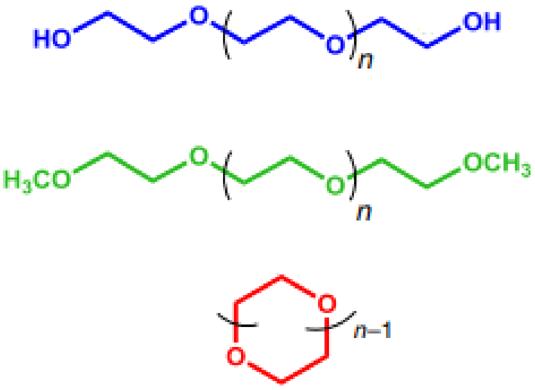

Figure 2.4- Linear and cyclised PEG surfactants used to study the dispersion stability of gold nanoparticles upon freezing, lyophilization or heating, adapted from[41].

Although AuNPs exhibit excellent biocompatibility, it is known that proteins can absorb into the surface of AuNPs and alter their pharmacokinetics and biodistribution in the cells.[216] Plasma proteins in blood are no exception, creating the so called “protein corona” around the surface of the AuNPs, leading to an accumulation in the liver, that acts as a biological filtration system, increasing toxicity on this organ and contributing to nonspecific distribution.[217] PEG was found to minimise nonspecific protein adsorption and therefore reduce the uptake of AuNPs by the liver and enhance targeting effects.[218] Clark and co-workers synthesised gold nanoparticles conjugated with transferrin (Tf) antibodies that bind to transferrin receptors in the blood-brain barrier (BBB) to enable crossing of the BBB and enter the central nervous system (Figure 2.5). To do so, they used a PEG linker, that is sensitive at mildly acidic pH, between the gold and the antibody to provide stability while circulating in the blood. When the linker was used as a stabilizing agent, antibody moieties were only released upon reaching the acidic vesicles, allowing free movement of the AuNPs to the brain.[219]

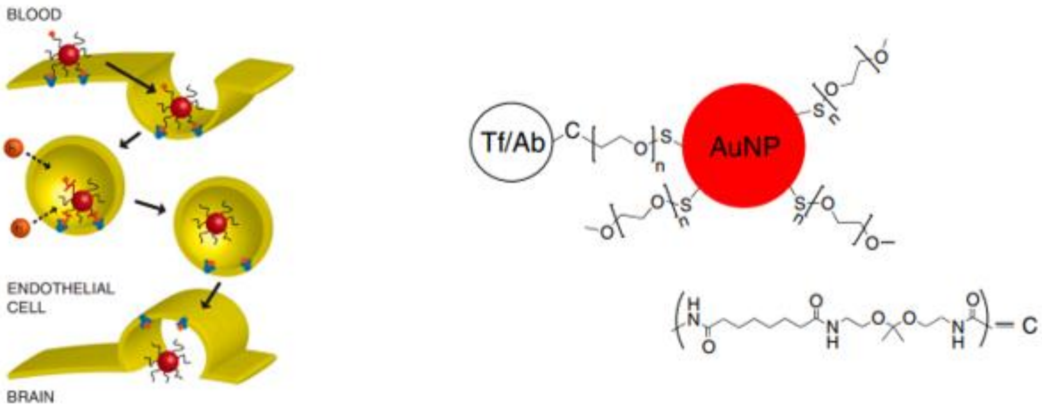

Figure 2.5- Proposed mechanism of action of the gold nanoparticles conjugated with a transferrin (Tf) antibody and an acid cleavable peg linker. After endocytosis, there is a rapid acidification of the endosome causes the release of the antibody to bind to the Tf receptors and allowing free movement of the gold nanoparticles (left), structure of the gold nanoparticles with the acid cleavable peg linker and the antibody (right). Adapted from reference[219].

Besides blood proteins, single stranded DNA is also able to absorb in AuNPs surface and this has been used for different applications such as drug delivery[220, 221] and biosensors[222, 223]. However, there is also the risk of nonspecific DNA binding interferes with the biological aim of the AuNPs. Zhang and co-workers coated AuNPs with single strand DNA and PEG and evaluated the rate of DNA hybridization with and without the surfactant coating.[224] By this study they showed that there is an enhancement on the DNA hybridization rate, due to PEG being able to block nonspecific DNA interactions with AuNPs.

Although PEG is the most common surfactant to stabilise AuNPs, it is not the only one used. CTAB[225, 226], oleic acid[227], tiopronin[228] and Triton X-100[229] can also be used to control the growth and monodispersity of the gold nanoparticles. Surfactants are also necessary for stabilisation of AuNPs before addition of a charged complex. AuNPs are usually prepared by an adapted Turkevich method[230], which sodium citrate is used as a reducing and capping agent. The layer of absorbed citrate anions keeps the particles separated, hence avoiding immediately aggregation after synthesis. Therefore, the functionalisation of a positively charged complex to the surface of the negatively charged AuNPs leads to a destabilisation and a flocculation of the particles. Flocculation can be defined as a random process of nondirectional and nonselective binding of molecules with opposite charges, when dissolved in a polar solvent like water.[231] Flocculation in AuNPs have been studied for a while, but Murthy and co-workers showed that upon the addition of a positively charged poly(L-lysine) (PLL) to the negatively charged AuNPs, formed a spherical floc structure.[231] However, this phenomenon usually creates structures with random sizes and shapes due to the lack of spatial and directional control, which can lead to a poor uptake in cells. Therefore, the type of surfactant used to coat the AuNPs needs to be carefully chosen according to the biological aim since different surfactants can interact very differently with cells membrane and influence cellular uptake.[232]

Fluorinated molecules are one more example of surfactants that have increasingly grown interest due to its properties. Fluorinated surfactants are lipophilic and chemically and thermally stable, with low surface tension and tuneable properties, making them very biocompatible, and thus very interesting for biomedical application.[233] Fluorocarbons moieties in surfactants have been used in the literature due to their ability to fluidize the lipidic monolayer which can be used to gain elasticity of the cell membrane and therefore improve the AuNPs uptake.[234, 235] Moreover, fluorocarbon surfactants have showed the ability to increase the luminescence lifetimes. Kondo and co-workers developed a micelle made of surfactants that contained fluorocarbon groups and hydrocarbon groups (Figure 2.6).[236] These structures showed unusual long lifetimes when compared to general surfactant micelles. This is due to its structure and the presence of very strong C-F bonds, the hydrophobic chain can come close by van der Waals forces and overlap with each other, providing extra stability to the micelle and longer lifetimes.[236]

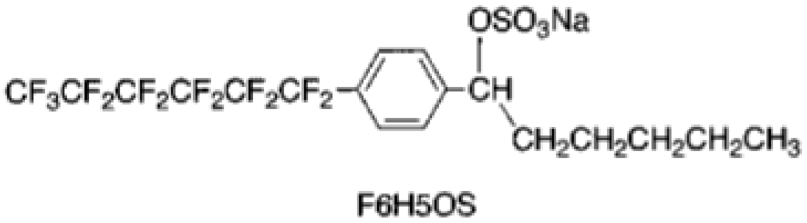

Figure 2.6- Chemical structure of fluorocarbon surfactant F6H5OS, adapted from[236].

Interestingly, this effect seems to also happen with ruthenium (II) complexes. Osborne and co-workers studied the luminescence effect of the ruthenium probe upon addition of the surfactant Zonyl FSA (Figure 2.7). This surfactant is a perfluorocarbon compound and its interaction with gold nanoparticles has been previously demonstrated.[196] Two out of the three different ruthenium probes analysed had an increase of up to 70% on the lifetime. The increase in lifetime is due the protection of $^3O_2$ quenching from the surfactant to the ruthenium (II) complex. In this study it was observed that by increasing the hydrophobicity of the ruthenium probe through increasing the aliphatic chain, the interaction with the surfactant increased and therefore improved the oxygen shielding.

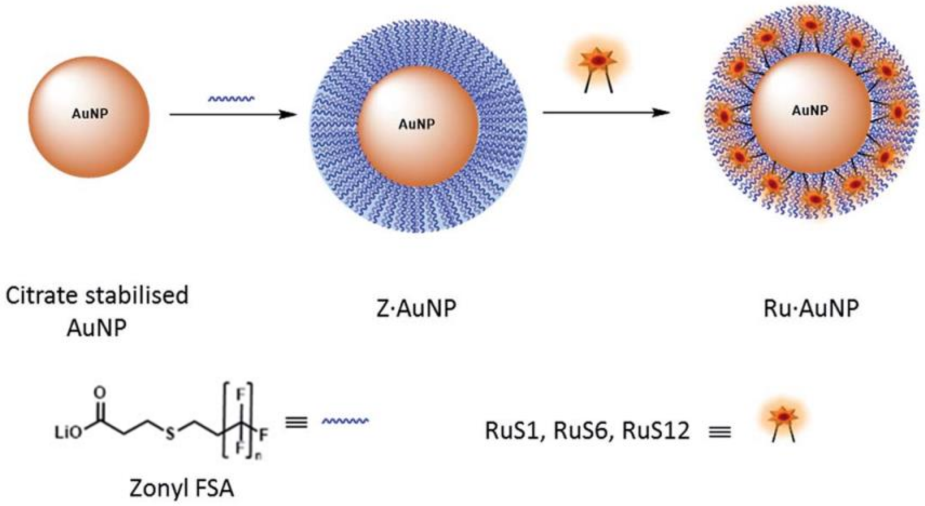

Figure 2.7- Schematic representation of the attachment of the fluorinated surfactant, zonyl FSA, and the ruthenium probes to a gold nanoparticle. Adapted from reference.[30]

Overall, functionalisation of metal complexes on AuNPs is an exciting new strategy for imaging and thus increasingly studies have been emerging.

Recent reports include investigation of DNA binding affinities and cellular imaging of luminescence ruthenium (II) complexes functionalised AuNPs, using ruthenium (II) complexes such as Ru(bpy)$_3$Cl$_2$, Ru(phen)$_2$Cl$_2$ and Ru(TAP)$_3$Cl$_3$ anchored with an aliphatic group containing a thiol at the end and attached to 4 nm AuNPs (Figure 2.8).[237] Within this study, they showed that the functionalised AuNPs showed affinity for DNA and at same time were able to monitor the uptake and localisation of the 4 nm AuNPs by confocal microscopy and TEM.[237] However, since no surfactant was used, the quantum yield of the ruthenium (II) complexes was lower on the nanoparticles when compared to the free complexes, due to an energy transfer quenching by interaction with the gold surface.[203]

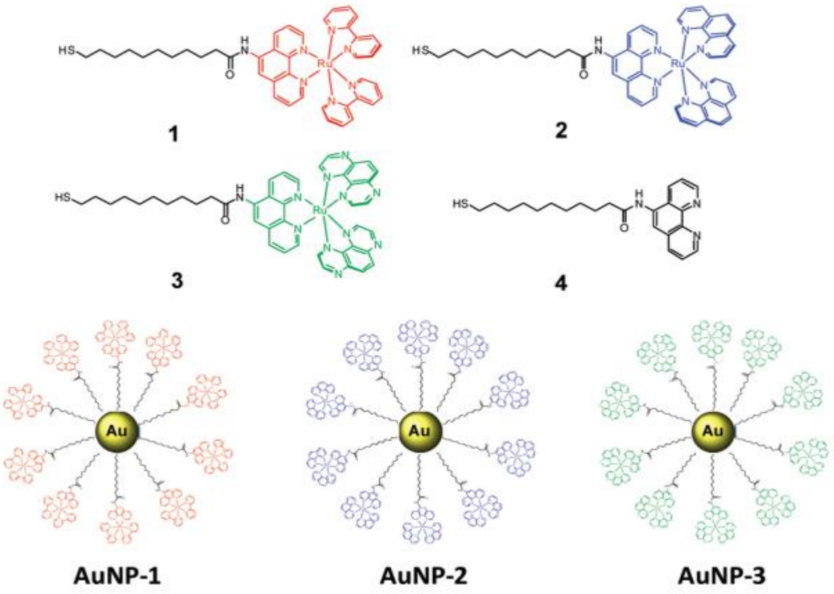

Figure 2.8- Structure of the ruthenium (II) complexes and representation of their attachment to AuNPs, adapted from[237].

Although, ruthenium coated gold nanoparticles (AuNP.Ru) are explored in the literature, there are no examples of luminescence optimization studies using different surfactants and probes on AuNPs. This optimization is required to further understand the role of the interaction between surfactant and ruthenium and therefore obtain enhanced luminescent gold nanoparticles.

2.2 Chapter Aims

In this chapter the luminescence behaviour effect of two different ruthenium (II) complexes (RuPhenL1 and RuPhenL2) attached to monodispersed gold nanoparticles will be analysed and the nanoparticles fully characterised. Both complexes contain two

(1,10-phenantroline) ligands, with the difference on the third ligand (Figure 2.9). RuPhenL1 contains a 2,2-bipyridine ligand with a long aliphatic chain and RuPhenL2 has a 1,10-phenantroline ligand with a shorter aliphatic chain attached. The differences on the third ligand between both ruthenium (II) complexes will be used to compare luminescence properties. The effect of three different surfactants (Zonyl FSA and two different sizes PEG – nominated as SPEG and LPEG) will also be studied and its effect on the ruthenium luminescence will be compared.

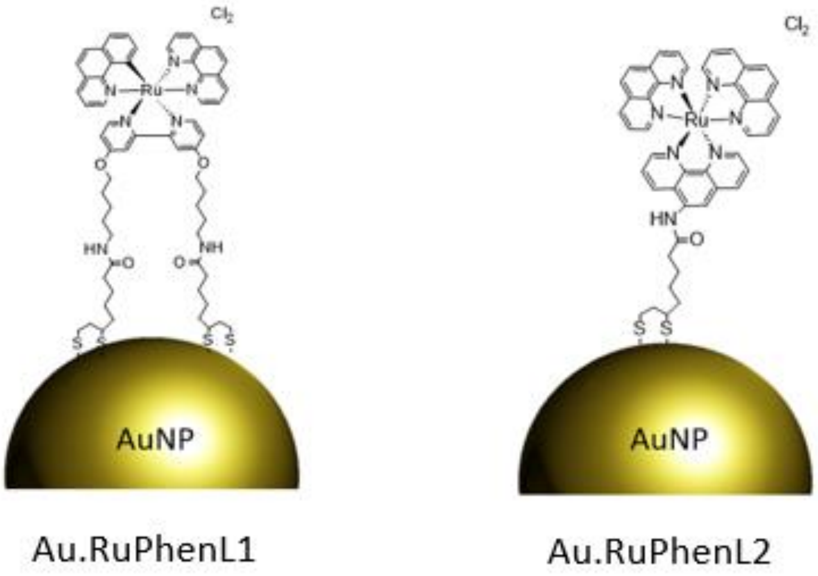

Figure 2.9- Schematic representation of gold nanoparticles functionalised with ruthenium (II) complexes RuPhenL1 (left) and RuPhenL2 (right).

2.3 Results and Discussion

2.3.1 Synthesis and properties of Ru (II) polypyridyl complexes RuPhenL1 and RuPhenL2

Two ruthenium (II) polypyridyl complexes with structures [Ru(1,10-phenanthroline)$_2$(L1)]Cl$_2$ (RuPhenL1) and [Ru(1,10-phenanthroline)$_2$(L2)]Cl$_2$ (RuPhenL2), were synthesised and fully characterised following previously published methods in the Pikramenou group.[195, 196, 238]

Figure 2.10 shows the schematic representation of the synthesis for RuPhenL1 and RuPhenL2. Before the synthesis of the final complexes, the synthesis of the linkers (L1 and L2) and the precursor ruthenium (II) complexes type [Ru(L)Cl$_2$]$^{2+}$ such as: [Ru(phen)$_2$Cl$_2$]$^{+2}$ was successfully carried out.

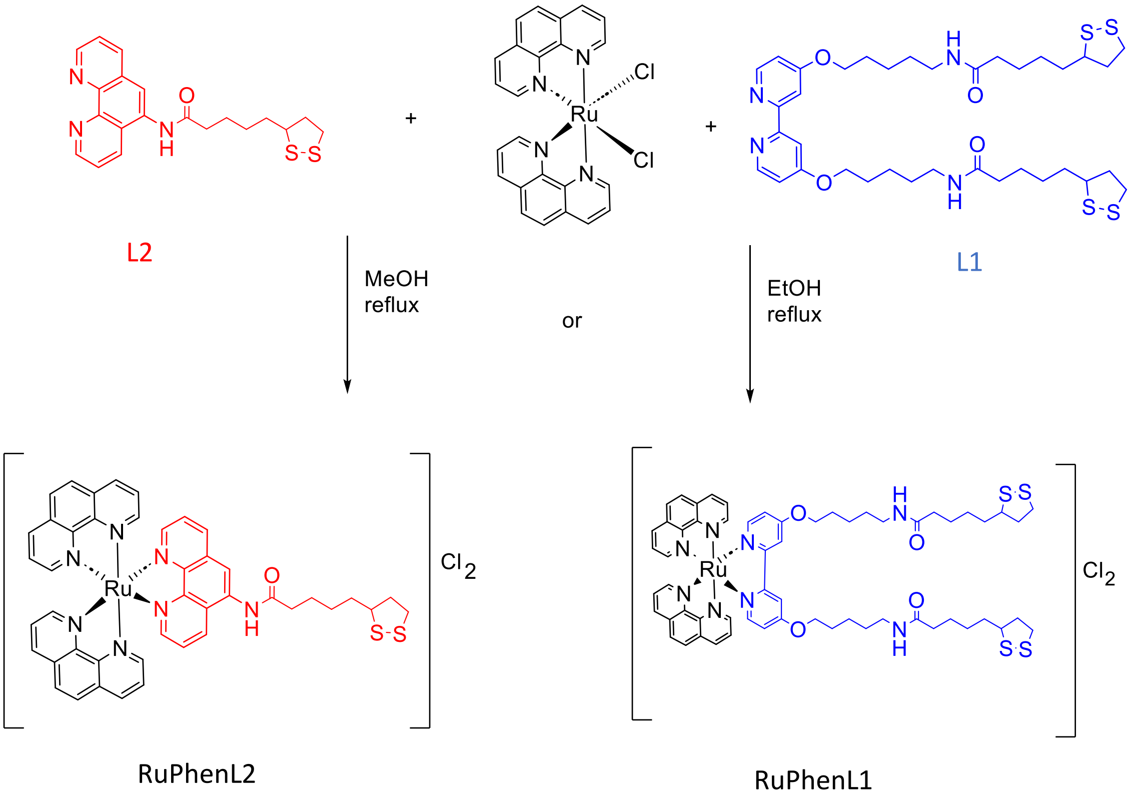

Figure 2.10- Schematic representation of general synthesis of the ruthenium (II) polypyridyl complexes RuPhenL1 (blue) and RuPhenL2 (red).

Synthesis of ligands L1 and L2

The synthesis of ligand L1 was carried out in six steps and the schematic representation of the reactions is shown in Figure 2.11. L1 ligand has been previously made by our group and showed an efficient attachment to gold surfaces and nanoparticles.[196, 238]

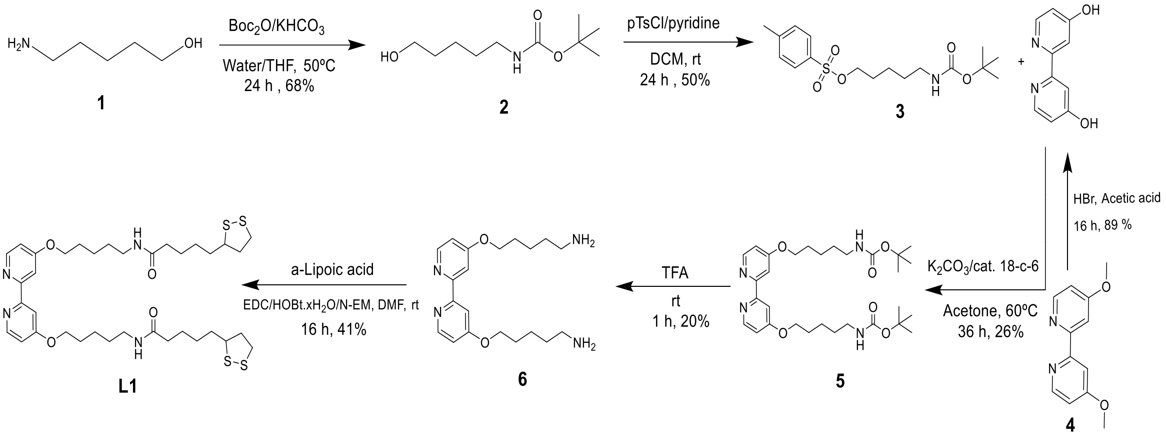

Figure 2.11- Schematic representation of the L1 ligand synthesis.

In brief, di-tert-butyl decarbonate (BOC) protection of the amine group of 5-amino-1-pentanol formed (**2**). Following the protection, conversion of the hydroxyl group into a tosyl group was carried out in a presence of a weak base (pyridine) (**3**); this step renders the alkyl chain susceptible to backside attack in a proceeding S_N2 reaction to produce 4,4-dihydroxy-2,2-bipyridine (**4**) A nucleophilic substitution reaction was carried out forming compound **5**. The deprotection is allowed by TFA (**6**) followed by the reaction of a carboxylic group and amine to form the final 4,4- Di(5-lipoamido-1-pentoxy)-2,2-bipyridine (L1).

The synthesis of the new ligand L2 was based on previous published methods[203] and in collaboration with Elena del Giorgio from the Pikramenou group. The synthesis was carried out in one step as shown in Figure 2.12, by a 1-ethyl-3-[3-dimethylaminopropyl]carbodiimide hydrochloride (EDC) coupling between the carboxylic acid of the α-lipoic acid and the amine on 1,10-phenanthroline-5-amine.

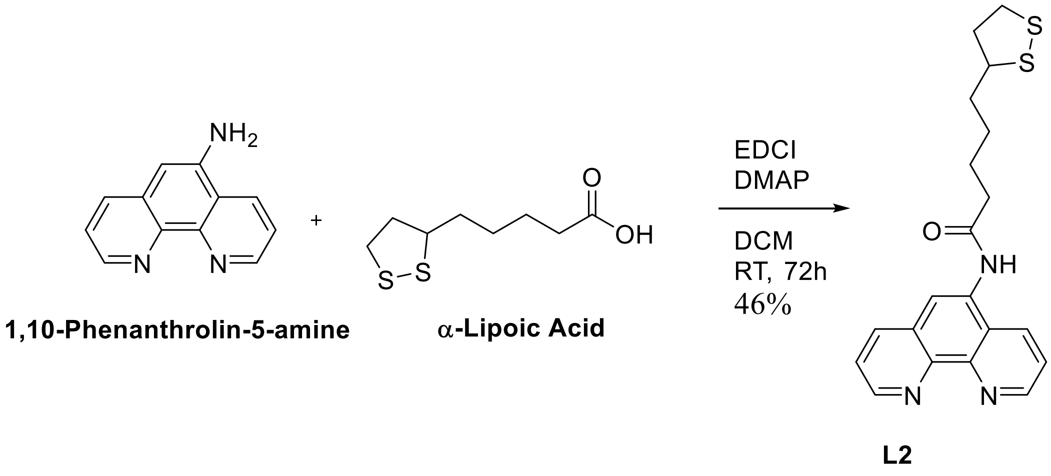

Figure 2.12- Schematic representation of the L2 ligand synthesis.

One advantage of ligand L2 is it required of only one step for synthesis and high atom economy, instead of the six steps needed for ligand L1. However, the L1 ligand contains a longer aliphatic chain, which increases the distance between the gold and ruthenium (II) complex. Moreover, L1 contains a 2,2-bipyridil ligand while L2 has a 1,10-phenanthroline, which although structurally similar it has different photophysical properties. Therefore, the comparison study between complexes, with the two different ligands L1 and L2, it is an important analysis to evaluate the influence of these ligands on the AuNPs luminescence.

2.3.2 Photophysical characterisation of RuPhenL1 and RuPhenL2

The absorption, steady state excitation and emission were recorded in aerated water with 2% methanol, for both complexes. The photophysical properties of similar complexes (RuS12, RuPhenS12) in acetonitrile have been studied previously by the Pikramenou group,[196, 238] and for that reason are not going to be studied.

The photophysical properties of RuPhenL1 and RuPhenL2 are similar (Figure 2.13). The absorbance (black lines) shows the metal to ligand charge transfer (MLCT) spin allowed (d - π*) from 400-500 nm with the maximum at 446 nm and 220nm which is similar to its parent Ru(Phen)$_3$Cl$_2$.[174] RuPhenL1 exhibits the MLCT bands at 456 nm and 230 nm. RuPhenL2 has a 10 nm blue shift in absorbance maxima compared to RuPhenL1, which is attributed to the 1,10-phenanthroline rigidity on L2 ligand. The singlet MLCT molar absorptivity for RuPhenL2 is 15000 M^{-1} cm^{-1} and RuPhenL1 has a molar absorptivity of ~14000 M^{-1} cm^{-1} . The fact that this last complex has a lower molar absorptivity when compared to RuPhenL2 is anticipated, since it is known that phenanthroline ligands have higher molar absorptivity than bipyridine ligands.[178, 239] The Ligand Centre (LC) state (π - π*) is assigned at 260 nm for RuPhenL2 and 264 nm for RuPhenL1.[48] The emission of both complexes is represented by the broad band in red between 580 and 680 nm region as is characteristic for ruthenium (II) complexes.[13, 174, 240-243] Similar to the absorption spectra, the emission spectra show a blue shift from the RuPhenL1 (625 nm) to RuPhenL2 (615 nm), indicating that the presence of 1,10-phenanthroline ligands raised the energy of ^{3}MLCT transition for RuPhenL2 and therefore a bigger gap between HOMO and LUMO.[178] This leads to an emitted light with higher energy and shorter wavelengths.

The excitation spectra mirror the absorbance, with the MLCT and LC in the same region for both complexes.

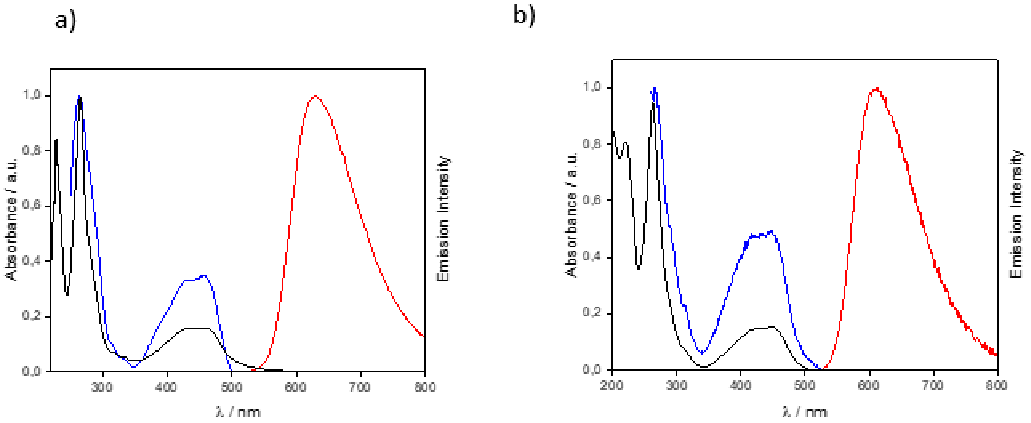

Figure 2.13- Absorption (black), excitation (blue) and emission (red) spectra of (20µM) a) RuPhenL1 (λ_{exc}=456 nm, λ_{em}=625 nm) and b)RuPhenL2 , (λ_{exc}=446 nm, λ_{em}=615 nm) in aerated H_2O with 2% MeOH.

The lifetime of the complexes $Ru(bpy)_3Cl_2$ and $Ru(Phen)_3Cl_2$ are 360 ns and 450 ns in aqueous solution, respectively. $Ru(Phen)_3Cl_2$ is expected to show a higher lifetime than $Ru(bpy)_3Cl_2$ due to its rigid structure and increased π-conjugation, increasing the gap between HOMO-LUMO. With a larger HOMO-LUMO gap, the likelihood of the molecule to undergo radiative decay is higher than nonradiative decay.[244] RuPhenL1 has a lifetime of 514 ns and RuPhenL2 has 574 ns, in aerated water solution with 2% MeOH (Figure 2.14). Since both complexes contain 1,10-phenanthroline ligands it is expected that the lifetime is higher than $Ru(bpy)_3Cl_2$. The mixed ligand complex, RuPhenL1, has a lower lifetime as in mixed ligand complexes, the probability of undergoing radiative or nonradiative decay depends on a variety of factors, including the type of ligands, their relative energy levels, and the electronic and molecular structure of the complex.[241]

Nakamaru and co-workers studied the luminescence of $Ru(Phen)_2$(4,4dimethylbypiridne) and $Ru(bpy)_2$(4,4dimethylbipyridine).[178] For both complexes, the lifetime decreases when compared with its parents $Ru(Phen)_3Cl_2$ and $Ru(bpy)_3Cl_2$, which is explained by a decrease in radiative decay and an increase on nonradiative decay. This is even more significant for mixed ligand complexes that contain 1,10-phenanthroline. The rate of nonradiative decay constant is lower for 1,10-phenanthroline than for bipyridyl ligands due to its rigid structure. So, when different ligands are added to the equation, the nonradiative decay is much more significant than for bipyridine.[178]

The increase in lifetime of RuPhenL1 and RuPhenL2 compared to parent $Ru(Phen)_3Cl_2$ is unexpected because in previous studies from the group it has been shown that the oxygens on the L1 ligand, for the complex $Ru(bpy)_2L1$, can quench the luminescence signal and the lifetime decreases.[238] However, in this case, replacement of two 2,2-bipyridine ligands for two 1,10-phenanthroline, the effect of oxygen quenching is reduced, demonstrating the advantage of using this ligand for luminescence studies. RuPhenL2, although very similar to its parent $Ru(Phen)_3Cl_2$ has an increased lifetime likely due to L2 ligand. The presence of an aliphatic chain with electrophilic groups attached to a 1,10-phenanthroline ligand may stabilise the lowest excited state, triplet MLCT, and therefore increase the gap between triplet MCLT and triplet MC decreasing the nonradiative decay pathway and therefore increase the lifetime.[245] However, it is noted that the luminescence lifetime signal is clearly weaker for RuPhenL2 than for

RuPhenL1. This effect is attributed to possible settlement and aggregation of particles in solution, which is an effect further explored in Chapter 3.

The quantum yields of the triplet MLCT for both complexes are 1.4 % for RuPhenL1 and 1.5 % for RuPhenL2, therefore, the substitution from a 2,2-bipyridine to a 1,10-phenanthroline, this does have a significant contribution to the quantum yield. RuPhenL1 has a lower quantum yield than Ru(Phen)$_3$Cl$_2$ (5 %) because of mixed ligand complexes interfering with its luminescence. Surprisingly, RuPhenL2 also has a smaller quantum yield than Ru(Phen)$_3$Cl$_2$. The reason for this could be related with changes on the nonradiative decay due to the alkyl chain, oxygen quenching from the L2 ligand or even possible self-quenching upon aggregation of the complex in solution. To be sure which is the reason, further studies, beyond the scope of this work, are required.

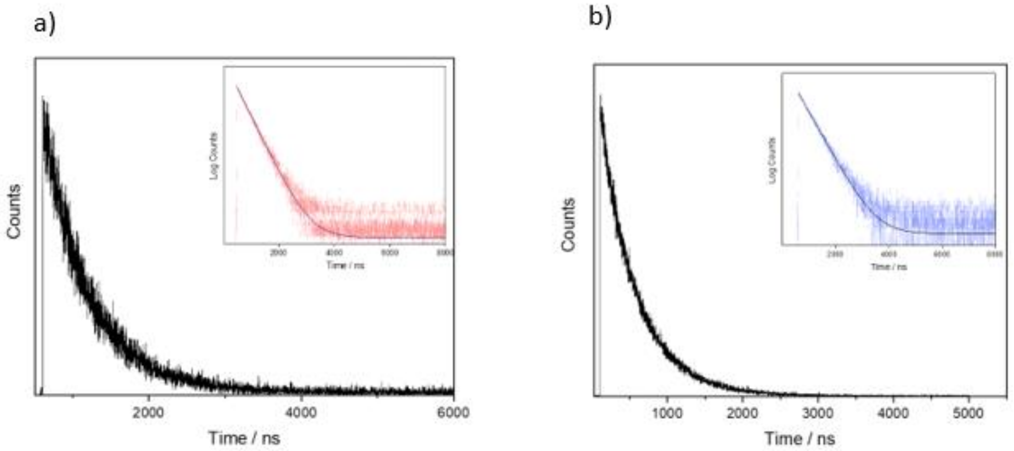

Figure 2.14- Luminescence lifetime decay of RuPhenL1 (a) and RuPhenL2 (b). Laser excitation source was at 445nm and collection wavelength of 620nm, with a 550nm filter. Decay curves were fitted with χ^2 values between 1.0 and 1.2 of all the lifetimes. The quantum yields obtained were 1.4 % and 1.5 % for RuPhenL1 (a) and RuPhenL2 (b), respectively.

2.3.3 Synthesis and characterisation of gold nanoparticles

Gold nanoparticles (AuNPs) were synthesised based on the modified Turkevich method.[230] This is a common method for synthesis as it produces AuNPs of tuneable size (5 nm-150 nm) which are nontoxic, stable and water soluble. The citrate ion that stabilizes the nanoparticles, can be easily exchanged by other molecules with higher affinity to gold, such as thiols, which therefore makes these AuNPs very easy to functionalise. However, while the Turkevich method is one of the most used, previous research in the group has found that the nanoparticles have a very large size distribution and lacks reproducibility. More recently, it has been suggested to invert the Turkevich method to obtain a faster nucleation and therefore a narrow size distribution.[246] To get a fastest nucleation, it is necessary to increase the rate of the reaction which is dependent on the formation of the precursors and pH.[247, 248] Thus, the synthesis of AuNPs in the Pikramenou group consist in bringing to reflux citric acid, used to create a suitable pH, forming a citrate buffer, and trisodium citrate which helps to reduce the Au^{3+} ion in the $HAuCl_4$ gold salt, to produce, H^+, CO_2 and Au^0. EDTA is also added to this solution to promote shape and size uniformity. Upon nucleation, spherical AuNPs will grow with more of a narrow size distribution of 12-14 nm size nanoparticles. To grow AuNPs with larger sizes, it is important that the smaller ones are monodisperse and uniform, so that the seeding process is also uniform. For this synthesis, ascorbic acid is also added, so it helps as reducing agent as well as stabilizing the seeding process of the remaining gold onto the smaller AuNPs (see experimental section).

In this work two different sizes of AuNPs were studied, 13 nm (Au13) and 25 nm (Au25) (Figure 2.15). Both set of particles were characterized by dynamic light scattering (DLS), surface plasmon resonance (SPR) band by UV-Vis and transmission electron microscopy (TEM). Although different techniques showed slight variations on the AuNPs sizes, these discrepancies fall within the error. Therefore, for the purpose of simplification, the AuNPs are going to be designated as Au13 and Au25 throughout this thesis.

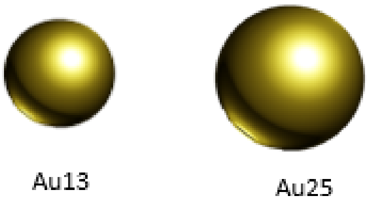

Figure 2.15- Schematic representation of both sizes gold nanoparticles 13nm (Au13) and 25 nm (Au25).

UV-Vis spectroscopy of Au13 shows an absorption band with a maximum, λmax, at 516 nm and Au25 at 519 nm, which is characteristic of their SPR and is in agreement with previous studies.[194-196] The size distribution by DLS confirmed that particles were made with sizes of 11.5 ± 2.9 nm for Au13 and 20.1 ± 5.0 nm for Au25, with a polydispersity index (PDI) of 0.09 and 0.08 respectively. A small PDI shows a narrow size distribution in solution and illustrate the AuNPs have similar sizes. TEM images show that the size of Au13 is 13 ± 1 nm and 23 ± 2 nm for Au25 which are in good agreement with the DLS results (Appendices- figure 2.29). Besides of the number distribution, DLS can also measure intensity and volume distribution, which gives information of the size by the volume of nanoparticles in solution or by the intensity of light scattered. Since size by intensity considers the scattered light, is, by definition, more accurate than size by number or volume, which will be considering every nanoparticle. However, for both

Au13 and Au25, the size by intensity is 18.2 ± 5.7 nm and 30.1 ± 8.8 nm, respectively. In comparison, size by number seems to resemble the size by TEM. Therefore, for simplicity, only size by number will be reported for this study.

2.3.4 Functionalisation of gold nanoparticles with the surfactants Zonyl FSA, SPEG and LPEG

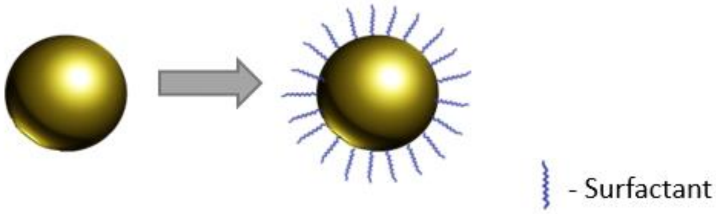

Figure 2.16- Schematic representation of gold nanoparticles functionalised with surfactant, which in this study can be Zonyl FSA, short PEG (SPEG) or long PEG (LPEG).

Surfactants are important to stabilise the AuNPs before coating with charged compounds (Figure 2.16), by reducing the surface tension between the nanoparticle and water, preventing aggregation of the particles. In previous studies, fluorinated surfactants increased the luminescence lifetime of ruthenium (II) complexes[195], so in this study, the commercially available Zonyl FSA, is used as one of the surfactants. Polyethylene glycol (PEG) is also commonly used as gold nanoparticles surfactant due to being nontoxic, inexpensive, and biocompatible. Therefore, two different sizes of PEG polymer, labelled as short PEG (SPEG) and long PEG (LPEG), were used as surfactants, and compared with the Zonyl FSA, upon addition of the ruthenium (II) complexes (Figure 2.17).

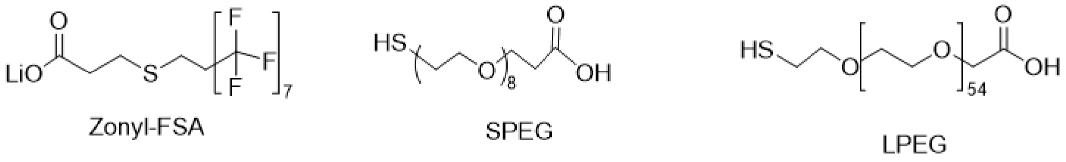

Figure 2.17- Chemical structure representation of the three surfactants Zonyl FSA, short PEG (SPEG) M_n=460 and long PEG (LPEG) M_n=2100, before coating with the ruthenium (II) complexes.

Both SPEG and LPEG contain thiol groups to allow attaching to the AuNPs, whereas Zonyl FSA binds through the S-bond from perfluorooctanesulfonamide group. To understand the optimal concentration of surfactant to add to the AuNPs, the binding curves of the concentration of surfactant vs SPR shift were analysed. While the surfactant is attaching to the gold, the SPR slightly increases until it reaches a plateau where no more coating is observed, and the AuNPs solution is saturated. The optimal concentration is then determined when the plateau is reached. Due to Zonyl FSA have been extensively studied in the Pikramenou group[194-196], the optimal concentration has been determined (10 µM), and for that reason it will not be showed in this study. From the binding curves, it was calculated that the optimal concentration for SPEG is 10 µM and for LPEG is 5 µM (Figure 2.18). For both surfactants, the polymers bind to the AuNPs via covalent interactions, until it reaches a saturation point. Non-linear regression was performed so the maximum specific binding was found for the AuNPs coated with PEG surfactant. The binding constant is 3×10^{-5} M^{-1} for Au13.SPEG and for 7×10^{-5} M^{-1} for Au13.LPEG. (Appendices-Table 7) The concentration maximum found to LPEG to reach a plateau was half of the SPEG concentration, hence the binding constant being bigger for LPEG surfactant. That is, at equilibrium, the concentration needed to achieve half of maximum binding is higher for SPEG than LPEG. Au25 are approximately half of the concentration of Au13 but have double of the surface area, so the same concentration of surfactant used for Au13, is also suitable to use for Au25.

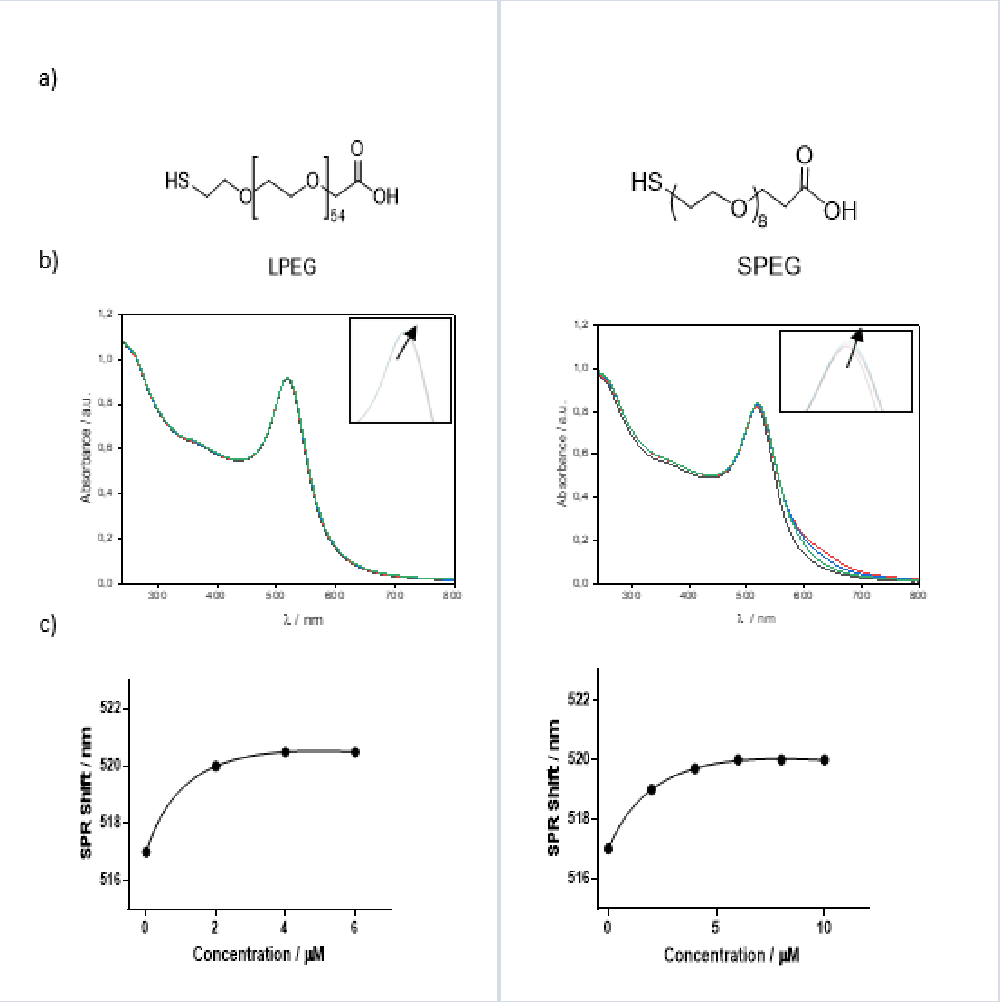

Figure 2.18- a) chemical structure of LPEG and SPEG surfactant, b) UV-Vis titration of LPEG and SPEG with a visible SPR band shifting upon binding to a 3.5 nM AuNPs solution c) fitting curve of concentration versus SPR shift, with a non-linear regression, used to find the binding constants.

DLS shows an increase on the size of AuNPs upon coating with surfactants. The size by number, for nanoparticles coated with Zonyl FSA (Au13.Z) is 19.3 ± 5.3 nm, 15.0 ± 4.2

nm for short PEG (Au13.SPEG) and 18.8 ± 5.1 nm for long PEG (Au13.LPEG) (Figure 2.19 and table 1). The sizes correspondent to Au25 are 22.6 ± 6.6 for Au25.Z, 22.6 ± 6.6 for AuNPs coated with short PEG and 25.1 ± 6.9 for AuNPs coated with LPEG. Important to note that although the hydrodynamic sizes slightly increase with the coating, throughout this work the AuNPs are still going to be labelled as Au13 and Au25, for simplicity.

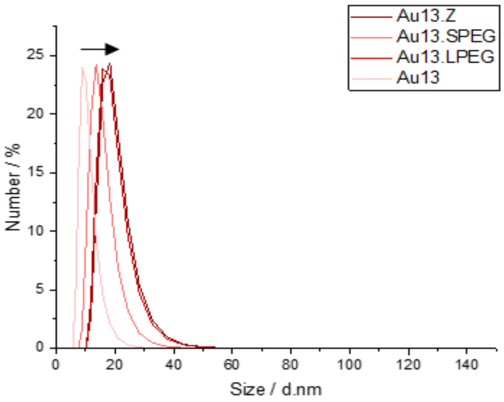

Figure 2.19- Size by number distribution on DLS of Au13 before and after coating with the surfactants to give, Au13.Z, Au13.SPEG, Au13.LPEG. Arrow shows the increase of sizes after coating.

Table 1- Sizes by number distribution and polydispersity index (PDI) comparison for citrate particles Au13 and Au25 with coated particles , Au13.Z, Au13.SPEG, Au13.LPEG, Au25.Z, Au25.SPEG and Au25.LPEG.

Dynamic Light Scattering (DLS)		**Au13.Z**	**Au13.SPEG**	**Au13.LPEG**	**Au13**
	Number distribution /nm	19.3 ± 5.3	15.0 ± 4.2	18.8 ± 5.1	11.5 ± 2.9
	PDI	0.25	0.19	0.24	0.09
		Au25.Z	**Au25.SPEG**	**Au25.LPEG**	**Au25**
	Number distribution /nm	22.6 ± 6.6	22.6 ± 6.6	25.1 ± 6.9	20.1 ± 5.0
	PDI	0.23	0.26	0.25	0.08

The difference on sizes is due to the different sizes of the surfactants used, which affects the hydrodynamic size of the nanoparticles given by DLS. Hydrodynamic size corresponds to the diameter of the nanoparticles dispersed in solution and therefore takes into account the electric dipole layer around the particles.[249]

Although, the surfactant LPEG is substantially bigger (~11 nm in length) than Zonyl (~2 nm) and SPEG (~1 nm) (Figure 2.20), the hydrodynamic size by DLS does not change, which can be explained by the type of conformation that these polymers can undergo upon attachment. Polymers like PEG can wrap in themselves in a “mushroom” or a “brush like” shape upon attachment to surfaces, depending on how closely pack the polymers are.[250] The mushroom formation occurs when the distance between each polymer side by side is bigger than the radius of the polymer itself, whereas the brush conformation happens when that distance is smaller than the radius of the polymer.[251-253] Since all polymers studied have different lengths it is possible that both undergo different conformations. However, to know exactly which conformation each polymer undergoes upon attachment to the AuNPs, further studies are required. Nonetheless, in this case, even though LPEG is longer than Zonyl and SPEG, the hydrodynamic sizes are very similar showing a possible dependence on the conformations taken by each polymer (Figure 2.21).

To compare the differences on size between citrate and surfactant coated particles, TEM images were also analysed, and the size of the particles was calculated by the average of 20 single AuNPs and processed by the software ImageJ. Figure 2.22 shows that all particles are monodisperse after coating with the surfactants. The AuNPs sizes are within the error of citrate AuNPs (Au13 and Au25). This is due to TEM only measure electronically dense metals and for that reason the polymer coating should not be visible under the microscope used.

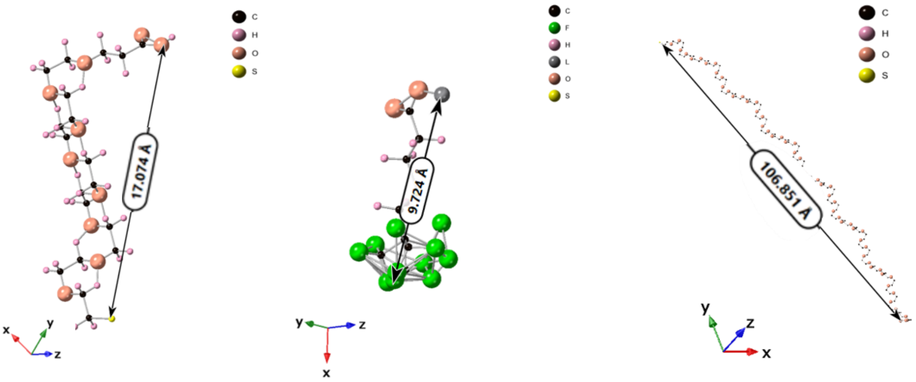

SPEG Zonyl FSA LPEG

Figure 2.20- Structures of the surfactants short PEG (SPEG), Zonyl FSA and long PEG (LPEG) relaxed to an energetically stable conformation by chem3D software. Images are obtained with a three-dimensional representation by CrystalMaker software with elements colour coded. The structures are represented as ball and stick models. The measured length for each surfactant is : SPEG= 17.074 Å, Zonyl FSA= 9.724 Å and LPEG= 106.851 Å.

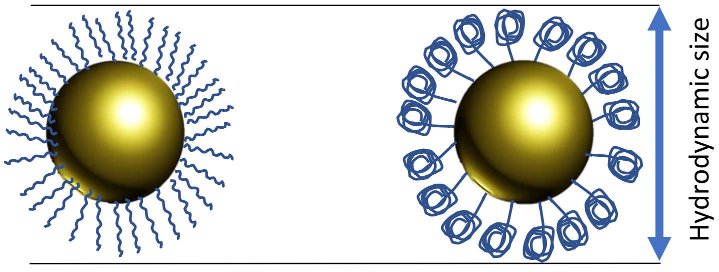

Brush like conformation Mushroom like conformation

Figure 2.21- Schematic representation of both conformations that PEG surfactant can undergo, brush and mushroom like shape, upon attachment to the gold nanoparticles. Representation showing that although different conformations are possible, the hydrodynamic size of particles (represented in a blue arrow) can be very similar.

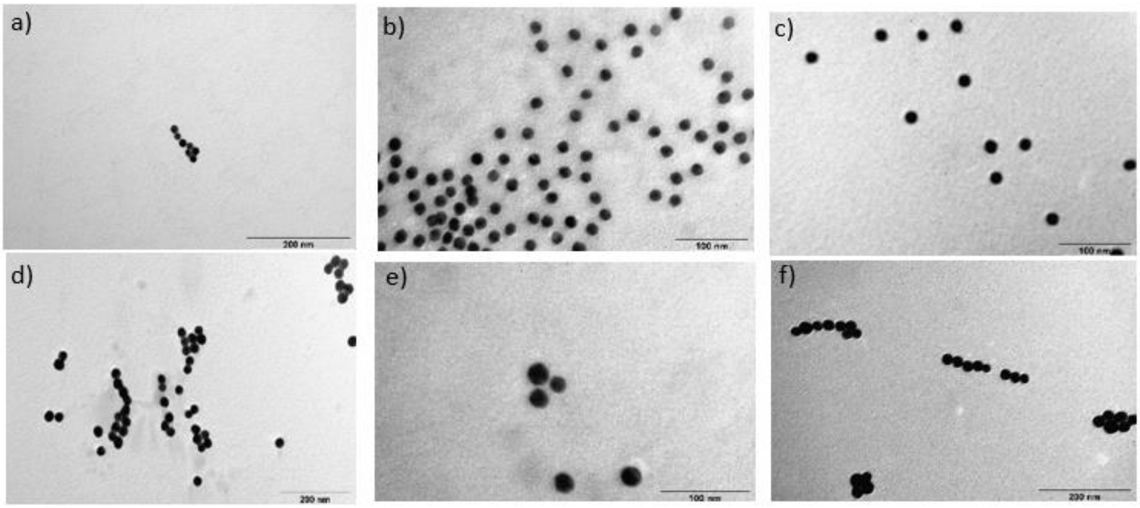

Figure 2.22- Transmission electron microscopy (TEM) of a) Au13.Z, b) Au13.SPEG, c) Au13.LPEG, d)Au25.Z, e) Au25.SPEG, and f) Au25.LPEG. TEM sizes were calculated by an average of 30 AuNPs and processed by ImageJ software. The sizes of the AuNPs were 13 ± 1 nm for Au13.Z, 15 ± 1 nm for Au13.SPEG and 14 ± 1 nm for Au13.LPEG. The sizes for Au25.Z were 23 ± 2 nm, for Au25.SPEG were 24 ± 1 nm and for Au25.LPEG were 23 ± 2 nm. Scale bars are 200 nm and 100nm.

2.3.5 Functionalisation of gold nanoparticles with luminescence ruthenium (II) complexes

The ruthenium (II) complexes, RuPhenL1 and RuPhen2 were attached to AuNPs through the S-bond of the thiol groups on the complexes (Figure 2.23). The coating process was developed by our group in previous studies[195], in which a 1 mM solution of ruthenium (II) complex in methanol is titrated into AuNPs (6.5 nM). Upon titration of RuPhenL2 and RuPhenL1 to AuNPs solution, a red shift in the λmax is visible, until it reaches a saturation point where no shift is observed, monitored by UV-Vis spectroscopy. The saturation point gives a good estimation of the maximum concentration of ruthenium attached to the particles. To make sure no unbound complex remains in solution, the AuNPs were purified by size exclusion chromatography.

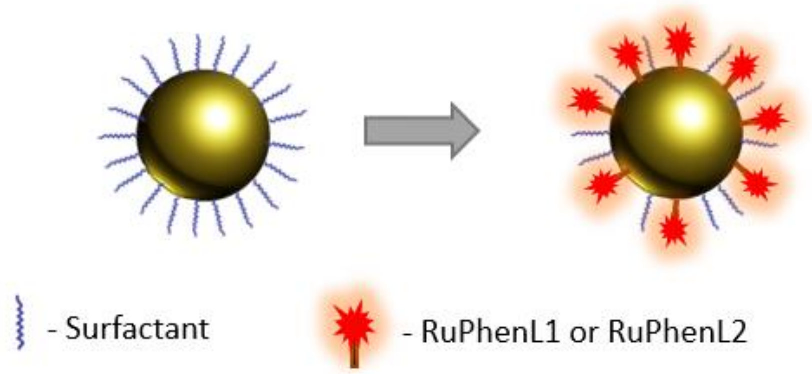

Figure 2.23- Schematic representation of coating ruthenium (II) complexes (RuPhenL2 and RuPhenL1) on the surface of gold nanoparticles, previously stabilised with surfactant.

The binding curves show the optimal concentration of RuPhenL2 is 80 µM for Au13.Z solution, whereas for Au13.SPEG and Au13.LPEG only 12 µM (Figure 2.24) was attached to AuNPs. Similarly, for RuPhenL1 (Appendices-figure 2.30), the optimal concentration of RuPhenL1 for AuNPs coated with Zonyl FSA (Au13.Z.RuPhenL1), is 60 µM of the complex but for SPEG (Au13.SPEG.RuPhenL1) and LPEG (Au13.LPEG.RuPhenL1) is 5 and 8 µM, respectively. The binding constants for the ruthenium (II) complexes upon AuNPs attachment were found to be 4×10^{-4} M^{-1} for Au13.Z.RuPhenL2, 3×10^{-3} M^{-1} for Au13.SPEG.RuPhenL2 and 5×10^{-5} M^{-1} for Au13.LPEG.RuPhenL2 (Appendices-table 7). RuPhenL1 attached to Au.PEG does not follow the standard binding curve appearance and therefore a binding constant was not possible to find for these particles. However, the optimal concentration for these particles (5 µM) was found by analysing the SPR shifts.

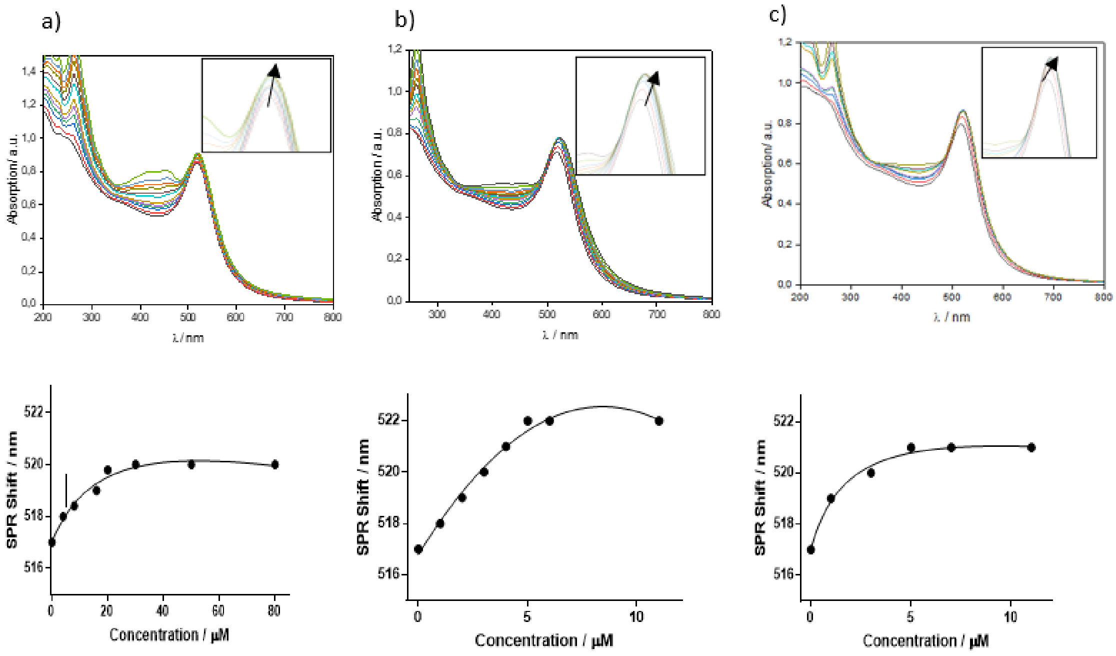

Figure 2.24- Titrations of a 1 mM stock solution in MeOH of RuPhenL2 in 6.5 nM AuNPs by UV-Vis spectroscopy and binding curves of concentration vs SPR shift with non-linear fitting curves to find the binding constants of a) Au13.Z.RuPhenL2, b)Au13.SPEG.RuPhenL2 and c) Au13.LPEG.RuPhenL2.

By analysing the absorbance λmax shifts, it gives a good indication of the ruthenium (II) complexes attachment. When the surface of the AuNPs is modified, the SPR shifts to higher values, since the AuNPs surface plasmon effect is dependent on the nanoparticles functionalisation.[147] This behaviour supports the attachment of the surfactants as demonstrated previously, but also the ruthenium (II) complexes, being the most noticeable shifts after the ruthenium coating (Table 2). Since it is possible to attach more ruthenium on AuNPs coated with Zonyl FSA than with PEG, the absorbance λmax shift is also higher. Analysis of the elemental composition of the AuNPs by inductively coupled plasma mass spectrometry (ICP-MS) showed higher ratio of ruthenium per nanoparticles coated previously with Zonyl FSA. According to ICP-MS, Au13.Z.RuPhenL2 has 400 complexes and Au13.Z.RuPhenL1 has 600 complexes per particle. AuNPs that were coated with PEG have less ruthenium per particles (200 ruthenium complexes per particle), which was indicated by maximum concentration of ruthenium (II) complexes added in titrations. As expected, for 25 nm AuNPs, the amount of ruthenium per nanoparticle is two times more than for 13 nm AuNPs, due to having a bigger size. (Appendices-Figure 2.31)

Table 2- Summary of SPR shifts upon attachment of surfactants and ruthenium (II) complexes. The SPR shifts were calculate by the difference in the λmax of each sample by UV-Vis after particles isolation.

Sample	**λmax**	**Shift / nm**	**Sample**	**λmax**	**Shift / nm**	**Sample**	**λmax**	**Shift / nm**
Au13	516	0	**Au13**	516	0	**Au13**	516	0
Au13.Z	518	2	**Au13.SPEG**	517	1	**Au13.LPEG**	517	1
Au13.Z.RuPhenL2	520	4	**Au13.SPEG.RuPhenL2**	522	6	**Au13.LPEG.RuPhenL2**	521	5
Au13.Z.RuPhenL1	521	5	**Au13.SPEG.RuPhenL1**	523	7	**Au13.LPEG.RuPhenL1**	522	6

The coating of AuNPs with RuPhenL1 and RuPhenL2 is also investigated using DLS (Figure 2.25 and appendices-tables 5 and 6). As expected, the size and polydispersity index (PDI) slightly increase upon coating for AuNPs of 13 nm and 25 nm size. After coating, the AuNPs in solution have different hydrodynamic sizes due to the attachment of surfactants and ruthenium (II) complexes but also due to the interaction of the nanoparticles with the solvent. For all the AuNPs studied, one single peak is observed showing that there is only one size population. However, for some cases this population has a higher standard deviation than others, showing a less monodispersed nanoparticles and therefore a higher PDI, due to the presence of small quantity of large artifacts, which scatter more light. However, by combining DLS data with UV-Vis, it is possible to conclude that RuPhenL1 and RuPhenL2 were successfully functionalised onto the surface of the AuNPs, the particles show good quality distribution, and do not aggregate after coating.

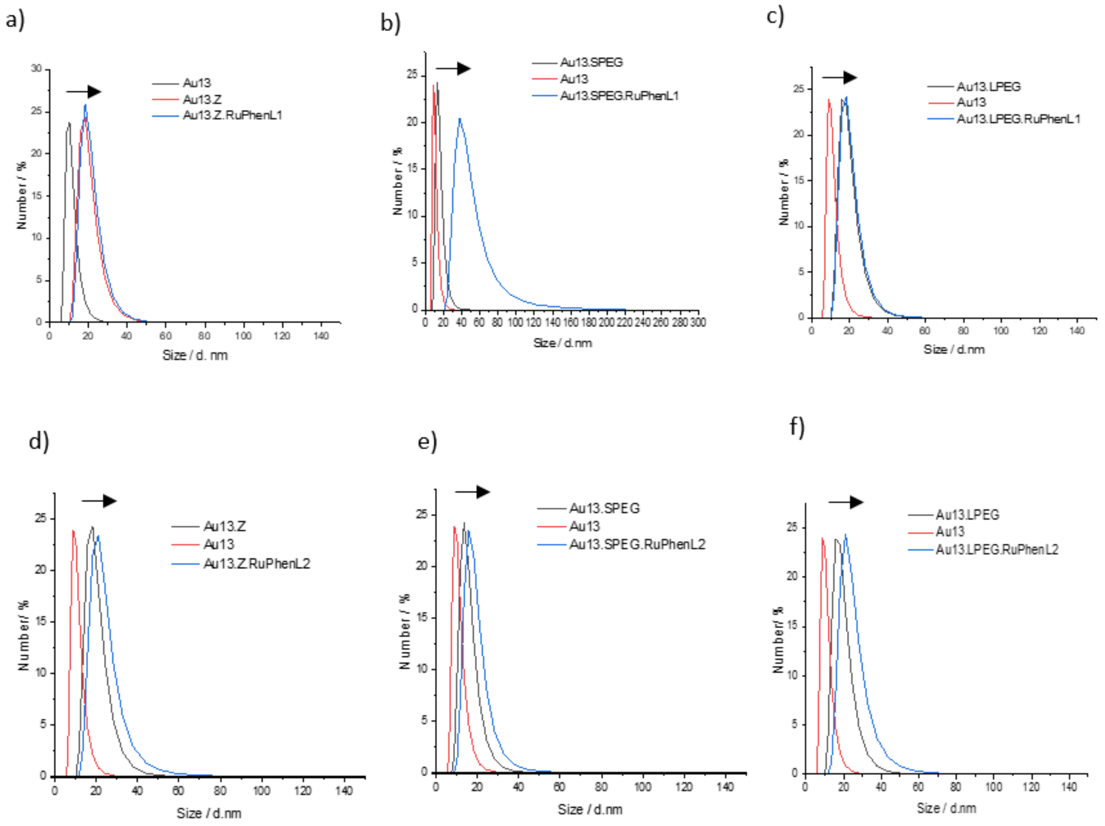

Figure 2.25- Increase of the size by number distribution of coated AuNPs with surfactants (Zonyl FSA, SPEG and LPEG) and ruthenium (II) complexes, RuPhenL1 and RuPhenL2 in comparison with citrate AuNPs.

Transmission electron microscopy showed AuNPs were monodisperse after coating (Figure 2.26). Au13 have sizes between 14-16 ± 1 nm and Au25 have sizes between 22-24 ± 1 nm, upon surfactant and ruthenium (II) complex coating (Appendices-table 6). While DLS clearly indicates an increase on hydrodynamic size after AuNPs coating, the same is not observed by TEM. Once again, this difference is attributed to the fact that the coating is not visualised and therefore further staining is required. In conclusion, AuNPs with three different surfactants coated with two different luminescent ruthenium (II) complexes were successfully synthesised and characterised as monodispersed, with no aggregation in solution. Therefore, the luminescence study of Au.RuPhenL1 and Au.RuPhenL2 was carried out, always considering the main aim of using the AuNPs as imaging agents.

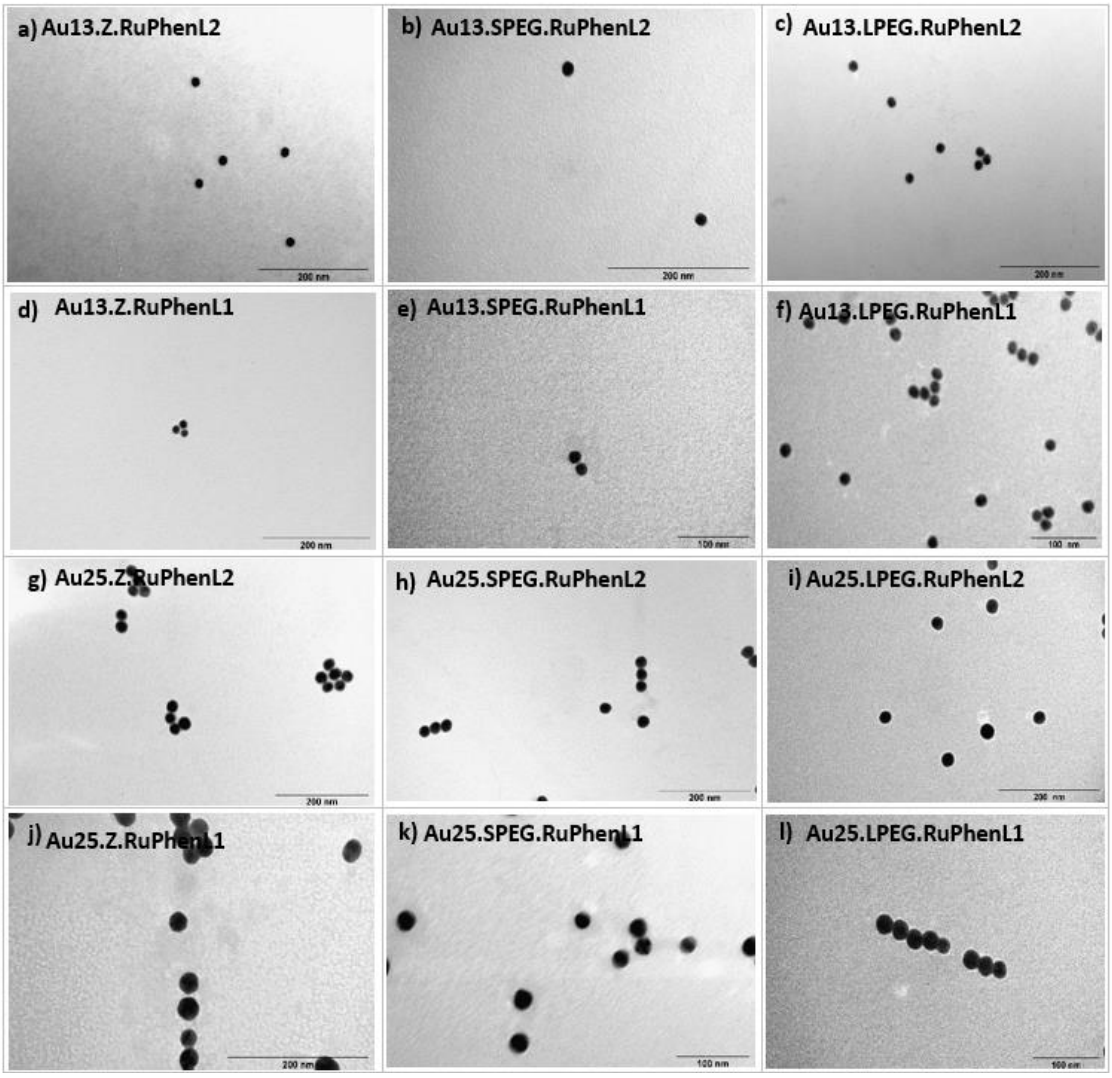

Figure 2.26- Transmission electron microscopy of coated AuNPs, where a-c) 13 nm AuNPs coated with RuPhenL2, d-f) 13 nm AuNPs coated with RuPhenL1, g-i) 25 nm AuNPs coated with RuPhenL2, j-l) 25 nm AuNPs coated with RuPhenL1. All the samples were previously coated with the different surfactants, Zonyl FSA, SPEG and LPEG. TEM sizes were calculated by an average of 15 AuNPs and processed by ImageJ software. Scale bars are 200 nm and 100 nm. The sizes of the AuNPs were 15 ± 1 nm, 15 ± 1 nm and 16 ± 1 nm for Au13.Z.RuPhenL2, Au13.SPEG.RuPhenL2 and Au13.LPEG.RuPhenL2, respectively. Au13.Z.RuPhenL1 has 15 ± 1 nm, Au13.SPEG.RuPhenL1 14 ± 2 nm and Au13.LPEG.RuPhenL1 has 16 ± 1 nm. For AuNPs25, the sizes were 24 ± 2 nm, 24 ± 3 nm, 24 ± 2 nm for Au25.Z.RuPhenL2, Au25.SPEG.RuPhenL2 and Au25.LPEG.RuPhenL2, and 23 ± 2 nm, 24 ± 2 nm, 22 ± 1 nm for Au25.Z.RuPhenL1, Au25.SPEG.RuPhenL1 and Au25.LPEG.RuPhenL1, respectively.

2.3.6 Luminescence studies of the ruthenium (II) complexes functionalised on AuNPs with Zonyl-FSA and PEG surfactants.

To study the photophysical properties of the ruthenium (II) complexes when attached to the AuNPs, UV-Vis spectroscopy, fluorescence emission and excitation spectra were analysed (Figure 2.27). The absorption spectrum shows a well-defined SPR band of λmax at 517 nm. The excitation profile for all Au.RuPhenL1 and Au.RuPhenL2 is characteristic of ruthenium (II) complexes in solution.

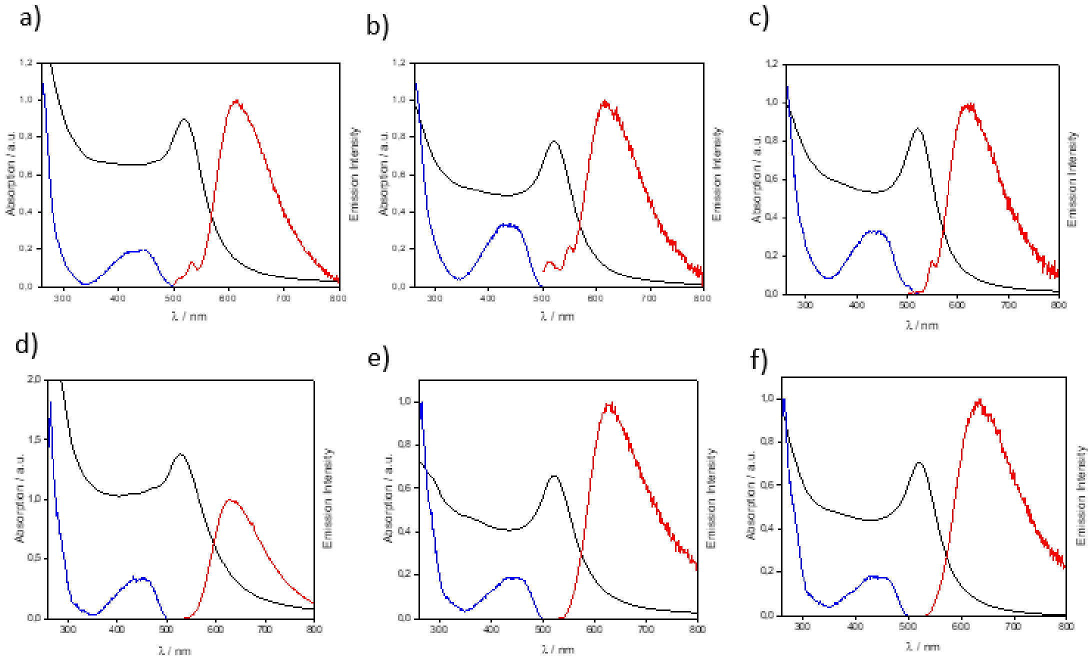

Figure 2.27- Absorption (black), emission (red) and excitation (blue) of 3.5 nM a) Au13.Z.RuPhenL2, b) Au13.SPEG.RuPhenL2, c) Au13.LPEG.RuPhenL2 (λ_{ex}= 446 nm, λ_{em}=615 nm) d) Au13.Z.RuPhenL1, e) Au13.SPEG.RuPhenL1 and f) Au13.LPEG.RuPhenL1 (λ_{ex}= 456 nm, λ_{em}=625 nm) in aerated water.

Figure 2.28 shows that there is not a significant shift on the λmax of the emission for either complex RuPhenL2 or RuPhenL1 after attachment to the AuNPs showing that there is no effect on the distance of complex to the AuNPs in emission of the triplet MLCT. No change in the MLCT could be due to presence of surfactant on the nanoparticles, protecting the ruthenium (II) complexes against interacting with each other and from solvent quenching. Previous studies have showed that when ruthenium (II) complexes attach to AuNPs with no surfactant, a 15 nm blue shift is observed.[238]

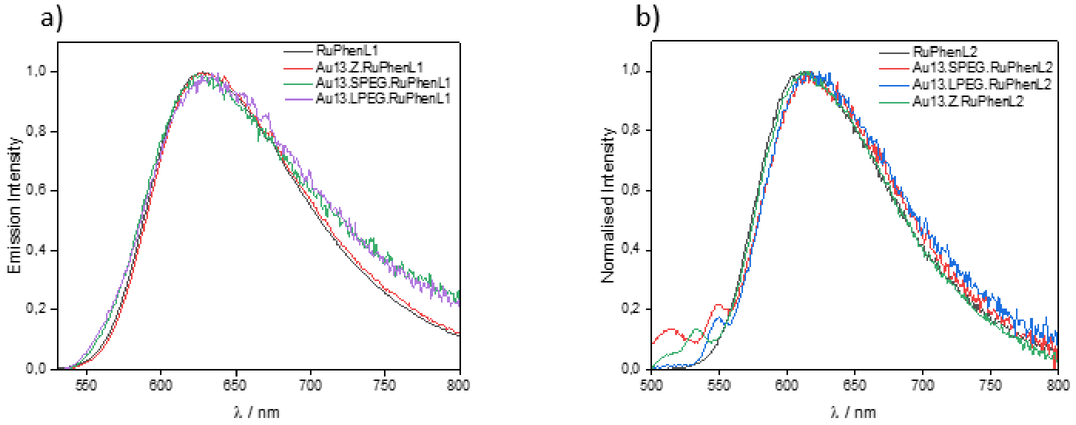

Figure 2.28- Overlayed emission of (left) RuPhenL1, Au13.Z.RuPhenL1, Au13.SPEG.RuPhenL1 and Au13.LPEG.RuPhenL1(λ_{ex}= 446 nm, λ_{em}=615 nm) and (right) RuPhenL2, Au13.Z.RuPhenL2, Au13.SPEG.RuPhenL2 and Au13.LPEG.RuPhenL2 (λ_{ex}= 456 nm, λ_{em}=625 nm). All the solutions are in aerated water.

The luminescence lifetimes are presented on table 3. Both complexes (RuPhenL1 and RuPhenL2) have a higher luminescence lifetime when attached to AuNPs. The AuNPs that have LPEG as surfactant, have the opposite effect and decrease the lifetime. For that reason, only Zonyl FSA and SPEG AuNPs will be analysed in further studies. Interestingly, Zonyl FSA and SPEG AuNPs do not quench ruthenium signal. Moreover, it seems to protect the complexes from $^3O_2$ quenching leading to an improvement of the luminescence lifetime. Au13.Z.RuPhenL1 has the highest lifetime. This could be attributed to the fact that RuPhenL1 is more hydrophobic than RuPhenL2. It is known that increasing hydrophobicity, increases the interaction with the surfactants, which allows a better protection from $^3O_2$ quenching and thus, higher lifetime. In conclusion, the luminescence lifetimes of ruthenium (II) complexes can alter on the nanoparticles, depending on the type and length of surfactant used.

In all the nanoparticles lifetimes, three components were found, unlike the ruthenium (II) complexes in solution, where only one component is observed. Luminescence lifetime process can involve multiple steps or pathways leading to the emission of light. Each of these pathways can have a different rate of efficiency. Furthermore, lifetimes can also be influenced by the local environment as for example the solvent where the solution is dissolved. In this case, the ruthenium (II) complexes are attached to AuNPs suspended in water, where a surfactant is also present. Therefore, there are differences in the different local environments, hence, it is not surprising that more than one component is observed for these luminescent AuNPs.

Table 3- Luminescence lifetimes recorded for RuPhenL2 and RuPhenL1, coated AuNP13 and AuNP25 in aerated water. Lifetimes were recorded using a 450 nm laser and were fitted with a χ^2 between 1.0 and 1.2.

Sample NAME	**Lifetimes / ns air**	**Sample NAME**	**Lifetimes / ns air**
RuPhenL2	583 (100%)	**RuPhenL1**	514 (100%)
Au13.Z.RuPhenL2	618 (75%), 115 (15%), 17 (11%)	**Au13.Z.RuPhenL1**	793 (70%), 293 (26%), 40 (4%)
Au13.SPEG.RuPhenL2	754 (80%), 89 (14%), 4 (5%)	**Au13.SPEG.RuPhenL1**	610 (50%), 52 (13%), 4 (37%)
Au13.LPEG.RuPhenL2	457 (80%), 30 (9%), 4 (10%)	**Au13.LPEG.RuPhenL1**	406 (70%), 16 (13%), 2 (17%)

Au25.Z.RuL2	465 (73%), 50 (17%), 9 (10%)	**Au25.Z.RuPhenL1**	565 (75%), 144 (20%), 11 (5%)
Au25.SPEG.RuL2	715 (75%), 78 (5%), 5 (19%)	**Au25.SPEG.RuPhenL1**	664 (55%), 77 (4%), 4 (40%)
Au25.LPEG.RuL2	459 (79%), 7 (14%), 1 (6%)	**Au25.LPEG.RuPhenL1**	184 (54%), 121 (30%), 3 (16%)

Table 4- Quantum yield of complexes RuPhenL2, RuPhenL1 and coated AuNPs in aerated water.

Sample Name	**ϕ / %**	**Sample Name**	**ϕ / %**
RuPhenL2	1.5	**RuPhenL1**	1.4
Au25.Z.RuPhenL2	5.2	**Au25.Z.RuPhenL1**	5.5
Au25.SPEG.RuPhenL2	8.0	**Au25.SPEG.RuPhenL1**	2.0

Quantum yield for the gold nanoparticles were difficult to obtain due to a very weak signal. However, quantum yields were recorded for AuNPs of 25 nm size, due to higher quantity of ruthenium coating and therefore higher signal (Table 4). For both complexes, the quantum yield mirrors the luminescence lifetime, in which the complexes in solution have the lowest quantum yield but when attached to the nanoparticles, the quantum yield increases. As seen in the lifetime, SPEG-AuNPs have a higher quantum yield than Zonyl FSA-AuNPs when coated with RuPhenL2. However, the opposite happens for the particles coated with RuPhenL1, where Zonyl FSA-AuNPs have the highest quantum yield. This shows that the luminescence of the AuNPs does depend on the surfactant used but also on the ruthenium (II) complex used, as different ruthenium (II) complexes can have very different behaviour when shared the same surfactant on the surface of the AuNPs. In this study it is possible to observe that for AuNPs functionalised with RuPhenL1, Zonyl FSA is the best surfactant to be used due to its higher lifetime and quantum yield, whereas for AuNPs coated with RuPhenL2, SPEG is the surfactant the allows increased luminescence.

2.4 Conclusions

Two ruthenium polypyridyl complexes with two different auxiliary ligands (RuPhenL1 and RuPhenL2) were successfully synthetised and characterised. Both complexes showed an emission by the MLCT band in the visible region, providing promising grounds for further biological studies and therapeutics. RuPhenL2 showed higher lifetime than RuPhenL1 due to its mix ligand structure, however, both complexes showed longer luminescence lifetime than its parent $Ru(Phen)_3Cl_2$. Two different sizes of gold nanoparticles, 13 nm and 25 nm were successfully synthesised and demonstrated to be monodispersed, with low polydispersity index and good quality distribution. To stabilise the AuNPs, three different surfactants were also functionalised on the AuNPs surface, Zonyl FSA, SPEG and LPEG. These surfactants are different not only on its structure but also on the conformation adapted when attached to the gold nanoparticles, influencing AuNPs hydrodynamic size. Surfactants and *posteriori* ruthenium attachment to the AuNPs was evidenced by increase of hydrodynamic size by DLS and slight red shifts on the AuNPs SPR band. Even with the presence of the surfactants on the nanoparticles, there is 400/ 885 (RuPhenL2) and 600 /1700 (RuPhenL1) per Au13 / Au25 respectively, showing that it is possible to coat gold nanoparticles with a considerable number of complexes without particles aggregation. The attachment of the ruthenium to the AuNPs did not affect the lowest excited state position since the emission of the ruthenium did not significantly change. However, the luminescence lifetime and quantum yield improved when attached to the gold due to the presence of the surfactants. Au.SPEG.RuPhenL2 had a ~30% increase and Au.Z.RuPhenL1 had a 50% increase on its lifetime compared to the complexes in solution. Interestingly, LPEG has the opposite effect and decrease the luminescence signal. This showed that the lifetime of ruthenium (II) complexes can be improved on the AuNPs depending on the type or length of surfactant used. Lastly, it was showed in this chapter, that a system of luminescence monodisperse AuNPs was successfully carried out and it is suitable for future cell studies.

2.7 Appendices

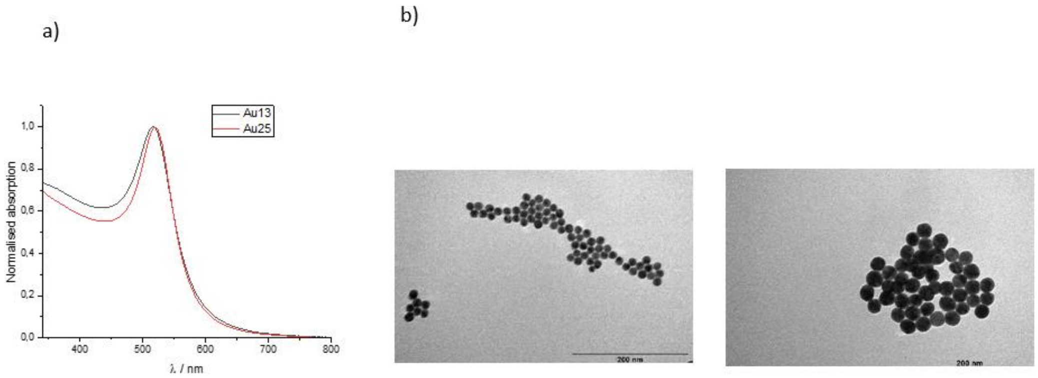

Figure 2.29- a) UV-Vis of Au13 (black) and Au25 (red) showing the SPR band at 516 nm and 519 nm, respectively. b) Transmission electron microscopy (TEM) of Au13 (left) and Au25 (right). TEM sizes were calculated by an average of 15 AuNPs and processed by ImageJ software. The sizes of Au13 were 13 ± 1.1 and 23 ± 1.8 nm for Au25. Scale bars are 200nm.

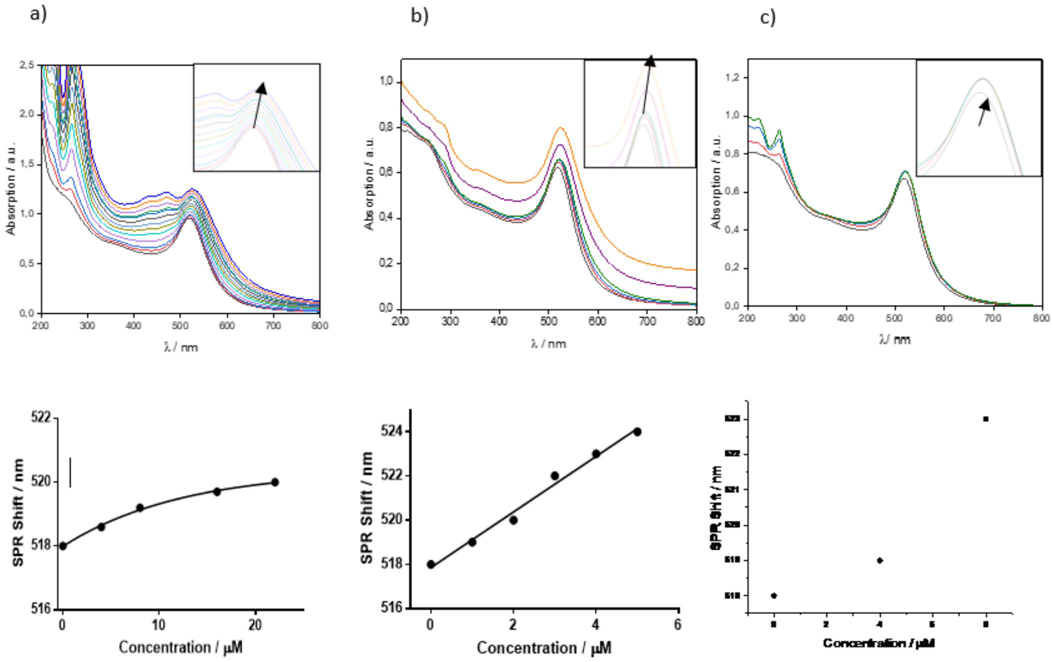

Figure 2.30- Titrations of a 1mM stock solution in MeOH of RuPhenBSS in 6.5nM AuNPs by UV-Vis, binding curves of concentration vs SPR shift and correspondents fitting curves with non-linear regression for a) Au13.Z.RuPhenL1, b)Au13.SPEG.RuPhenL1. c) Au13.LPEG.RuPhenL1 was not possible to perform any fitting due to the lack of points.

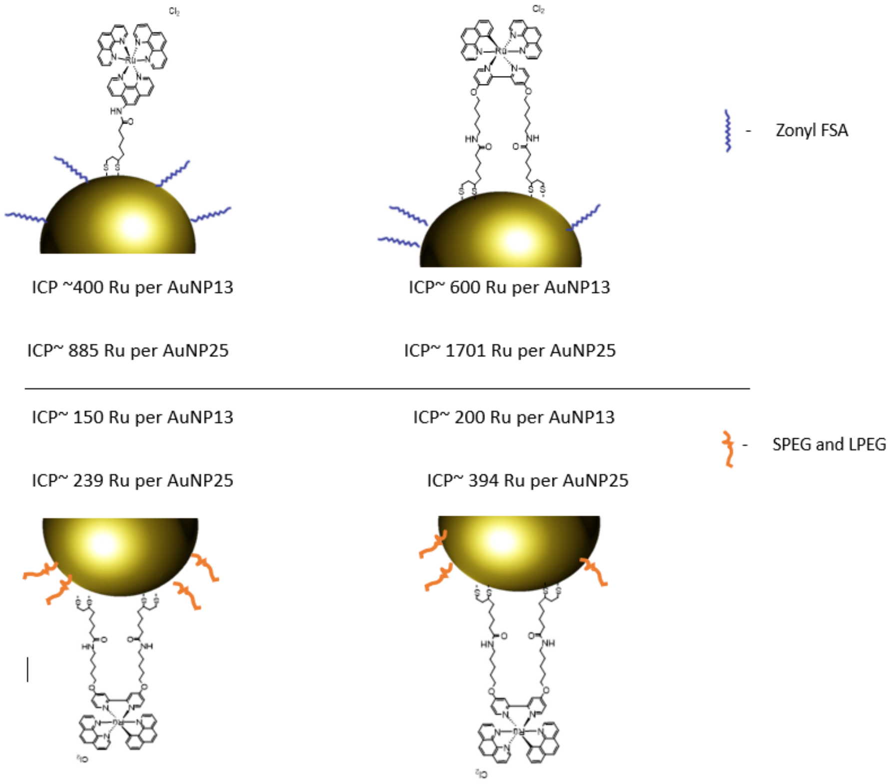

Figure 2.31- Representation of AuNPs coated with the different surfactants and ruthenium (II) complexes and the amount of ruthenium (II) complexes per nanoparticles given by ICP-MS

Table 5- Size by number distribution and polydispersity index of citrate and coated Au13 by DLS.

	Dynamic Light Scattering **(DLS)**	
	Number distribution / nm	Polydispersity Index (PDI)
Au13	11.5 ± 2.9	0.09
Au13.Z	19.3 ± 5.3	0.23
Au13.SPEG	15.0 ± 4.2	0.19
Au13.LPEG	18.4 ± 5.1	0.16
Au13.Z.RuPhenL2	22.9 ± 7.5	0.36
Au13.SPEG.RuPhenL2	24.6 ± 6.9	0.35
Au13.LPEG.RuPhenL2	23.8 ± 7.2	0.28

Au13.Z.RuPhenL1	23.1 ± 7.4	0.29
Au13.SPEG.RuPhenL1	29.0 ± 8.3	0.36
Au13.LPEG.RuPhenL1	19.3 ± 5.3	0.23

Table 6- Size by number distribution and polydispersity index of citrate and coated Au25 by DLS.

	Dynamic Light Scattering (DLS)	
	Number distribution / nm	Polydispersity Index (PDI)
Au25	20.1 ± 5.0	0.08
Au25.Z	22.6 ± 6.6	0.23
Au25.SPEG	22.6 ± 6.6	0.26
Au25.LPEG	25.1 ± 6.9	0.25
Au25.Z.RuPhenL2	24.0 ± 9.1	0.30
Au25.SPEG.RuPhenL2	32.9 ± 11.9	0.29
Au25.LPEG.RuPhenL2	31.2 ± 9.2	0.22
Au25.Z.RuPhenL1	26.5 ± 13.8	0.25
Au25.SPEG.RuPhenL1	46.7 ± 18.7	0.19
Au25.LPEG.RuPhenL1	23.0 ± 7.2	0.29

Table 7- Binding constant for surfactant PEG and ruthenium (II) complexes upon gold nanoparticles functionalisation. Bmax corresponds to the maximum specific binding in nm. Kd is the equilibrium dissociation constant in M. When in equilibrium, is the concentration needed to achieve half binding. Ka is the equilibrium association constant in M^{-1}.

	Au13.LPEG	**Au13.SPEG**	**Au13.Z. RuPhenL2**	**Au13.SPEG .RuPhenL2**	**Au13.LPEG. RuPhenL2**	**Au13.Z. RuPhenL1**
Bmax / nm	6.016	5.853	6.315	10360	6.010	7.072
Kd / M	1.500	3.094	22.10	348.6	2.098	28.97
Ka / M^{-1}	666667	323206	45249	2869	476644	34528

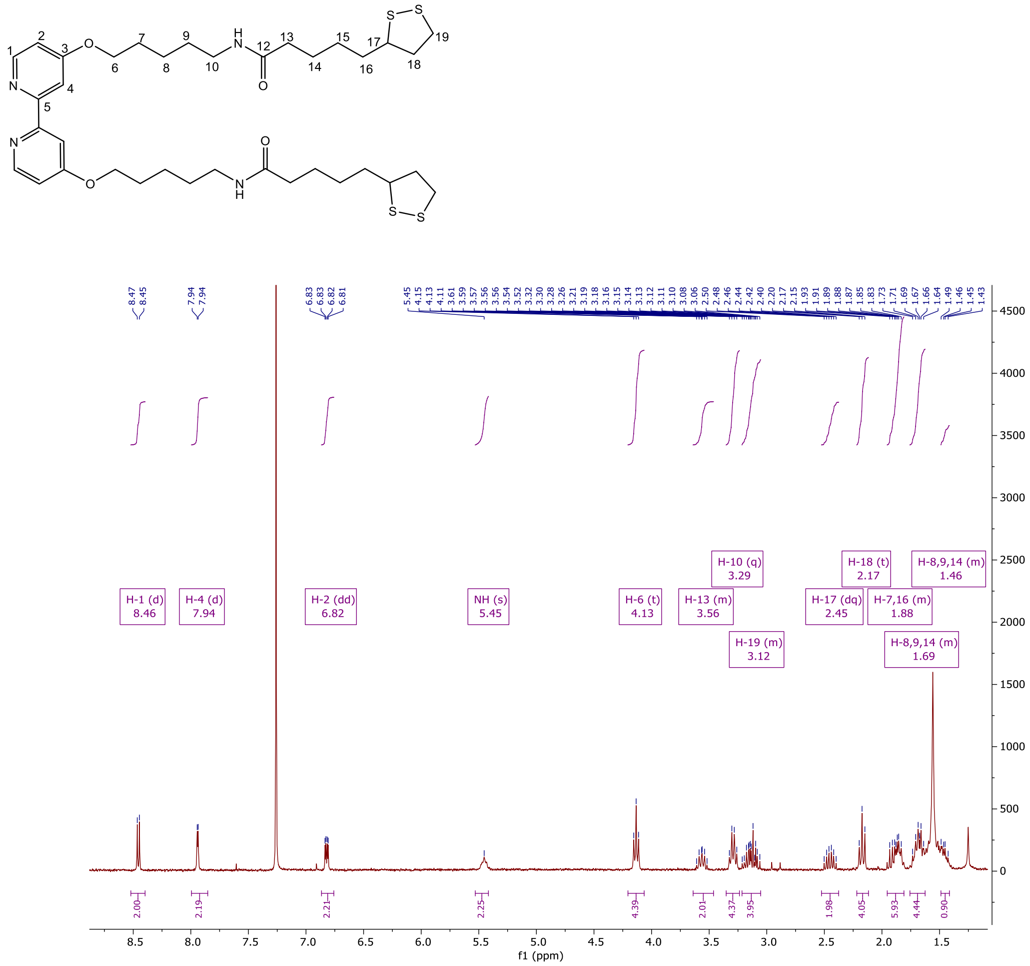

Figure 2.32- ^{1}H-NMR of L1 ligand in $CDCl_3$.

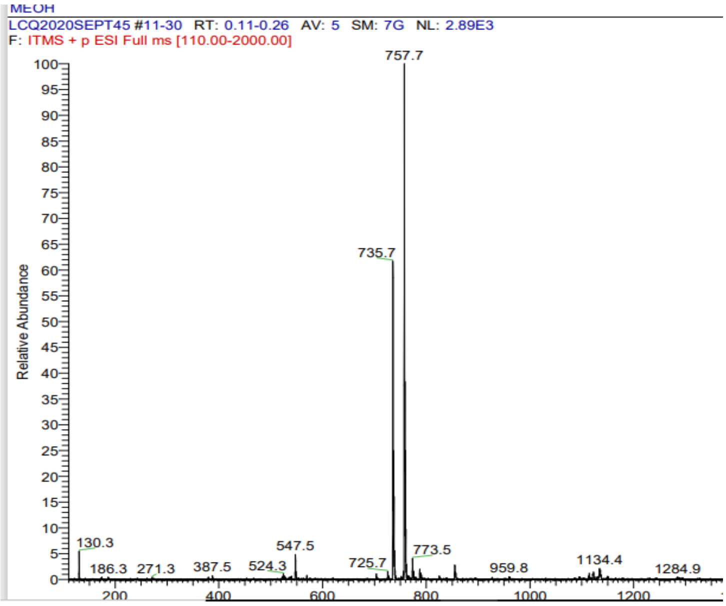

Figure 2.33- L1 ligand ESI^{+} MS with the fragments 757.7 and 735.7 which corresponds to $(M+Na)^{+}$ and $(M+H)^{+}$.

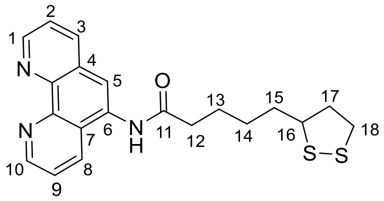

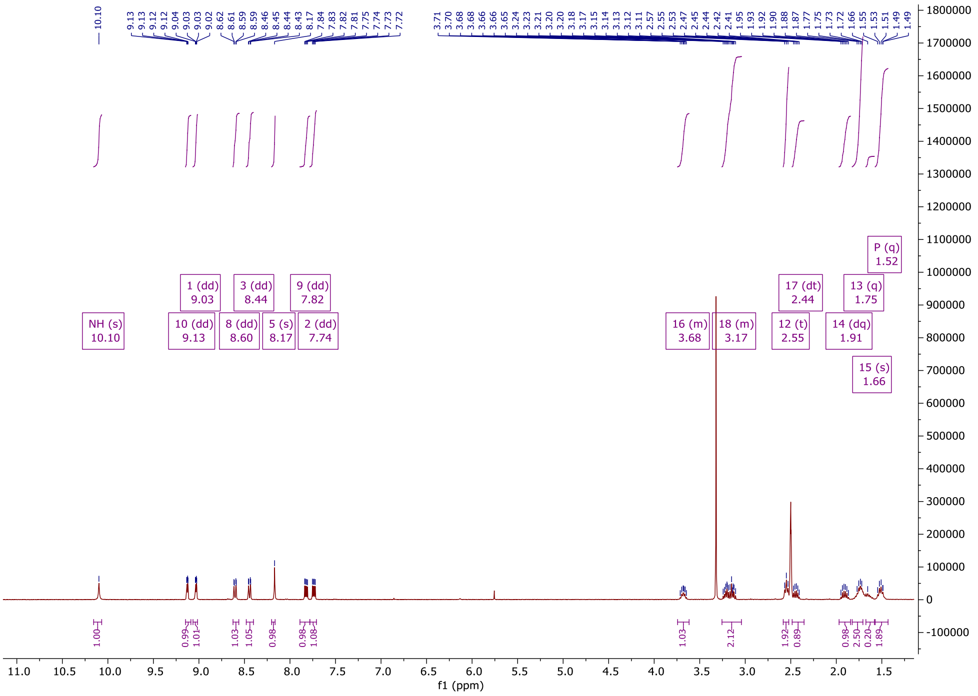

Figure 2.34-^{1}H-NMR of L2 ligand in DMSO-d_6.

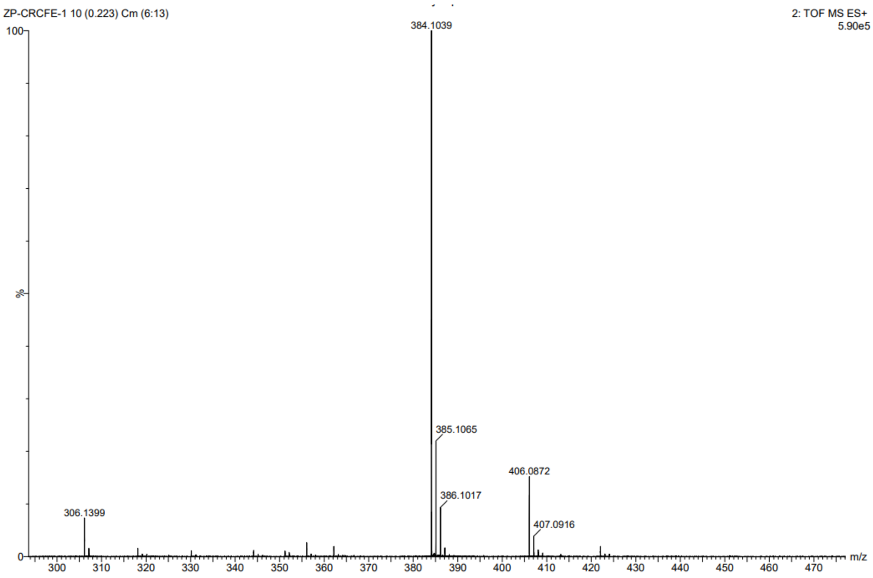

Figure 2.35- L2 ligand ESI$^+$ MS, with the fragment 384.10, 406 corresponds to $(M+H)^+$.

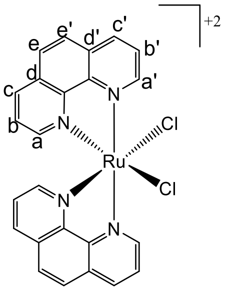

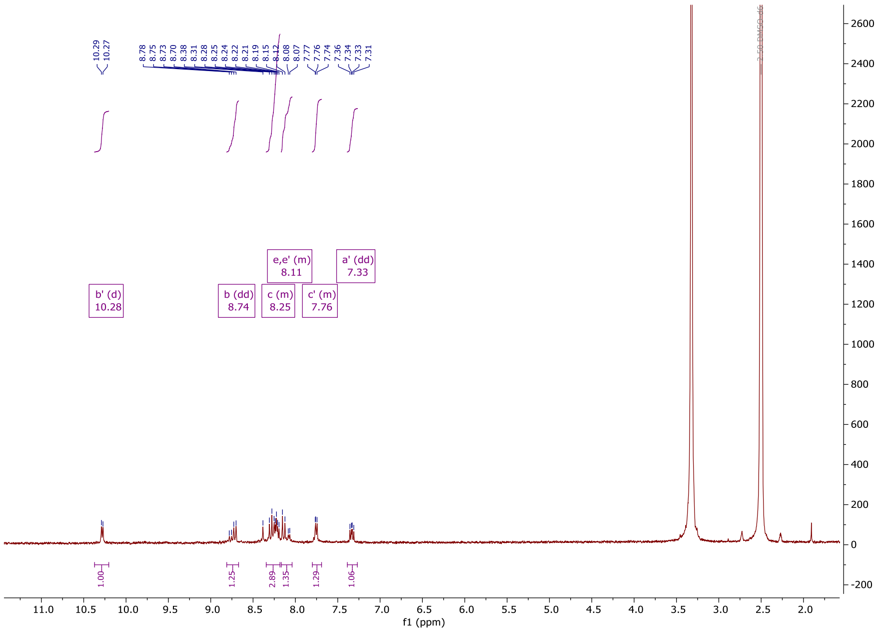

Figure 2.36-^{1}H-NMR of $RuPhen_2Cl_2$ in DMSO-d$_6$.

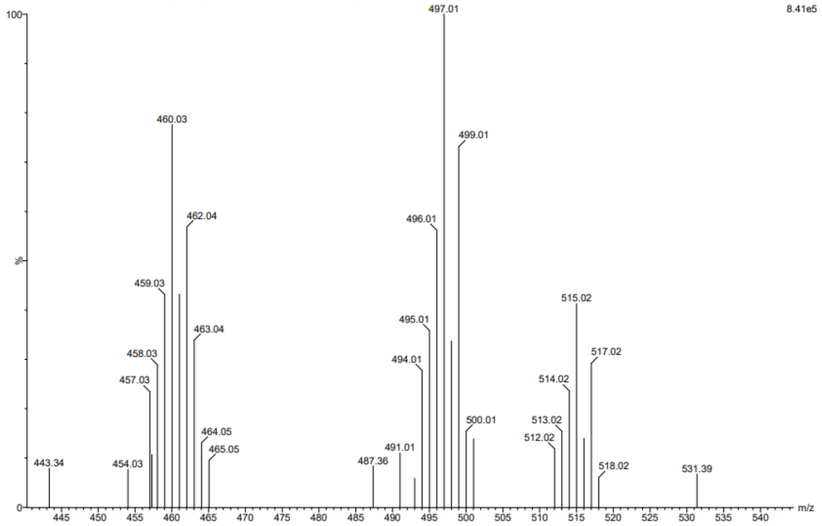

Figure 2.37- $RuPhen_2Cl_2$ ESI$^+$ MS with the main fragment 497 (M-Cl)$^+$.

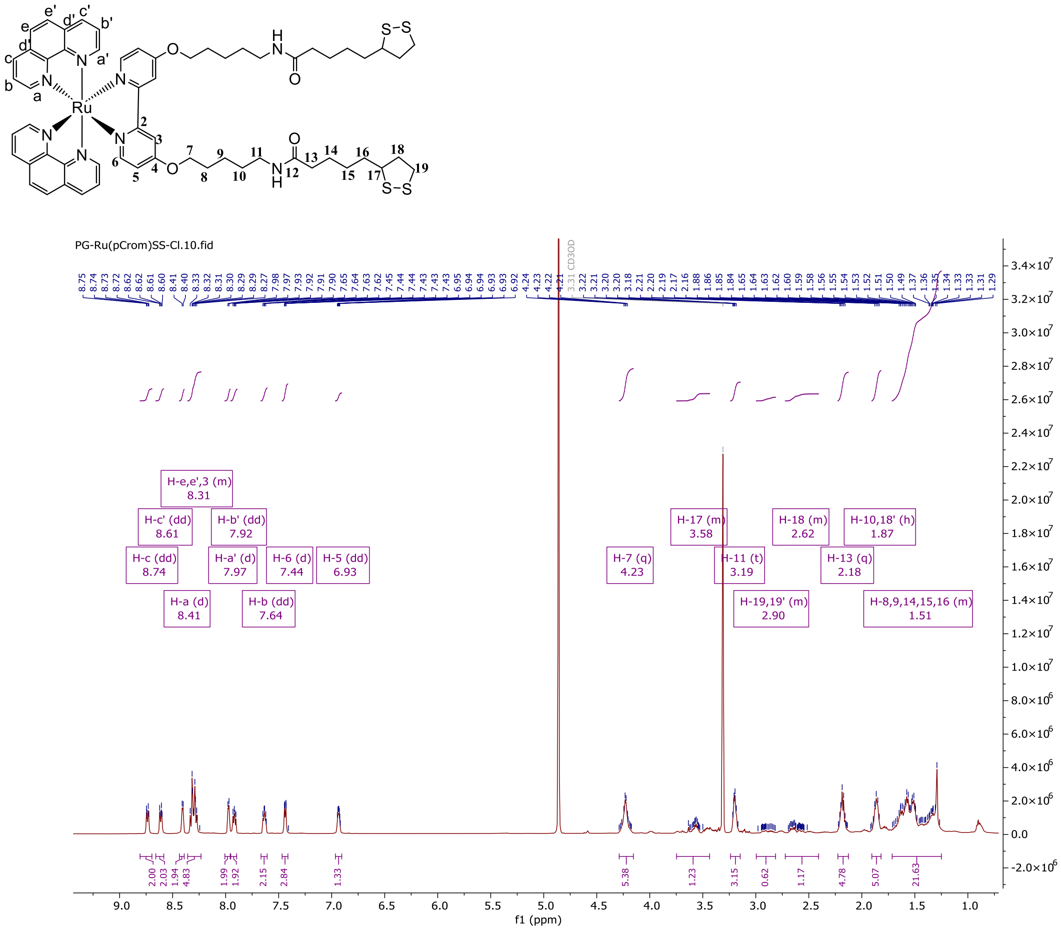

Figure 2.38-^{1}H-NMR of RuPhenL1 in MeOD.

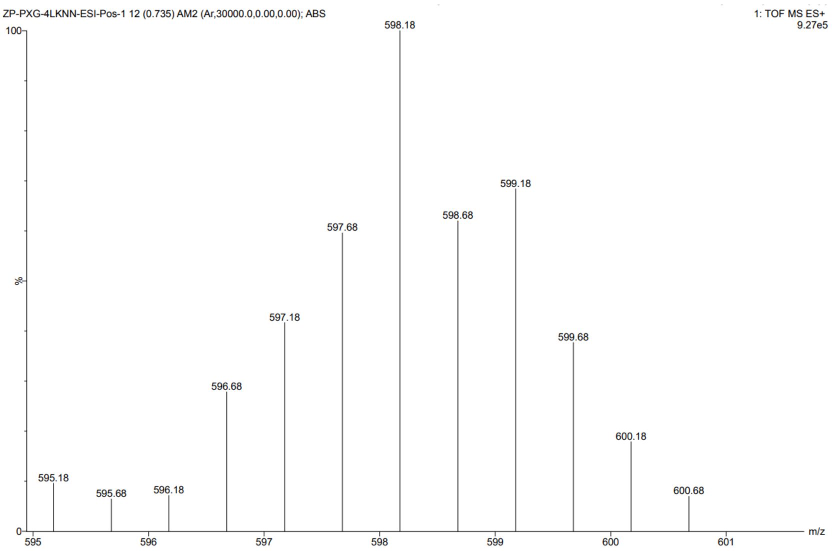

Figure 2.39- RuPhenL1 ESI^{+} MS with the fragment 598 (M-2(PF6))$^{2+}$.

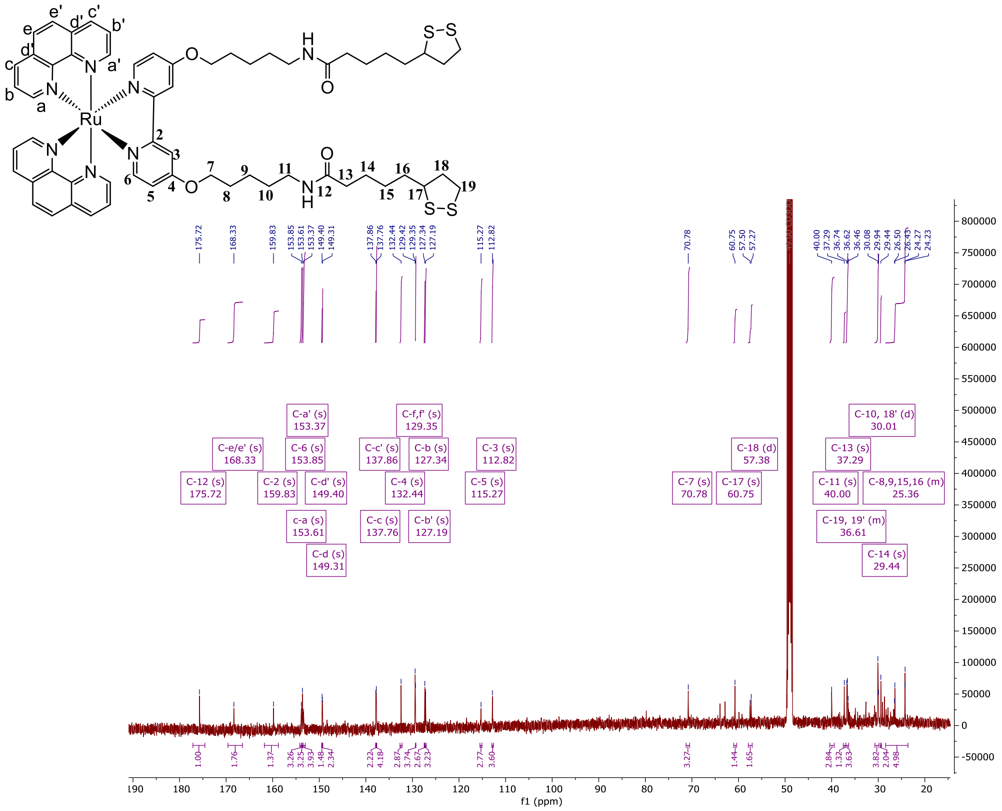

Figure 2.40-^{13}C-NMR of RuPhenL1 in MeOD.

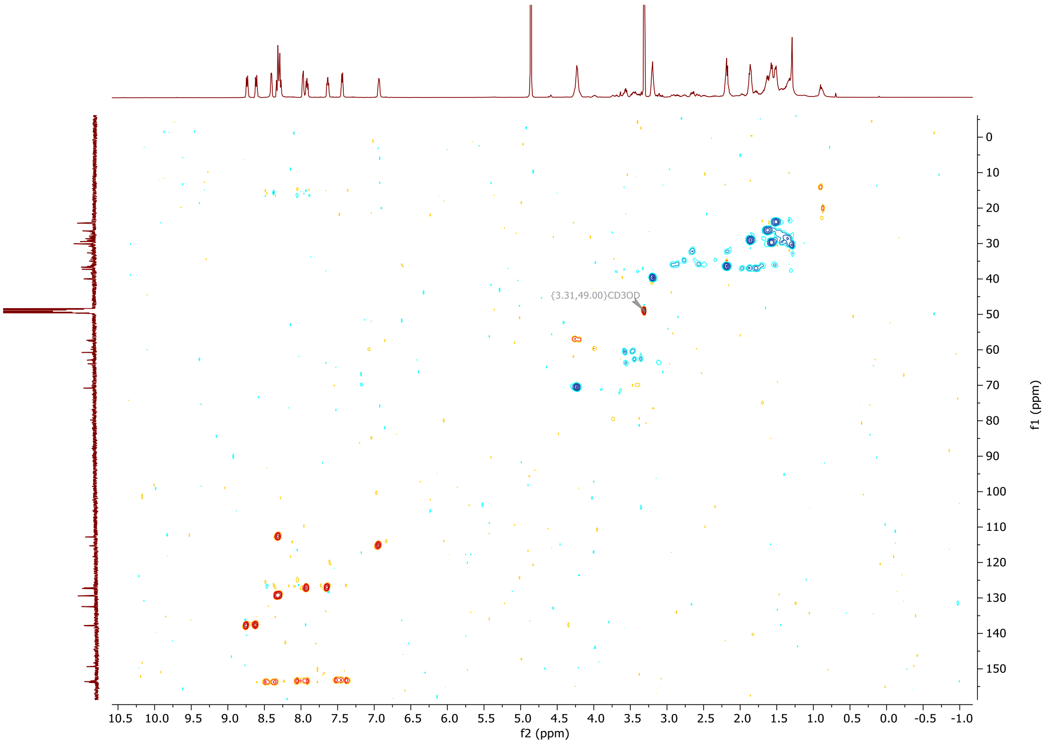

Figure 2.41- 2D HSQC of RuPhenL1 in MeOD.

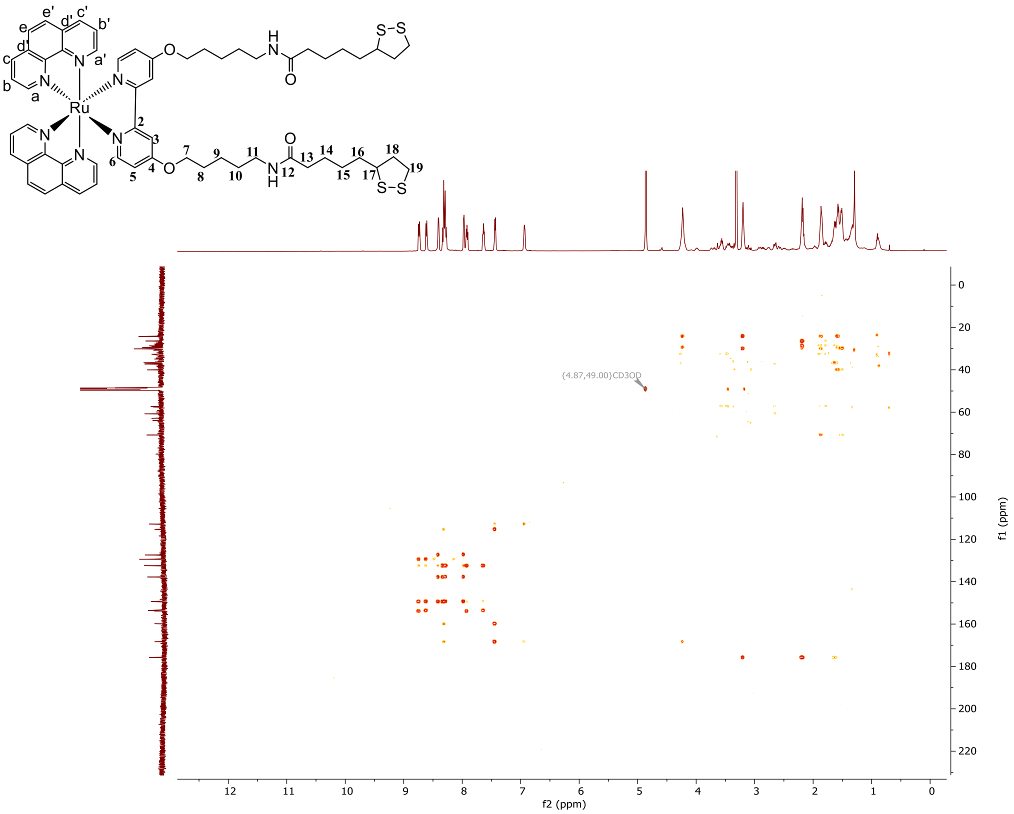

Figure 2.42-2D HMBC of RuPhenL1 in MeOD.

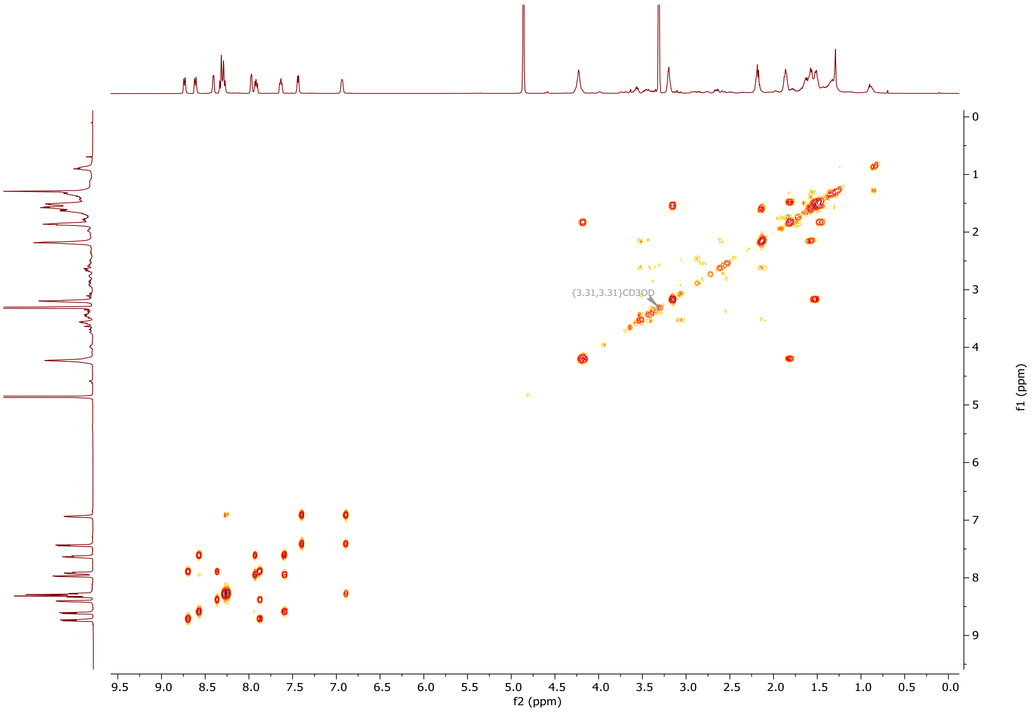

Figure 2.43- 2D COSY of RuPhenL1 in MeOD.

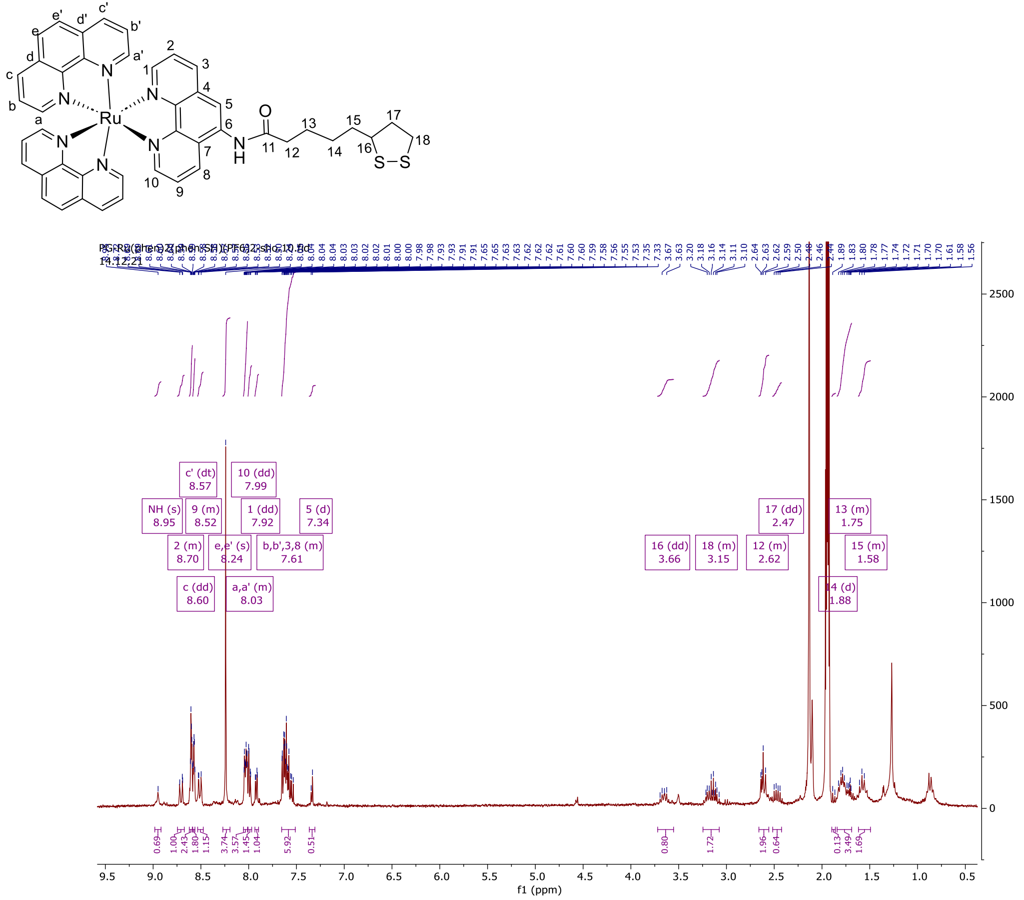

Figure 2.44-^{1}H-NMR of RuPhenL2 in CD_3CN.

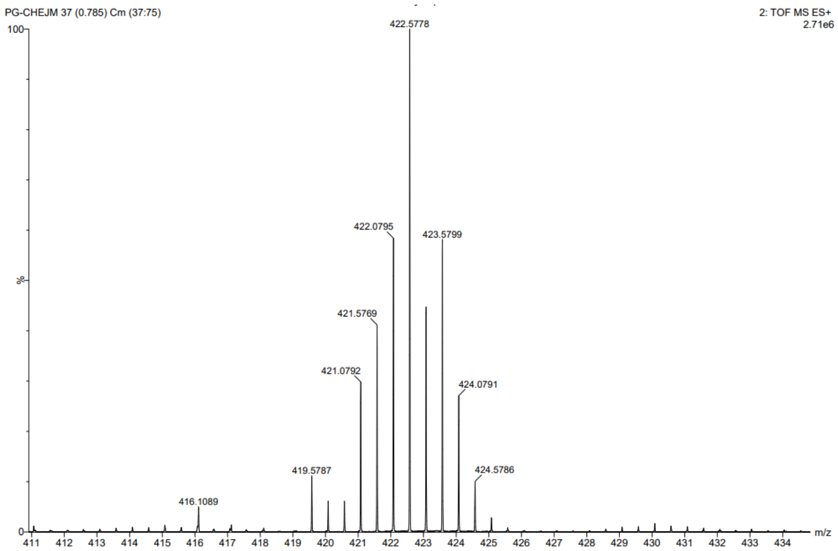

Figure 2.45- RuPhenL2 ESI$^+$ MS with the fragment 422.6 $(M-2(PF6))^{2+}$.

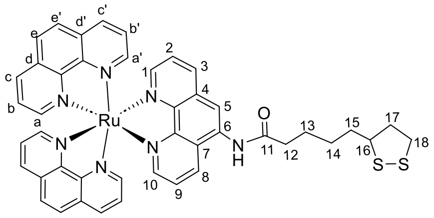

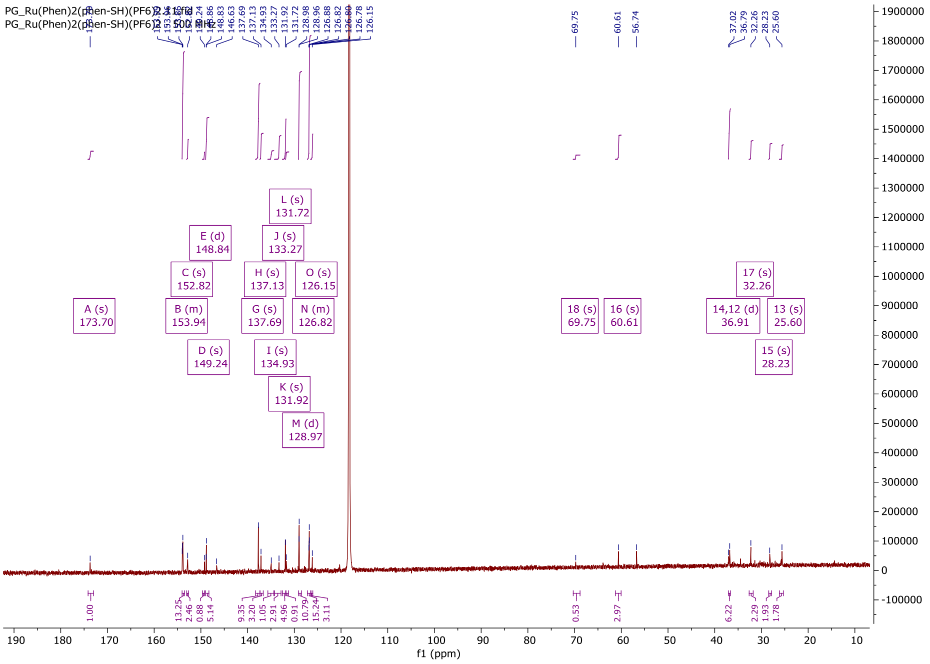

Figure 2.46- 13C-NMR of RuPhenL2 in CD3CN.

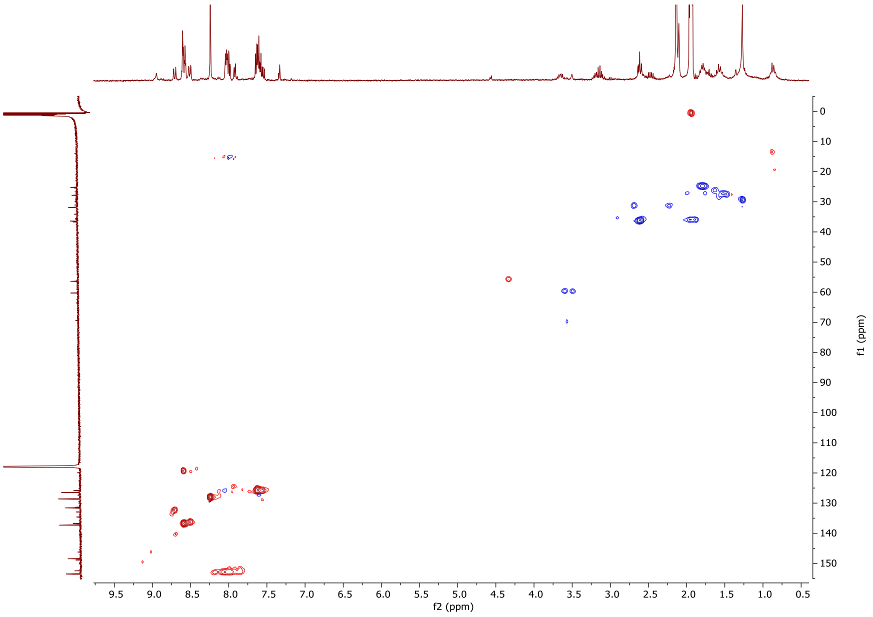

Figure 2.47-2D HSQC of RuPhenL2 in CD_3CN.

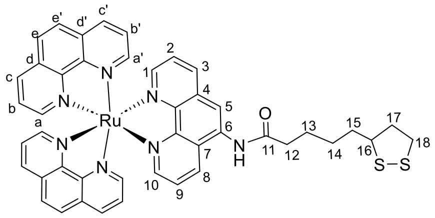

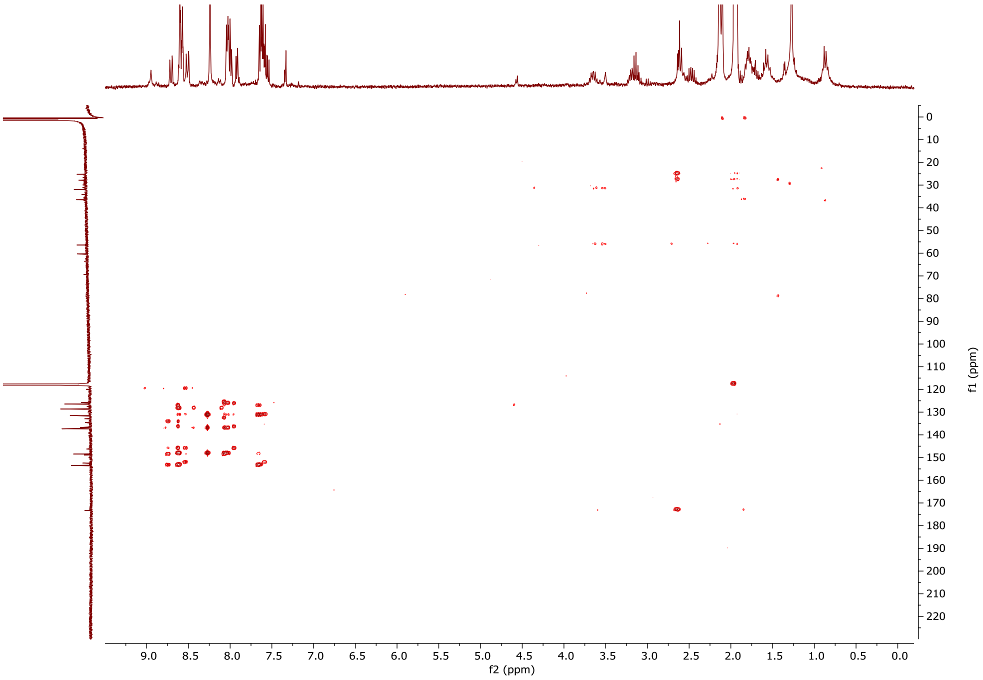

Figure 2.48-2D HMBC of RuPhenL2 in CD_3CN.

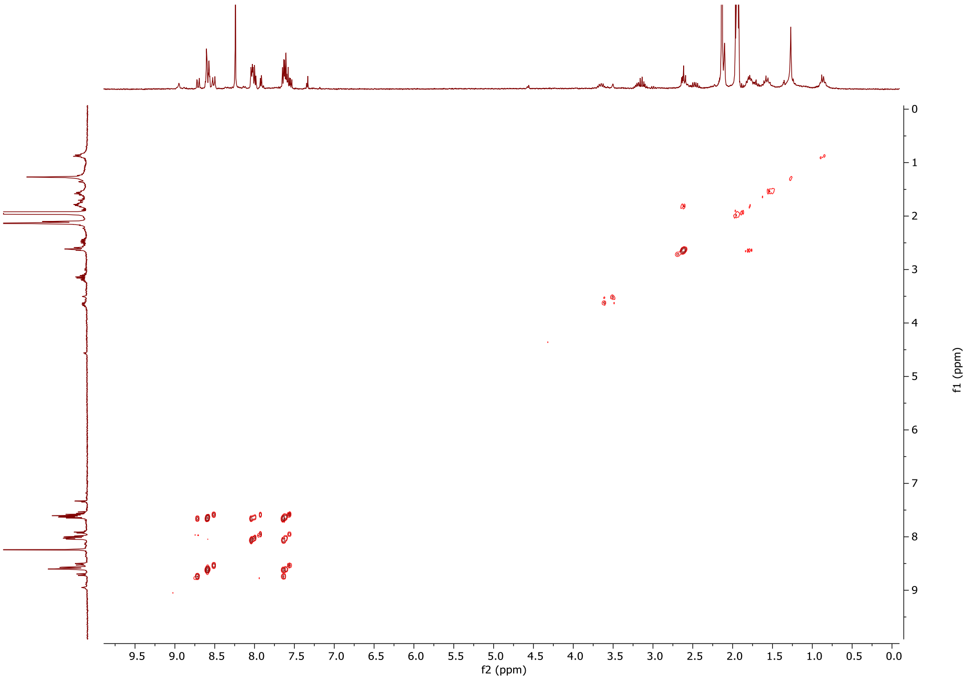

Figure 2.49-2D COSY of RuPhenL2 in CD_3CN.

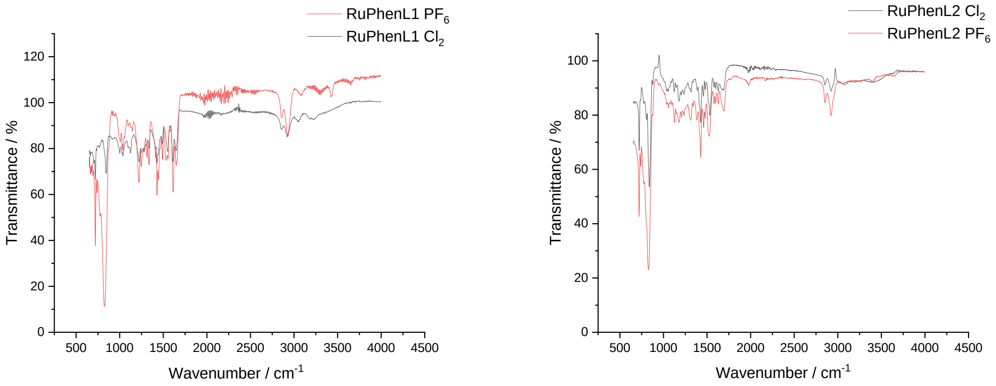

Figure 2.50- FTIR of RuPhenL1 and RuPhenL2 with PF_6 or chloride salt.

3. Luminescent gold nanoparticles for DNA recognition

3.1 Introduction

3.1.1 Stereoselectivity of ruthenium(II) tris phenanthroline in binding DNA

Given the importance of targeting DNA for biological applications, many studies have been undertaken to explore if and how different structures are able to interact with DNA.[254] However, since DNA is a polymorphic structure with different conformations, targeting can be challenging for small molecules.[80] Ruthenium (II) polypyridyl complexes, are one of the main metals studied for DNA interaction due not only to their attractive luminescence characteristics but also because they offer the possibility to choose ligands according to the ability to fit between base pairs. Moreover, Ruthenium (II) complexes are also positively charged which permits electrostatic attractions. Therefore, two of the main and first ruthenium (II) complexes studied for DNA interactions are Ru(bpy$_3$)Cl$_2$ and Ru(phen$_3$)Cl$_2$.[255] The nature of the interaction between ruthenium metal complexes and DNA relies upon the characteristics of the ligands, particularly the presence of an aromatic π-system that facilitates π-π stacking, the planarity of the ligand and its ability to penetrate the base pairs of DNA.[80] Soon it was found that Ru(bpy$_3$)Cl$_2$ did not have the ideal characteristics for an effective interaction with DNA.[256] The 2,2'-bipyridyne ligand possesses a small π-system making it difficult for π-π stacking and it cannot penetrate the double helix due to its length and nonplanarity.[256] In comparison, Ru(phen$_3$)Cl$_{2,}$ due the 1,10-phenanthroline's rigid structure, planarity, and bigger π-system than 2,2'-bipyridine, allows an easier interaction between base pairs of DNA undergoing partial intercalation. Ru(phen$_3$)Cl$_2$ has the optimal characteristics to bind to

DNA through intercalation, however, the binding mode of this complex led to interesting findings.[257] Well-known DNA intercalators, like ethidium bromide, exhibit specific characteristics upon DNA binding, such as a significant hypochromic effect with a red shift, an increase on luminescence upon DNA binding, an increase on DNA viscosity and an increase on distance between base pairs.[258, 259] When an intercalator interacts with the DNA base pairs, the π* orbital of the intercalative ligand can couple with π orbital of the base pairs, leading to a decrease in π- π* transition energy, resulting in a red shift in the intra ligand (IL) band visible on UV-Vis spectroscopy.[85, 86] Moreover, the coupling of a π orbital with partially filled electrons decreases the transitions probabilities, resulting in a hypochromic effect.[176, 260] Besides, when an intercalator binds to the DNA base pairs, reduces its accessibility to water molecules, preventing luminescence quenching and resulting in an emission intensity increase.[87] (Further details on DNA binding techniques can be found on Chapter 1- section 1.2.2.2). Although $Ru(phen_3)Cl_2$ had a hypochromic effect (12 % decrease in absorbance) and an increase on luminescence intensity (48 %), these effects were smaller than known intercalators. Moreover, this complex upon DNA interaction, decrease the viscosity and the distance between base pairs on the helical axis of DNA, which is the opposite behaviour of an intercalator.[261] Ultimately, a hypothesis was raised that $Ru(phen_3)Cl_2$ had a partial intercalation between the base pairs involving just one ring of the 1,10-phenanthroline.[95] Due to its structure, only one of the rings of one 1,10-phenanthroline ligand fits between the base pairs and the other two ligands are free to direct the enantiomeric selection.[95, 256, 262] $Ru(phen_3)Cl_2$ is a chiral complex, which has an enantiomeric preference in binding to DNA. As observed on figure 3.1, for Δ enantiomer, the two free ligands thar are not stacked between the base pairs, can fit very closely along the groove, whereas for Λ enantiomer, the ligands are sterically repelled by the phosphate backbone of the duplex.[95] Moreover, an hypochromic effect and an increase on luminescence lifetime seems to be stronger for the Δ isomer than the Λ isomer when interact with B-DNA, showing the higher affinity for B-DNA of one enantiomer versus the other.[257]

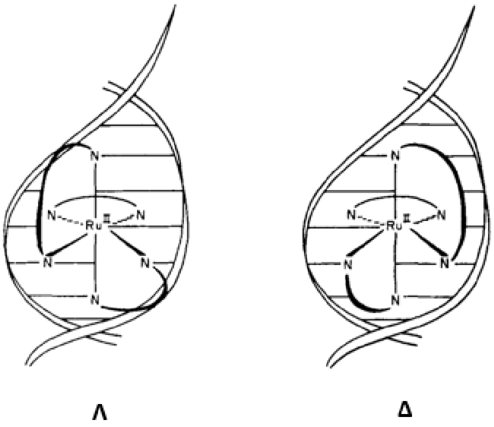

Figure 0.1- Schematic representation of B-DNA double helix and intercalation of Λ and Δ enantiomers of $RuPhen_3$. Image adapted from [95].

Studies of different 1,10-phenanthroline functionalities ruthenium (II) complexes showed that the racemic complex $Ru(TMP)_3$ (TMP= 3,4,7,8- tetramethylphenanthroline) displays preference for A form of DNA. This complex showed to be too big to fit between the base pairs of a B-DNA, however through electrostatic and hydrophobic interactions, it can bind very well in the major grove of A-DNA.[263] More recently, Boynton and co-workers studied a sterically expansive aromatic ruthenium (II) complex with the ligand benzo (c-1,7) naphthyridine-1-isoquinoline and two 2,2'-bipyridines ligands, that is selective for DNA mismatches (Figure 3.2).[264] The binding of the complex is assumed to be through metalloinsertion, with an affinity of 500 times higher for mismatched sites than for well-matched double helix due to its sterically bulky ligands that can only fit in destabilised DNA forms.[264, 265] Although these studies have been an important breakthrough on the field of DNA interactions, the discovery of the light switch effect exponentially increased the studies of some particular ruthenium (II) polypyridyl complexes for DNA binding.

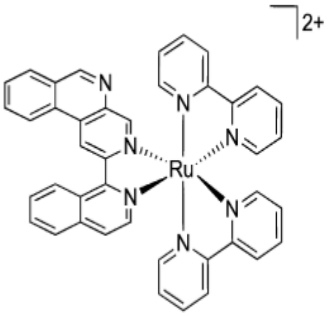

Figure 0.2- Chemical structure of $[Ru(bpy)_2(BNIQ)]^{2+}$, from[264].

3.1.2 Light switch effect

In 1990, $[Ru(bpy)_2(dppz)]^{2+}$, dppz = dipyrido[3,2-a:2',3'-c phenazine] (Figure 3.3) was found to be a molecular "light switch" for DNA by displaying photoluminescence behaviour when binds to DNA in nonaqueous solution at room temperature.[266] This complex has an extensive planar aromatic ligand, dppz, that can easily intercalate with DNA, but also it can be used as a luminescent probe for nucleic acids.[266] Moreover, soon it was realised that $[Ru(phen)_2(dppz)]^{2+}$ also binds to DNA by intercalation and has the same luminescent behaviour as $[Ru(bpy)_2(dppz)]^{2+}$ and therefore, an extensive investigation on these complexes binding mode was caried out.

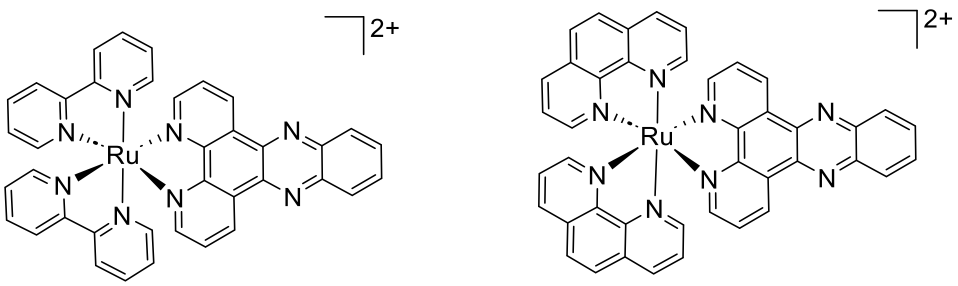

Figure 0.3- Chemical structures of (L) $[Ru(bpy)_2(dppz)]^{2+}$and (R) $[Ru(phen)_2(dppz)]^{2+}$.

Studies have shown that the most likely binding site of $[Ru(phen)_2(dppz)]^{2+}$ is the minor groove for both enantiomers, Δ and Λ.[267] Although, the Δ enantiomer contributes for around 80% of the luminescence increase, both enantiomers bind strongly to DNA, which was proven by linear dichroism (LD) as well as luminescence titration with binding affinities of 10^8 M^{-1} which is much higher than its parent complex $Ru(phen_3)Cl_2$ (10^3 M^{-1}).[95, 260] Interestingly, each enantiomer has two lifetime components when interacted with calf thymus DNA, one in the range of 700 ns and another one on the range of 200 ns. This effect can be related with a difference in the local environment. For example, the long lifetime showed in $[Ru(phen)_2(dppz)]^{2+}$ is hypothesised to be related to sequences of closely bound intercalators and the short lifetimes relies on isolated intercalators, thereby differing in solvent exposure and neighbouring complexes interactions.[260,268] Prior to existence of crystal structure of the complex $[Ru(phen)_2(dppz)]^{2+}$, the difference on luminescence upon DNA binding, compared to aqueous solutions, was attributed to the presence of two metal to ligand charge transfer (^{3}MLCT) states on the dppz ligand.[269-271] However, more recently, the existence of a dark and bright state have been explored.[272,273] The bright state (^{3}MLCT') corresponds to the

2,2´-bipyridine portion of the dppz ligand and the dark state (^{3}MLCT’’) is associated with the phenazine portion of dppz (Figure 3.4). The ^{3}MLCT’ or bright state is the first state to be populated followed by intersystem crossing and population of the dark state. However, the ^{3}MLCT’’ energy is related to the solvent, more specifically with the polarity of the solvent and its ability to form hydrogen bonds with the phenazine fragment. For the light switch to occur, there is an enthalpic competition that favours dark state and entropic competition that favours bright state. The increase of solvent polarity stabilises the dark state, which will increase the gap between dark and bright state and therefore increase the non-radiative decay from the dark state. This model explains the results observed previously, where luminescence was observed when the complexes were dissolved in nonaqueous solvents.[266] Moreover, this model also supports why the complexes are luminescent upon DNA binding, since DNA

can shield the nitrogen atoms from the phenazine and prevent hydrogen binding from solvents.

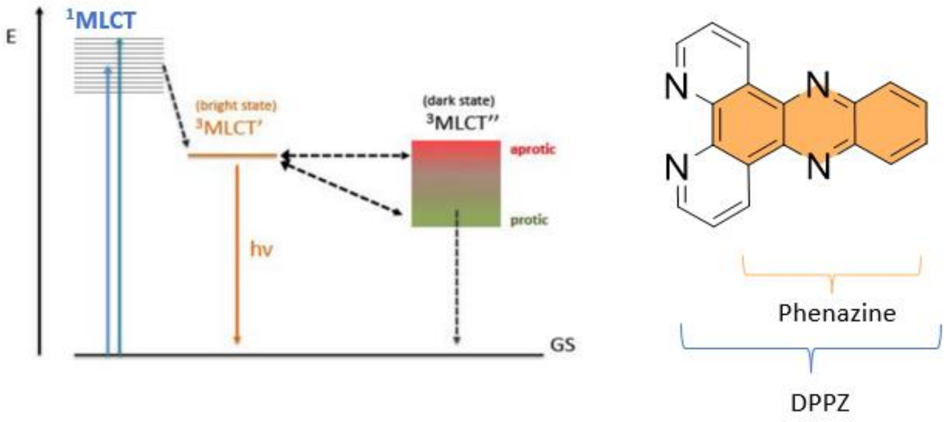

Figure 0.4- General jablonski diagram representing the excited states and transitions of the "light switch effect" for $[Ru(bpy)_2(dppz)]^{2+}$ or $[Ru(phen)_2(dppz)]^{2+}$ and the solvent influence. GS= ground state. Image adapted from[80] and chemical structure of dipyrido[3,2-a:2',3'-c phenazine.

Since the discovery of the "light switch effect", multiple complexes carrying a dppz ligand or a derivative of it, have been studied for diagnosis and therapeutics purposes.[274-276] These particular complexes offer potential for use in cellular imaging, especially for nucleus staining. However, such complexes must overcome some difficulties such as cellular uptake and nucleus permeabilization.[31] A study demonstrated that different ruthenium (II) complexes that carried a dppz ligand as one of the ancillary ligands, realised that they are not internalised in the nucleus for Hela cells.[31] Although, all the complexes were uptake by the cells after 2 hours for the complex $[Ru(DIP)_2(dppz)]^{2+}$, where DIP is 4,7-diphenyl-1,10-phenanthroline (Figure 3.5), and after 4 hours for complexes $[Ru(phen)_2(dppz)]^{2+}$ and $[Ru(bpy)_2(dppz)]^{2+}$, they all were localised in the cytoplasm of the cells. Interestingly, the most bulky complex, $[Ru(DIP)_2(dppz)]^{2+}$, has the fastest internalisation on cells, showing that one of the most important factors on complexes internalisation is its lipophilicity, rather than the size of the complex itself.[31]

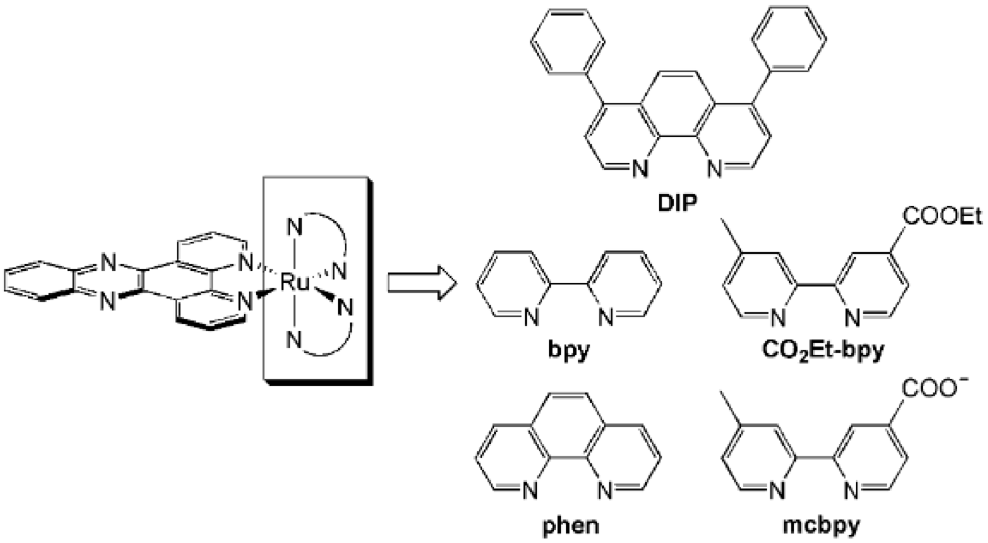

Figure 0.5- Chemical structures of dipyridophenazine Ru (II) complexes, adapted from[31].

Although many studies have been taking advantage of the “light switch effect” seen in dppz complexes and other similar complexes[277], not all the ruthenium (II) complexes bearing a dppz ligand have that effect. However, that does not mean that these complexes cannot be used for diagnosis purposes. Recently, Elgar and co-workers showed that even though not all the complexes have the “light switch effect”, it is still possible to use them as fluorescent probes and take advantage of their DNA intercalation behaviour, by using FRET (Forster resonance energy transfer) pairs with other fluorophores bound to the DNA.[278] FRET relies on dipole-dipole coupling between the excited state of a fluorophore donor to the ground state of a fluorophore acceptor. Therefore, in this study, upon ruthenium (II) complex binding to DNA, the ^{3}MLCT emission state undergoes resonance energy transfer with a fluorophore previously linked to DNA, resulting in a red-shit emission and a significant lifetime increase. Furthermore, this strategy shows anticancer properties by affecting DNA replication.

Beyond cancer diagnosis, Ru-dppz complexes have also been studied for therapeutic purposes within bioinorganic research. Gasser's group is one of the main groups dedicated to explore derivatives of Ru-dppz complexes with the aim to maintain the DNA interaction behaviour of these complexes but increase its phototoxicity upon visible light irradiation.[279, 280] Besides, other groups made new complexes of the type $[Ru(dppz)_2(LL)]^{2+}$ and found out that the complexes are multi-intercalators[78] by binding two or even the three ligands to DNA. This leads to a more significant distortion of the double helix and consequently, creates a physical barrier that prevents DNA replication. This complex combined with an inhibitor for breast cancer, allowed the enhancement of cell cycle arrest and apoptosis. However, it was also found that this complex has poor aqueous solubility and moderate potency, which limits its effect.[281, 282] Thereby, although the exciting results in this field, there are still a lot to develop and hence, other strategies need to be considered in order to allow these type of complexes to move forward into clinical trials.[283]

3.1.3 Gold nanoparticles and DNA hybrids

Due to their easy surface modification and biocompatibility, AuNPs emerged to facilitate some of the challenges that the drugs by themselves face, such as targeted drug delivery. The conjugation of drugs into nanocarriers might also prevent drug deactivation by other biomolecules and its bioavailability and stability enhancement.[284] Kang and co-workers synthetised 30 nm gold nanoparticles functionalised with PEG and bioconjugated with a peptide responsible for cell adhesion to the extracellular matrix (ECM) and a nuclear localisation signal peptide. [285] With this system, they managed not only to specifically target cancer cells but also target the nucleus of the cells. They also found that the bioconjugated AuNPs were cytotoxic to cancer cells by disrupting the cell cycle through DNA damage, resulting in apoptosis.[285] Conjugation of AuNPs with DNA moieties, have showed promising results and therefore, hairpins[286], single and double stranded DNA[287-289], aptamers[290] and others have been attached to AuNPs for biological applications. The first DNA-AuNPs hybrid, was introduced in 1996, by two different groups, Mirkin and Alivisatos and co-workers, for targeted drug delivery and imaging.[291, 292] Since then, many others followed and created DNA-AuNPs systems that can be used for biosensing and diagnosis.[293, 294] Deka and co-workers, made a competitive bio sensor of AuNPs and DNA hybrids to monitor helicase activity.[289] Helicases are enzymes that can unwind the DNA and play a key role in multiple processes such as DNA replication, repair and RNA transport. This new hybrid system involves the functionalisation of AuNPs with a self-assembled monolayer of DNA and oligo-ethylene glycol (TOEG6) to give nanoparticle stability and specificity. When no enzyme is present, the solution of the AuNPs is purple due to the aggregates formed by the DNA binding. However, when helicase is added to the solution, with ATP, the solutions turn red due to the unwinding of the DNA and consequent disruption of the aggregates (Figure 3.6). This strategy allows to assess the helicase activity not only by eye but also with a simple UV-Vis spectrophotometer.[289]

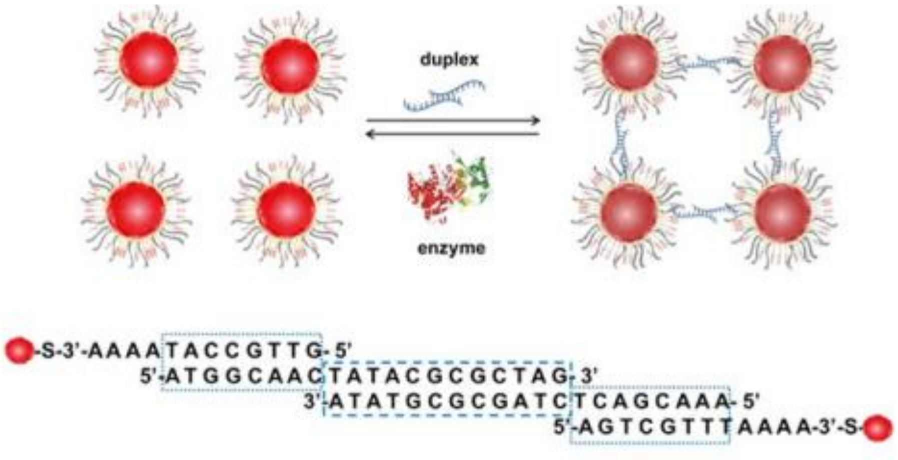

Figure 0.6- Diagram illustrating the formation of DNA-AuNPs aggregates and consequent disruption of the DNA double helix upon helicase addition. Adapted from[289]

DNA-AuNPs hybrids can also be used to achieve gene detection, regulation[295, 296] and targeted delivery[297]. Some drugs lack specificity, causing damage to healthy cells as well as the tumour. However, aptamers can specifically recognise the tumour and distinguish it from healthy cells.[298] Luo and co-workers, built a AuNP- aptamer/hairpin system for targeted delivery of doxorubicin (clinical approved anticancer drug). The DNA aptamer possess great affinity with a peptide overexpressed in leukemia cell line CCRF-CEM, and upon illumination with plasmon resonance light, the cytotoxic effect of doxorubicin was enhanced.[299] Yang and co-workers constructed a nano cage of AuNPs for the delivery of siRNA, which interferes with expression of specific genes and thus, prevents translation.[300] To enhance the treatment efficacy, doxorubicin (DOX) was also added by intercalation into double stranded DNA fragments (DNA1-5) also conjugated on the nanoparticle (Figure 3.7). The gold cages were then closed off with aptamers (AS1411) to allow specificity and single stranded DNA around it, linked with a cleavable peptide

(MMP-2). When the nanocage reaches the tumour, the enzymes MMP2 - overexpressed in cancer cells, can break the peptide chain and release doxorubicin, at same time that laser irradiation is applied the tumour cells. Within this system, this study showed a combined genetic, chemotherapeutic and photothermal therapy where a nearly complete tumour regression in mouse was observed.[300]

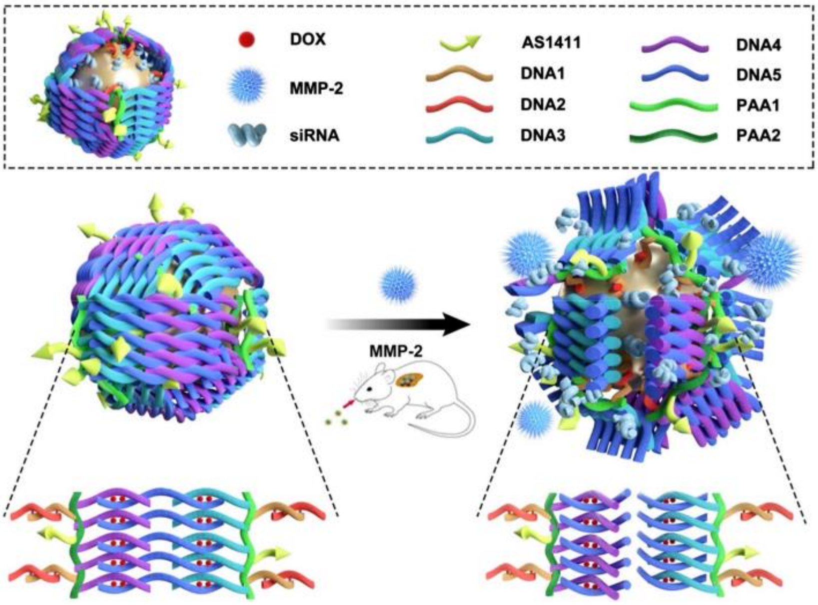

Figure 0.7- Schematic illustration of the gold nanocages for targeted lung cancer therapy, showing the DOX releasing mechanism by breaking the peptide chain by the overexpressed MMP-2 enzymes on cancer cells, adapted from[300].

3.1.4 Recognition of gold nanoparticles with DNA

Although many advances have been made on DNA-AuNPs hybrids for diagnosis or therapy, there are very few examples on literature that show evidence of AuNPs interacting with DNA. Elmes and co-workers are one of the few studies that showed that it is possible to show DNA interaction with luminescence AuNPs (Figure 3.8).[237]

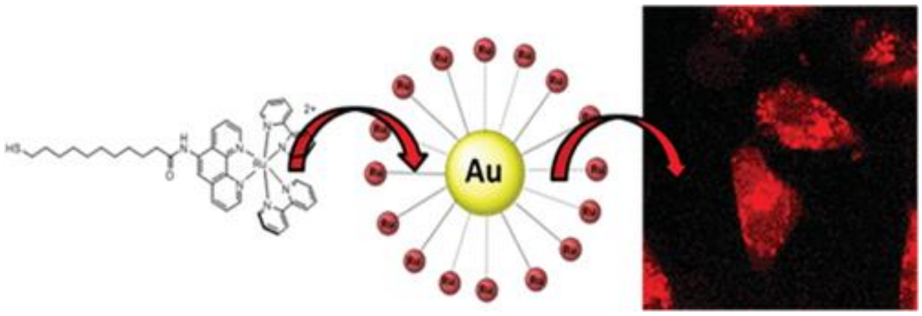

Figure 0.8- Diagram illustrating gold nanoparticle functionalised with a luminescent ruthenium (II) complex for imaging in cancer cells. Adapted from[237]

Using ruthenium (II) complexes with ligands such as 2,2-bipyridine, 1,10-phenanthroline or 1,4,7,10- tetraazaphenanthrene (tap), to stabilise gold clusters during gold nucleation, they formed 4 nm positively charged AuNPs. The AuNPs showed to have a 10^5 M^{-1} affinity to DNA binding, and a hypochromic effect with a red shift in the MLCT band in the UV-Vis absorption spectra. This study also showed a nonspecific localization of the AuNPs in the cytoplasm and nucleus, detected by microscopy techniques. Simultaneously, the positively charged AuNPs showed high binding affinity with DNA by fluorescence spectroscopy.[237]

Although this study contributed for a breakthrough on DNA interactions with nanoparticles, it is noted that the AuNPs are positively charged and therefore easy to interact with the negatively charged DNA. Perhaps, due to that limitation, the behaviour of negatively charged AuNPs with DNA has not been much explored. In the Pikramenou group, Caballero and co-workers purposed a new system of a negatively charged gold nanocarrier that not only allows highly loading of a platinum drug, but also bears fluorophores and DNA intercalator moieties that allow strong bind and DNA wrap around the nanoparticles, allowing enhanced cytotoxcicity.[284] In this work, the AuNPs are used not only as nano carriers but also play a key role to tackle tumour cells. The DNA interaction of the AuNPs was proved by linear dichroism and DLS techniques. By fluorescence confocal microscopy and TEM it was also demonstrated that although the particles are localised mainly in the cytoplasm, after 24h some AuNPs reached the nucleus, showing that specific targeted functionalisation is not always needed. Overall, this study shows promising results by demonstrating that negatively charged AuNPs functionalised with metal complexes can interact with DNA.

3.2 Chapter Aims

In this chapter the luminescence effect of a new ruthenium (II) complex, RuDppzL2 complex bearing two dipyrido[3,2-a:2′,3′-c phenazine ligands and a 5-(1,2-dithiolan-3-yl)-N-(1,10-phenanthrolin-5-yl)pentanamide ligand (L2), (see Chapter 2 for synthesis details), will be studied upon attachment to AuNPs (Figure 3.9). The interaction of DNA with AuNPs coated with RuDppzL2 and RuPhenL2 will be studied, and binding affinities compared. The efficient binding of the complexes to calf thymus DNA and linear plasmid DNA will be studied by linear dichroism, fluorescence, and microscopy.

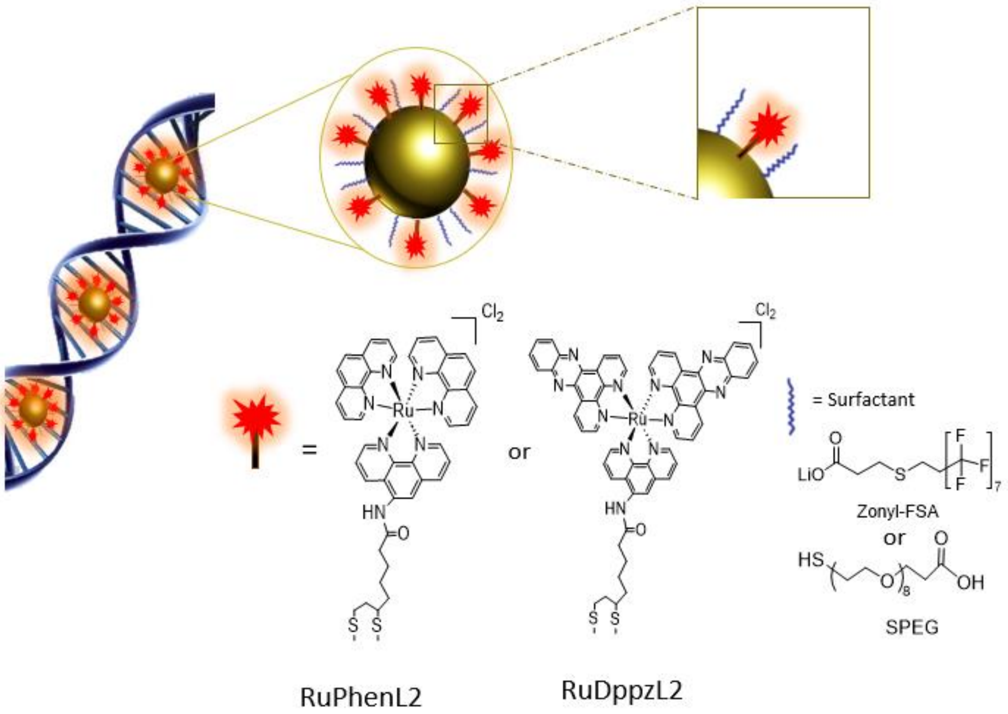

Figure 0.9- Graphical illustration of the interaction of DNA and AuNPs functionalised with ruthenium (II) complexes, RuPhenL2 and RuDppzL2.

3.3 Results and Discussion

3.3.1 Synthesis and photophysical properties of the ruthenium (II) polypyridyl complex RuDppzL2

Typically, the complexes type $[Ru(L1)_2(L2)]^{2+}$ are synthesised through the intermediate $[RuCl_2(L1)_2]$ as described on chapter 2. However, for more sterically hindered ligands such as dppz, this method has drawbacks, such as poor control of stoichiometry and thermal instability. Therefore, our collaborator Gilles Gasser and his group proposed a different mechanism to synthesise these types of complexes involving cis-$[RuCl_2(DMSO)_4]$ as starting material.[301] Therefore, the ruthenium (II) complex

$[Ru(dppz)_2(L2)]Cl_2$ or simply called RuDppzL2 was provided by Maria Dalla Pozza from the Gilles Gasser group at Chimie ParisTech, PSL University. The synthesis procedure can be found in the Experimental section at the end of this Chapter.

The absorption, steady state excitation, emission and luminescence lifetime were measured for this complex in aerated water/methanol. The absorbance spectrum showed to be similar to its parent $[Ru(phen)_2(dppz)]^{2+}$, revealing the metal to ligand charge transfer (MLCT) spin allowed (d - π*) from 400-500 nm with the maximum at 450 nm and a shoulder at 430 nm. The π- π* transition of dppz ligand is observed with peaks at 270 nm and 370 nm.[260] Interestingly, although with a weak signal, the complex under study is still emissive with an emission maximum of 675 nm, contrary to $[Ru(phen)_2(dppz)]^2$ that does not show any emission in aqueous solution.[260] However, it is possible to observe that the peak observed at 370 nm, which corresponds to the π- π* transition of dppz ligand, does not contribute to the emission of the complex, since it is not visible on the steady state excitation spectrum. Although the signal is weak, this complex has a luminescence lifetime of 428 ns in aerated water/methanol. An 18 nm shift is observed when comparing the absorption (λ_{max}= 277 nm) and excitation spectra for the π- π* transition of dppz ligand (λ_{max}= 259 nm). This could be due higher absorbance of the solution, causing an artifact.

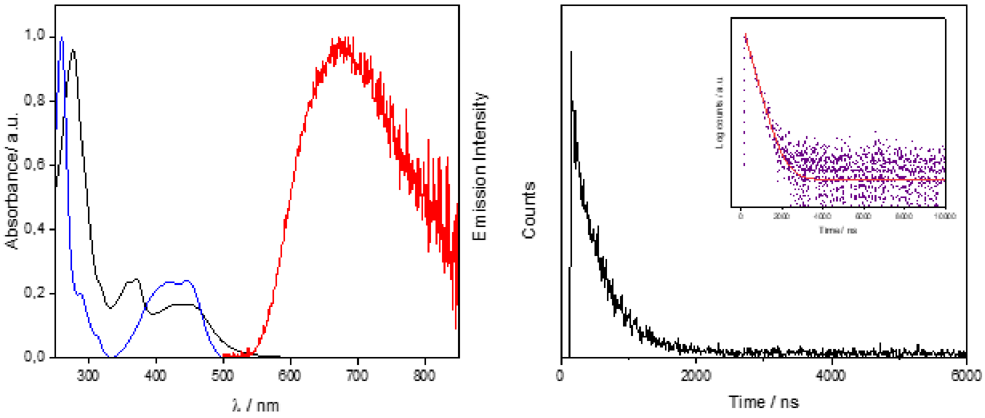

Figure 0.10- a) Absorption (black), excitation (blue) and emission (red) of 20µM RuDppzL2 (λ_{exc}=450 nm, λ_{em}=675 nm) in aerated H_2O with 2% MeOH. b) Luminescent lifetime decay of RuDppzL2. Laser excitation source was at 445nm and collection wavelength of 620nm, with a 550nm filter. Decay curves were fitted with χ^2 values between 1.0 and 1.2.

DLS showed, on Figure 3.11, aggregates of RuDppzL2 in water/ methanol with 28 ± 9 nm size with a PDI of 0.5 in a freshly made solution. Overtime, the size of these aggregates increased, and two different size populations were found after 24 hours, 85 ± 24 nm and 317 ± 60 nm. Interestingly, this effect not only observed in water/methanol, but also in pure methanol, showing aggregates with sizes of 188 ± 38 nm after 24 hours of the solution been made. Moreover, both absorption and emission decreased overtime, showing that there is no luminescence enhancement with the increase of aggregate sizes (Figure 3.11-B and C).

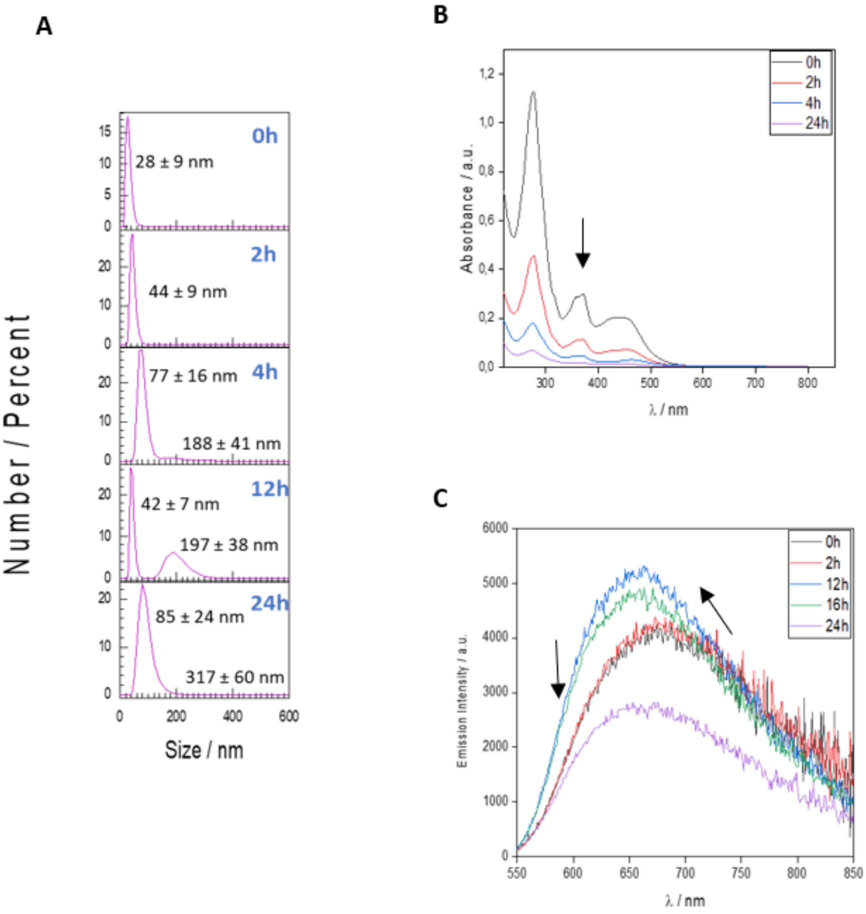

Figure 0.11- Time dependence optical properties of a 20 µM RuDppzL2 solution in water with 2% MeOH. A- Dynamic Light Scattering (DLS) recorded the size by number from 0h to 24h. B- Absorption spectroscopy overtime and C- emission recorded overtime. Before each measurement, the solution was stirred for 3 minutes to avoid sedimentation. Black arrows show decrease in absorption intensity and emission intensity.

It has been reported that ruthenium (II) complexes that seemed completely dissolved in a mixture of DMSO-water solution, had formed aggregates of nanometre size.[302] Gasser group, saw ruthenium aggregates in PBS, even at low concentration.[303] It was believed that this behaviour might be caused by a reduction of electrostatic repulsion between positively charged complexes. PBS is a water-based solvent that contains salts such as sodium chloride. The high ionic strength of the solvent can enhance the attraction of the positively charges, surrounded by the negative charges of the salt and therefore, increase the aggregation effect.

An aggregation effect it is not uncommon for compounds with extensive aromatic rings, since these ligands undergo π-π stacking interactions when aggregate. Moreover, due to the variety of the different charge transfer electronic states, aggregation on metal complexes can affect their emission properties in different ways depending on the specific characteristics of the complex.[304] The most common effect is aggregation induced emission (AIE).[305] However, it is also possible to observe aggregation caused-quenching (ACQ). This effect has been extensively studied in organic molecules but there are fewer examples observed for metal complexes in solution. Although there is not a single mechanism that explains both AIE and ACQ effects, it is assumed that these behaviours emerge from a competition between radiative and non-radiative decay pathways.[304] In a very recent study, two similar trinuclear complexes of copper and silver showed completely different emission properties upon aggregation induced by the addition of water to the dissolved complex in THF.[306] The copper complex showed a AIE effect with 20 times increase on emission after aggregation due to a tight packing with strong hydrogen bonding interactions. The silver complex demonstrated a ACQ behaviour where the emission decreased 5 times after aggregation assumed to be due to lose molecule packing and weak π-π* interactions.

Upon the discovery of nanometre size aggregates on the complex RuDPPZL2, the possibility of other complexes having the same effect is intriguing. Previously, RuPhenL2 demonstrated a relatively weak luminescent lifetime signal in solution, as shown in Chapter 2, which could be explained by an aggregation effect. Therefore, two solutions in water/methanol of different concentrations of RuPhenL2, were analysed by DLS after 24 hours. As observed in Figure 3.12, both solutions exhibited aggregates, in which 20 µM solution shows a 30 nm aggregates size whereas a 60 µM solution of RuPhenL2 demonstrated aggregates of 260 nm. As bigger aggregates are formed at the highest concentration, thereby shows a dependence relation between concentration and aggregation size. To evaluate the DNA interaction with the ruthenium (II) complexes, the aggregation effect will need to be considered. Within this work, the ruthenium (II) complexes will be functionalised into AuNPs and therefore the interaction analysed will be between the AuNPs and DNA. However, it is important to note that the aggregates can influence the concentration of ruthenium (II) complexes added to the AuNPs and that should be considered.

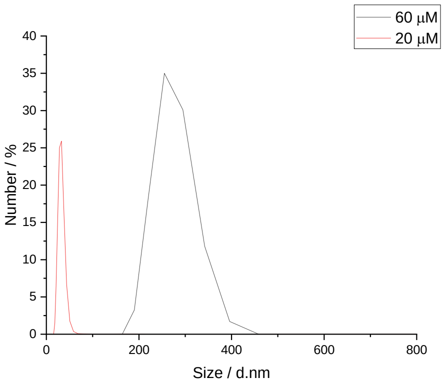

Figure 0.12- Size by number distribution measured by DLS of a 20 µM and 60 µM RuPhenL2 solutions in water with 2% MeOH, after 3 minutes stirring to avoid sedimentation.

3.3.2 Functionalisation of gold nanoparticles with surfactants and RuDppzL2

Similarly, to the ruthenium (II) complexes on Chapter 2, RuDppzL2 is attached to the AuNPs through the thiol group in L2 ligand to make Au.RuDppzL2. The coating process involved a titration of a 1 mM RuDppzL2 solution to a solution of AuNPs resuspended in water (6.5 nM) until reaching a plateau of maximum amount of RuDppzL2 added and no shift on the SPR is observed (Figure 3.13).

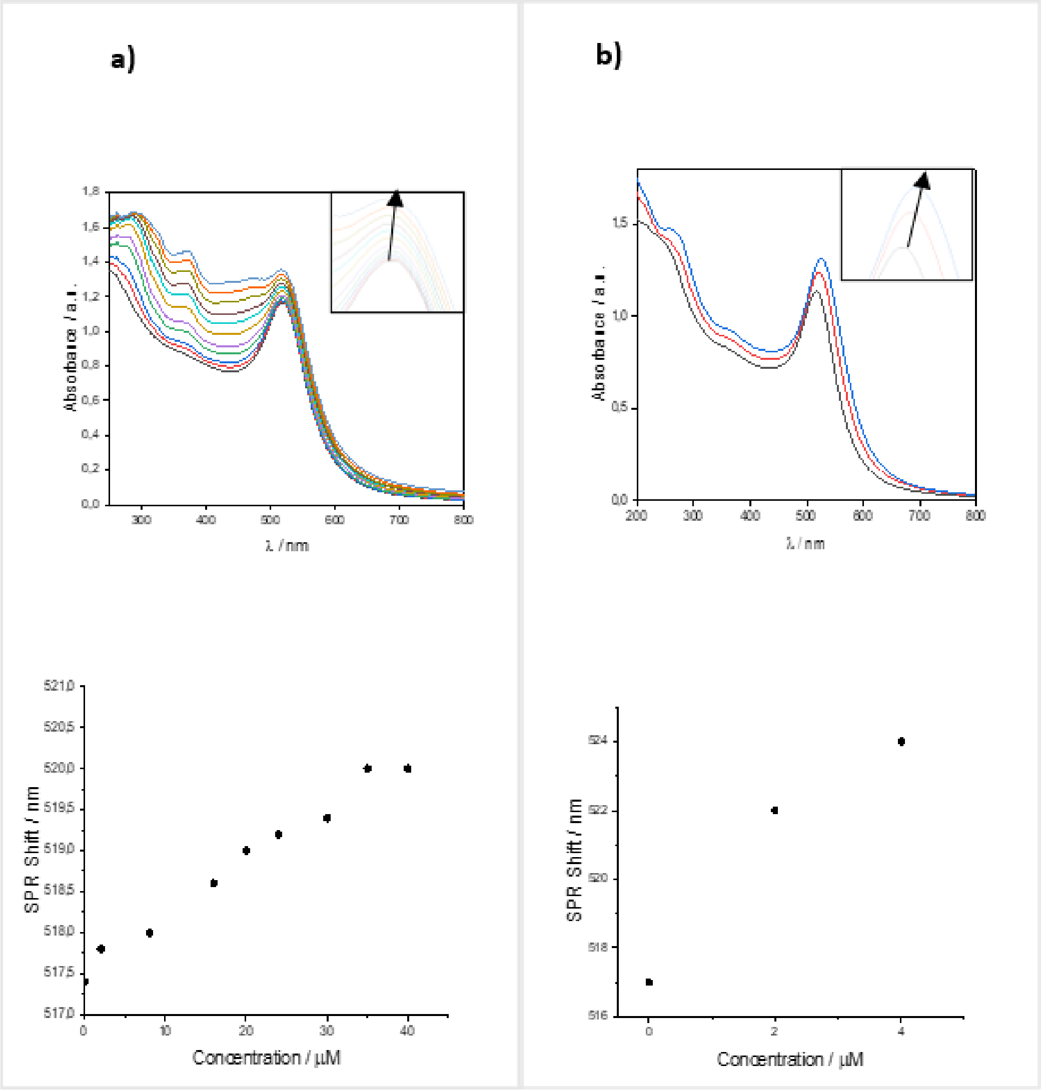

Figure 0.13- Titrations of a 1 mM stock solution in MeOH of RuDppzL2 in AuNPs 13 nm (6.5 nM) by UV-Vis spectroscopy and binding curves of concentration vs SPR shift a) Au.Z.RuDppzL2 and b) Au.SPEG.RuDppzL2.

The optimal concentration of RuDppzL2 added to AuNPs previously stabilised with Zonyl FSA is 40 µM, whereas for AuNPs previously coated with SPEG, only 4 µM is possible to add. The attachment of RuDppzL2 to the AuNPs, does not have a saturation point and as a result the binding affinities was not possible to calculate. Thus, the optimal concentration for Au.RuDppzL2 was found through analysis of the SPR shifts. It is also noted that the optimal concentration of RuDppzL2 (40 µM for Au13.Z.RuDppzL2 and 4 µM for Au13.SPEG.RuDppzL2) to the AuNPs is significantly less than for the complexes RuPhenL2 (80 µM for Au13.Z.RuPhenL2 and 10 µM for Au13.SPEG.RuPhenL2). This is no surprise, since this complex has two dppz ligands, which are much more sterically hindered than 1,10-phenanthroline ligands. Moreover, this could also be related with the formation of bigger aggregates for RuDppzL2 in a fresh made solution, in comparison with RuPhenL2. ICP-MS also demonstrated that less ruthenium (II) complexes were attached to AuNPs, since only 300 ruthenium (II) complexes were found to be attached to AuNPs of 13 nm size compared to 400 of RuPhenL2. The same was observed for 25 nm AuNPs, where only 100 ruthenium of RuDppzL2 was attached to AuNPs compared to 200 of RuPhenL2 (see Chapter 2, appendices-figure 2.31).

After coating, the Au.RuDppzL2 in solution have different hydrodynamic sizes due to the attachment of surfactants and ruthenium (II) complexes but also due to the interaction of the particles with the solvent (Figure 3.14). The hydrodynamic size increased 25 % for AuNPs coated with PEG (15 ± 4.2 nm) and 58 % when coated with Zonyl FSA (19 ± 5.3 nm) in comparison to citrate AuNPs (12 ± 2.9 nm) (Appendices-tables 10 and 11). Upon RuDppzL2 coating, there is an increase of ~94 % (24.0 ± 7.1 nm) in relation to the citrate

AuNPs. For 25 nm AuNPs, the increase is not so evident, nevertheless there is a ~25 % size increase after coating with RuDppzL2 since the size increases from 20.0 ± 5.0 nm to 25 ± 8.0 nm. Beyond the SPR change observed in UV-Vis, the hydrodynamic size increase can be used as evidence to show that the AuNPs were successfully coated with the surfactants and RuDppzL2. For all the AuNPs, only one single peak is observed on the DLS size distribution, demonstrating only one size population for each set of particles. It is important to note that although ruthenium (II) complex aggregates have been observed in solution, these were not found upon attachment to the nanoparticles.

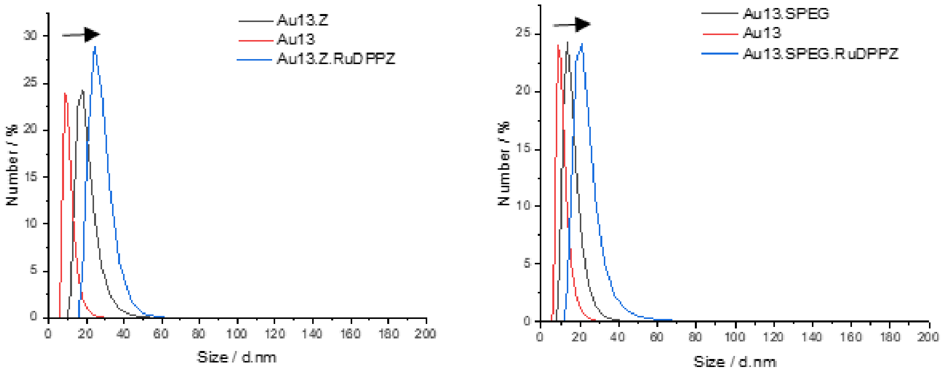

Figure 0.14- Increase of size by number distribution of coated AuNPs with surfactants (Sonyl FSA and SPEG) and ruthenium (II) complex (RuDppzL2) in comparison with citrate AuNPs.

To observe the monodispersity of AuNPs after coating, TEM images were analysed. As observed in figure 3.15 the AuNPs are single particles with uniform size and shape. By taking the average of 20 AuNPs diameter, all the samples have an optimal size of 15 ± 1 nm for 13 nm AuNPs and 23 ± 2 nm for 25 nm AuNPs. DLS clearly indicates an increase on hydrodynamic size after AuNPs coating, however the same is not observed by TEM. Although the difference in size is within the error, this is attributed to the fact that in

TEM the coating is not visualised and therefore further staining is required. In conclusion, AuNPs coated with RuDppzL2 were successfully synthesised and characterised as monodispersed, with no aggregation in solution.

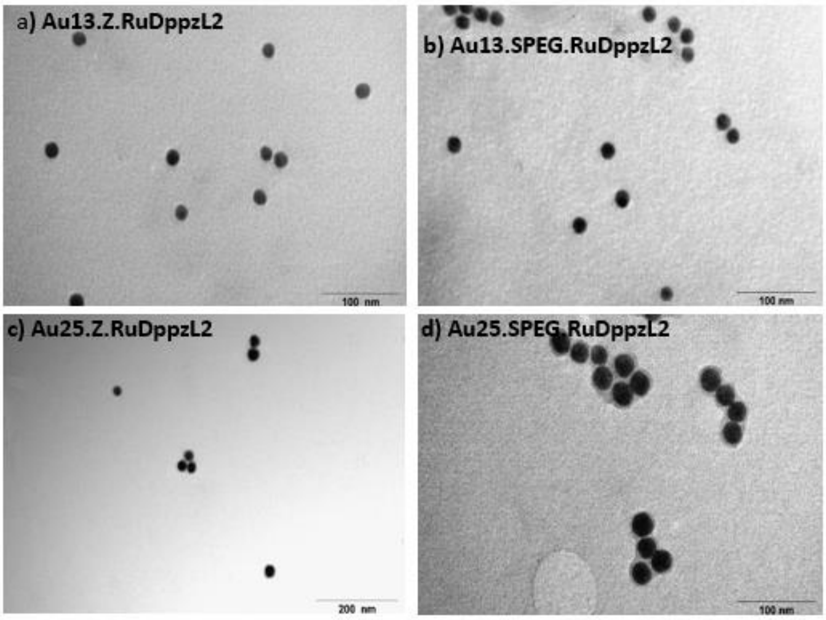

Figure 0.15- Transmission electron microscopy of coated AuNPs, where a) Au13.Z.RuDppzL2, b) Au13.SPEG.RuDppzL2, c)Au25.Z.RuDppzL2 and d) Au25.SPEG.RuDppzL2. TEM sizes were calculated by an average of 20 AuNPs and processed by ImageJ software. Scale bars are 500, 200 and 100 nm. The sizes of the AuNPs were 15 ± 1 nm, for Au13.Z.RuPhenL2, Au13.SPEG.RuPhenL2 and 23 ± 2 nm For Au25.Z.RuDppzL2 and Au25.SPEG.RuDppzL2.

3.3.3 Photophysical studies of RuDppzL2 coated gold nanoparticles

To study the photophysical properties of RuDppzL2 when attached to the AuNPs, absorption, emission and excitation spectra were analysed (Figure 3.16 and appendices- figure 3.29). The SPR peak is easily identified and well defined on the absorption spectra at 518 nm for 13nm and 522 nm for 25 nm AuNPs. The excitation profile shows the bands attributed to RuDppzL2, in which 277 nm and 370 nm corresponds to the Ligand Centre (LC) state (π - π*) and the MLCT at 450 nm. The AuNPs functionalised with Zonyl FSA and

RuDppzL2 (Au.Z.RuDppzL2), the emission maintains the same than the ruthenium solution freshly made (675 nm) (Figure 3.17). Interestingly, on the set of AuNPs coated with SPEG and RuDppzL2 (Au.SPEG.RuDppzL2), there is a blue shift in comparison with the ruthenium (II) complex in solution. The emission maximum shifted from 675 nm to 577 nm on Au13.SPEG.RuDppzL2 and 600 nm for Au25.SPEG.RuDppzL2. This blue shift could be related to the packing between RuDppzL2 and SPEG around the AuNPs. As seen previously in Chapter 2, SPEG has a bigger length than Zonyl FSA. Steric hindrance is also pronounced for RuDppzL2 due to its bulky dppz ligands. Therefore, it is possible that the packing of RuDppzL2 on Au.SPEG is different than Au.Z, causing a shift on the emission maximum. The luminescence of the complex [Ru(bpy)$_2$(dppz)]$^{2+}$ has been studied previously in a micellar environment, where it is observed a blue shift on the absorption maximum when the length of the alkyl chain increases.[307] In this study it was hypothesised that this was due to the dppz ligand being buried in the micellar core, preventing water quenching.

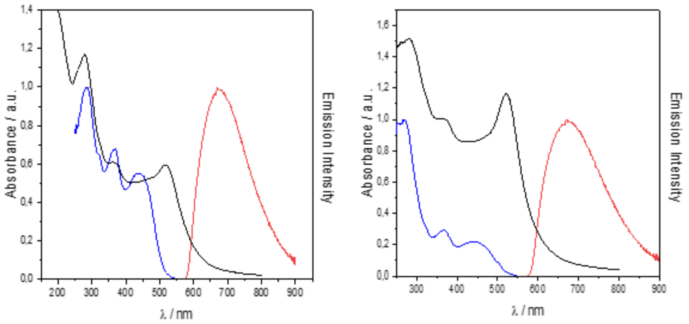

Figure 0.16- Absorption (black), emission (red) and excitation (blue) spectra of 3.5 nM Au13.Z.RuDppzL2 (left) and 1.5 nM Au25.Z.RuDppzL2 (right) (λ_{ex}= 450 nm, λ_{em}=675 nm) in aerated water.

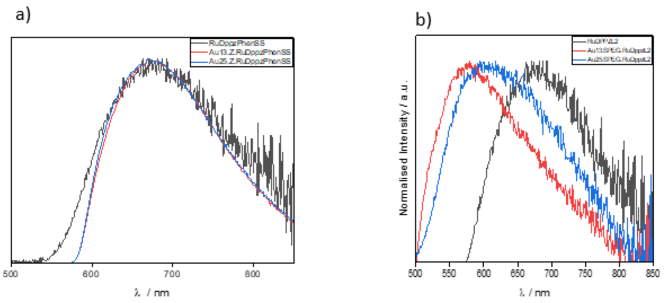

Figure 0.17- (a) Overlayed emission of RuDppzL2, Au13.Z.RuDppzL2 and Au25.Z.RuDppzL2 (λ_{ex}= 450 nm, λ_{em}=675 nm). All the solutions are in aerated water. (b) Overlayed emission of RuDppzL2 (black) (λ_{ex}= 450 nm, λ_{em}=675 nm), Au13.SPEG.RuDppzL2 (red) (λ_{ex}= 450 nm, λ_{em}=577 nm) and Au25.SPEG.RuDppzL2 (blue) (λ_{ex}= 450 nm, λ_{em}=600 nm). All the solutions are in aerated water.

The luminescence lifetimes are presented in table 1. Although RuDppzL2 attached to AuNPs (Au.Z.RuDppzL2, Au.SPEG.RuDppzL2) has a higher emission signal than RuDppzL2 in solution, its lifetime decreases. However, the quantum yield increases. While RuDppzL2 in solution has a quantum yield of 0.1 %, on the AuNPs the quantum yield increases to 2.9 %. This could be related with a plasmonic enhancement from the AuNPs. The optical properties of materials can be significantly influenced by the presence of surface plasmons (see Chapter 1). Therefore, this can also affect the luminescence properties of the ruthenium (II) complexes attached to the surface of AuNPs. The enhanced electromagnetic field around the Au.RuDppzL2 can result in increased rates of energy transfer to the ruthenium (II) complex leading to a faster decay of the excited state.[308] Nevertheless, plasmonic enhancement can also increase the quantum yield of RuDppzL2 when attached to the AuNPs by increasing the likelihood of incident photons absorption and thus increasing the efficiency of the conversion of absorbed photons into emitted photons.[308, 309]

Table 8- Luminescence lifetimes recorded for RuDppzL2 in water/methanol, Au13.Z.RuDppzL2, Au13.SPEG.RuDppzL2 and Au25.Z.RuDppzL2, Au25.SPEG.RuPhenL2 in aerated water. Lifetimes were recorded using a (λ_{exc}=450 nm) laser and were fitted with a χ^2 between 1.0 and 1.2. nd- not determined.

Sample Name	**Lifetimes / ns air**
RuDppzL2	428 (100%)
Au13.Z.RuDppzL2	473 (27%) , 64 (28%), 16 (45%)
Au13.SPEG.RuDppzL2	426 (62%), 13 (11%), 2 (28%)
Au25.Z.RuDppzL2	110 (26%), 37 (43%), 8 (31%)
Au25.SPEG.RuDppzL2	nd

3.3.4 DNA interactions with luminescent gold nanoparticles by electron microscopy

After successfully coating the AuNPs with RuDppzL2, the DNA interaction between the AuNPs coated with ruthenium (II) complexes RuPhenL2 or RuDppzL2 were studied. It is important to note that for this chapter AuNPs functionalised with RuPhenL1 was not studied due to its structural similarities with RuPhenL2, which therefore would not differ on DNA interaction.

Although many studies have showed that AuNPs can interact and even target DNA by functionalising nucleic acids or other biological moieties on AuNPs (see section 3.1.3), there are not many studies that show evidence of DNA interactions with negatively charged AuNPs functionalised with ruthenium (II) complexes. Most approaches involve positively charged AuNPs, due to the negatively charged DNA backbone.[237] To examine whether Au.RuPhenL2 and Au.RuDppzL2 retained their negatively charged after being coated with the ruthenium (II) complexes, zeta potential measurements were employed.

Zeta potential measures the surface charge of nanoparticles in solution. In a colloidal system, dispersed particles have two layers of oppositely charged ions on the surface, forming two layers. The inner layer is called stern and represents the layer with strongly bonded ions, and a diffuse layer that has loosely bond ions that are distributed according to their electrical forces. The voltage measured between the diffuse layers and the media defines the zeta potential, i.e, when the zeta potential is highly negatively charged (> -10) the particles are stable but if they have a lower zeta potential (-10< x<10) then the particles have a bigger tendency to aggregate.[310] The zeta potential measured was between -15 and -26 ± 5 mV for Au.RuDppzL2 and Au.RuPhenL2. (Appendices-figure 3.30), suggesting that although the surface is coated with positive ruthenium compounds, the surface charge is still negative and relatively stable. Due to DNA being also negatively charged, an obvious experiment to observe an interaction between Au.RuDppzL2, Au.RuPhenL2 and DNA (DNA-AuNP.Ru) would be a size measure by DLS and a zeta potential analysis before and after DNA addition. However, it was not possible to obtain reliable zeta potential for the interaction between DNA-AuNP.Ru through this technique.

To obtain visual information on the interaction between DNA-AuNP.Ru, transmission electron microscopy (TEM) was used. The samples were stained with 4% uranyl acetate solution to visualise the ctDNA. As observed in figure 3.18-A,B, Au.SPEG.RuDppzL2 appear wrapped up in strings of DNA. As it is known, DNA is negatively charged due to its phosphate groups. When negatively charged AuNPs are in proximity of a DNA fragment there is an increase of local charge that forces these fragments to acquire a more rigid conformation or stiffening (Figure 3.19). In this case, there is natural repulsion of the DNA backbone adapting this “spaghetti shape” conformation around the AuNPs.[311] This behaviour had already been proposed by our group in a previous study, in which AuNPs were coated with a lipoic acid and a known intercalator anthraquinone.[284] In this study, there was an increase on LD signal (unusual for an intercalator) suggesting a bending of ctDNA, leading to a “wrap” of ctDNA around the AuNPs.

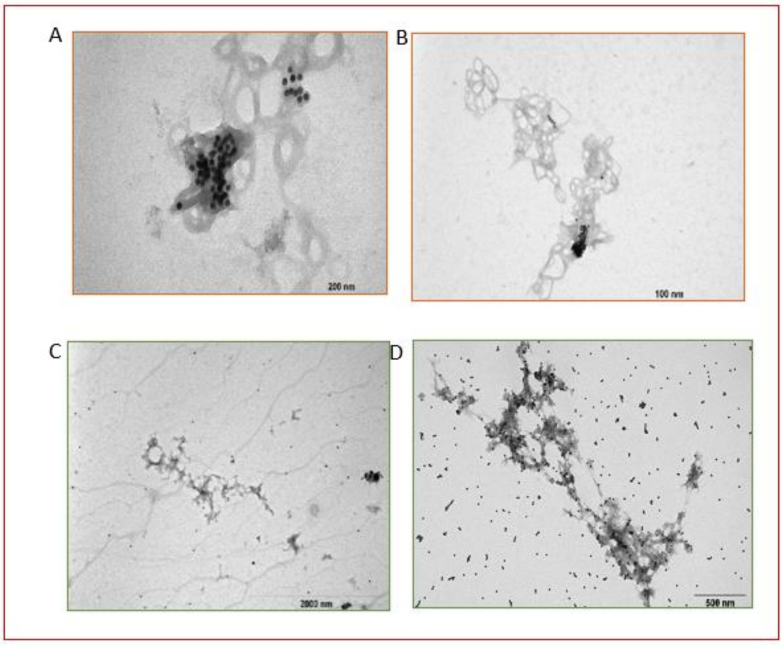

Figure 0.18- Transmission electron microscopy (TEM) images of a 3.5 nM solution of AuNPs, after the addition of 16 µM ctDNA. The TEM grid was previously stained with 4% uranyl acetate for DNA visualisation. A and B- Au.SPEG.RuDppzL2, C- Au.Z.RuDppzL2, D- Au.SPEG.

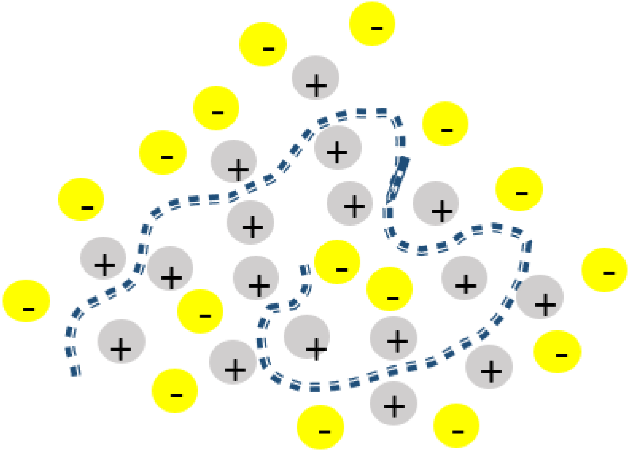

Figure 0.19- Simplified diagram of a DNA fragment adapting a rigid conformation “spaghetti shape” due to attractions and repulsion forces from the positively and negatively charged molecules.

Interestingly, this behaviour seems to only happen on the Au.RuDppzL2 and Au.RuPhenL2 that contain SPEG as surfactant. When the surfactant used is Zonyl FSA, there is no evidence of DNA interaction (Figure 3.18-C). Moreover, the DNA seems to get a different configuration, suggesting that the Zonyl FSA might not help the binding and therefore the DNA chains does not need to adapt a more rigid conformation. For the best of our knowledge this is the first time where images of negatively charged AuNPs coated with ruthenium (II) complexes, wrapped in DNA are showed. Carnerero and co-workers initially showed that 15 nm negatively charged AuNPs can bind to the enzyme T4 DNA ligase.[312] By TEM, they showed that although some nanoparticles interacted with a giant double stranded DNA (T4 DNA), a certain proportion remained unbound and continues dispersed on the grids. That is consistent with what is observed in this work. As a control, AuNPs only functionalised with SPEG were observed under the electron microscope after addition of ctDNA. Figure 3.18-D, shows that although some of the

Au.SPEG interact with DNA, most of them are dispersed on the grid, suggesting that the functionalisation of the AuNPs with the ruthenium (II) complexes is determinant for the DNA-AuNPs interaction.

Scanning transmission electron microscopy with energy dispersive X-ray (STEM-EDX) establishes the chemical composition by indicating the chemical elements present in a sample. So, using the same carbon grids in which TEM images of DNA-AuNP.Ru assemblies were obtained, three essential chemical elements were identified as present on the samples. As expected, gold, Au, and ruthenium, Ru, were identified as demonstrated in figure 3.20, as well as phosphorus, P, indicating the presence of DNA. Analysing the images, most of the phosphorous signal found is around the Au.SPEG.RuDppzL2 demonstrating the interaction previously showed by TEM.

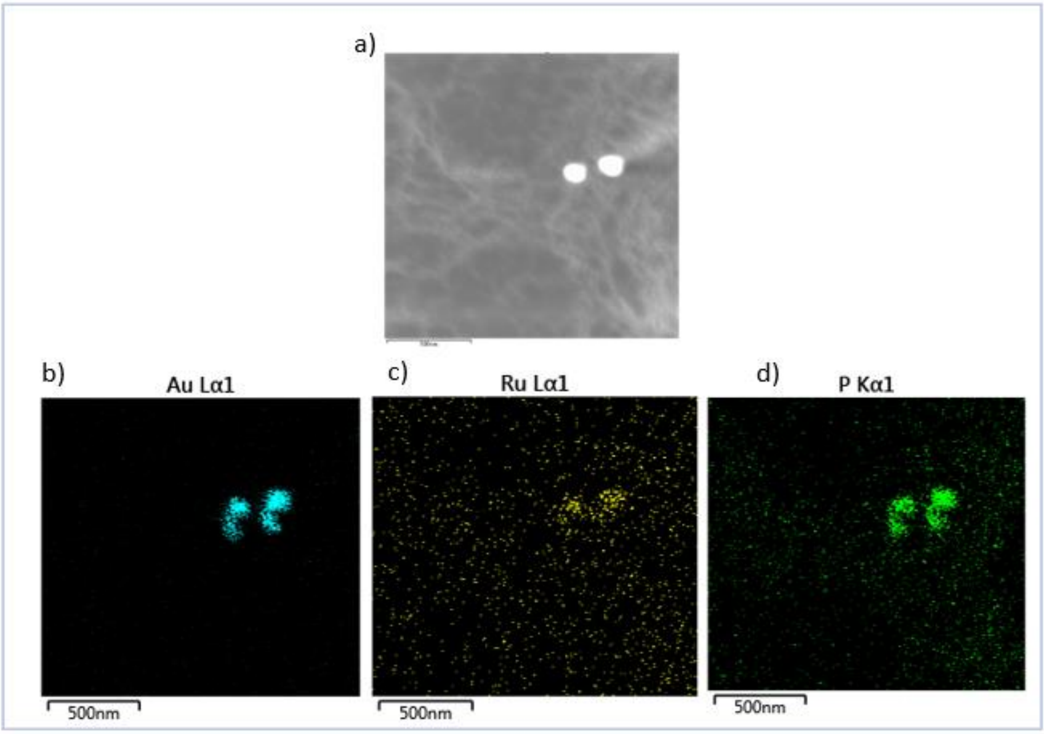

Figure 0.20- STEM-EDX images of a sample containing a 3.5 nM solution of Au.SPEG.RuDppzL2 with 16 µM ctDNA. Original image from STEM in grey (a) and at the bottom the signal of the

elements identified as present on the sample, b) gold (Au), c) ruthenium (Ru) and d) phosphorous (P).

To further analyse the interaction of DNA-AuNP.Ru, PBR-322 linearized plasmid DNA, with 4000 base pairs, was added to a solution of Au.RuDppzL2 and Au.RuPhenL2. The plasmid DNA was prepared and purified by a QAIquick PCR kit (see Experimental section). Confirmation of linearization and size was determined using an agarose gel electrophoresis and compared with a 1kb DNA ladder. (Appendices-figure 3.31)

Au.RuDppzL2 and Au.RuPhenL2 were analysed on TEM before and after staining with 4% uranyl acetate solution. As observed on Figure 3.21, before staining, only the AuNPs are visible. After staining, the plasmid DNA fragments are visible and its interaction with Au.RuDppzL2 and Au.RuPhenL2 is clear. According to the TEM images, even though the ruthenium (II) complexes attached to the AuNPs are different, since one is coated with RuPhenL2 and the other with RuDppzL2, that did not interfere with the binding to the DNA. As seen previously for ctDNA, the AuNPs previously coated with Zonyl FSA did not seem to bind to plasmid DNA. (Appendices-figure 3.32). The reason for this can be due to different factors, such as the hydrophobic nature of the fluorinated tail which can cause a change in DNA conformation, thus preventing the interaction. It has been showed before that hydrophobic liposomes can change DNA conformation to a more condensed form, so it minimizes their exposure to water.[313] A different study demonstrated that a fluorinated surfactant FC134 aggregated on the surface of the DNA to form a hydrophobic complex leading to a change in conformation of DNA from B to Z form.[314] Therefore, for the next experiments, only AuNPs coated with SPEG as surfactant were studied.

In figures 3.20 and 3.21, it is also observed an agglomeration like “bunches of grapes”. Interestingly, there seem to be two single strands of DNA on each side of the bunch, as if the DNA had partially uncoiled and exposed more bases of the DNA. This type of unwound of DNA has been visualised before on TEM for DNA replication on bubble stage[315, 316] (Figure 3.22). Therefore, this is a very promising effect for a therapeutic strategy in the future by preventing DNA replication on tumour cells, using AuNPs coated with ruthenium (II) complexes. Moreover, the AuNP alignment due to DNA could be very useful, in a near future, to similar luminescent AuNPs systems for DNA origami studies. As known in the literature, nanoscale structures have unique chemical, electronical and optical behaviour that can be easily tuned by simply modifying the size of the nano structures.[292, 317] Using DNA origami to make these structures, besides offering a controlled interaction between particles, prevents aggregations, and also gives the possibility of engineering interactions with a molecule of interest.[318] These properties can lead to several applications such as chemical sensors[319], spectroscopic enhancers[320] and bioimaging.[321]

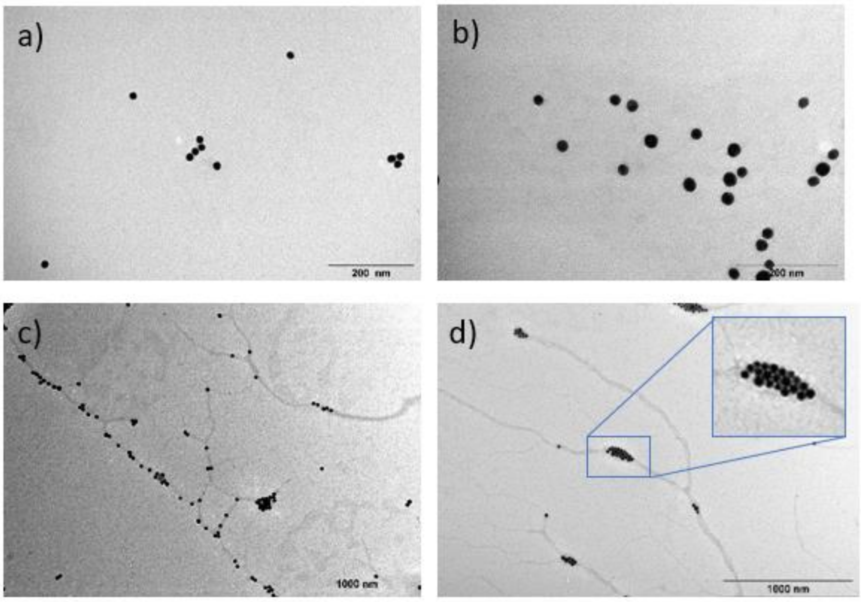

Figure 0.21- TEM images before (a,b) and after staining (c,d) with uranyl acetate of Au13.SPEG.RuPhenL2 (c) and Au25.SPEG.RuPhenL2 (d) with plasmid DNA PBR-322.

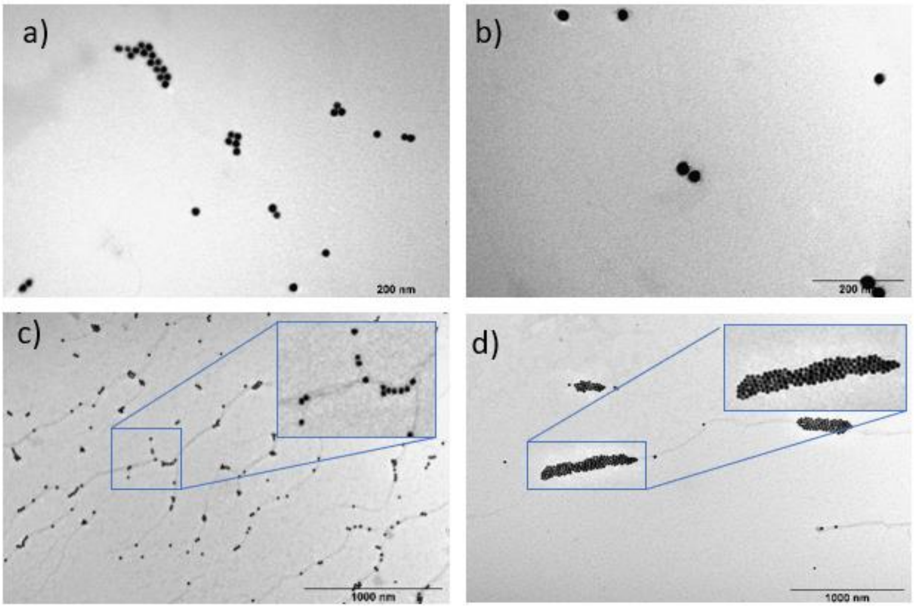

Figure 0.22- TEM images before (a,b) and after staining (c,d) with uranyl acetate of Au13.SPEG.RuDppzL2 (c) and Au25.SPEG.RuDppzL2 (d) with plasmid DNA PBR-322.

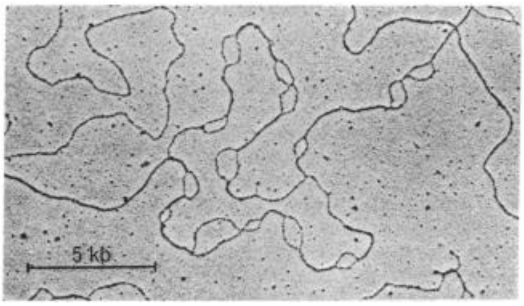

Figure 0.23- Graphical scheme of DNA replication at bubble or “eye” stage where the DNA is unwound to two single strands.[315, 316]

In the samples containing linear plasmid DNA, it was possible to identify the elements gold, phosphorus, and ruthenium by STEM-EDX (Figures 3.23, 3.24 and 3.25). The strings of DNA showed in grey on the TEM images have the same signal observed by the phosphorous signal, making clear that the fragments observed on TEM are DNA. Important to note that the phosphorus signal is also detected on the nanoparticle, evidencing the AuNPs interaction with the plasmid DNA. On figure 3.24, it is also possible to visualise an uncoiling of the DNA and thus a separation of DNA into two single strands.

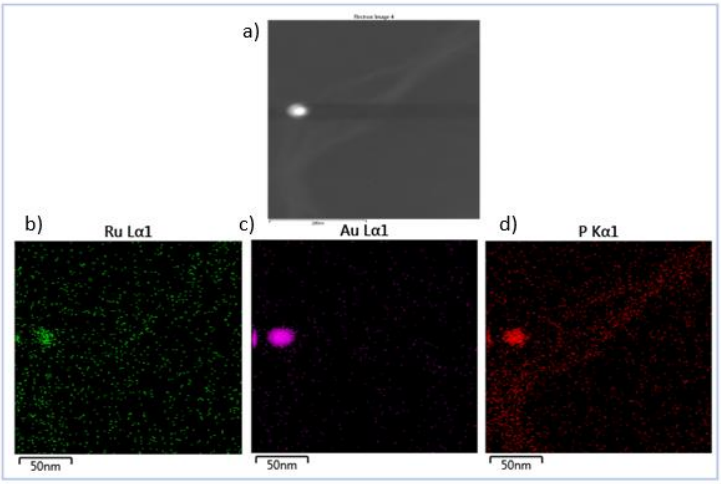

Figure 0.24- STEM-EDX images of Au.SPEG.RuDppzL2 (3.5 nM) with plasmid PBR-322 DNA. Original image from STEM in grey (a) and at the bottom the signal of the elements identified as present on the sample, b) ruthenium (Ru), c) gold (Au) and d) phosphorous (P).

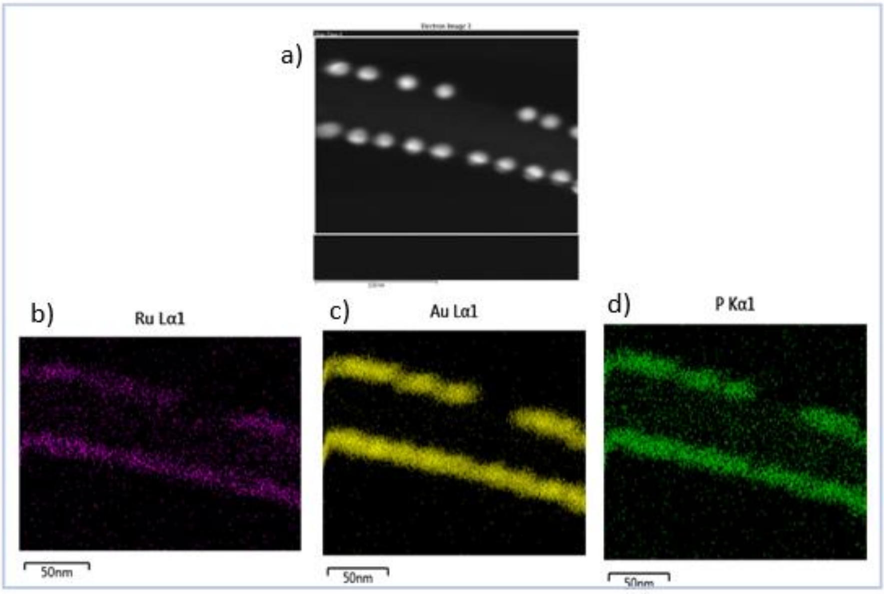

Figure 0.25- STEM-EDX images of a Au.SPEG.RuPhenL2 (3.5 nM) with plasmid PBR-322 DNA. Original image from STEM in grey (a) and at the bottom the signal of the elements identified as present on the sample, b) ruthenium (Ru), c) gold (Au) and d) phosphorous (P).

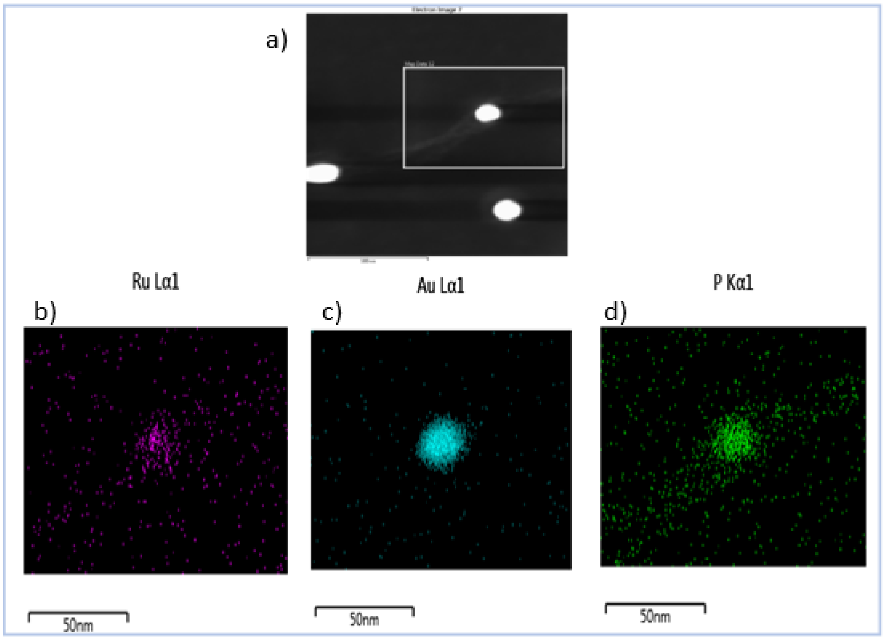

Figure 0.26- STEM-EDX images of Au.SPEG.RuPhenL2 (3.5 nM) with plasmid PBR-322 DNA. Original image from STEM in grey (a) and at the bottom the signal of the elements identified as present on the sample, b) ruthenium (Ru), c) gold (Au) and d) phosphorous (P).

3.3.5 DNA interaction with luminescence gold nanoparticles by spectroscopy

To further analyse the DNA-AuNP.Ru assemblies at different concentrations, a UV-Vis titration was carried out. No change on the SPR band broadness was observed, suggesting no aggregation of the ruthenium coated AuNPs upon DNA addition. With an increase of DNA concentration, however, a change on the absorption intensity is seen. For Au.SPEG.RuDppzL2, increasing the concentration of DNA leads to an absorption increase of 8% (Figure 3.27-a), while for the Au.SPEG.RuPhenL2 an addition up to 17 µM of DNA results in a decrease of 16%, followed by an increase in absorption at higher concentrations (Figure 3.27-b). This result suggests that the DNA addition reached a saturation point at 17 µM, beyond which no further DNA binding to the Au.SPEG.RuPhenL2 has occurred. As a control, Au.SPEG were analysed upon DNA addition, which showed a not significant change of 1.6% on the λmax (Appendices-figure 3.33). The binding constants, calculated through UV-Vis titrations, of Au.SPEG.RuDppzL2 and Au.SPEG.RuPhenL2 upon DNA interaction are respectively, 1.3×10^6 and 7.6×10^6 M^{-1}. Thus, one can conclude that the calculated binding affinity (Ka) of the AuNPs with ruthenium coated is considerably higher than the AuNPs coated only with surfactant SPEG (7.6×10^5 M^{-1}) . In the literature, AuNPs coated with $[Ru(phen)_3]^{2+}$ with a thiolate aliphatic chain, had a binding constant of 5.5×10^5 M^{-1}, showing a considerable lower affinity than Au.SPEG.RuDppzL2 and Au.SPEG.RuPhenL2.[237] The binding affinity calculated for Au.SPEG.RuDppzL2 and Au.SPEG.RuPhenL2 are in the range of the Ka values for classical intercalators (10^6-10^8 M^{-1}) such as ethidium bromide or $[Ru(phen)2(dppz)]^{2+}$, which can suggest that intercalation can be one of the mode of interaction. On the other hand, lower binding constants are usually associated with electrostatic interactions and partial intercalation.[322] Two of the main characteristics of a good DNA intercalator are associated with an increase in emission and a hypochromic effect. Figure 3.27-c,d shows that for both samples, Au.SPEG.RuDPPZL2 and Au.SPEG.RuPhenL2, the interaction with DNA did not decrease the emission signal of the AuNPs. However, there is not a significant increase on emission signal. Surprisingly, although Au.SPEG.RuPhenL2 shows a hypochromic effect (Figure 3.27-b), Au.SPEG.RuDPPZL2 demonstrates a hyperchromic effect (Figure 3.27-a).

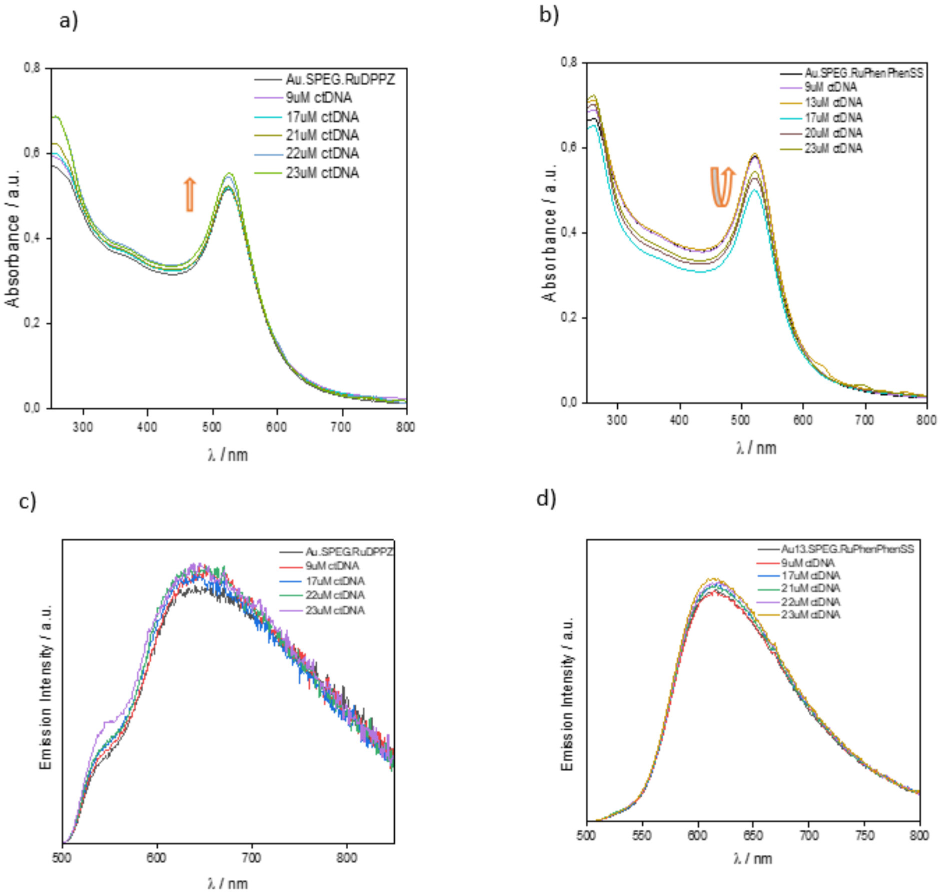

Figure 0.27- UV-Vis titration of ctDNA (50 µM in Tris-HCl buffer, pH=7.4) into (a) Au.SPEG.RuDppzL2 (3.5 nM), (b) Au.SPEG.RuPhenL2 (3.5 nM). Fluorescence emission of ctDNA (50 µM in Tris-HCl buffer, pH=7.4) titration into (c) Au.SPEG.RuDppzL2 (3.5 nM) and (d) Au.SPEG.RuPhenL2 (3.5 nM).

This behaviour was unexpected, since $[Ru(Phen)_2Dppz]^{2+}$ is well stablished in the literature as an intercalator, having a characteristic hypochromic effect and a light switch effect.[95, 260, 267] In order to understand if the behaviour of Au.SPEG.RuDppzL2 originates from the AuNPs or the RuDppzL2 complex, the interaction of the ruthenium (II) complex in solution with DNA was also analysed (Appendices-figure 3.34). As expected, the absorbance had a hypochromic effect and a red shift of 3 nm after DNA binding, which is a common effect of an intercalator.[323] Moreover, similarly to its parent $[Ru(Phen)_2Dppz]^{2+}$, this complex has a light switch effect in which is very weakly luminescent in the absence of DNA but strongly increases its luminescence in the presence of DNA.[260] Since the complex RuDppzL2 has an intercalation behaviour expected when interacts with DNA, one can hypothesise that the hyperchromic effect of Au.SPEG.RuDPPZL2 has to be related with the interaction of the AuNPs with DNA.

The absorbance and emission changes can also be a good indication on how the DNA is affected by the AuNPs. A hypochromic effect suggests a contraction and a conformation change of the DNA helix, which is typically observed by stacking interactions with the base pairs, whereas a hyperchromic effect can indicate electrostatic interactions or partial uncoiling of the helix structure.[260, 322, 324, 325] An hyperchromic effect on AuNPs upon DNA binding has been demonstrated before in the group, in which a wrap of DNA around the AuNPs was hypothesised.[284]

To further understand the interaction of DNA-AuNP.Ru, linear dichroism (LD) measurements were carried out. Linear dichroism is a spectroscopic technique where the samples are oriented and the linear polarised light observed is measured, giving information of orientation and conformation of a molecule. Figure 3.28 shows the LD spectra for Au.SPEG.RuDppzL2, Au.SPEG.RuPhenL2 and Au.SPEG. In a typical LD spectrum for DNA, the signal tends to negative values such as an upside-down absorbance spectrum. This is due to the π-π* transitions of the base pairs being polarised within the plane, i.e, the absorbance of the DNA molecule is perpendicular to the orientation axis.^{90} When a molecule is added to the DNA solution, it is expected to see a change in the signal only if this molecule binds to DNA.

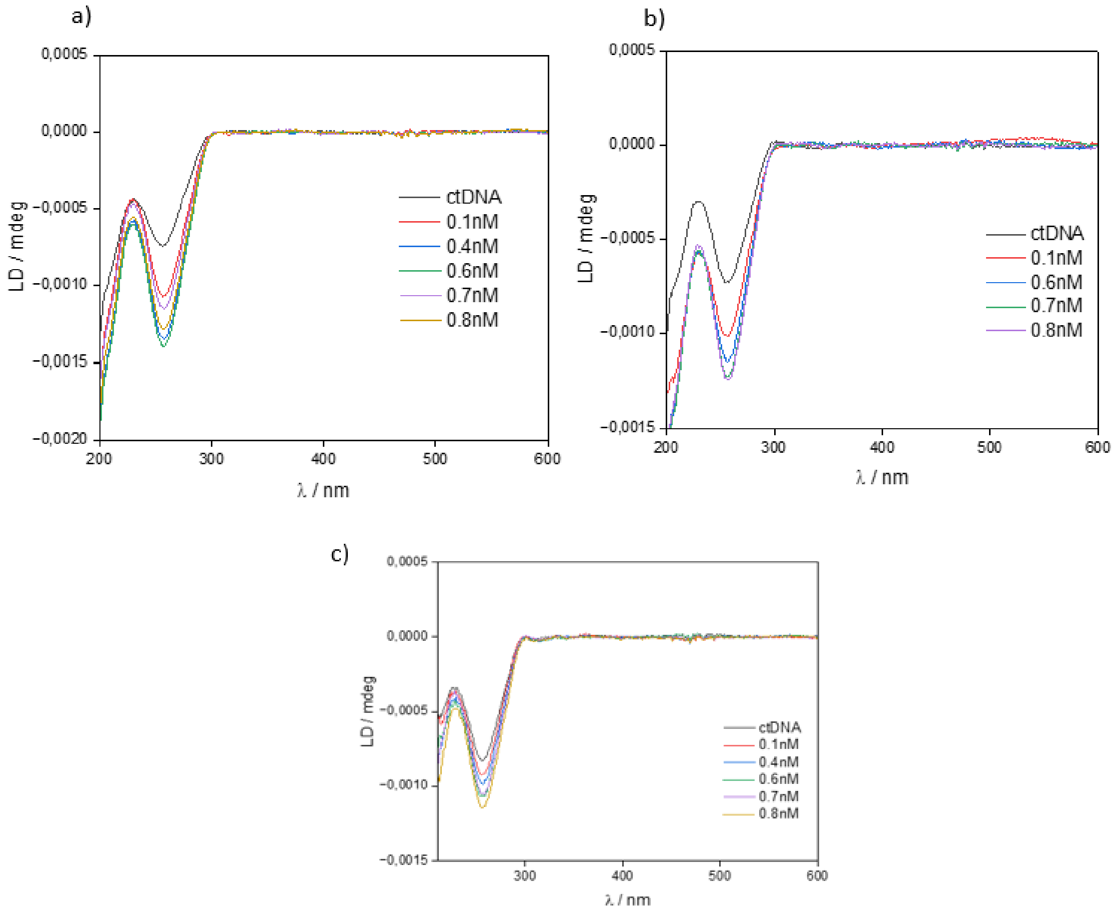

Figure 0.28- Linear dichroism spectra of Au.SPEG.RuDppzL2 (a), Au.SPEG.RuPhenL2 (b) and Au.SPEG (c) titration into ctDNA solution (50 µM in Tris-HCl buffer, pH=7.4) and comparison with the ctDNA signal (black line). For all the spectra, the baseline (Tris-HCl buffer, pH=7.4) was subtracted. Legends show final concentration of AuNPs (0.1-0.8 nM).

In Au.SPEG.RuDppzL2 and Au.SPEG.RuPhenL2, an increase in magnitude is observed upon addition of the AuNPs. This increase is typical for an intercalator of the DNA base pairs. The same is observed upon increase of Au.SPEG.RuDppzL2 and Au.SPEG.RuPhenL2 addition, suggesting that there is an increase of interaction between the AuNPs and the base pairs and a stiffening of DNA.[268, 326, 327] Au.SPEG.RuDppzL2 has the biggest increase in magnitude (88%) upon 0.8 nM of nanoparticles addition, suggesting a significant reduction of DNA orientation. After the addition of the same concentration of Au.SPEG.RuPhenL2, a 69% change is observed on LD magnitude, which although weaker than Au.SPEG.RuDppzL2, there is still a significant reduction on DNA orientation. However, only a 37% increase on magnitude was observed when Au.SPEG was measured, suggesting that although the gold nanoparticles can bind to DNA, the presence of the ruthenium (II) complexes are essential for a strong interaction.

The increase on LD magnitude for Au.SPEG (Figure 3.28-c) suggests a stiffening of the DNA, which contradicts the DNA-AuNPs previous study in the group. As mentioned previously, Caballero et all., showed a decrease in LD magnitude, leading to believe that there is a bending and coiling effect on DNA which wraps around the AuNPs.[284] In the case of Au.SPEG a wrap of ctDNA around the nanoparticles is also possible to be visualised by TEM (see section 3.3.4). However, the LD data shows otherwise, suggesting the formation of loops on DNA. This has first been suggested upon TEM study of Au.SPEG.RuDppzL2 and Au.SPEG.RuPhenL2 with plasmid DNA, in which it seem there was an unwound of DNA and the separation of the double strand into single strands with AuNPs in the middle. This could explain the stiffening of DNA and therefore the increase in LD magnitude. However, to be able to draw any further conclusions, analysis of the samples in cryo-TEM is purposed as future work, so that the images are acquired in solution instead of dried on a surface.

Circular dichroism (CD) can be a very useful technique to detect conformational changes in DNA due to the absorption of right-handed and left-handed circularly polarised light of the chiral backbone of DNA. Therefore, a CD experiment was conducted for Au.SPEG and Au.SPEG.RuDppzL2 and Au.SPEG.RuPhenL2 with ctDNA. However, no changes on the CD spectrum were observed for any of the AuNPs. This could be due to the loops formed on the DNA being in a small proportion preventing a detectable conformation change by CD. However, this hypothesis needs to be further investigated.

Analysing all the several techniques used to study the interaction of DNA-AuNPs, we conclude that there is interaction between the AuNPs and DNA (Table 2). Au.SPEG did not show a significant change by UV-Vis spectroscopy upon ctDNA addition, however a slight magnitude increase was observed by linear dichroism, showing that Au.SPEG might interact with DNA. This interaction seems to be relatively weak, since the binding affinity calculated was 7.6 x 10^5 M^{-1}, suggesting that the binding mode of Au.SPEG to DNA is by electrostatic interactions. An interaction effect is also showed by TEM images of AuNPs with plasmid DNA, suggesting that an uncoiling behaviour. However, these electrostatic interactions are weak, and therefore the attachment of RuDppzL2 and RuPhenL2 to the AuNPs are essential for a stronger binding. An increase on magnitude on LD upon addition of DNA, suggests that there is an intercalation process, which would be expected due to the RuDppzL2 and RuPhenL2 similarities with $[Ru(phen)_2(Dppz)]^{2+}$

and $[Ru(Phen)_3]^{2+}$, respectively. However, while Au.SPEG.RuPhenL2 has a hypochromic effect in the presence of DNA, Au.SPEG.RuDPPZL2 showed a hyperchromic effect. Overall, it is possible to understand that the AuNPs have different sides that can interact with DNA, indicating that more than one binding mode can be in place. However, to confirm the suggested interaction other studies need to be done in the future, such as viscosity, computational studies and competition assays using known intercalators such as ethidium bromide.

Table 9- Summary of techniques that prove DNA-AuNPs interaction with suggested binding mode after results comparison. Nd- not determined.

	Au.SPEG	**Au.SPEG.RuDppzL2**	**Au.SPEG.RuPhenL2**
Absorption	No change	Hyperchromic	Hypochromic
Emission	nd	No change	No change
Binding affinity (Ka / M^{-1})	10^5	10^6	10^6
LD (magnitude)	Increase	Increase	Increase
TEM/EDX	No visible interaction	Visible interaction	Visible interaction
Suggested binding mode	Electrostatic	Intercalation and electrostatic	Intercalation and electrostatic

3.4 Conclusions

A new nano system of Au.RuDppzL2 was successfully synthesized, characterised and its luminescence behaviour studied. Au.RuDppzL2 showed a higher quantum yield than RuDppzL2 in solution (water/methanol) and a lower luminescence lifetime due to a plasmonic enhancement from the AuNPs. Au.RuDppzL2 was also evaluated according to its interaction with DNA and compared with Au.RuPhenL2. Visualization of the DNA wrapping around both the nano systems Au.SPEG.RuDppzL2 and Au.SPEG.RuPhenL2 was possible by TEM and STEM-EDX as well as their linearization upon addition of plasmid linear DNA. Moreover, it was possible to visualise a possible uncoiling of the double strand DNA when interacting with the Au.SPEG.RuDppzL2 and Au.SPEG.RuPhenL2, which could be used as a therapeutic strategy in the future, by preventing DNA replication. Au.SPEG.RuDppzL2 showed an hyperchromic effect which is characteristic of electrostatic interactions, whereas Au.SPEG.RuPhenL2 demonstrated to have a hypochromic effect, which usually is correlated with an intercalator behaviour. Moreover, both Au.SPEG.RuDppzL2 and Au.SPEG.RuPhenL2 demonstrated an increase of magnitude on the linear dichroism signal suggesting an intercalator behaviour between the AuNPs and the DNA base pairs. Furthermore, both Au.SPEG.RuDppzL2 and Au.SPEG.RuPhenL2 have relatively strong binding affinities indicating once more an intercalation behaviour. It is concluded that, Au.SPEG.RuDppzL2 and Au.SPEG.RuPhenL2 enhance the affinity and binding to DNA in comparison with Au.SPEG. Furthermore, different binding modes can be suggested for the interaction, such as electrostatic by van der Waals forces between the base pairs and the AuNPs, and intercalation between the aromatic ligands of RuDppzL2 and RuPhenL2 and the base pairs of DNA. Overall, this study showed that luminescence AuNP.Ru can bind to DNA and therefore these nano systems can be potential strong candidates to be used for different applications such as imaging, biosensors, and therapeutics.

3.7 Appendices

Table 10- Size by number distribution and polydispersity index of citrate and coated Au13 by DLS.

	Dynamic Light Scaterring (DLS)	
	Number distribution / nm	Polydispersity Index (PDI)
AuNP13	11.5 ± 2.9	0.09
Au13.Z	19.3 ± 5.3	0.23
Au13.SPEG	15.0 ± 4.2	0.19
Au13.Z.RuDppzL2	24.0 ± 7.1	0.29
Au13.SPEG.RuDppzL2	22.4 ± 7.1	0.34

Table 11-Size by number distribution and polydispersity index of citrate and coated Au25 by DLS.

	Dynamic Light Scaterring (DLS)	
	Number distribution / nm	Polidispersity Index (PDI)
AuNP25	20.1 ± 5.0	0.08
Au25.Z	22.6 ± 6.6	0.23
Au25.SPEG	22.6 ± 6.6	0.26
Au25.Z.RuDppzL2	25.2 ± 8.0	0.35
Au25.SPEG.RuDppzL2	24.0 ± 6.1	0.38

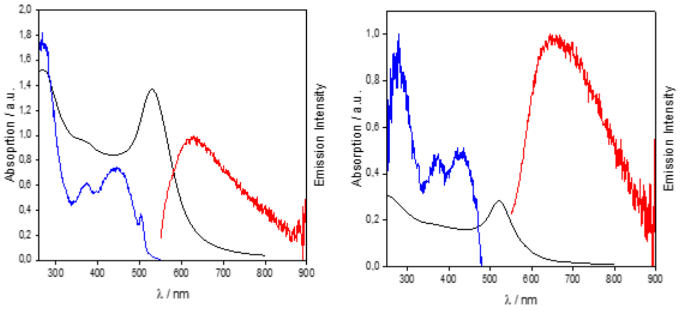

Figure 0.29- Absorption (black), emission (red) and excitation (blue) spectra of 3.5 nM Au13.SPEG.RuDppzL2 (left) and 1.5 nM Au25.SPEG.RuDppzL2 (right) (λ_{ex}= 450 nm, λ_{em}=675 nm) in aerated water.

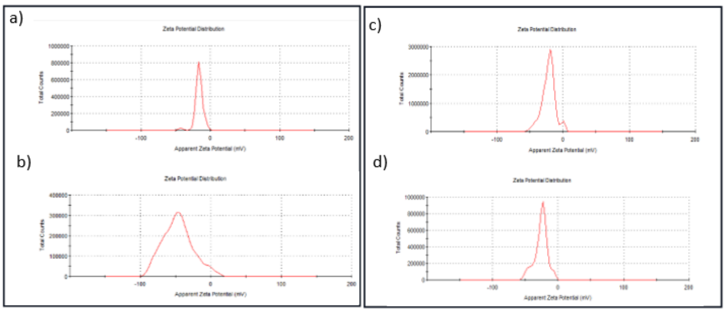

Figure 0.30-(L) Zeta potential distribution of Au.SPEG.RuPhenL2 before (a) and after (b) DNA addition. (R) Zeta potential distribution of Au.SPEG.RuDppzL2 before (c) and after (d) DNA addition.

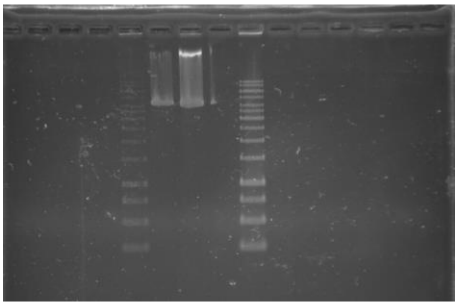

Figure 0.31- Agarose gel demonstrating a 1 kb DNA ladder (from 250 bp to 25.000 bp) on the first and last lanes. Middle lanes represent the plasmid pBR322 plasmid studied.

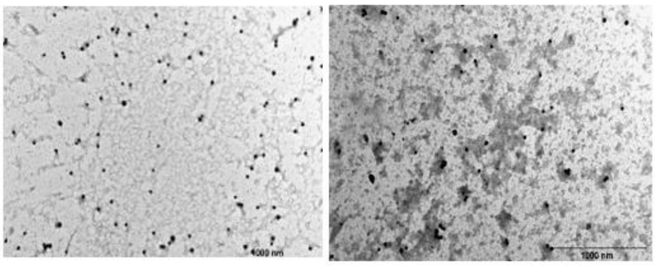

Figure 0.32- Transmission electron microscopy (TEM) images of a 3.5 nM solution of AuNPs, after the addition of 16 µM ctDNA. The TEM grid was previously stained with 4% uranyl acetate for DNA visualisation. (L) Au.Z.RuDppzL2 and (R) Au13.Z.RuPhenL2 with plasmid DNA PBR-322.

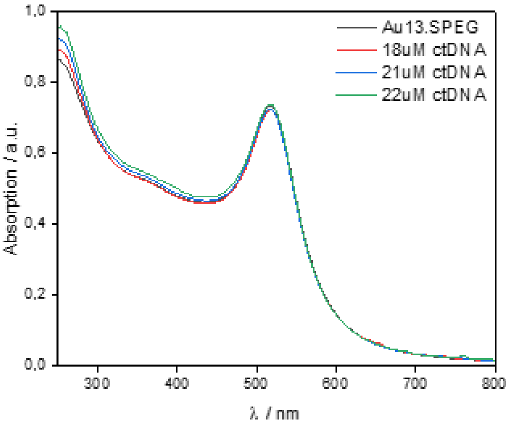

Figure 0.33- UV-Vis titration of ctDNA (50 µM in Tris-HCl buffer, pH=7.4) into Au.SPEG (3.5 nM).

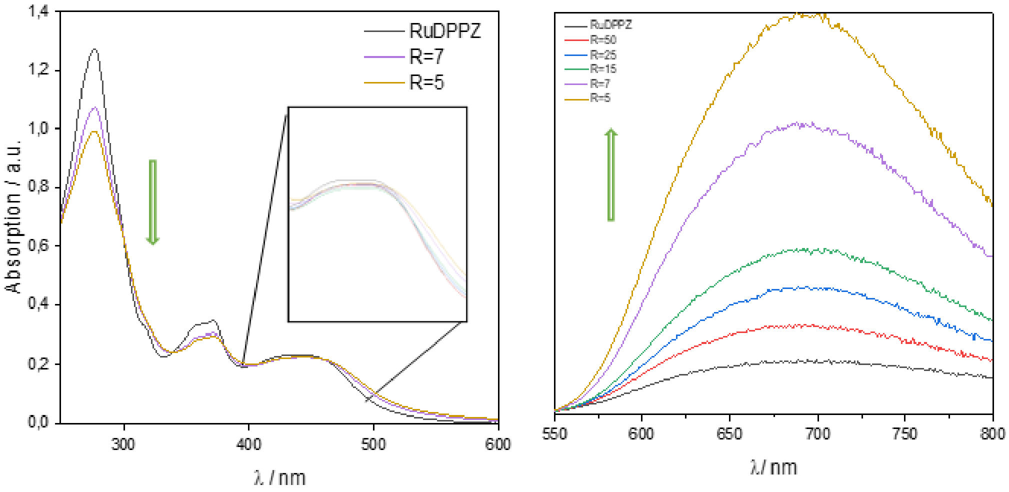

Figure 0.34-(L) UV-Vis titration of ctDNA (50 µM in Tris-HCl buffer, pH=7.4) into RuDppzL2 demonstrating a significant hypochromic effect and red shift. (R) Emission titration of of ctDNA (50 µM in Tris-HCl buffer, pH=7.4) into RuDppzL2 showing an emission increase upon addition of DNA. R= ratio of base pairs per complex.

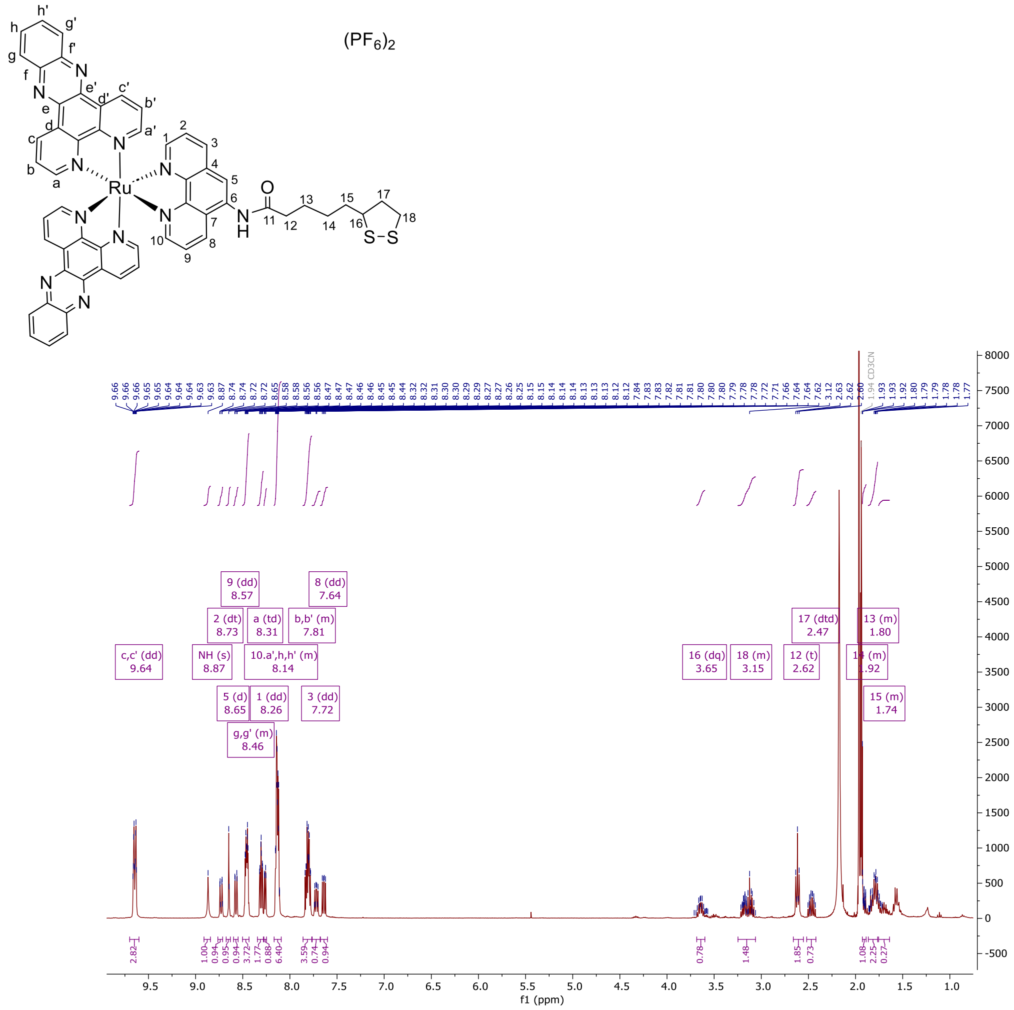

Figure 0.35-^{1}H-NMR of RuDppzL2 in CD$_3$CN.

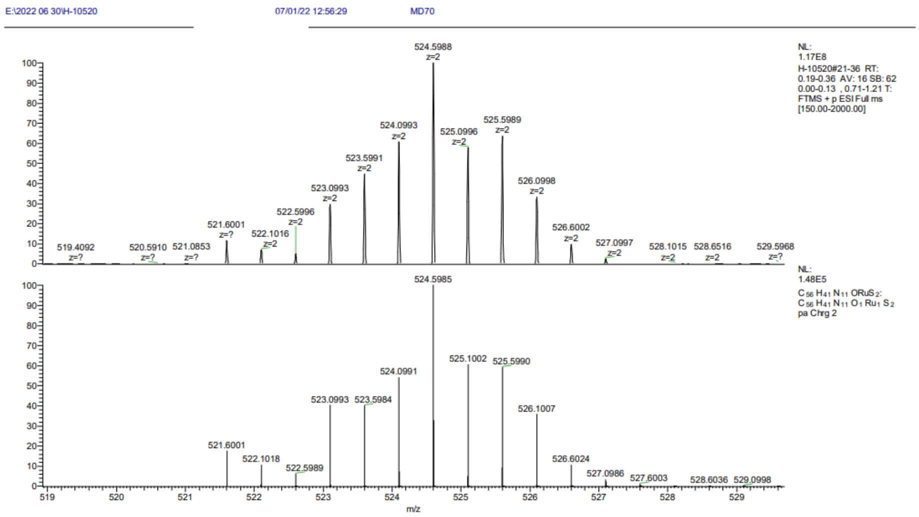

Figure 0.36- Theoretical (top) and observed (bottom) of RuDppzL2 ESI+ MS with the fragment 524.6 (M-PF$_6$)$^+$.

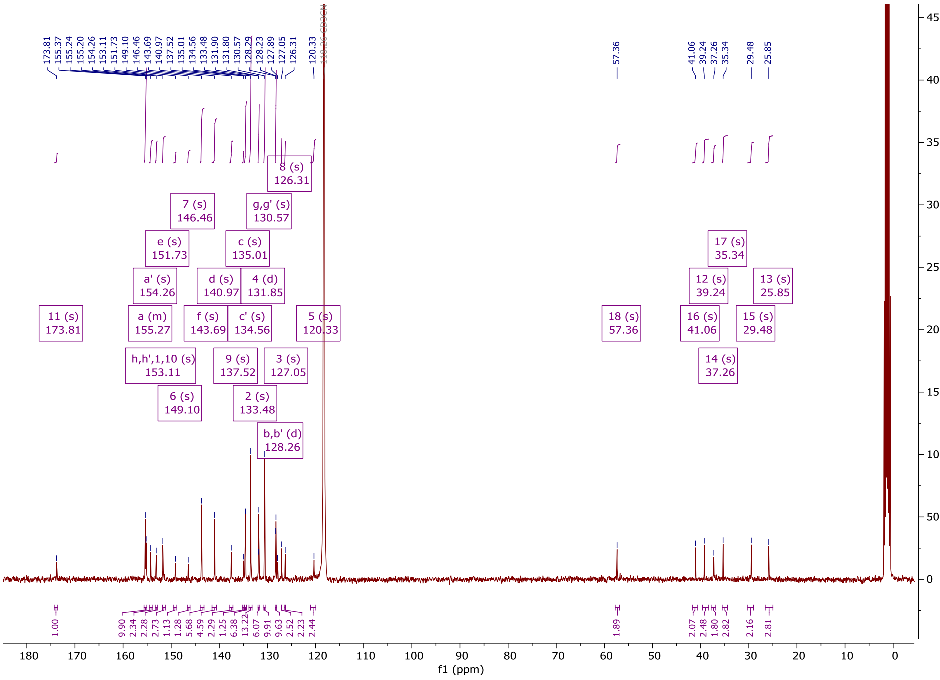

Figure 0.37-^{13}C-NMR of RuDppzL2 in CD_3CN.

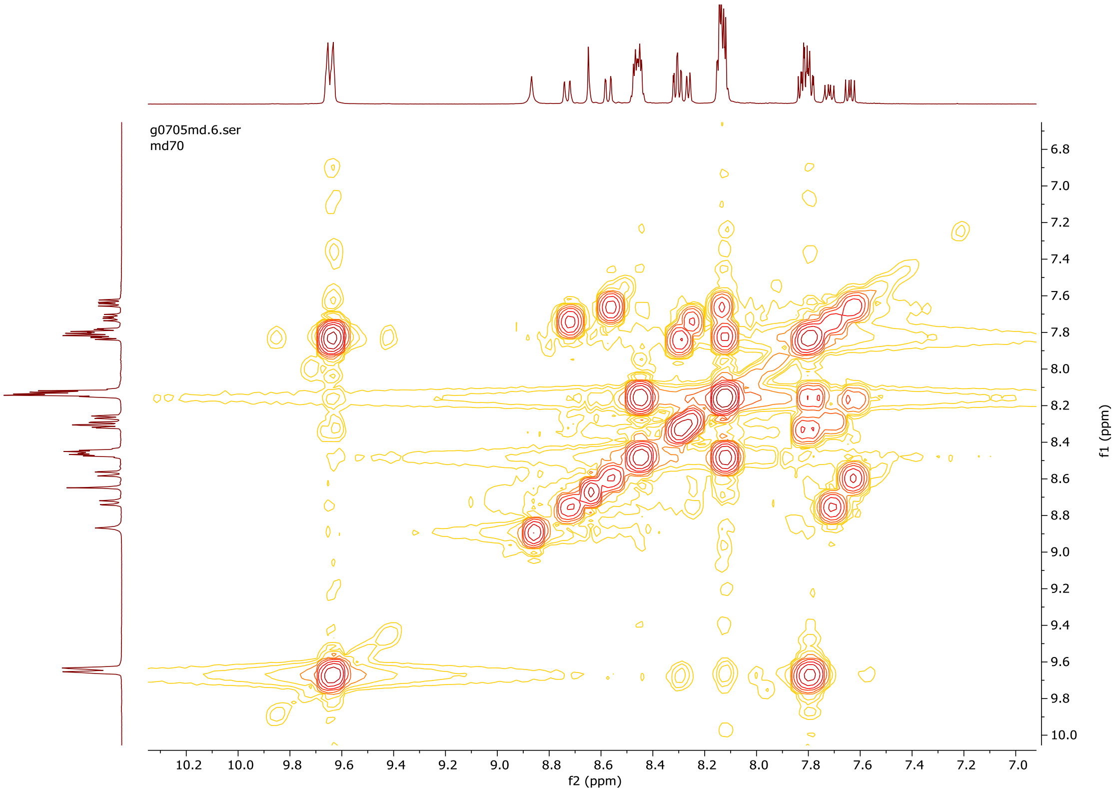

Figure 0.38-2D COSY of RuDppzL2 in CD_3CN.

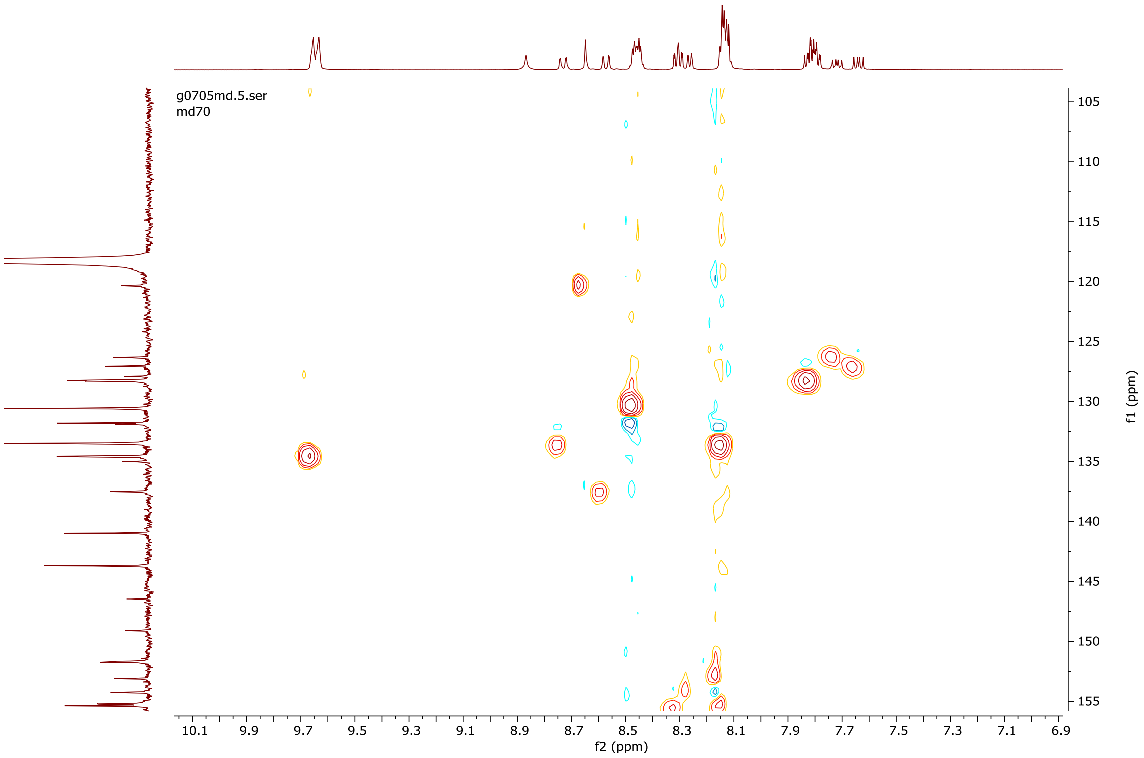

Figure 0.39-2D HMBC of RuDppzL2 in CD_3CN.

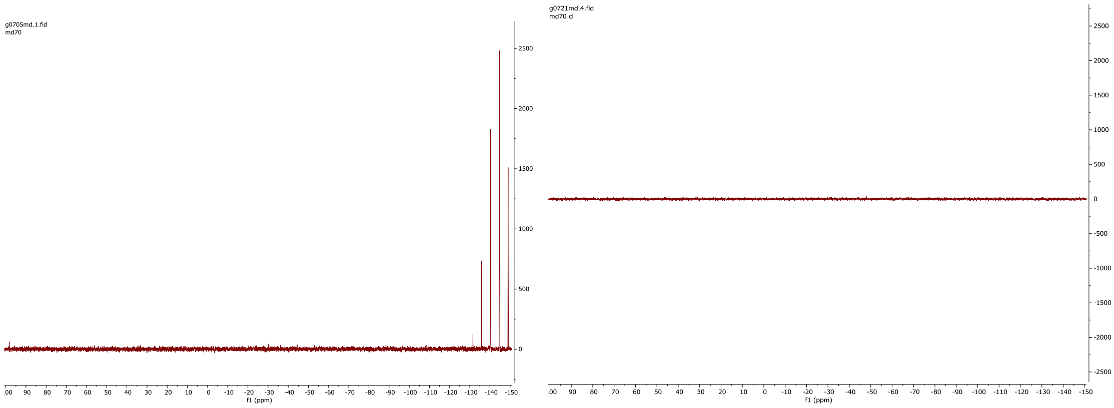

Figure 0.40-^{31}P-NMR of RuDppzL2 before (left) and after (right) counter ion exchange.

4. Luminescent ruthenium gold for nuclear targeting in cancer cells

4.1 Introduction

4.1.1 Ruthenium functionalised gold nanoparticles for diagnosis

Ruthenium (II) complexes coated with AuNPs, can be studied for examples, as biological sensors or cell imaging to monitor drug delivery.[166, 237] In general ruthenium (II) complexes have large Stokes shift and long lifetimes, which minimize the risk of autofluorescence detection on the microscope, excitation (λexc= 450 nm) and emission (λem= 600 nm) in the visible region and tuneable luminescent profile by for example modifying functional groups of the ligands attached to the ruthenium (II) complex.[328] AuNPs are easily functionalised, with tuneable sizes, a large surface area allowing functionalisation with multiple probes and biocompatible. Moreover, AuNPs are electron dense nanomaterials allowing multimodal imaging.[147] (see Chapter 1 and 2, section 2.1, for further details). Leung and co-workers coupled $Ru(bpy)_3Cl_2$ with a lipoic acid, and through a thiol bond, attached onto AuNPs capped with DMAP (4-dimethylaminopyridine), leading to positively charged AuNPs.[329] In this study they found that when the ruthenium (II) complex, $Ru(bpy)_3Cl_2$, is attached to AuNPs, a Förster resonance energy transfer (FRET) from the probe to the gold nanoparticles was observed. But when a esterase enzyme (hydrolyses ester, amide and thioester bonds) was added, the ruthenium (II) complex can be released from the AuNPs and the luminescence is increased (Figure 4.1).[329] This study was used to determine an assay method for the esterase detection based on the quenching of AuNP.Ru conjugates.

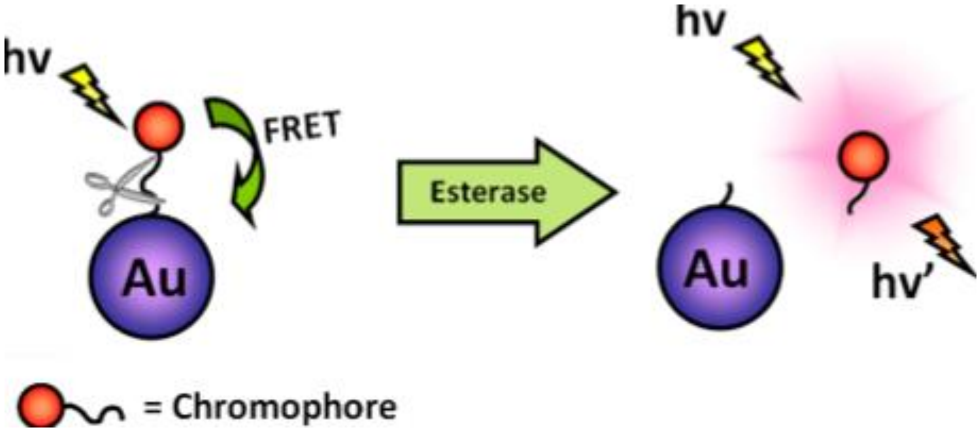

Figure 4.1- Schematic representation of the enzyme esterase releasing the $Ru(bpy)_3Cl_2$, leading to luminescence enhancement.[329]

Gunnlaugsson's group synthesised luminescent AuNPs using different ruthenium (II) complexes (Figure 4.2-1) and demonstrated that the Ru(II) complexes luminescence was preserved even upon cell uptake.[237] However, due to the small size of AuNPs (4-5 nm), the uptake mechanism was challenging to elucidate. Therefore, the same group, investigated bigger gold nanoparticles (averaged 15 nm size) functionalised with the same ruthenium (II) complexes (Figure 4.2) and detected the AuNPs by fluorescence confocal and TEM.[330] After 24h the AuNPs accumulate in the cytosol of the HeLa cells, inside vesicles. However, it is noted that the ruthenium signal is quenched, which could be related with the absence of surfactant that could protect the ruthenium (II) complex from $^3O_2$ quenching. Furthermore, the lack of surfactant also influenced the stability of the AuNPs, where large aggregates were observed after 16h.

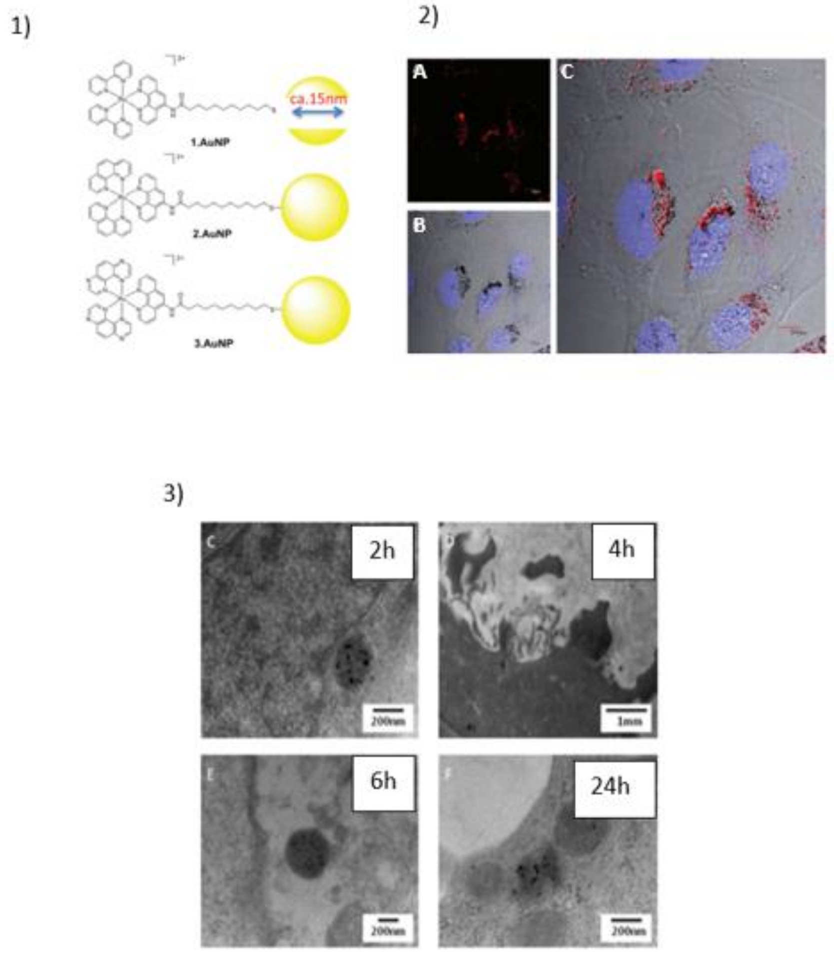

Figure 4.2- (1)-Schematic representation of Ruthenium (II) polypyridyl complexes- AuNPs hybrid materials on 15 nm gold nanoparticles sizes. (2)- fluorescence confocal microscopy images of Hela cells treated with 20 µM of 3.AuNP for 24 h. Ruthenium signal (A), nuclear DAPI stain (B) and overlapped images (C). (3)- TEM images of Hela cells incubated with 3.AuNP for 2,4,6, and 24 h, adapted from[330].

The development of ruthenium (II) polypyridyl complexes for imaging have been extensively studied[56, 331-333]. However, although the conjugation of ruthenium (II) complexes onto AuNPs are an attractive strategy for cell imaging, there are only a few studies in this area. Due to the advantages of using AuNPs as nano probes and nano carriers, it is believed that AuNP.Ru conjugates are a promising diagnosis strategy in a near future and therefore, should be further explored.

4.1.2 Cell uptake mechanism for gold nanoparticles

The design of functional AuNPs for intracellular imaging requires a deep understanding of the mechanisms of these nanoparticles, entering and leaving the cells, allowing the control of AuNPs cellular accumulation and better understanding of cytotoxicity.[147] However, physiochemical properties of AuNPs, such as shape, size and surface modification, have an important role on their biological effects.[334] Chithrani and co-workers were one of the first groups that analysed the uptake of citrate AuNPs and compared with transferrin coated AuNPs.[335, 336] They compared the uptake of the AuNPs in different cell lines, with different sizes (14, 50 and 74 nm) and different shapes such as spherical and rods. Transferrin is one of the serum proteins and enters the cells by receptor mediated endocytosis.[337] However, when compared AuNPs coated with this proteins and citrate AuNPs, both entered STO, Hela and SNB19 cells.[335] In fact, transferrin-AuNPs had three times less uptake than citrate AuNPs.[336] This was an interesting discovery, since citrate-AuNPs are negatively charged and therefore their cellular uptake in hindered due to repulsion between the nanoparticles and the negatively charged membrane.[338] It was then hypothesised that the AuNPs uptake could be related with a nonspecific adsorption of serum proteins onto the gold surface, inducing a mechanism of receptor-mediator endocytosis.[339, 340] This mechanism involves the transport of cargo molecules from the plasma membrane into the cell cytoplasm.[341]

This process happens due to the binding of receptors on the surface of the cell membrane to the cargo molecules, creating a membrane vesicle (Figure 4.3).

The transferrin-AuNPs only have two receptors to interact when reached the cell membrane, whereas the citrate AuNPs could interact with a variety of serum proteins and therefore several receptors could allow the AuNPs uptake. Furthermore, it was then hypothesized that the rates and amount of uptake of AuNPs is dependent on the presence of these proteins and the time it takes to interact with receptors so that an invagination process occurs.[335, 336] Nowadays, it is accepted that AuNPs can be internalised by different ways, as shown if figure 4.3. 1) clathrin-mediated endocytosis and 2) caveolin-mediated endocytosis, which involves the formation of plasma membrane invaginations, known as “little cages”. Moreover, 3) clathrin and caveolin-independent pathways were also observed for AuNPs cell uptake, in which the cell membrane itself initiates a physical deformation and form a vesicle, capturing the AuNPs. 4) Phagocytosis is a process where there is an engulfing of the AuNPs and 5) macropinocytosis is performed by ripples of the cellular membrane.[334, 342, 343] All the pathways presented involve the formation of AuNP-protein system, recognition by the cell membrane receptors, engulfment into a vesicle and transported into the cell cytoplasm.[340, 344] Later, these vesicles will activate the signal pathways, ending in release of the AuNPs into the cytoplasm or secretion to the outside of the cell.[345, 346]

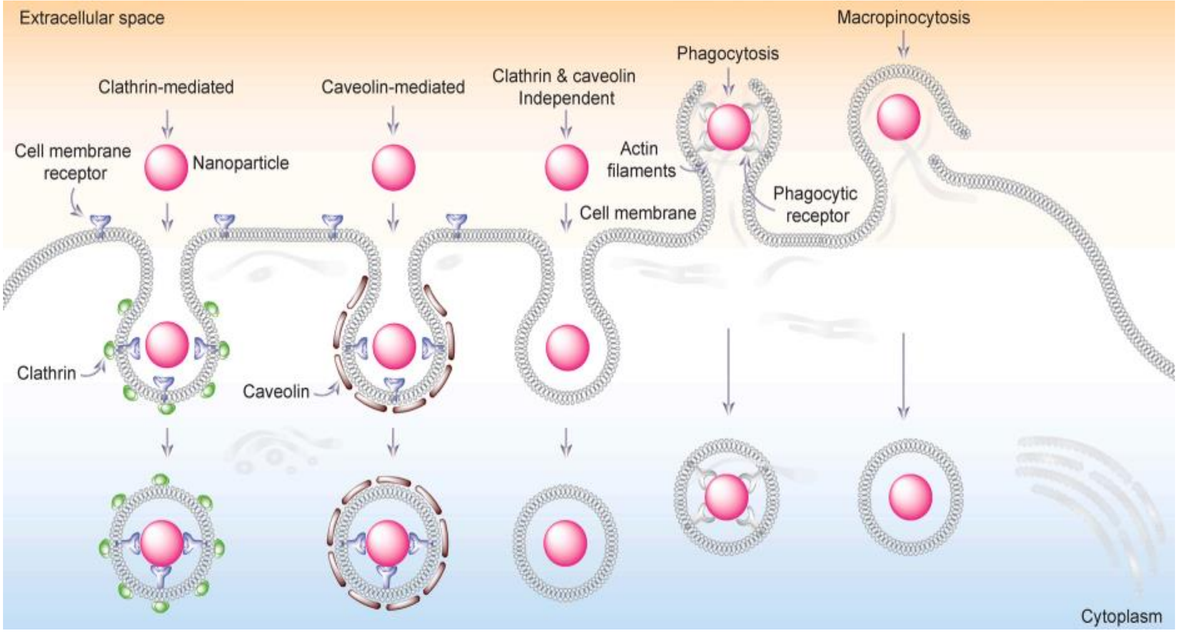

Figure 4.3- Schematic representation of the different endocytosis mechanisms of nanoparticles internalisation in cells, adapted from[343].

Besides coating, shape, and size of AuNPs, can also influence the uptake inside the cells. Chithrani et al, compared spherical AuNPs and gold nanorods (AuNRs) and concluded that although both shapes entered the cells via endocytosis mechanisms, the number of spherical nanoparticles inside the cells was significantly larger than rods.[336] In a different study, nano triangles (AuNTs) had a better uptake followed by AuNRs and finally nanostars (AuSTs).[347] The reasons for this, is yet to be clarified, but it is hypothesised that can be related with a reduction of binding sites requiring a higher energy for membrane bending.[347] When different sizes of AuNPs were compared, differences on the uptake were also found. 50 nm AuNPs had a significant higher uptake than 14 or 74 nm AuNPs, leading to believe that the uptake of different sizes of AuNPs is very dependent on the “wrapping time”, i.e, how a membrane encloses a nanoparticle.[336] TEM images showed that for that reason, 14 nm nanoparticles could enter the cells as clusters, whereas 50 nm single AuNPs could be enclosed by the membrane, as shown by Figure 4.4. However, smaller AuNPs tend to be distributed in different organelles of the cells and even enter the nucleus.[343]

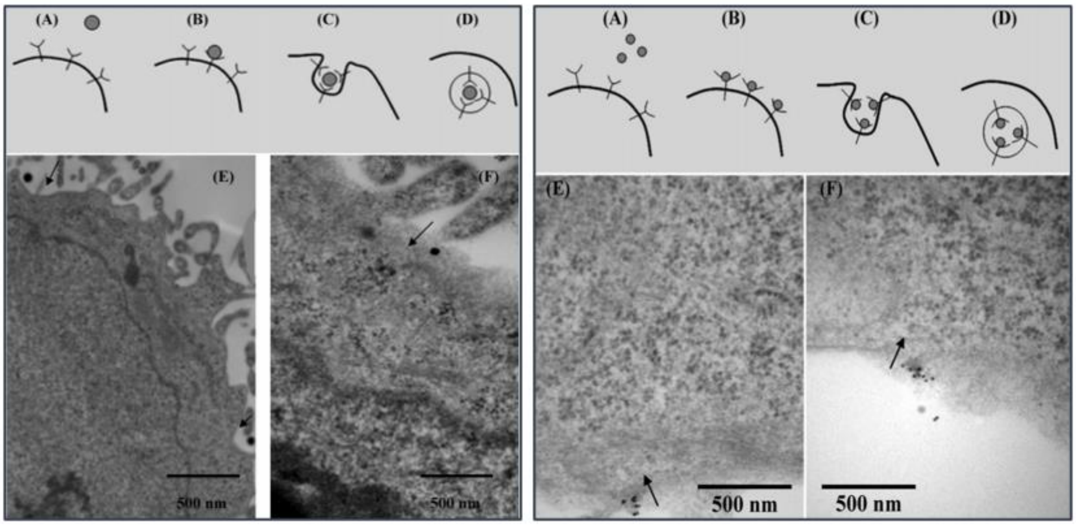

Figure 4.4- Different stages of the cellular uptake process of 50 nm (left) and 14 nm (right) transferrin coated AuNPs by TEM, adapted from[335]. Schematic representation of the receptor mediator endocytosis pathway, where the AuNPs bind to membrane receptor (B), membrane invagination (C) followed by internalisation inside of vesicles (D).

Recently, our group studied the uptake of 13 nm AuNPs coated with Zonyl FSA as surfactant and a luminescence ruthenium (II) complex RuS12 (Figure 4.5), managing to track the AuNPs into the lysosomal pathway and endosomal release by TEM and fluorescence confocal microscopy.[194] It was then established that these AuNP.Ru conjugates could have three different uptake mechanisms that included direct passive and translocation, clathrin-mediated endocytosis and macropinocytosis, which had evidence to be the major mechanism of uptake. Macropinocytosis is a transport mechanism where no receptors are involved. Instead, there is a membrane ruffling that engulfs the outer cargo into endocytic vesicles.[348] During this study, conformational changes in the membrane were visible through TEM. In all the cases, all the pathways lead to an endosomal release of the AuNPs, followed by autophagy to degrade the AuNPs after 24 h. No evidence of the AuNPs in the nucleus was found for these AuNPs.

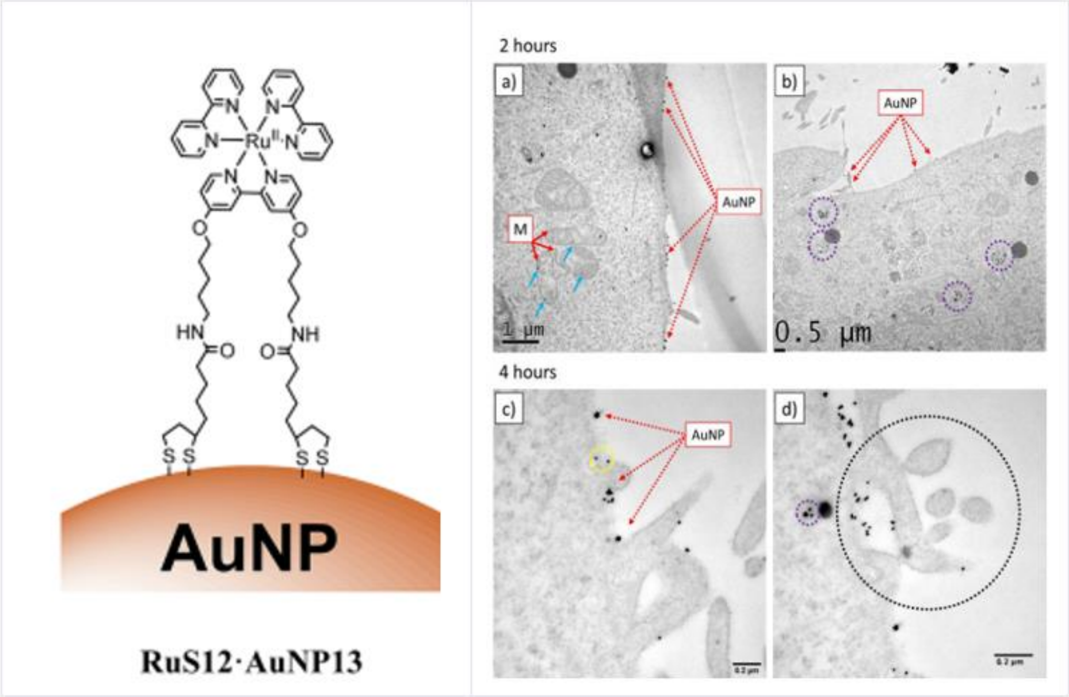

Figure 4.5- (L) Structure of RuS12 attached to AuNP surface, (R) TEM images demonstrating the uptake of RuS12.AuNP13 in A549 cell after 2 h (a,b) and 4 h (c,d) incubation. Red arrows indicate RuS12.AuNP13. Images a and b show few RuS12.AuNP13 accumulating in mitochondria, but the majority can be found in vesicles in the vicinity of the cytoplasmic membrane (purple dotted circles). Image c demonstrates RuS12.AuNP13 in the cytoplasmic membrane and in d the black dotted circle demonstrates evidence of membrane ruffling consistent with cellular uptake via macropinocytosis, obtained from[194].

4.1.3 Gold nanoparticles for nuclear targeting

Targeting the cell nucleus with AuNPs has been an attractive but challenging aim due to their difficulties to reach the cellular nuclei. The AuNPs need to first enter the cell, which can be challenging, then they need to escape from the vesicles and reach the nucleus outer membrane, pass the nuclear pore complex and the inner nuclear membrane (Figure 4.6), imposing further restrictions regarding size and coating.

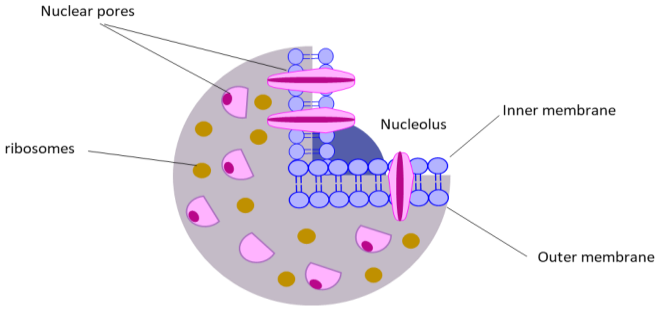

Figure 4.6- Simplified representation of nucleus constituents in eukaryotic cells.

There are two different ways for the AuNPs to reach the cell nucleus, passive diffusion or active transport.[343] An example of AuNPs passive diffusion to the nucleus was demonstrated by Huo et al, where they coated AuNPs with sizes 2, 6, 10 and 16 nm with tiopronin, which is a well-known pharmaceutical drug used for the treatment of rheumatoid arthritis.[349] Then they also coated with a triplex forming oligonucleotide (TFO- gene targeting tool that binds to DNA) to direct the AuNPs into the nucleus. Interestingly, they realise that only small AuNPs (2 and 6 nm) could enter the nucleus on MCF-7 cancer cells, whereas 10 and 16 nm AuNPs only accumulated inside vesicles in the cytoplasm. Hence, they concluded that only small AuNPs could go through the nuclear pore complex, which is reported to allow molecules smaller than 9 nm to enter the nucleus.[350] On the other hand, Kang et al proved that bigger AuNPs can also enter the nucleus by active transport when they coated 30 nm AuNPs with a peptide that targets surface proteins in cancer cells (RGD) and a nuclear localisation signal (NLS) peptide to target the nucleus of the HSC (human oral squamous carcinoma) cancer cells.[285] In this study, the AuNPs were able to colocalise in the nucleus and damage the cancer cells by causing a cytokinesis arrest and a binucleate cell, leading to a complete failure of cell division resulting in apoptosis (Figure 4.7).

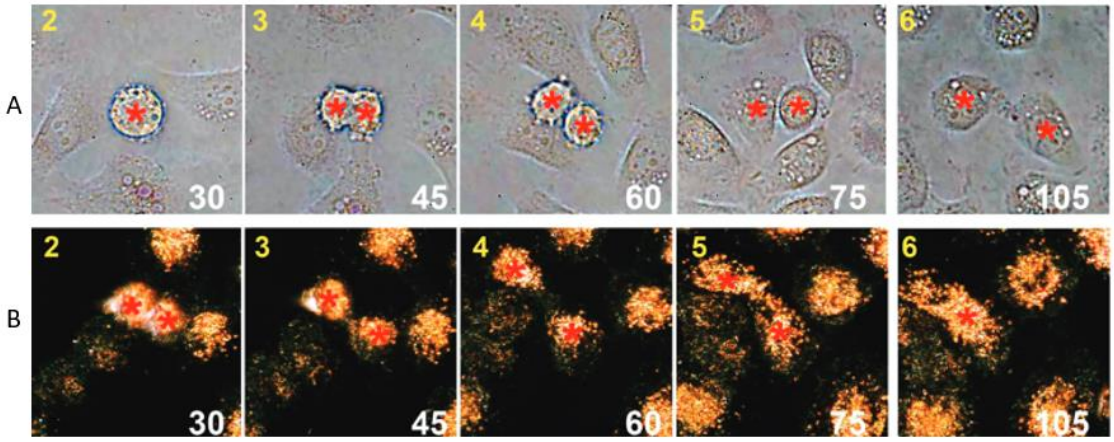

Figure 4.7- Real time images of cancer cell division showing an apparent cytokinesis arrest B4, followed by binucleate cell formation (B6) in the presence of RGD/NLS-AuNPs. This phenomenon is not observed in no treated cells (A), adapted from[285]

4.1.4 Gold nanoparticles and ruthenium (II) complexes for Photodynamic therapy

Learning the cell pathway of AuNPs is crucial to understand the best strategy to use these nanomaterials for therapeutic aims. AuNPs coated with molecules of interest, can enhance the toxicity effect by being an effective nano-carrier.[221, 351-353] Toxicity of AuNPs is mostly concentration and cell line dependent, however, studies have showed that citrate gold nanoparticles (with no other coating) can produce reactive oxygen species (ROS).[354] However, with a careful and effective design, AuNPs can also be used to enhance the photosensitiser ROS production.[154] Oo and co-workers functionalised a 19 nm, 66 nm and 106 nm AuNPs with the photosensitiser protoporphyrin IX and revealed a significant enhancement of almost double of the ROS production comparing with the photosensitiser alone, upon light irradiation at 530 nm.[355] This enhancement was not only dependent on the uptake of the AuNPs but also its size. The contribution of high localised plasmonic field increases with AuNPs size, leading to an increase in ROS production.

With the attractive properties of ruthenium (II) complexes for photodynamic therapy (PDT), is no surprise that $[Ru(phen)_2(dppz)]^{2+}$ and $[Ru(bpy)_2(dppz)]^{2+}$ and its derivatives complexes were also tested since DNA has showed to be an effective target on PDT. Gasser group has been extensively studying these complexes and has confirmed the ability of these complexes to generate singlet oxygen species with quantum yields above 50% in acetonitrile and between 1-6 % in PBS. [279, 280, 356] This difference is due to PDT being dependent on the solvent used because of quenching effects. Nevertheless, Gasser group showed that a complex bearing a OMe group in the dppz ligand (ruthenium (II) complex (2), in figure 4.8 showed to be highly phototoxic (phototoxic indices with a 12 fold increase of known photosensitiser) for Hela and MRC-5 cell lines by $^1O_2$ production upon irradiation at 350 and 420 nm. Moreover, this ruthenium (II) complex showed to have high DNA affinity as intercalator (Kb~10^{-6} M^{-1}) and nuclear localisation.[52, 280]

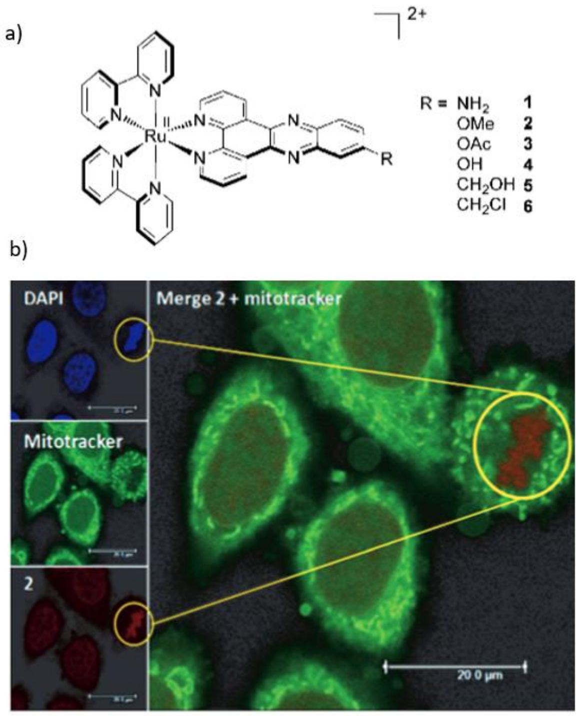

Figure 4.8- (a) Structures of ruthenium (II) complexes tested by Gasser group for PDT in Hela and MRC-5 cells, (b) cellular localisation of complex (2) in Hela cells after 2h incubation by confocal microscopy. The cells were stained with DAPI and Mitotracker for nucleus and mitochondria visualisation.

However, in general ruthenium (II) complexes have some limitations as photosensitisers such as, low solubility in water, they are excited by short wavelength visible light which limits deeper radiation penetration and cellular uptake can be very limited.[357] For an effective cytotoxicity effect by PDT in a deeper tissue, the photosensitiser needs to excite at or as close as possible to the near infrared region.[358] Besides, if the photosensitiser is localised in intracellular organelles such as nucleus, mitochondria, or lysosomes the reactivity and therefore the toxicity effect is much higher, upon light activation.[51] In order to allow the photosensitiser to accumulate inside these specific organelles at a sufficient concentration to produce an effect, other strategies to modify the traditional photosensitisers need to be considered. The use of nanoparticles for therapeutic effects has the big advantage of allowing a prolonged circulation and accumulation in the tumour due to the enhanced permeability and retention effect due to their nano size.[359] Therefore, several studies have demonstrated the efficacy on using nanoparticles as nano carriers for PDT drugs and a progressed to preclinical studies.[360-363] Although these have not reached clinical trials, AuNPs have been extensively explored for PDT and proved it can increase efficacy of PDT.[364] The combination of the useful properties of ruthenium (II) complexes to be used as photosensitisers and gold nanoparticles as nano-carriers can be an attractive strategy to improve PDT effectiveness and therefore it should be explored.

4.2 Chapter Aims

The localisation and uptake of AuNP.Ru conjugates (Au.RuPhenL1, Au.RuPhenL2 and Au.RuDppzL2) in A549 cell line will be studied by confocal luminescence microscopy and transmission electron microscopy. The cellular uptake between different AuNPs sizes will be compared as well as its cytotoxicity in the dark and upon visible light irradiation. The final aim of this chapter is to purpose a theranostics mechanism (Figure 4.9) to tackle A549 cells by using the luminescent nano systems for cell imaging and photodynamic therapy upon visible light irradiation.

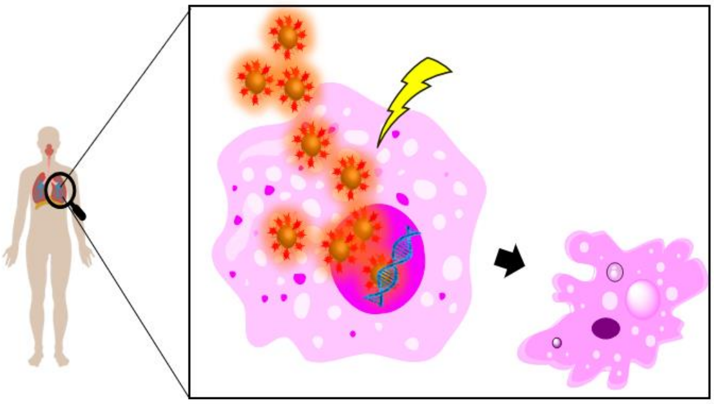

Figure 4.9- Schematic representation of a theranostics strategy using luminescent ruthenium AuNPs to image and tackle cancer cells.

4.3 Results and Discussion

4.3.1 Cell survival assays in A549 cells

To evaluate the cellular uptake and localisation of the AuNPs in A549 cells, it is essential to analyse the cytotoxicity. An MTT (3-(4,5-dimethylthiazol-2-yl)-2,5-diphenyltetrazolium bromide) viability test was performed, where 3.5 nM Au13 and 1.3 nM Au25 AuNPs functionalised with RuPhenL1, RuPhenL2 and RuDppzL2 (AuNP.Ru) were used as stock solutions. MTT viability test is a colorimetric assay based on the reduction of a yellow salt (MTT) to purple formazan crystals by metabolic active cells, which means the darker the purple solution is, the greater the number of viable cells. This can be quantified by measuring absorbance at 500-600 nm.[365, 366]

Since the AuNP.Ru conjugates are suspended in MilliQ water, the highest concentration tested, was half of the stock solutions to avoid water toxicity. By analysis of figure 4.10, even at the highest concentration studied, the AuNPs are very weakly toxic (≥ 60% viability for all the AuNPs tested). Au.RuDppzL2 are considered not toxic since the cells viability never dropped below 80%.[367] This could be related with the fact the RuDppzL2 is weakly toxic itself, in comparison with RuPhenL1 and RuPhenL2. It was then determined that a non-toxic concentration where the AuNP.Ru would not cause noticeable damage to the cells, would be 0.9 nM for 13 nm sized Au.RuPhenL1, Au.RuPhenL2 and Au.RuDppzL2 and 0.3 nM for 25 nm sized Au.RuPhenL1, Au.RuPhenL2 and Au.RuDppzL2. Therefore, these concentrations were used for the microscopy experiments, in order to evaluate the uptake of the AuNPs by the A549 cells. Previous studies have shown that similar ruthenium coated AuNPs were not toxic up to 0.9 nM to A549 cells.[194] Therefore, even though Au13.Z.RuPhenL1 seems to be the only that presents toxicity at this concentration, this was not considered statistical significant when compared with the negative control, since p-value > 0.05.

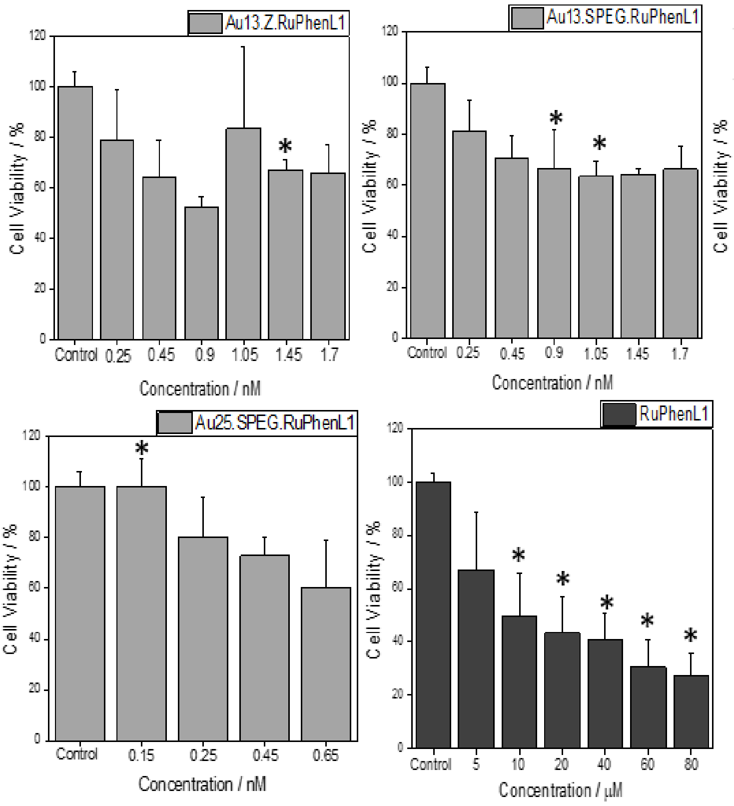

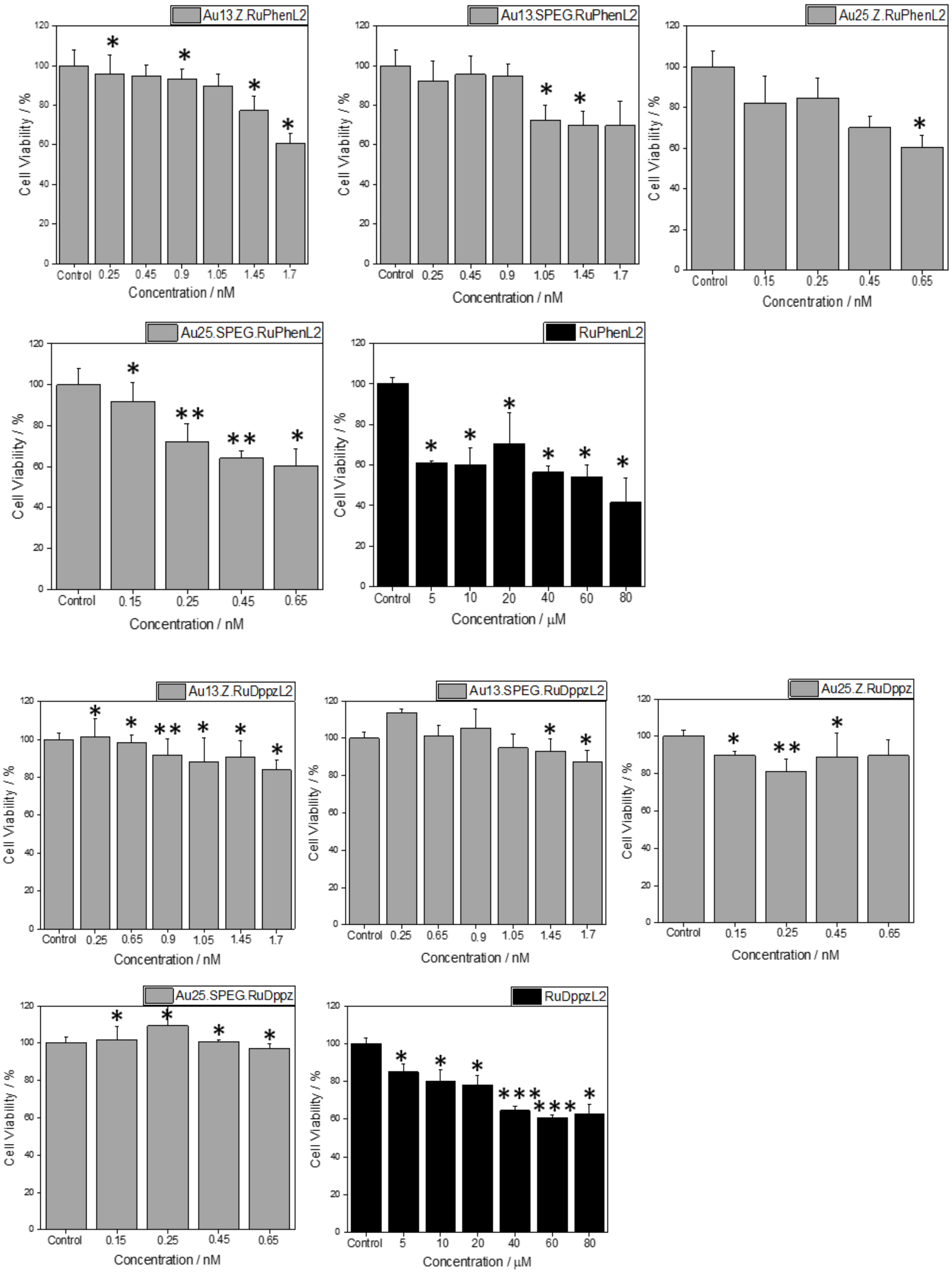

Figure 4.10- Cytotoxicity in A549 cells determined using the MTT cell viability assay of the AuNP.Ru conjugates (grey) and RuPhenL1, RuPhenL2 and RuDppzL2 (black) after treatment for 24 h. Control= untreated A549 cell. P value, obtained from ANOVA analysis followed by a T-Test, is represented by * = $p < 0.05$, **< 0.01, ***< 0.001. When no * is observed $p > 0.05$.

4.3.2 Cellular uptake and subcellular localisation of ruthenium gold nanoparticles in cells

4.3.2.1 Confocal luminescence microscopy of nanoparticles in A549 cells

The cellular uptake efficacy and subcellular localisation in A549 cells was evaluated by live cell imaging, after incubating 0.9 nM of 13 nm sized Au.RuPhenL1, Au.RuPhenL2 and Au.RuDppzL2 and 0.3 nM of Au.RuPhenL1, Au.RuPhenL2 and Au.RuDppzL2. The cells were treated for 2, 4 and 12 h. To determine the ability of the luminescent AuNPs to localize in the nucleus, a commercial dye, Hoechst, was used. The AuNP.Ru visualisation was possible through the red channel that corresponds to the ruthenium signal (λexc = 488 nm, λem= 620−800 nm) and the nucleus of the cells was stained with Hoechst which can be visualise through the blue channel (λexc= 405 nm, λem = 410−455 nm). After 2 h of incubation, the ruthenium signal is detected, indicating that after that short period of time the AuNP.Ru penetrate the cell membrane and localise in the intracellular space (Figure 4.11 and appendices- figure 4.31). Au.SPEG was also analysed using confocal imaging, showing no signal, therefore indicating that the red signal is generated by the ruthenium (II) complexes. Even though the luminescent signal of the ruthenium was detected during live cell imaging in A549 cells, both the luminescence intensity and the co-localisation signal were considerably weak, demonstrating that possibly a longer time is needed for an effective cell internalisation of these AuNPs systems.

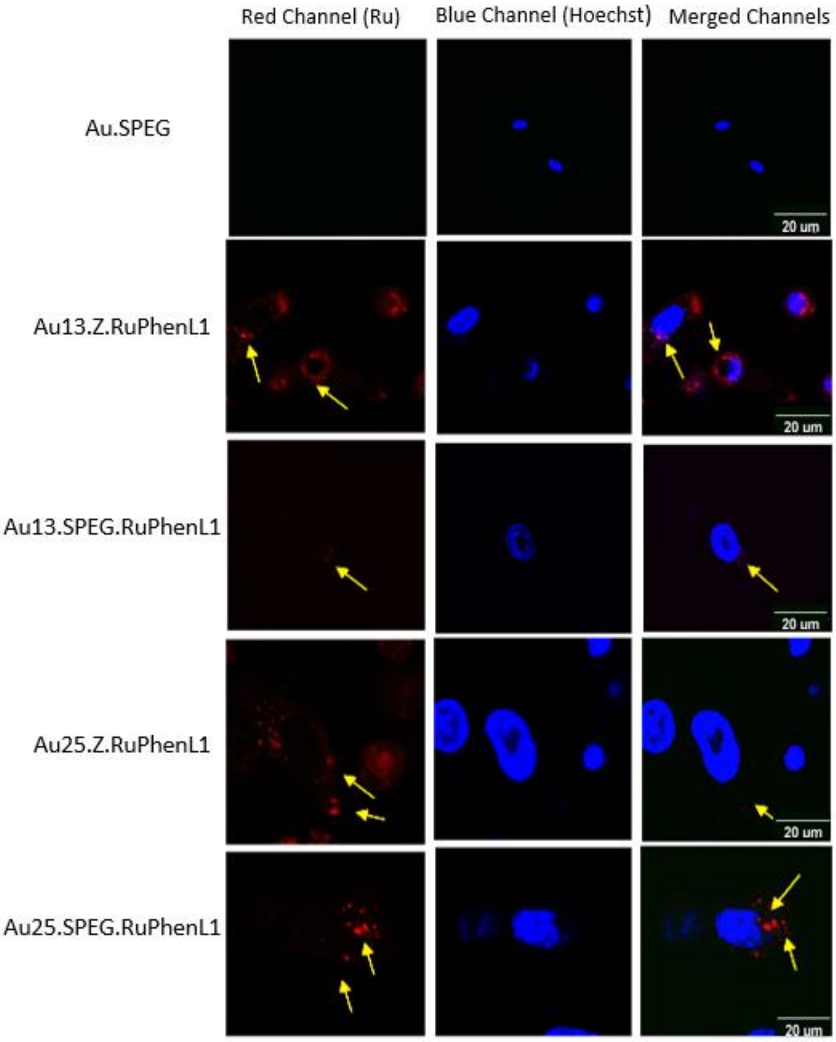

Figure 4.11- Fluorescence confocal microscopy images of A549 cells after treatment with 0.9 nM of Au.SPEG and Au13.RuPhenL1 and 0.3 nM of Au25.Z.RuPhenL1 and Au25.SPEG.RuPhenL1, for 2 h. Red channel (λexc = 488 nm, λem 620−800 nm) and blue channel (λexc= 405 nm, λem = 410−455 nm). Yellow arrow indicating the AuNP.Ru signal. (Scale bar = 20 μM).

A549 cells were also treated with AuNP.Ru conjugates for 4 h, which after that time, it was possible to detect a stronger ruthenium signal inside the cells, indicating a possible higher cellular uptake (Figure 4.12). The ruthenium (II) complexes signal on the AuNPs was found to overlap with the Hoechst dye that represents the nucleus of the cells. After 4 h, Au.RuPhenL1 and Au.RuPhenL2 can be found very close to the A549 cell nucleus, with no apparent influence of the surfactant (Zonyl FSA or SPEG) on the uptake (Figure 4.12).

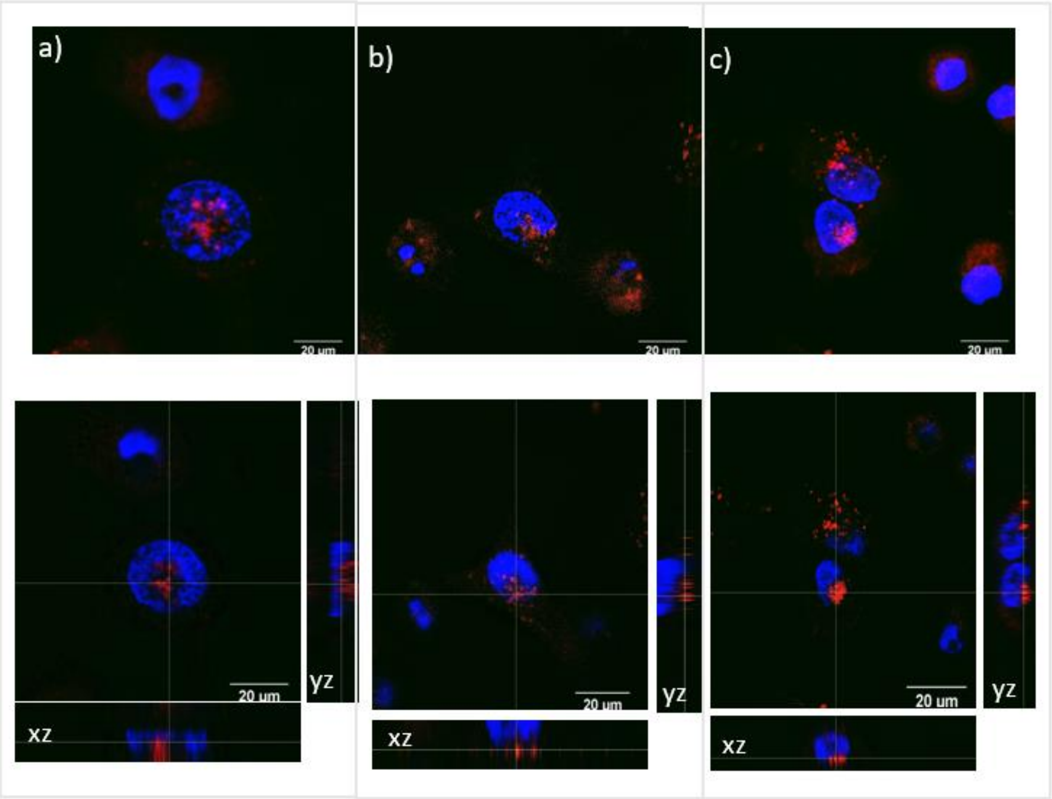

Figure 4.12- Cumulative Z projections (above) and cross sections (below) of Z-stacking images from confocal microscope of A549 cells after treatment for 4 h with 0.9 nM of a) Au13.SPEG.RuPhenL1, b) Au13.Z.RuPhenL1 and c) Au13.Z.RuPhenL2. Red channel (λ_{exc} = 488 nm, λ_{em} 620–800 nm) and blue channel (λ_{exc}= 405 nm, λ_{em} = 410–455 nm). (Scale bar = 20 µM).

After 12 h, both Au.Z.RuDppzL2 and Au.SPEG.RuDppzL2 were found to be localised in cytoplasm and nucleus of the cells. Similar behaviour was found for AuNPs coated with RuPhenL1 and RuPhenL2 (Figures 4.13-4.18 and appendices 4.32-4.34). Even though, the ruthenium signal on the AuNPs was detectable in live A549 cells, after 2 and 4 h of treatment, the luminescence signal was more pronounced after 12 h, suggesting that the cellular uptake is time dependent. The strong ruthenium signal observed within the intracellular environment during live cell imaging, after 12 h of treatment, confirms that the photostability of the ruthenium (II) complexes is not compromised upon attachment to the AuNPs. The use of AuNPs as a vehicle to deliver targeting complexes in cancer cells has been previously reported to improve the bioavailability of the complexes inside the cells.[368] However, most of the published studies of ruthenium (II) complexes with or without gold nanoparticles, does not show nuclear internalisation without a nuclear targeting peptide.[45, 369]

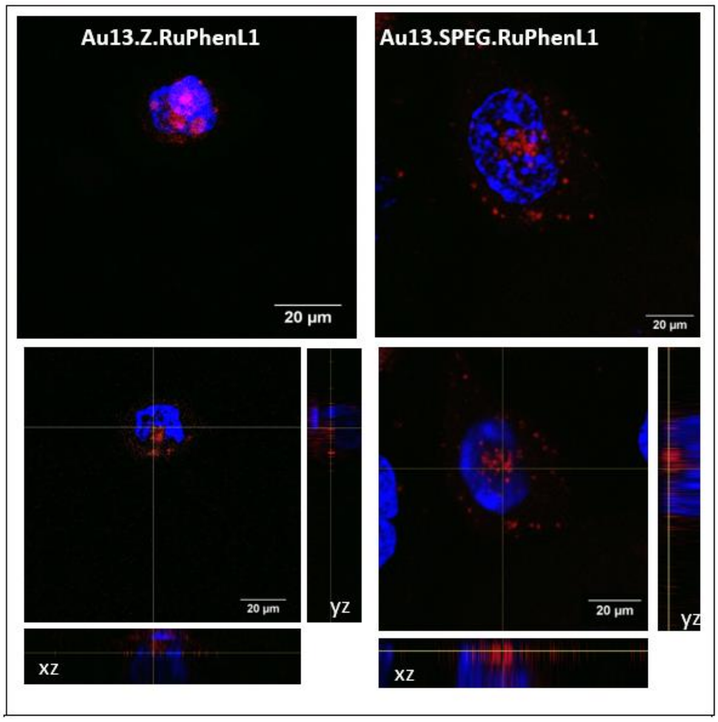

Figure 4.13- Cumulative Z projections (above) and cross sections (below) of Z-stacking images from confocal microscope of A549 cells after treatment for 12 h with 0.9 nM of Au13.Z.RuPhenL1 and Au13.SPEG.RuPhenL1. Red channel (λexc = 488 nm, λem 620−800 nm) and blue channel (λexc= 405 nm, λem = 410−455 nm). Scale bar = 20 µM.

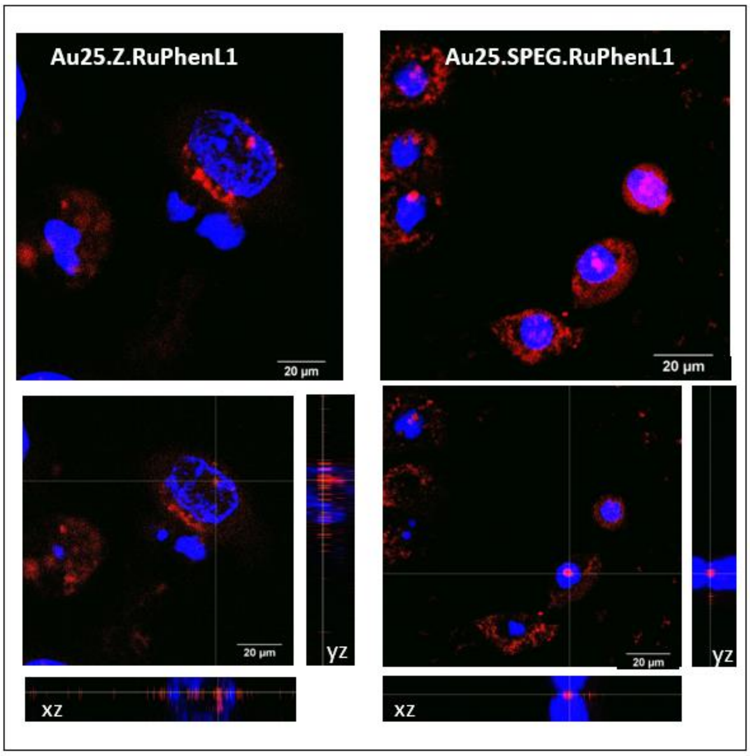

Figure 4.14. Cumulative Z projections (above) and cross sections (below) of Z-stacking images from confocal microscope of A549 cells after treatment for 12 h with 0.3 nM of Au25.Z.RuPhenL1 and Au25.SPEG.RuPhenL1. Red channel (λexc = 488 nm, λem 620−800 nm) and blue channel (λexc= 405 nm, λem = 410−455 nm). Scale bar = 20 µM.

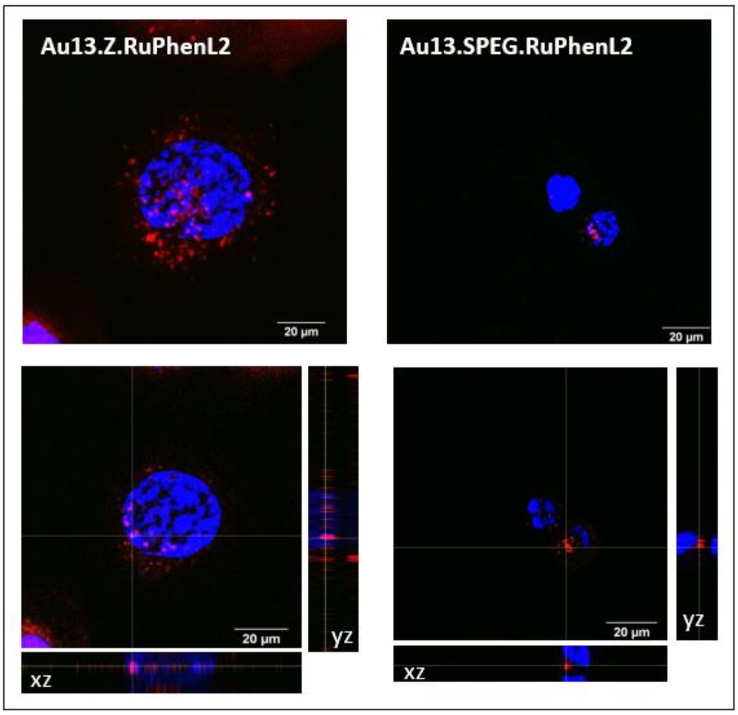

Figure 4.15- Cumulative Z projections (above) and cross sections (below) of Z-stacking images from confocal microscope of A549 cells after treatment for 12 h with 0.9 nM of Au13.Z.RuPhenL2

and Au13.SPEG.RuPhenL2. Red channel (λexc = 488 nm, λem 620−800 nm) and blue channel (λexc= 405 nm, λem = 410−455 nm). Scale bar = 20 µM.

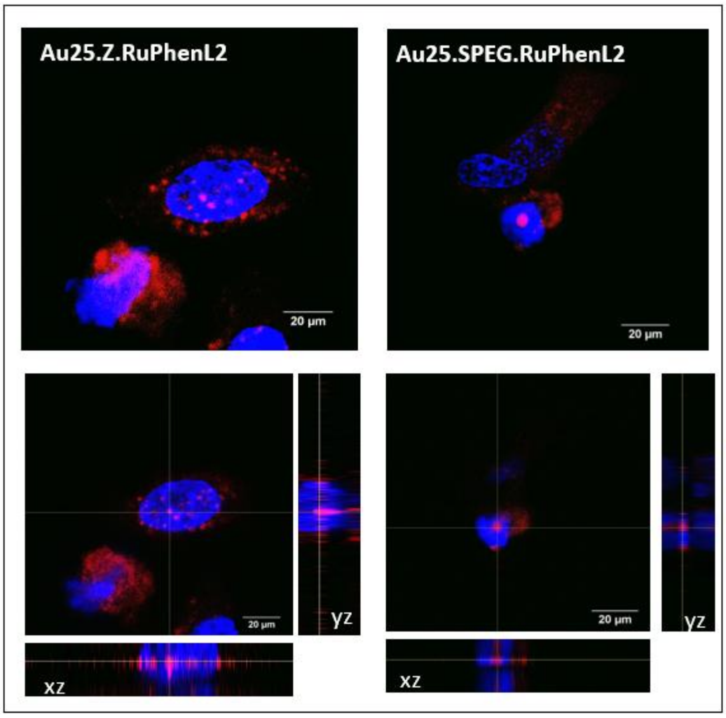

Figure 4.16- Cumulative Z projections (above) and cross sections (below) of Z-stacking images from confocal microscope of A549 cells after treatment for 12 h with 0.3 nM of Au25.Z.RuPhenL2 and Au25.SPEG.RuPhenL2. Red channel (λexc = 488 nm, λem 620−800 nm) and blue channel (λexc= 405 nm, λem = 410−455 nm). Scale bar = 20 µM.

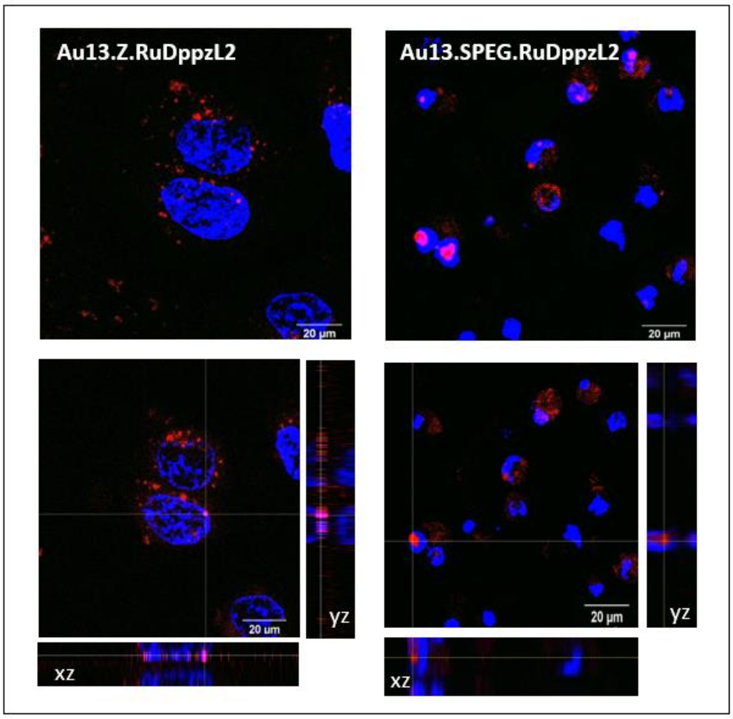

Figure 4.17- Cumulative Z projections (above) and cross sections (below) of Z-stacking images from confocal microscope of A549 cells after treatment for 12 h with 0.9 nM of Au13.Z.RuDppzL2 and Au13.SPEG.RuDppzL2. Red channel (λexc = 488 nm, λem 620−800 nm) and blue channel (λexc= 405 nm, λem = 410−455 nm). Scale bar = 20 µM.

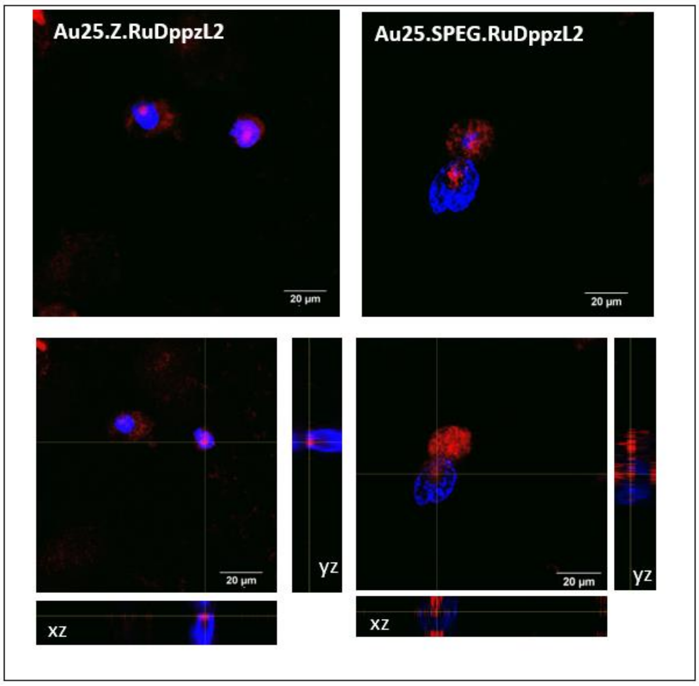

Figure 4.18- Cumulative Z projections (above) and cross sections (below) of Z-stacking images from confocal microscope of A549 cells after treatment for 12 h with 0.3 nM of Au25.Z.RuDppzL2 and Au25.SPEG.RuDppzL2. Red channel (λexc = 488 nm, λem 620−800 nm) and blue channel (λexc= 405 nm, λem = 410−455 nm). Scale bar = 20 µM.

4.3.2.2 Transmission electron microscopy of nanoparticles in A549 cells

The cellular uptake and subcellular localisation of the AuNP.Ru conjugates in A549 cells was further evaluated by TEM. Similarly, to confocal microscopy studies, the cells were treated with 0.9 nM of 13 nm sized Au13.RuPhenL1, Au13.RuPhenL2 and Au13.RuDppzL2 and 0.3 nM of 25 nm sized Au25.RuPhenL1, Au25.RuPhenL2 and Au25.RuDppzL2, for 4 and 12 h.

TEM studies revealed the presence of AuNPs inside A549 cells. There is evidence of AuNPs trapped within endosomal vesicles, which is a characteristic of the endocytic uptake mechanism, a common uptake of nanoparticles by the cells (Figure 4.19-A to D).[370] After 12 h, organelles such as lysosomes, autophagic vacuoles and lamella bodies are found in the cells (Figure 4.19-E to H). After being trapped in endosomes, the AuNPs have different possible pathways, such as degradation pathway via lysosomes, or recycling pathway which usually lies in the membrane of the cell or Golgi co-localisation.[371] No evidence of the AuNPs on the Golgi apparatus is observed. Moreover, in previous studies by the group, ruthenium coated AuNPs were found to be trafficked to the lysosomes by the endo-lysosomal pathway.[194] Lysosomes is usually the point before degradation starts by autophagy. This can be confirmed by the presence of the AuNPs in autophagic vacuoles and lamella bodies. Lamella bodies in A549 cells are organelles involved in storage and secretion of lung surfactant which are capable of binding to lysosomes. Although the presence of AuNPs in autophagosomes, means degradation, these AuNPs do not seem to be degraded. In fact, the autophagosomal vesicle membrane seems to break and the AuNPs are released into the cytoplasm (Figure 4.19-E to H).

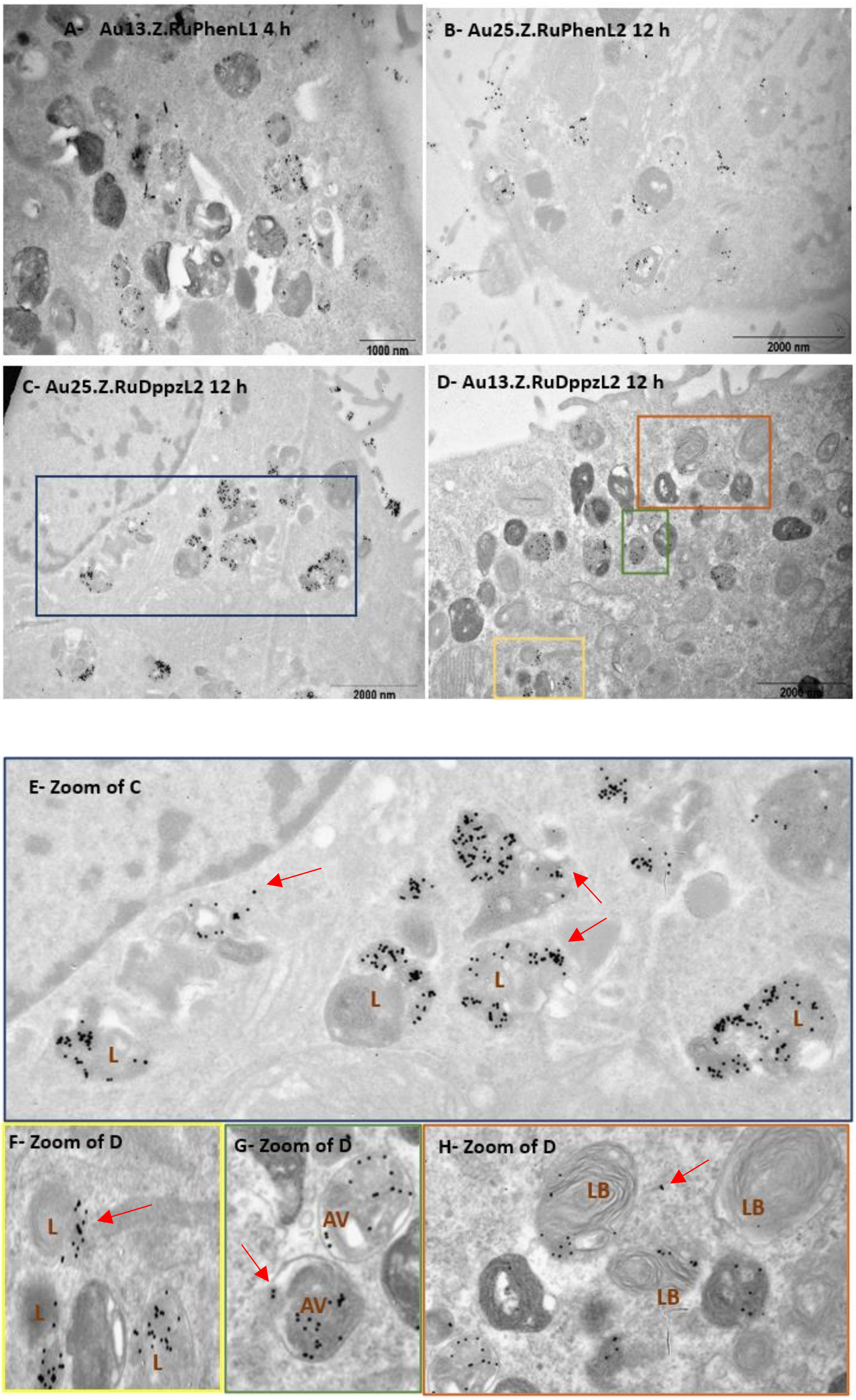

Figure 4.19- TEM images of A549 cells after treatment after 4 and 12 h with 0.9 nM for Au13 or 0.3 nM for Au25 of AuNPs coated with RuPhenL1, RuPhenL2 or RuDppzL2. L= lysosomes, AV= autophagic vacuoles, LB= Lamella bodies.(scale bar= 1000 and 2000 nm). AuNPs escaping vesicles represented by red arrows.

TEM imaging also allowed the visualisation of AuNP.Ru reaching the nucleus of some cells. After 4 h, Au25.Z.RuDppzL2 was found to go through the nuclear membrane and accumulate inside the nucleus. Figure 4.20 shows that these AuNP25.Z.RuDppzL2 freely navigate through the cytoplasm and reach the nucleus. Evidence of AuNP.Ru reaching the nucleus of the cells after 4 h can also be found for Au13.SPEG.RuPhenL2, Au25.Z.RuPhenL2 and Au25.SPEG.RuPhenL1 (Figures 4.21 and 4.22). These results show that not only the AuNPs can reach the nucleus of the A549 cells, but also that after a short period of time of 4 h, there is clearly evidence that both sizes 13 and 25 nm AuNP.Ru are able to go through the nuclear membrane. Therefore, for the best of our knowledge, this is the first time that 13 nm and 25 nm AuNP.Ru are visualised entering the nucleus of mammalian cells by TEM. Contrarily to what has been published on the literature, where only nanoparticles of 9 nm or below were able to go through the nuclear pore complex (NPC), these ruthenium coated AuNPs do seem to go through the nuclear membrane without a size restriction.[372] The transport in and out of particles in the nucleus is very different from the cell membrane. The nucleus envelope consists of two membranes that are penetrated by these large structures called nucleus pore complexes. Due to their size, small molecules/particles (9 nm or below) can easily penetrate and passively diffuse through the NPC. When bigger particles get into the nucleus, this is only possible through active transport, where the NPC dilates to allow the transport of particles up to 39 nm in diameter.[373] Due to a signal mediated passage, NPC can allow bigger particles/molecules to get into the nucleus, when these particles bind to signal receptors. There are two types of signals: nuclear signalization signal (NLS) and nuclear retention signal (NRS), in which particles/molecules would pass through the

NPC by binding to NLS receptors and accumulate in the nucleus due to the NRS.[374] However, the AuNP.Ru in study do not contain any NLS moiety and therefore that cannot be the mechanism of uptake into the nucleus. There are a few studies that show proteins without a NLS moiety are able to internalise and accumulate in the nucleus of cells.[375, 376] These proteins would not be able to interact with the NLS receptors in the NPC but they seem to interact with other proteins that contain a functional NLS and therefore go through the nucleus pore complex. This seems to be the most likely explanation for the 13 nm and 25 nm ruthenium coated AuNPs being able to go through the NPC and reach the cell nucleus.

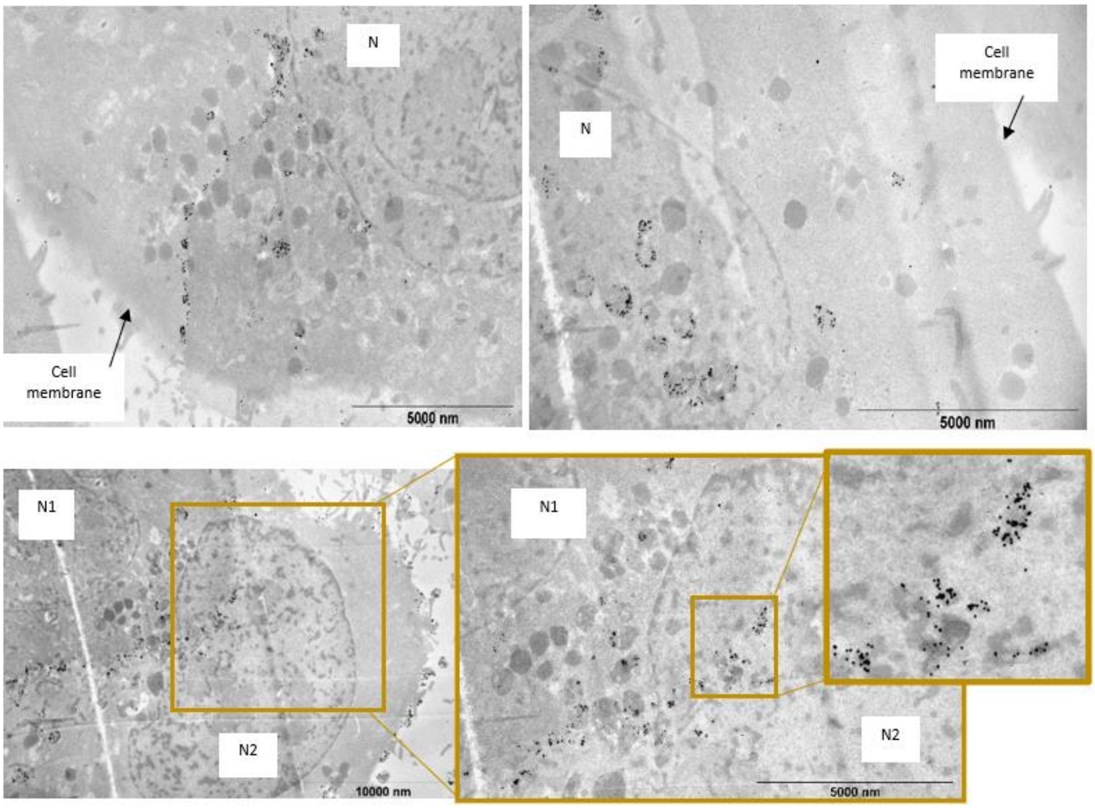

Figure 4.20- TEM images of three different A549 cells after treatment with 0.3 nM Au25.Z.RuDppzL2 for 4 h.N1- nucleus one, N2- nucleus two.(scale bar= 5000 and 10000 nm).

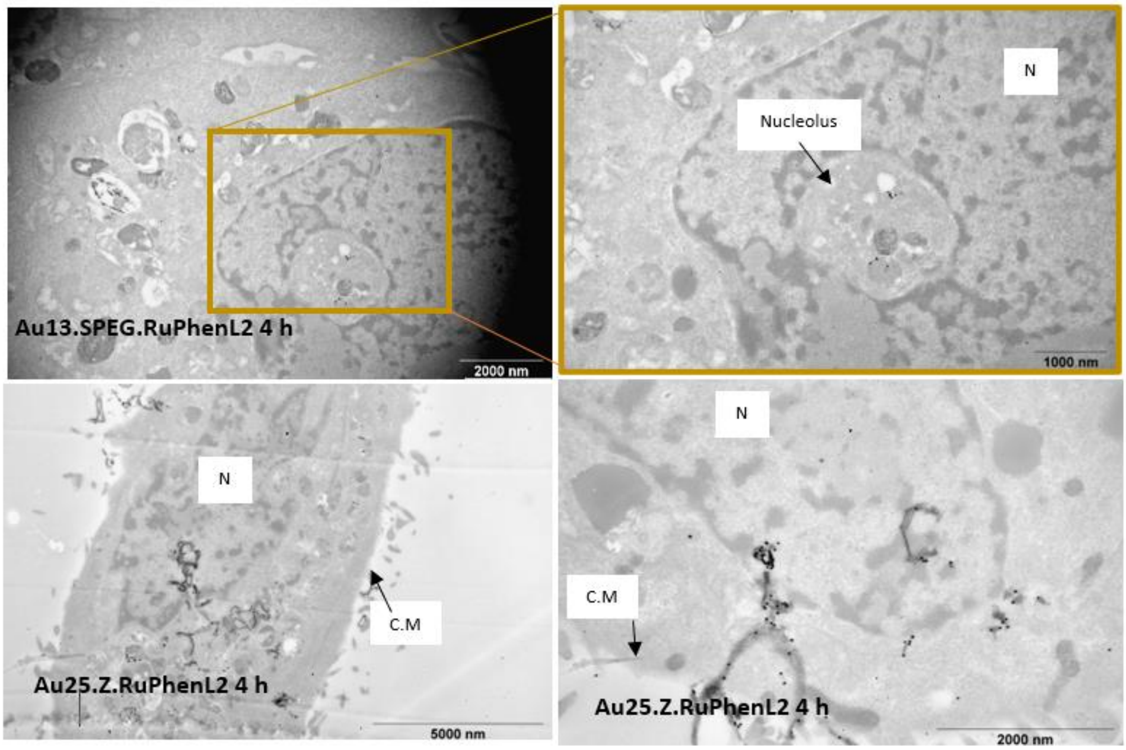

Figure 4.21- TEM images of three different A549 cells after treatment with 0.9 nM of Au13.SPEG.RuPhenL2 and 0.3 nM of Au25.Z.RuPhenL2 and Au25.Z.RuPhenL2 for 4 hours. C.M- cell membrane, N-Nucleus. (scale bar= 2000, 1000 and 5000 nm)

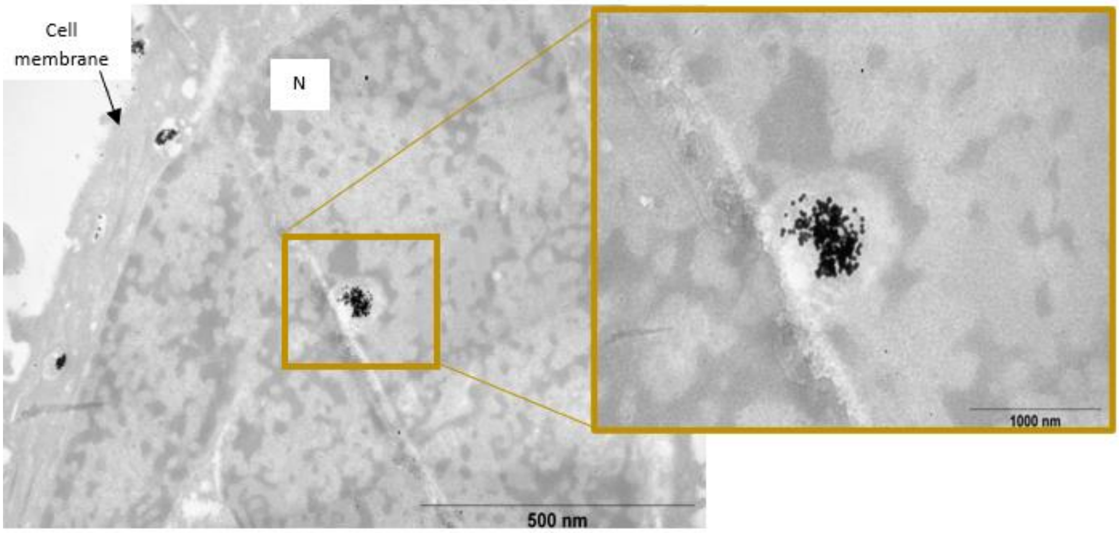

Figure 4.22- TEM images of A549 cell after treatment with 0.3 nM of Au25.SPEG.RuPhenL1 for 4 h. N-nucleus. (scale bar= 500 and 1000 nm).

After 12 h of cell treatment with the AuNP.Ru conjugates, TEM images showed their accumulation in both cytoplasm and nucleus of the cells. Au13.SPEG.RuDppzL2, Au25.SPEG.RuDppzL2 and Au25.SPEG.RuPhenL1 showed clear evidence of being internalised in the nucleus of A549 cells (Figures 4.23 to 4.25). Overall, for both time points studied (4 and 12 h) it was possible to observe evidence of nucleus internalisation by TEM for all the AuNP.Ru conjugates in A549 cells.

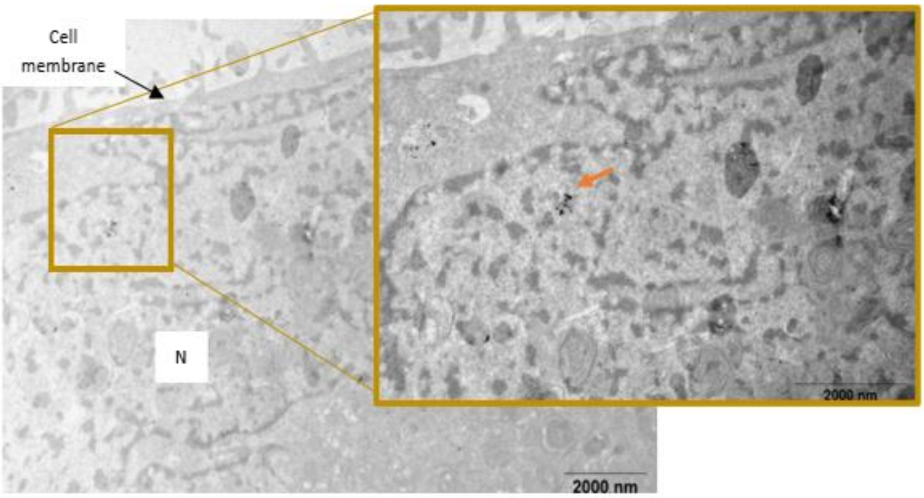

Figure 4.23- TEM images of A549 cell after treatment with 0.9 nM of Au13.SPEG.RuDppzL2 for 12 hours. N-nucleus. (scale bar= 2000 nm).

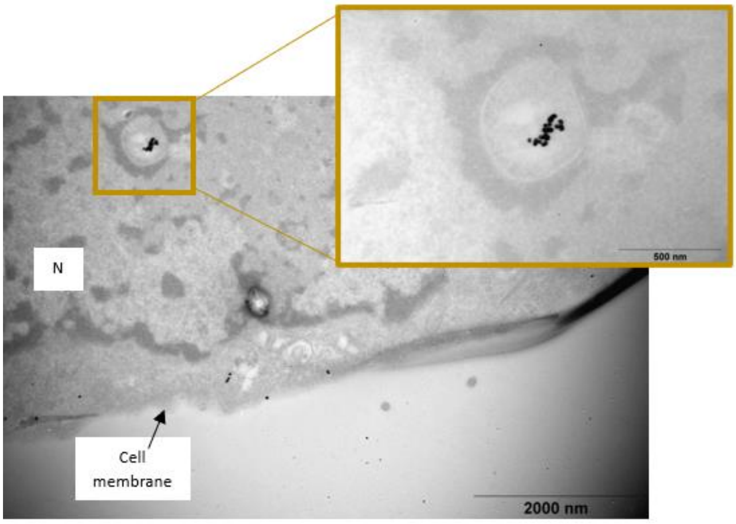

Figure 4.24- TEM images of A549 cell after treatment with 0.3 nM of Au25.SPEG.RuDppzL2 for 12 h. N-nucleus. (scale bar= 2000 nm).

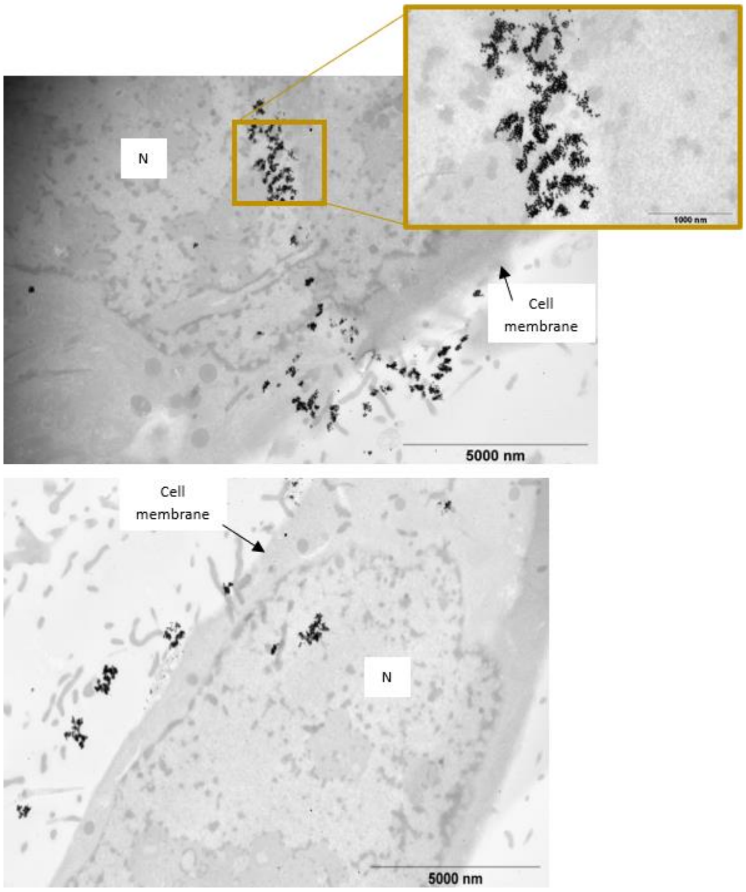

Figure 4.25- TEM images of two different A549 cells after treatment with Au25.SPEG.RuPhenL1 for 12 h. N-nucleus. (scale bar= 5000 nm).

4.3.2.3 Quantification of AuNPs uptake by A549 cells by ICP-MS

Understanding how many AuNPs can be internalised by the cells in a specific period of time, can give important information for a range of medical and biological applications, such as the maximum drug delivery capability or even maximum quantity to allow imaging. ICP-MS is considered a highly sensitive elemental analysis technique for determining the unique mass of metals thus, this technique was carried out to quantify the uptake of the AuNPs by A549 cells. In order to understand how many AuNPs are inside the cells, the cells were treated with 0.9 for 13 nm AuNPs or 0.3 for 25 nm AuNPs nM for 12 h. It is important to note that these are preliminary results since only one biological sample was performed. To be able to test the accuracy and statistical significance, more than one biological replica will be needed.

Through ICP-MS analysis of whole cell lysates it was determined that the number of AuNPs per cell was lower for AuNP.Ru of 13 nm size (average 2500 AuNPs per cell) than AuNP.Ru of 25 nm (average 4600 AuNPs per cell), indicating that 25 nm size AuNPs have a better size for uptake (Figure 4.26). It has been previously reported that the optimal radius size of gold nanoparticles to be uptake by endocytosis is between 25 and 30 nm.[377] However, the size of the AuNPs does not seem to affect the uptake when the AuNPs are coated with RuDppzL2. Au13.Z.RuDppzL2 and Au25.Z.RuDppzL2 had the highest uptake inside the cells (5400 AuNPs per cell). Au25.Z.RuPhenL1 had the second highest uptake (5200 AuNPs per cell), followed by Au25.Z.RuPhenL1, Au25.SPEG.RuPhenL1 with 4300 AuNPs per cell and Au25.SPEG.RuDppzL2 (4000 AuNPs per cell). The fact that AuNPs coated with RuDppzL2 had a considerably higher uptake could be due a higher lipophilicity. Previous studies have showed that increasing the aromatic rings on the ligands of the metal complexes, increased the lipophilicity which facilitated the uptake by the cells.[31, 378-380] Comparing the coating of the two surfactants on AuNPs, Zonyl FSA and SPEG, Au13.Z.RuDppzL2, Au25.Z.RuDppzL2 and Au25.Z.RuPhenL2 had a 46 %, 33 % and 55 %, respectively, increase of uptake than their AuNPs parents coated with SPEG. SPEG is a hydrophilic surfactant[381], whereas Zonyl FSA is lipophilic and hydrophobic, which helps on increasing the lipophilicity and enhances the uptake of the AuNPs by the cells.[194]

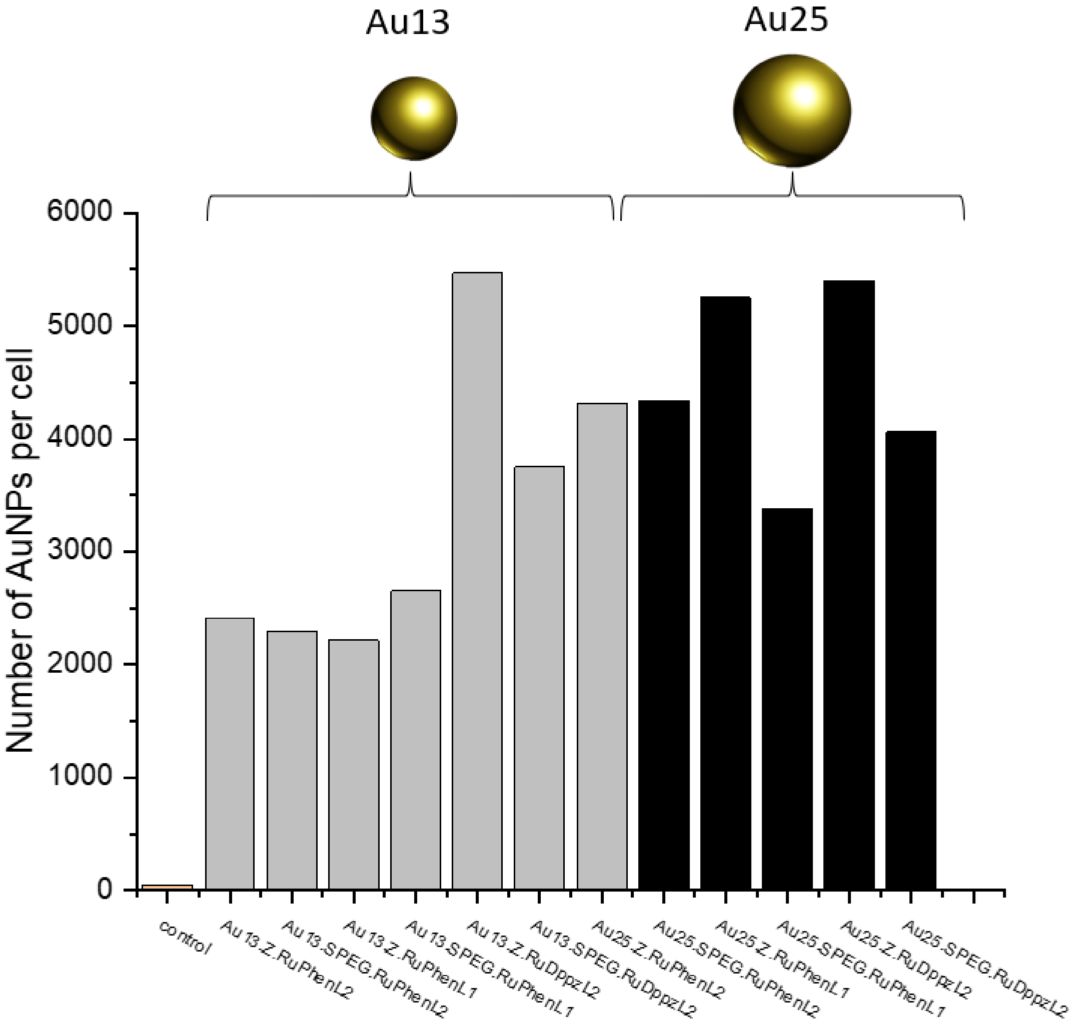

Figure 4.26- ICP-MS of lysates A549 cells for the quantification of gold inside the cells. The cells were incubated with 0.9 nM Au13 and 0.3 nM Au25 particles and incubated for 12 h, prior the analysis. N = 1. Control= untreated A549 cells.

4.3.3 Phototoxicity of AuNPs in A549 cells

Ruthenium (II) complexes are known for their remarkable properties as photosensitisers and therefore have been extensively explored in PDT research. AuNPs, besides being promising nano carriers, have also showed their efficacy in ROS production and PDT enhancement. Therefore, studying the potential phototoxicity of the AuNP.Ru conjugates was of great interest in this research. Additionally, the high affinity with DNA found for AuNP.Ru (see Chapter 3 for further details), could allow an efficient oxidation of the genetic material and thus enhance PDT effect. Therefore, the toxicity of Au.Z.RuPhenL1, Au.Z.RuPhenL2 and Au.Z.RuDppzL2 in the dark and upon visible light irradiation was studied. Conjugating ruthenium (II) complexes with AuNPs, allows a PDT treatment with a higher wavelength light than what is usually used for ruthenium (II) complexes, since AuNPs λ_{max} is 518 nm for Au13 and 520 nm for Au25. Higher wavelengths irradiation is always advantageous in PDT, since it allows a deeper penetration of the light in human tissues. However, a higher wavelength setup was not available and thus, an attempt to simulate a cell irradiation setup was carried out with a commercially available GSW IP65 green lamp (λmax= 535 nm) (Figure 4.27). It is known that the distance between the light source and the cells is extremely important on phototoxicity.[382, 383] If the distance is too big, the light might not have an effect, but if the distance is too small it might affect the viability of the cells. Since the green lamp used has never been tested for this type of experiment before, a control experiment was carried out with two different distances (10 mm and 20 mm) between the lamp and the irradiated plate. By comparing the cell viability of A549 cells in a 96 well plate left in the dark with a 96 well plate of A549 cells irradiated, it become clear that a 10 mm distance influenced the cell viability (Appendices- figure 4.34). However, when the distance between lamp and cell plate was increased to 20 mm, there was no significant effect observed from the lamp, on the cell's viability (Figure 4.28).

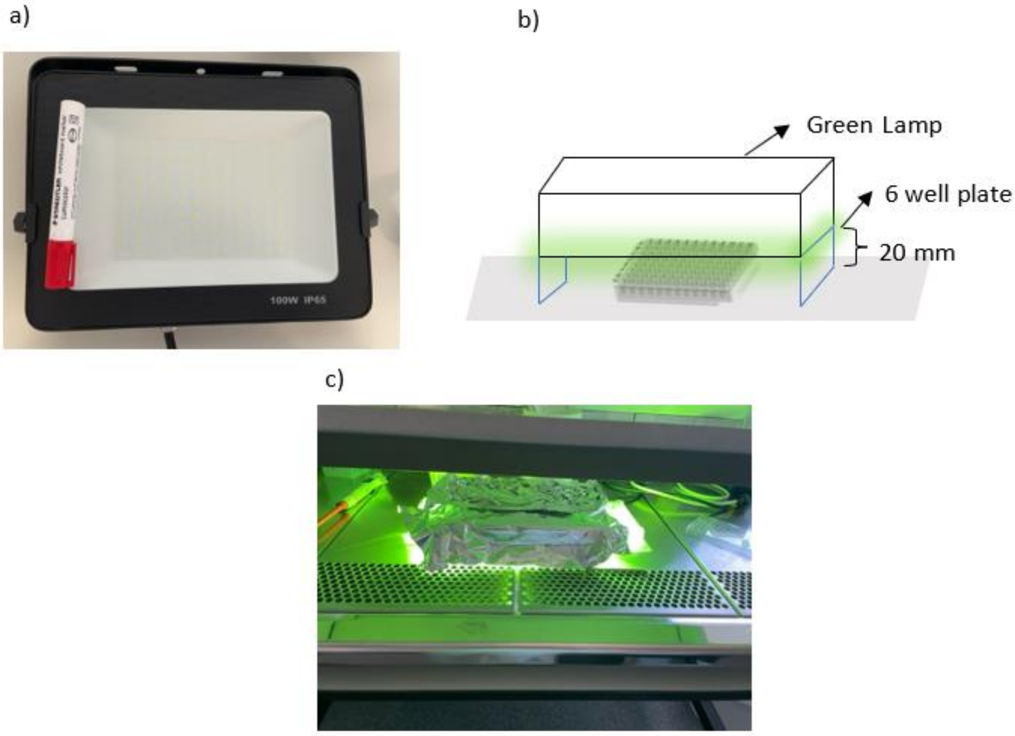

Figure 4.27- (a) Green lamp used for phototoxicity experiments, (b) Graphic illustration of irradiation set-up. Lamp was supported by two 6 well plates in each side, giving a distance between lamp and plate of 20 mm, (c) top view photograph of the irradiation set-up.

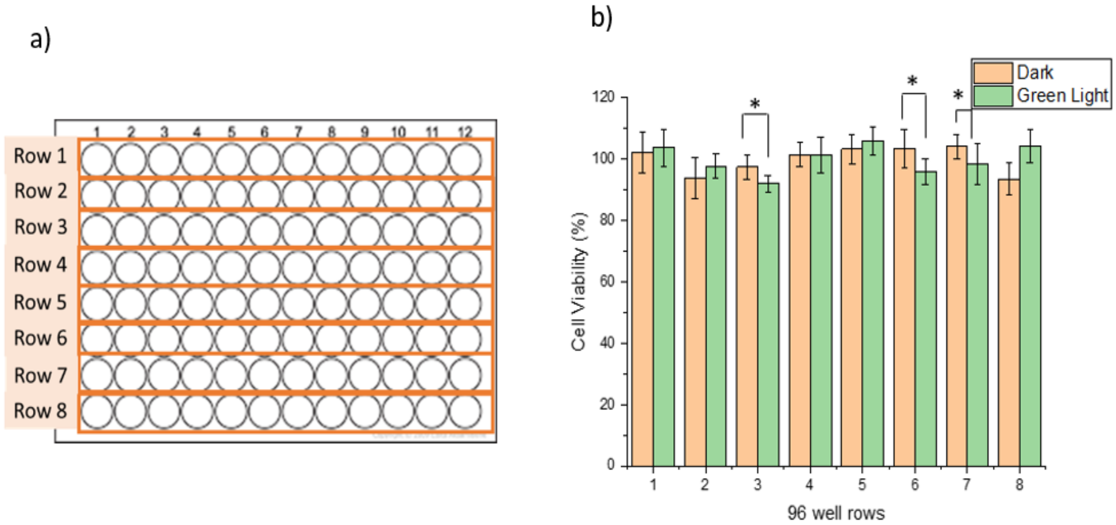

Figure 4.28- a) Representation of a 96 well plate of negative controls (A549 cells) with the indication of the rows used to compare the viability between dark and irradiated plate. (b) Phototoxicity by MTT assay of negative control (A549 cells) in a 96 well plate. Each number on the x axis corresponds to each row of the plate, in both dark and irradiated plates. P value, obtained by a T-Test, is represented by *< 0.05.

Since the green lamp did not influence the cell viability, the set-up described was used for the phototoxicity experiment with the AuNPs samples. The graphs on Figure 4.29 showed the cell viability through MTT assays between dark and irradiated cells, after treatment for 24 h with AuNPs citrate (Au13 and Au25), and functionalised with Zonyl FSA (Au13Z, Au25.Z) and AuNP with the ruthenium (II) complexes RuPhenL2, RuDppzL2 and RuPhenL1 (Au13.Z.RuPhenL2, Au25.Z.RuPhenL2, Au13.Z.RuDppzL2, Au25.Z.RuDppzL2, Au13.Z.RuPhenL1 and Au25.Z.RuPhenL1).

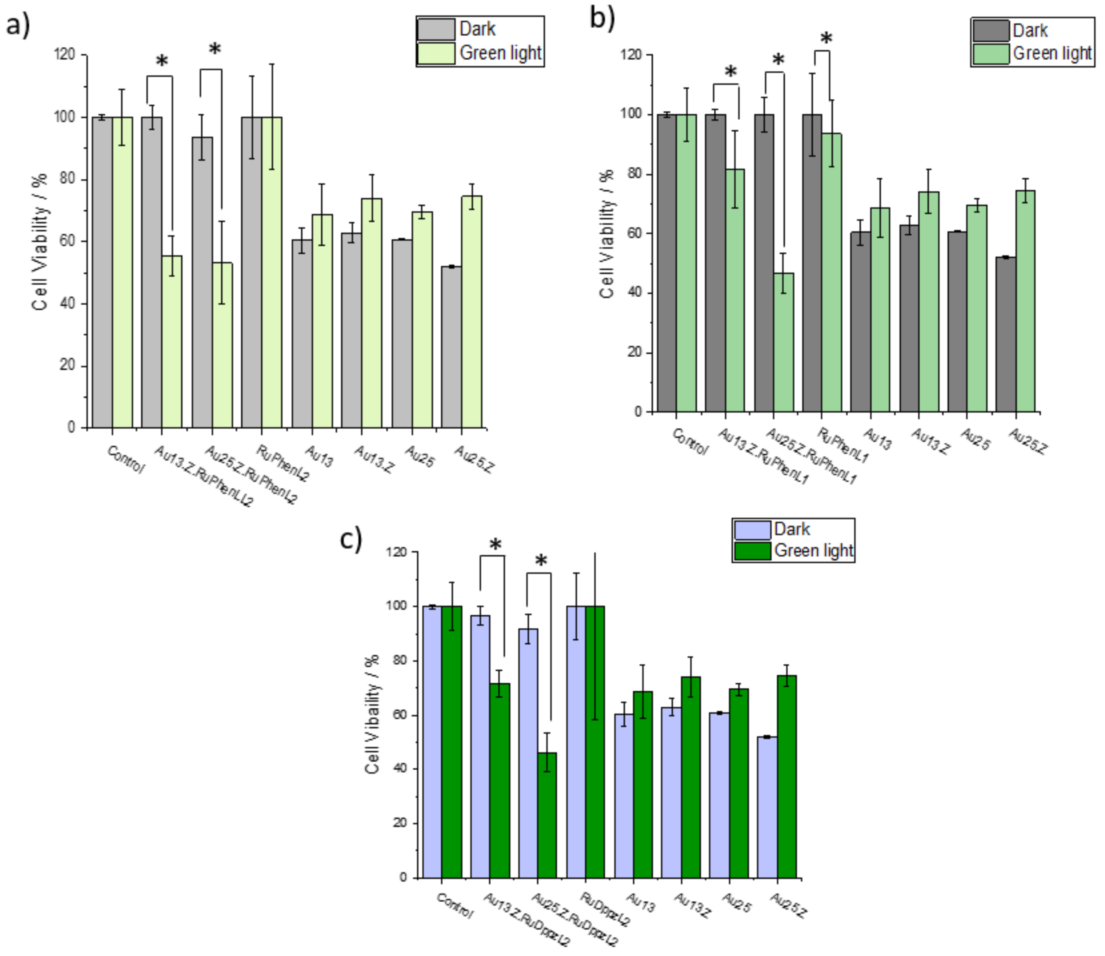

Figure 4.29- Phototoxicity of A549 cells by MTT assay after treatment for 24 h with 0.9 nM of Au13, Au13.Z, Au13.RuPhenL1, Au13.RuPhenL2, Au13.RuDppzL2 and 0.3 nM of Au25, Au25.Z and Au25.RuPhenL1, Au25.RuPhenL2, Au25.RuDppzL2 (a) Comparison between RuPhenL2 and AuNP.RuPhenL2, (b) Comparison between RuDppzL2 and AuNP.RuDppzL2, (c) Comparison between RuPhenL1 and AuNP.RuPhenL1. Control= untreated A549 cells. To simplify the analysis, the samples with viability > 100%, were settled as 100%. P value, obtained by a T-Test, is represented by *< 0.05.

As observed, all the AuNP.Ru conjugates show no toxicity in the dark for A549 cells after 24 h treatment at the concentrations tested. However, upon green light irradiation, the cell viability significantly dropped, demonstrating the effectiveness of AuNP.Ru as photosensitisers. The cell viability after irradiation of Au.RuPhenL2 is 55 % and 53 % for 13 nm and 25 nm AuNPs, respectively, revealing that for phototoxicity there is no significant difference on AuNPs sizes in these samples. However, Au.RuDppzL2 and Au.RuPhenL1 showed significant differences on phototoxicity between Au13 and Au25. Au13.RuDppzL2 had 72 % of cell viability and 46 % for Au25.RuDppzL2. Au13.RuPhenL1 revealed 82 % of cell viability and 47 % for Au25.RuPhenL1. The fact that a bigger size AuNPs had a higher efficacy on cell death, can be explained by the fact that these AuNPs have a higher cell uptake and therefore, the phototoxicity effect is higher.

Observing the graphs on figure 4.29, it is also possible to study the cell viability of the ruthenium (II) complexes, RuPhenL1, RuPhenL2 and RuDppzL2. The concentration of complexes used was of 0.3 µM, due to being the maximum concentration of ruthenium (II) complexes attached to the AuNPs. At this concentration, none of the complexes has a phototoxic effect for A549 after 24 h, revealing that the ruthenium (II) complexes need to be attached to the AuNPs to generate cell death. Moreover, citrate AuNPs (Au13 and Au25) and Zonyl FSA functionalised AuNPs (Au13.Z and Au25.Z) were also studied as controls for phototoxicity with the green light. No significant difference is observed between dark and light showing that AuNPs without ruthenium do not have a light effect. However, the samples Au13, Au25, Au13.Z and Au25.Z and are significantly more toxic than AuNP.Ru conjugates at the concentrations tested. This could be due to the ruthenium (II) complexes be able to shield the AuNPs and prevent any intrinsic toxicity. However, it is important to mention that these are only preliminary results since this experiment has only been done once and therefore further repeats are needed. Nevertheless, it is important to note that to generate a phototoxic system, both ruthenium (II) complexes and AuNPs are required, leading to an enhancement of ruthenium (II) complexes' phototoxicity by the AuNPs in A549 cells.

4.4 Conclusions

In this chapter the uptake and localisation of Au.RuPhenL1, Au.RuPhenL2 and Au.RuDppzL2 conjugates were studied, after 2, 4 and 12 h of treatment in A549 cells. By fluorescence confocal microscopy, although very weak, it was possible to detect the AuNP.Ru signal only after 2 h of incubation. However, after 4 h, this signal was significant higher, demonstrating an increase of uptake overtime. Both fluorescence confocal microscopy and TEM showed a successful internalisation by Au.RuPhenL1, Au.RuPhenL2 and RuDppzL2 in the cells with accumulation in the cytoplasm and the nucleus of the cells. Although the AuNP.Ru conjugates do not exhibit any nucleus receptor signals, a clear nucleus internalisation is observed after 4 and 12 h of incubation for AuNPs of 13 and 25 nm sizes. By TEM, endosomal vesicle, autophagic vacuoles and lamella bodies were also observed after 12 h, which is a characteristic of the endocytic uptake mechanism followed by a lysosomal degradation pathway. However, in most of the TEM images where nucleus internalisation is observed, these organelles are not observed, suggesting that the AuNP.Ru can internalise in the cells by different mechanisms. Furthermore, it was shown that the uptake is size dependent, where AuNP.Ru of 25 nm had a higher uptake than 13 nm, except for Au.Z.RuDppzL2 that had the highest uptake in 13 nm and 25 nm nanoparticles. With the aim of using AuNP.Ru conjugates as a theranostics systems, the phototoxicity was also studied using a green visible light (λmax= 535 nm). All the cells were treated with Au.Z.RuPhenL1, Au.Z.RuPhenL2 and Au.Z.RuDppzL2, in the nanomolar range and revealed no toxicity in the dark for A549 cells. However, after irradiation there was a significant drop to half of the cell viability. This difference between dark and light was not visible on AuNPs without a ruthenium (II) complex attached, nor for the ruthenium (II) complexes alone, on the concentrations tested, showing that the attachment of ruthenium (II) complexes on AuNPs surface is required for a phototoxicity effect. Au25.Z.RuDppzL2 and Au25.Z.RuPhenL1 showed the biggest drop on cell viability after light irradiation, showing more than 50 % of cell death. Although preliminary, these are very promising results for a theranostics system using these AuNP.Ru conjugates for cell imaging and treatment with visible light.

4.7 Appendices

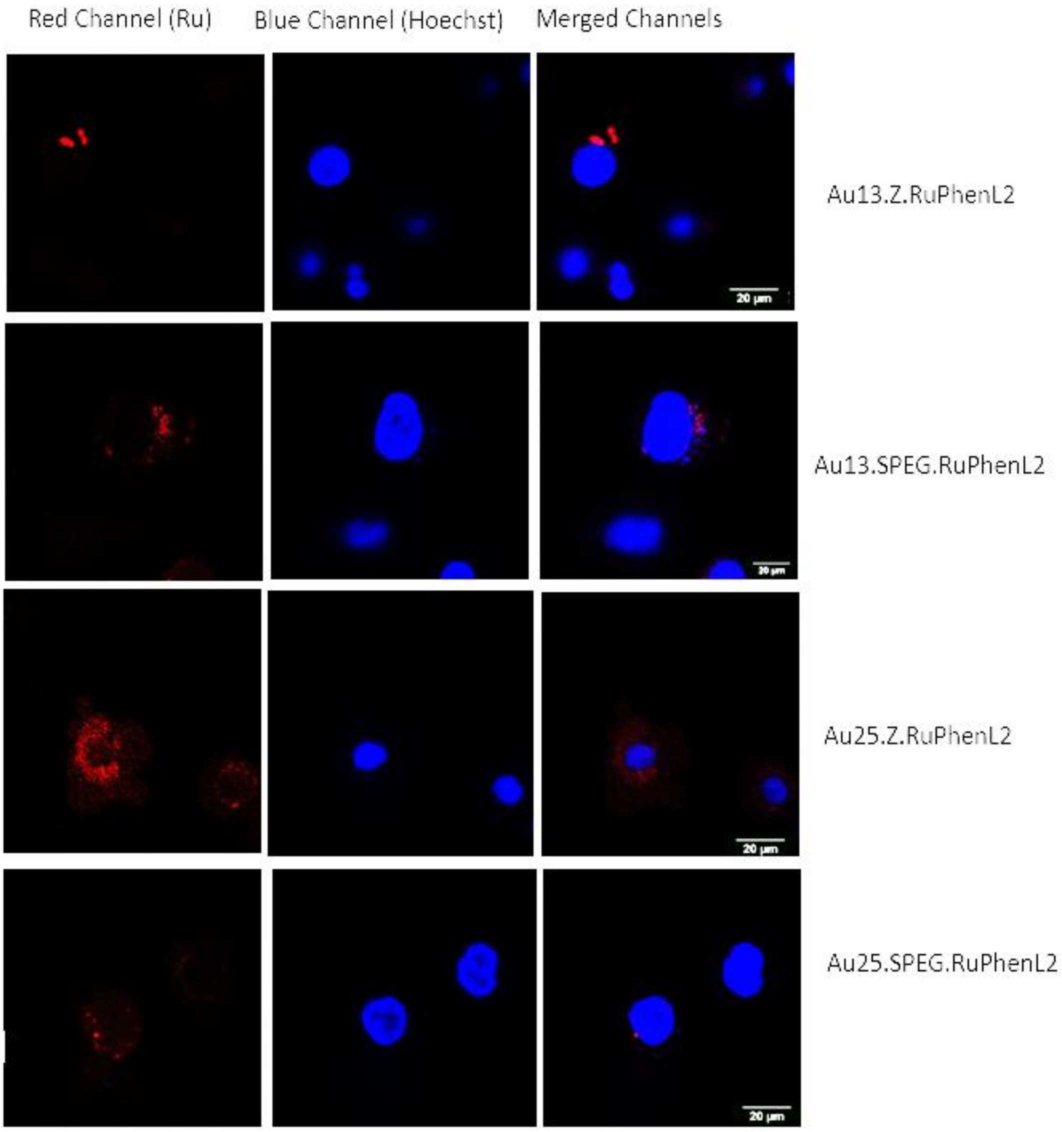

Figure 4.30- Confocal microscopy images of A549 cells after treatment with 0.9nM of Au.RuPhenL2 coated with Zonyl FSA or SPEG, for 2 h, (Scale bar = 20 μM).

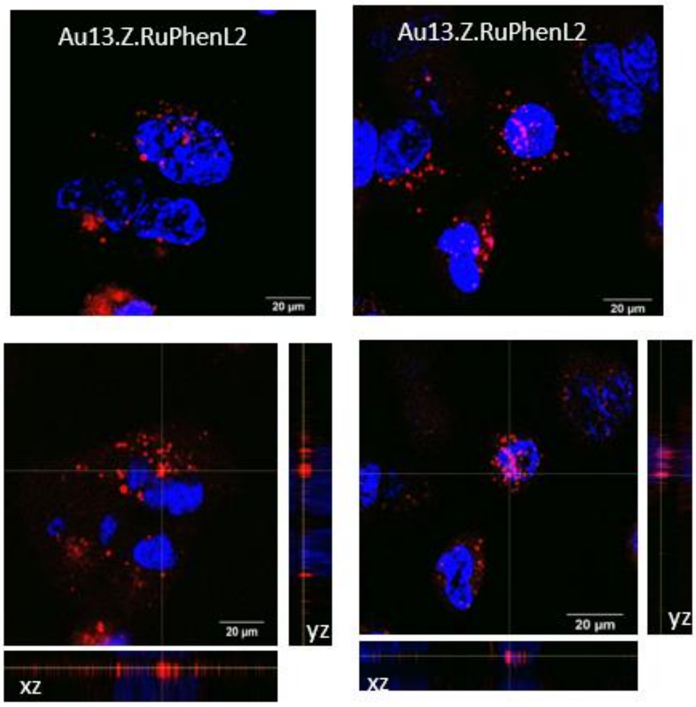

Figure 4.31- Cumulative Z projections (above) and cross sections (below) of Z-stacking images from confocal microscope of A549 cells after treatment for 12 h with 0.9 nM of Au13.Z.RuPhenL2. Scale bar = 20 μM). Red channel (λ_{exc} = 488 nm, λ_{em} =620−800 nm) and blue channel (λexc= 405 nm, λem = 410−455 nm).

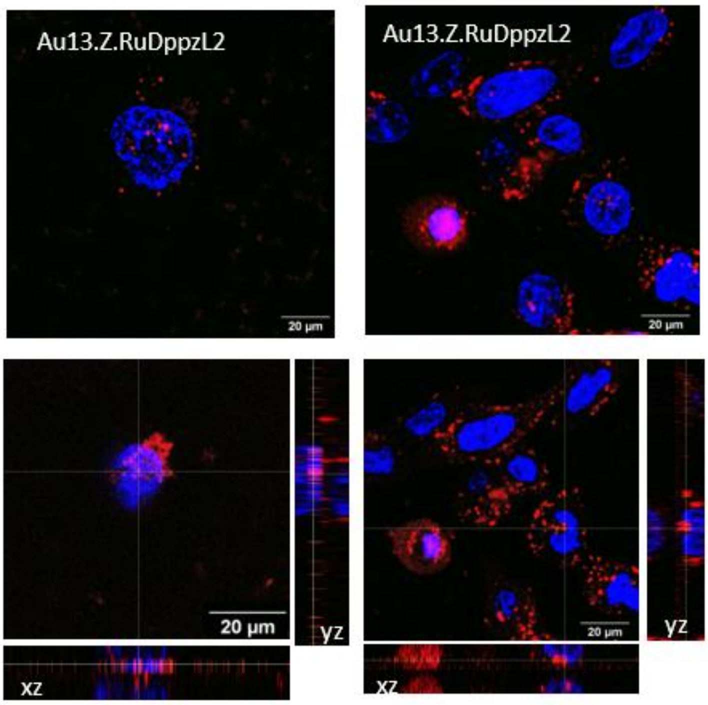

Figure 4.32- Cumulative Z projections (above) and cross sections (below) of Z-stacking images from confocal microscope of A549 cells after treatment for 12 h with 0.9 nM of

Au13.Z.RuDppzL2. Scale bar = 20 µM). Red channel (λexc = 488 nm, λem 620–800 nm) and blue channel (λexc= 405 nm, λem = 410–455 nm).

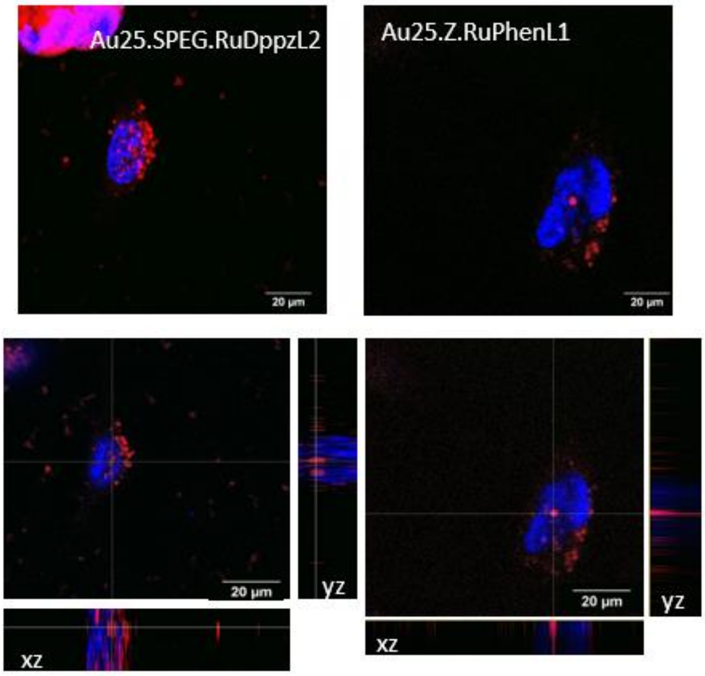

Figure 4.33- Z projections (above) and cross sections (below) of Z-stacking images from confocal microscope of A549 cells after treatment for 12 h with 0.3 nM of Au25.SPEG.RuDppzL2 and Au25.Z.RuPhenL1. Scale bar = 20 µM). Red channel (λexc = 488 nm, λem 620–800 nm) and blue channel (λexc= 405 nm, λem = 410–455 nm).

135,5224	186,612	124,8197	110,778	153,4518	157,8884	95,45572	116,4953	144,7158	62,52418	72,86102	72,90676
112,4246	180,6203	147,3686	130,0796	122,5328	140,0048	89,78417	81,3226	161,5475	60,8776	96,78213	68,79032
78,66978	122,2126	129,7137	137,8093	71,26018	115,672	98,4287	80,27062	151,0734	90,97337	88,1376	73,50135
112,7448	97,8341	119,5598	146,0422	97,05655	75,97122	85,71347	74,69055	117,2271	96,279	60,8776	62,38696
132,8239	114,7573	113,8425	152,2169	122,6242	127,1523	127,8384	136,2085	113,0192	114,8945	99,9838	89,60122
71,67183	77,38911	64,2165	83,74672	71,67183	87,543	97,10229	90,15008	106,5701	110,5951	67,23522	68,97327
83,97541	55,8464	54,33703	116,3581	86,07937	99,06904	94,03783	62,84435	93,44323	70,11673	87,77169	62,84435
47,8422	46,56153	47,70499	116,9527	73,40988	112,699	76,88599	122,9444	85,43904	71,80905	98,70313	80,22488

Figure 4.34- Cell viability of A549 cells in a 96 well-plate upon irradiation with 535 nm green lamp, at 10 mm distance between light and irradiated cells. Numbers in red correspond to viability below 100%.

5. General conclusions and future studies

In this thesis, three novel luminescent ruthenium (II) complexes functionalised on the surface of AuNPs were developed as DNA probes for the imaging and therapy of A549 cancer cells.

In the second chapter, Au.RuPhenL1 and Au.RuPhenL2 was successfully synthesized, characterised, and demonstrated to be monodispersed, with a low polydispersity index and good quality distribution. To stabilise the AuNPs, three different surfactants were attached, which influenced the luminescence of the ruthenium (II) complexes. Both Zonyl FSA and SPEG increased the luminescence lifetime and quantum yield for Au.RuPhenL2 and Au.RuPhenL1. However, LPEG had the opposite effect on the ruthenium (II) complexes luminescence quantum yield and lifetime. This supported conclusion that the type and length of surfactant attached to the AuNPs must be considered, due to its influence on the probes' luminescence.

In the third chapter, a third novel system, Au.RuDppzL2 was successfully synthesised and characterised. Both Au.RuPhenL2 and Au.RuDppzL2 were shown to be DNA probes by interacting with calf thymus and plasmid DNA. This interaction was seen by TEM, EDX and spectroscopy studies, including UV-Vis and linear dichroism. Au.RuPhenL2 and Au.RuDppzL2 had high binding affinities comparable with known intercalators such as ethidium bromide, however Au.RuDppzL2 had the strongest interaction with DNA. Two different binding modes were suggested for the interaction, such as electrostatic by van der Waals forces and intercalation between DNA base pairs and AuNP.Ru. A possible DNA uncoiling upon AuNP.Ru binding is visualised by TEM and EDX.

In the knowledge that AuNP.Ru conjugates are luminescent and bind to DNA, the uptake and localisation of AuNP.Ru by A549 cells was studied in the forth chapter. The AuNP.Ru signal was observed by fluorescence confocal microscopy and TEM after 2, 4 and 12 h of incubation in the cells. Au.RuPhenL1, Au.RuPhenL2 and Au.RuDppzL2 not only accumulated in the cytoplasm, but also in the nucleus of the cells. Given that one of the aims of this project is to employ the AuNP.Ru conjugates as DNA probes, the fact that these nanomaterials could access the nucleus is a promising result. Moreover, Au.RuDppzL2 showed the highest uptake in A549 cells for 13 and 25 nm sized AuNPs. On the other hand, Au.RuPhenL1 and Au.RuPhenL2 demonstrated a size dependence upon uptake, since the 25 nm AuNPs had a significantly higher uptake. All AuNP.Ru conjugates demonstrated phototoxic behaviour upon light irradiation with no effect on the cells in the dark. Au.RuPhenL1 and Au.RuDppzL2 showed more than 50 % of cell death in light. These results demonstrate the exciting potential of AuNP.Ru conjugates to act as photosensitisers and thus, these results should be further investigated for photodynamic therapy. Furthermore, the fact that these novel luminescent AuNPs can interact with DNA, allows for an even more efficient therapeutic effect by generating DNA oxidation. A further investigation is then proposed on the abilities, in particular, of Au.RuDppzL2 since this nano system showed the strongest interaction with DNA, the highest uptake in both 13 and 25 nm AuNPs with accumulation in the cell nucleus, and killed, in the nanomolar range, more than 50 % of cells by light, revealing no cytotoxicity in the dark.

Despite the exciting results, there is still a need to investigate AuNP.Ru further in order to develop an effective theranostics system. For additional studies on the interactions between AuNP.Ru and DNA, we propose viscosity studies, computational studies and competition assays using known intercalators such as ethidium bromide. DNA uncoiling should also be investigated by gel electrophoresis and AFM. For biological studies, the cell uptake experiment by ICP-MS and the phototoxicity experiment would need to be repeated on different days to ensure an accurate and statistically significant result. As a longer-term plan, the reason for phototoxicity of AuNP.Ru conjugates under irradiation needs to be explored and therefore, ROS experiments are purposed. Additionally, it is important to understand if AuNP.Ru are specific to cancer cells and to which cell lines, and therefore, other cancerous and non-cancerous cell lines should be studied. Finally, a biological moiety such as an antibody, could be added to AuNPs, to allow for more effective targeting.

In conclusion, this thesis represents a step forward for the development of an efficient luminescent gold-based nanoparticles theranostics strategy of cancer research.

6. General Methods and Procedures

6.1 General Procedures

Starting materials and solvents were purchased from Sigma Aldrich, Fisher Scientific and Alfa Aesar and used without any further purification. All air- and moisture-sensitive reactions were performed under a nitrogen atmosphere using Schlenk techniques, unless stated otherwise. All the reactions were conducted with oven-dried glassware and magnetic stirring. Reactions were monitored by thin layer chromatography (TLC) carried out on silica gel plates 60 F_{254}, purchased from Merck, and using 254 nm UV light for visualization. Column chromatography was carried out using silica gel with mesh size of 230-400, packed in glass columns. Room temperature is 23-25ºC. The ruthenium (II) complex $[Ru(dppz)_2(L2)]Cl_2$ or simply called RuDppzL2 was kindly provided by Maria Dalla Pozza from the Gilles Gasser group at Chimie ParisTech, PSL University as well as its characterisation by NMR, MS and UV-Vis. Milli-Q (ultra-pure) water was used throughout all work to dissolve DNA solutions, AuNPs and complexes. For the experiments involving DNA, fresh buffer of 1 mM Tris-HCl with 20 mM NaCl, pH 7.4 was made up before each experiment, except stated otherwise. For all the biological experiments, cell media DMEM supplemented with foetal bovine serum (10 % V/V) (FBS), L- glutamine (2 mM), penicillin (100 U/mL) and streptomycin (100 µg/mL) was used.

6.2 Instrumentation

For the characterisation of all organic and organometallic compounds the NMR experiments were carried out on a Bruker AVANCE III 300 (^{1}H: 300 MHz: 75 MHz), or

Bruker AVANCE NEO 400 NMR spectrometer (^{1}H: 400 MHz: 101 MHz), coupling constants are quoted in Hz. Chemical shifts (δ) were reported relative to the residual solvent signal: CDCl3 δ= 7.26, D2O δ=4.79, DMSO δ= 2.54 for ^{1}H NMR. All NMR spectra were analysed with MestRENova. Electrospray mass spectrometry was carried out on a Waters Micromass Q-TOF, and MALDI mass spectrometry on a Bruker Flextreme MALDI-TOF.

For the ruthenium compounds and gold nanoparticles characterisation the UV-visible absorption spectra were collected using 1 cm path length polished quartz cuvettes on an Agilent Cary 60 or Cary 5000 spectrometer, at room temperature. Luminescence spectrums were collected using 1cm path length polished quarts cuvettes on an FLS1000 fluorescence spectrometer, at room temperature. The spectra were corrected for lamp and instrument response and all the graphs were plotted using OriginPro 2023. Longpass filters were employed with cutoff wavelength of 500 or 530 nm as appropriate. Luminescent lifetimes were recorded with EPL-450 laser as an excitation source and fitted using Edinburgh Instruments FAST software with estimated error of ± 10 %. Quantum Yields were measured with an integrated sphere apparatus from Edinburgh Instruments and analysed with Fluoroacle software.

For the gold nanoparticles characterisation, the Dynamic Light Scattering (DLS) results were collected using zeta size and Nano ZS Malvern instruments Ltd. TEM images were obtained by Joel 1400 Bio electron microscope and Formvar carbon support films from EMResolutions. The images were analysed by ImageJ software. STEM-EDX results were obtained by an Oxford Instruments Aztec Energy system from EMResolutions. The images of STEM-EDX were kindly obtained by Dr Theresa Morris. ICP-MS analysis was performed by a 7500cx ICPMS with an Agilent integrated auto-sampler at the Chemistry department at the University of Warwick or in a Perkin Elmer 300X Nexion at the Department of Geography, Earth and Environmental Sciences at University of Birmingham and the data was acquired with Perkin Elmer Syngistix for ICP-MS version 3.1 software.

Uptake of the AuNP.Ru conjugates into A549 cells by confocal microscopy was investigated using Zeiss LSM900 inverted confocal microscope with Airyscan with a 63X and 100X oil immersion objective lens. Images were acquired in fluorescence mode. The fluorescence channels were: blue channel (Hoechst from Thermofisher): λ_{exc}= 405 nm and λ_{em}= 410-455 nm and red channel (AuNP.Ru conjugates): λ_{exc}= 458 nm and λ_{em}= 610-800 nm. TEM images were obtained by Joel 1400 Bio electron microscope and Formvar carbon support films from EMResolutions. All images were processed by imaging software ImageJ. Cytotoxicity by MTT colorimetric assay was evaluated by measuring the absorbance at 590 nm using a Tecan Infinite 200 Pro plate reader. ICP-MS analysis was performed by a Perkin Elmer 300X Nexion at the Department of Geography, Earth and Environmental Sciences at University of Birmingham and the data was acquired with Perkin Elmer Syngistix for ICP-MS version 3.1 software. For the phototoxicity assays, it was used a GSW IP65 green lamp of 100 watts.

6.3 Synthetic Procedures

6.3.1 Synthesis of Ligand L1

N-(Boc)-5-amino-1-pentanol (2)

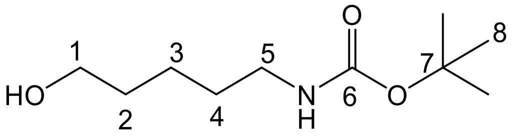

To a solution of 5-amino-1-pentanol (10.00 g, 48.8 mmol) in H_2O:THF (70 mL, 1:1), potassium bicarbonate (28.28 g, 141,1 mmol) was added. The white suspension was cooled in an ice bath to 5 ºC, and then di-*tert*-butyl dicarbonate (22.24 g, 51.0 mmol) dissolved in H_2O: THF (80mL, 1:1) was added dropwise over 15 minutes. The resulting biphasic mixture was then heated to 50 ºC and stirred for 24 h. The organic phase was separated and concentrated in vacuo until it formed a white microsuspension. The suspension was washed twice with H_2O: Et_2O (150 mL, 2:1) and the organic layer separated. The combined Et_2O extracts were dried with Na_2SO_4, filtered and the solvent removed in vacuo to give a clear orange oil. (13.14 g, 68 %).

δ_H(300 MHz; $CDCl_3$) 4.57 (1 H, s, NH), 3.62 (2 H, td, J=6.6, 5.0, 1.5, H-1), 3.11 (2 H, q, J=6.6, H-5), 1.79 (1 H, s, OH), 1.43 (9 H, s, H-8), 1.35-1.65 (6 H, m, H-2,3,4).

MS (ESI^+) m/z: 226 $(M+Na)^+$. NMR assignments are consistent with previously reported values.[238]

N-Boc-5-amino-1-tosylpentane (3)

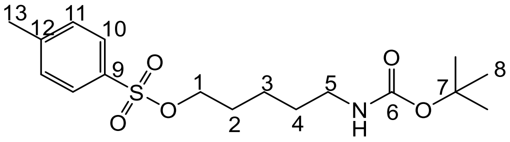

A solution of para-toluene sulfonyl chloride (8.97 g, 47.1 mmol) and **2** (7.80 g, 38.4 mmol) in anhydrous CH_2Cl_2 (50 mL) was cooled in an ice bath to 5 ºC. The pyridine (11 mL, 149.0 mmol) was added dropwise over 5 minutes. The solution was allowed to warm to room temperature and stirred for 24 hours. After which, the yellow mixture was concentrated in vacuo and washed with H_2O: Et_2O (100 mL, 1:1). The organic phase was separated, concentrated in vacuo (5 mL) and triturated in hexane (50 mL). The resulting white precipitate was filtered to give a white powder. (6.88 g, 50%);

δ_H(300 MHz; $CDCl_3$) 7.78 (2 H, d, J=8.0, H-10), 7.35 (2 H, d, J=8.0, H-11), 4.49 (1 H, s, NH), 4.02 (2 H, t, J=6.4, H-1), 3.06 (2 H, q, J=6.4, H-5), 2.45 (3 H, s, H-13), 1.66 (2 H, m, H-4), 1.43 (9 H, s, H-8), 1.25-1.50 (4 H, m, H-2,3).

MS (ESI$^+$) *m/z*: 380 (M+Na)$^+$. NMR assignments are consistent with previously reported values.[238]

4,4- dihydroxy-2,2- bipyridine (4)

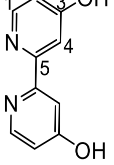

Hydrobromic acid 48 wt % solution (24 mL) was added to a solution of 4,4-dimethyl-2,2-bipyridne (2.95 g, 13.6 mmol) in glacial acetic acid (170 mL) and heated in reflux overnight at 118ºC. The resulting solution was concentrated in vacuo, dissolved in water (20 mL) and ammonium hydroxide added dropwise until the dark red solution turns to a pink/purple solution with a white precipitate, (from pH 1 to pH 7). The resulting white precipitate was filtered and dried to give a white powder. (2.29 g, 89 %);

δ_H(300 MHz; D_2O) 6.41 (2 H, dd, J=2.3, 5.8, H-2), 6.88 (2 H, d, J=2.3, H-4), 7.93 (2 H, d, J=5.8, H-1). MS (ESI$^+$) *m/z*: 189.1 $(M+H)^+$ NMR assignments are consistent with previously reported values.[238]

4,4-di-(N-Boc)-5-amino-1-pentoxy)-2,2-bipyridine (5)

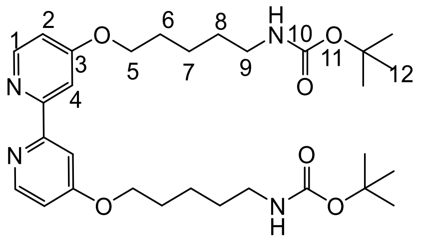

Potassium carbonate (2.22 g, 15.8 mmol) was added to a solution of **3** (6.67 g, 15.7 mmol), **4** (0.94 g, 4.9mmol) and 18-crown-6 (catalytic) in acetone (208 mL). The mixture was heated at 60ºC in reflux and stirred for 36 hours. Upon the completion of the reaction, the mixture was hot filtered to give a white precipitate upon cooling in an ice bath to 5 ºC. The white precipitate was filtered, and the solution concentrated in vacuo (~10 mL) and the resulting precipitate filtered. The combined precipitate was dried to give a white powder. (0.70 g, 26 %);

δ_H(300 MHz; $CDCl_3$) 8.47 (2H, d, J=5.7, H-1), 7.95 (2 H, d, J=2.5, H-4), 6.83 (2 H, dd, J=2.5, 5.7, H-2), 4.58 (2 H, s, NH), 4.13 (4 H, t, J=6.4, H-5), 3.14 (4 H, d, J=6.4, H-9), 1.84 (4 H, q, J=6.8, H-6), 1.50-1.60 (8 H, m, H-7,8), 1.43 (18 H, s, H-12).

MS (ESI^+) *m/z*: 581$(M+Na)^+$. NMR assignments are consistent with previously reported values.[238]

4,4-di-(5-amino-1-pentoxy)-2,2-bipyridine (6)

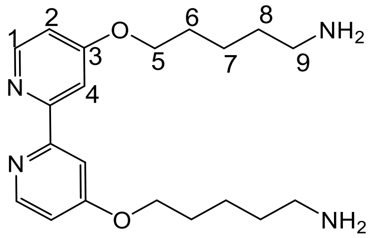

A solution of **5** (0.70 g, 1.7 mmol) in trifluoroacetic acid was stirred for 1 hour. The resulting white solution was concentrated in vacuo and the solution was washed (20 mL NaOH/20 mL chloroform). The organic layer was dried (Na_2SO_4), filtered and the solvent removed to give a white powder. (0.08 g, 20 %);

δ_H(300 MHz; $CDCl_3$) 8.45 (2 H, d, J=5.7, H-1), 7.94 (2 H, d, J=2.5, H-4), 6.82 (2 H, dd, J=2.5, 5.7, H-2), 4.14 (4 H, t, J=6.5, H-5), 2.73 (4 H, tt, J=4.4, 6.6, H-9), 1.85 (4 H, dd, J=4.1, 8.8, H-6), 1.50-1.58 (8 H, m, H-7,8), 1.24 (4 H, s, NH).

MS (ESI^+) *m/z*: 381 $(M+Na)^+$. NMR assignments are consistent with previously reported values.[238]

4,4- Di(5-lipoamido-1-pentoxy)-2,2-bipyridine (L1)

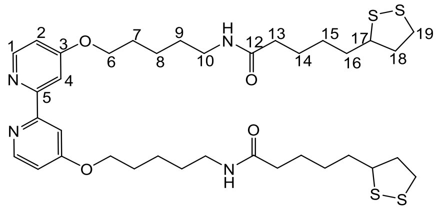

A solution of hydroxybenzotriazole hydrate (0.180 g, 2.7 mmol) and α-lipoic acid (0.240 g, 2.3 mmol) in DMF (4.5 mL) was cooled in an ice bath to 5 ºC. After adding 1-ethyl-3-(3-(dimethylamino)propyl)carbodiimide (EDC) (0.200 g, 2.6 mmol) the solution was allowed to warm to room temperature and stirred for an hour. A solution of **6** (0.88 g) and N-ethylmorpholine (0.067 g, 2.4 mmol) in dry DMF (6 mL) was added to the reaction mixture and stirred overnight. The resulting precipitate was filtered, triturated with $CHCl_3$, filtered once more followed by washes with $CHCl_3$. The resulting white powder was dried *in vacuo.* (0.07 g, 41 %);

δ_H(300 MHz; $CDCl_3$) 8.46 (2H, d, J= 5.7, H-1), 7.92 (2H, d, J= 2.5, H-4), 6.82 (2 H, dd, J= 2.5, 5.7 H-2), 5.45 (2 H, br s, NH), 4.13 (4 H, t, J= 6.3, H-6), 3.57 (2 H, dd, J= 6.2, 8.0, H-13), 3.30 (4 H, q, J=6.5, H-10), 3.04-3.20 (4 H, m, H-15, 19), 2.45 (2 H, dq, J=5.5, 6.4, 12.5, H-17), 2.20 (4 H, t, J=7.4, H-18), 1.85-1.98 (6 H, m, H-7,16), 1.40-1.75 (12 H, m, H-8,9,14).

MS(ESI$^+$) m/z: 757 (M+Na)$^+$. NMR assignments are consistent with previously reported values.[238]

6.3.2 Synthesis of ligand L2

Synthesis of ligand 5-(1,2-dithiolan-3-yl)-N-(1,10-phenanthrolin-5-yl)pentanamide (L2)

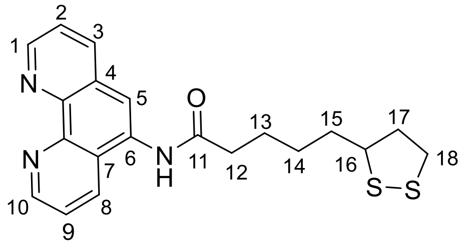

1,10-Phenantholin-5-amine was dissolved in DCM for 1 hour at 0°C followed by the addition of α-Lipoic acid, 1-Ethyl-3- (3-dimethylaminopropyl)carbodiimide (EDCI) and finally 4- dimethylaminopyridine (DMAP). The reaction was allowed to reach room temperature, being afterwards stirring for further 72 hours, under nitrogen. After that time, the solvent was evaporated, leaving a yellow oil. 50 mL of water was added, and the solution was centrifuged for 15 minutes at maximum speed. The water supernatant was removed, and this process was repeated three times. After it, 50 mL of acetonitrile was added and centrifuged again for 15 minutes. The resulting precipitate was filtered and washed with more acetonitrile, until obtain a pale-yellow thin powder. (485 mg, 46%)

δ_H(300 MHz; $CDCl_3$) 10.10 (1H, br s, NH), 9.13 (1H, dd, J=1.6, 4.3, H-10), 9.03 (1H, dd, J= 1.6, 4.3, H-1), 8.60 (1H, dd, J=1.7, 8.3, H-8), 8.44 (1H, dd, J=1.7, 8.3, H-3), 8.17 (1H, s, H-5), 7.82 (1H, dd, J=4.2, 8.4, H-9), 7.74 (1H, dd, J=4.2, 8.4, H-2), 3.68 (1H, dq, J=6.2,8.7, H-16), 3.11-3.24 (2H, m, H-18), 2.55 (2H, t, J=7.3, H-12), 2.44 (1H, dt, J=6.3, 12.4, H-17), 1.91 (1H, dq, J=6.8, 13.3, H-14), 1.70 (2H, dq, J=6.1, 11.7, H-13), 1.52 (2H, q, J=7.7, H-15).

δ_C(100 MHz; $CDCl_3$) 172.76 (NH), 150.32 (C-1), 146.31 (C-11), 144.24 (C-6), 136.25 (C-3), 132.18 (C-8), 128.56 (C-7), 125.12 (C-4), 124.05 (C-2), 123.29 (C-9), 120.50 (C-5), 56.62 (C-17), 38.62 (C-12), 36.26 (C-12), 34.67 (C-14), 28.90 (C-15), 25.47 (C-13).

Assignments from HSQC and HMBC.

MS(ESI$^+$) m/z: 384.10 (M+H)$^+$.

6.3.3 Synthesis of ruthenium (II) complexes

The compounds were prepared via a modification to the methods outlined by Sullivan *and co-workers*,[384] , Shreeve,[385] and Adams *and co-workers*[238]

Synthesis of Bis-(1,10-phenanthroline)-ruthenium chloride

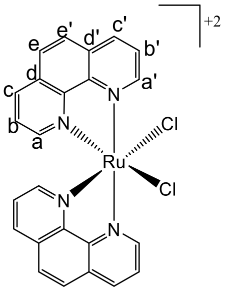

Ruthenium(III) chloride trihydrate (0.400 g, 1.5 mmol), 1,10-phenanthroline (0.550 g, 3.0 mmol) and lithium chloride (0.450 g, 10.6 mmol) were dissolved in DMF (5 mL). The reaction mixture was stirred for 8 hours at 153 ºC in reflux. After cooling to room temperature, acetone (4 mL) was added, and the mixture left in the freezer overnight. The product was precipitated and isolated by filtration and washing with water (25 mL) and ether (25 mL) to give a black powder. (0.556 g, 43 %)

δ_H(300 MHz; DMSO-d_6): 10.28 (1H, dd, J-1.3, 5.4, H-a), 8.70 (1H, dd, J-1.3, 8.3 , H-b), 8.28 (1H, d, J-8.9, H-c), 8.25 (1H, m, H-e,e’), 8.15 (1H, d, J-8.9, H-c’), 7.75 (1H, dd, J-1.3, 5.4, H-a’), 7.34 (1H, dd, J- 1.3, 8.3, H-b’).

MS(ESI$^+$) m/z: 497 (M-Cl)$^+$

UV-Vis- [MeCN, l_{max} / nm (ε / M^{-1} cm^{-1})]: 267 (19900), 350 (3600), 480 (2600).

Synthesis of RuPhenL1

[Ru(phen)$_2$(L1)](PF$_6$)$_2$

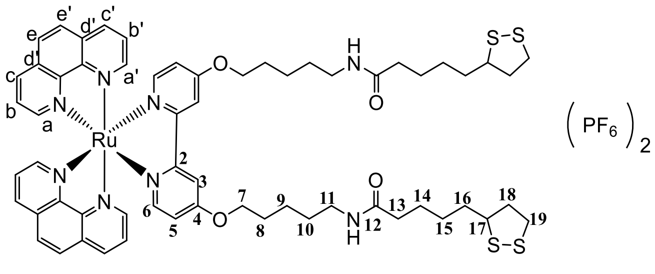

A solution of Ru(II) dichloride complex (0.045 g, 0.08 mmol) and L1 (0.063 g, 0.09 mmol) dissolved in ethanol (40 mL) was heated to 80 ºC and stirred for 16 hours. The red solution was cooled to room temperature and concentrated *in vacuo*. H_2O (35 mL) was added, and the red solution became a cream coloured mixture, that was filtered. NH_4PF_6 (0.25 g, 1.5 mmol) in 2 mL of MeOH was added to the filtered solution, stirred and re-filtered to give an orange precipitate. That precipitate was washed with cold H_2O and

Et_2O. The orange solid was dissolved in a minimal amount of acetonitrile, and the solvent was removed in vacuo to give a red powder. The product was then subjected to column chromatography (neutral aluminium, 3% MeOH in DCM). (0.02 g, 20%)

δ_H(400 MHz; CD_3CN): 8.63 (2H, dd, J=1.3, 8.3, H-c), 8.51 (2H, dd, J=1.3, 8.3, H-c’), 8.29 (2H, dd, J=1.3, 5.3 H-a), 8.20-8.33 (4H, m, H-e,e’), 8.09 (2H, d, J=3.3, H-3), 7.86 (2H, dd, J=1.3, 5.3, H-a’), 7.81 (2H, dd, J=5.2, 8.2, H-b), 7.52 (2H, dd, J=5.2, 8.2, H-b’), 7.36 (2H, d,J= 6.5, H-6), 6.78 (2H, dd, J=2.6, 6.5, H-5), 6.46 (1H, S, NH), 4.21 (4H, td, J=2.9, 6.5, H-7), 3.55 (2H, dq, J= 6.3, 8.9, H-17), 3.17-3.23 (4H, m, H-11, 19), 2.36 (2H, dt, J=6.3, 12.6, H-18), 2.08 (4H, t, J=7.2, H-13), 1.75- 1.82 (4H, dt, J=2.5, 4.9, H-10,18’), 1.49-1.66 (4H, m, H14), 1.44-1.56 (16H, m, H-8,9,15,16).

MS(ESI^+) m/z: 598 $(M-2(PF6))^{2+}$

UV-Vis- [λ_{max} / nm (ε / M^{-1} cm^{-1})]: 456(14079), 426 (sh), 265 (90000)

FTIR - [KBr, cm^{-1}]: 827 cm $^{-1}$ (PF_6 stretching)

[Ru(phen)$_2$(L1)]Cl$_2$

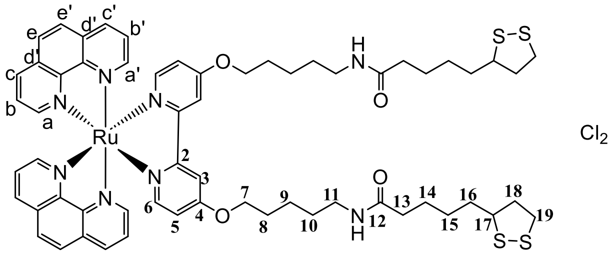

The orange powder was dissolved in acetonitrile/water (1:2) and subjected through a dowex-Cl column to exchange the counter ion from PF6 to Cl. Then was washed with acetone and dried under vacuum. (0.02 g, 20%)

FTIR- No peak at 827 cm $^{-1}$ observed.

δ_H(400 MHz; MeOD): 8.74 (2H, dd, J=2.9, 8.5, H-c), 8.61 (2H, dd, J=2.9, 8.5, H-c’), 8.40 (2H, d, J=5.2, H-a), 8.26-8.34 (4H, m, H-e,e’,3), 7.97 (2H, d, J=5.2, H-a’), 7.92 (2H, dd, J=5.2, 8.3, H-b’), 7.63 (2H, dd, J=5.2, 8.3, H-b), 7.44 (2H, d, J=6.0, H-6), 6.93 (2H, dd, J=2.3, 4.5, H-5), 4.23 (4H, td, J=2.4, 6.4, H-7), 3.43-3.60 (1H, m, H-17), 3.20 (4H, t, J=5.3, H-11), 3.15-3.22 (2H, m, H-19,19’), 2.40 (1H, dd, J=5.8, 12.3, H-18), 2.18 (4H, td, J= 4.4, 7.3, H-13), 1.82-1.90 (6H, m, H-10,18’), 1.20-1.70 (16H, m, H-8,9,14,15,16).

δ_C(500 MHz; MeOD): 175.7 (C-12), 168.3 (C-e,e’), 159.8 (C-2), 153.8 (C-6), 153.6 (C-a), 153.4 (C-a’), 149.4 (C-d), 149.3 (C-d’), 137.9 (C-c’), 137.8 (C-c), 132.4 (C-4), 129.4 (C-f,f’), 127.3 (C-b), 127.2 (C-b’), 115.3 (C-5), 112.8 (C-3), 70.8 (C-7), 60.8 (C-17), 57.4 (C-18), 40.0 (C-11), 37.3 (C-13), 36.6 (C-19,19’), 30.0 (C-10,18’), 29.5 (C-14), 24.1 (C-8,9,15,16).

Assignments from HSQC, HMBC and COSY.

Synthesis of RuPhenL2

[Ru(phen)$_2$(L2)](PF$_6$)$_2$

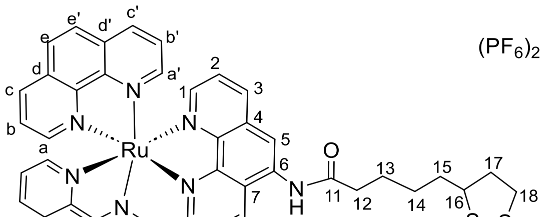

A solution of Ru(II) dichloride complex (0.050 g, 0.05 mmol) and L2 (0.019 g, 0.106 mmol) dissolved in methoxy ethanol (20 mL) was heated to 120 ºC and stirred for 48 hours. The reaction was allowed to cool down to room temperature and filtered to remove a dark purple precipitated. To the red solution, the solvent was reduced, and 20 mL of ether was added. The solution was left in the fridge for 48 hours to allow precipitate formation. The red precipitate formed was filtered was washed with cold ether, until a thin red powder was collected. The product was then subjected to column chromatography (neutral aluminium, acetonitrile 6 : 1 water).

δ_H(400 MHz; CD_3CN): 8.97 (1H, s, NH), 8.72 (1H, d, J= 8.7, H-2), 8.60 (2H, ddd, J=1.2, 2.3, 3.3, H-c), 8.58 (2H, ddd, J=1.2, 2.3, 3.3, H-c'), 8.51 (1H, d, J= 8.5, H-9), 8.24 (4H, s, H-e,e'), 8.03 (4H, dd, J= 7.5, 4.1, H-a,a'), 7.99 (1H, dd, J=1.2, 5.2, H-10), 7.92 (1H, dd, J=1.2, 5.2, H-1), 7.65-7.53 (6H, m, H-b,b',3,8), 7.34 (1H, d, J=4.4, H-5), 3.67-3.59 (1H, dq, J= 6.2, 8.9, H-16), 3.22-3.07 (2H, m, H-18), 2.62 (2H, t, J= 7.4, H-12), 2.51-2.43 (1H, dtd, J=5.4, 6.5, 12.9, H-17), 1.91-1.89 (1H, d, J=7.1, H-14), 1.84-1.72 (2H, m, H-13), 1.61-1.52 (2H, m, H-15).

δ_C(100 MHz; CD_3CN): 173.10 (C-11), 153.94 (C-a,a'), 152,82 (C-1,10), 149.24 (C-7), 148.84 (C-d), 137.69 (C-c), 137,13 (C-9), 134.93 (C-d'), 133.27 (C-4), 131.92 (C-2), 131.72 (C-6), 128.97 (C-e,e'), 126.82 (C-3,8), 126.15 (C-b,b'), 120.21 (C-c'), 69.75 (C-18), 60.61 (C-16), 36.91 (C12,C14), 32.26 (C-17), 28.23 (C-15), 25.60 (C-13). Assignments from HSQC and COSY.

MS(ESI^+) m/z: 422.6 $(M-2(PF6))^{2+}$

UV-Vis- [λ_{max} / nm (ε / M^{-1} cm^{-1})]: 448 (15291), 420 (sh), 263 (74375)

FTIR - [KBr, cm^{-1}]: 827 cm^{-1} (PF_6 stretching)

[Ru(phen)$_2$(L2)]Cl$_2$

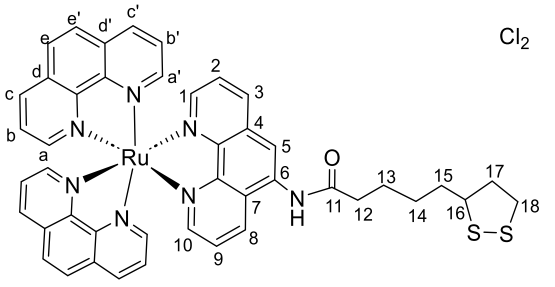

The orange powder was dissolved in acetonitrile/water (1:2) and subjected through a dowex-Cl column to exchange the counter ion from PF6 to Cl. Then was washed with acetone. The product was subjected to a LH-20 column in methanol, collected again and dried under vacuum. (15 mg, 25%)

FTIR- No peak at 827 cm $^{-1}$ observed.

δ_H(400 MHz; MeOD): 8.76 (1H, d, J=8.8, H-2), 8.72-8.68 (4H, m, H-c,c'), 8.62 (1H, d, J=8.3, H-9), 8.52-8.50 (1H, m, NH), 8.32 (4H, s, H-e,e'), 8.17-8.09 (5H, m, H-a,a',10), 8.08-8.06 (1H, m, H-1), 7.77-7.66 (4H, m, H-b,b',3,8), 7.38-7.33(1H, m, H-5), 3.58-3.47 (1H, dq, J= 6.2, 8.9, H-16), 3.22-3.07 (2H, m, H-18), 2.62 (2H, t, J= 7.4, H-12), 2.51-2.43 (1H, dtd, J=5.4, 6.5, 12.9, H-17), 2.33-2.15(2H, d, J=7.1, H-14), 1.97-1.40 (4H, m, H-13,15).

[RuCl$_2$(DMSO)$_4$]

This compound was synthesised following the literature procedure.[386]

Yield: 72%

bis-(1,10-Phenanthroline-5,6-dione)ruthenium(II) chloride

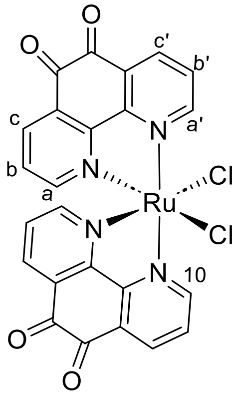

Synthesis provided by Maria Dalla Pozza: Dichloro*tetrakis*(dimethyl sulfoxide) ruthenium(II), and 1,10- phenanthroline-5,6-dione (2 eq.) were dissolved in dry DMF under a nitrogen atmosphere and brought to reflux for 4 hours. After the reaction mixture was let to cool down, DMF was removed *in vacuo* and the black residue was then dissolved in 4 mL of methanol. The solution was left overnight at 4 °C to precipitate the black microcrystalline solid, which was collected by filtration and washed with diethyl ether followed by drying *in vacuo.* The procedure was followed according to the literature.[387] Yield : 67 %

δ_H(400 MHz; DMSO-d^6): = 10.12 (2H, d, *J* = 5.7, H-c), 8.49 (2H, d, *J* = 7.7, H-a), 8.10 (2H, d, *J* = 7.7, H-a’), 8.02 (2H, t, *J* = 6.9, H-b), 7.77 (2H, d, *J* = 5.7, H-c’), 7.34 (2H, t, *J* = 6.9, H-b’).

Synthesis of [Ru(L2)(phendione)$_2$](PF$_6$)

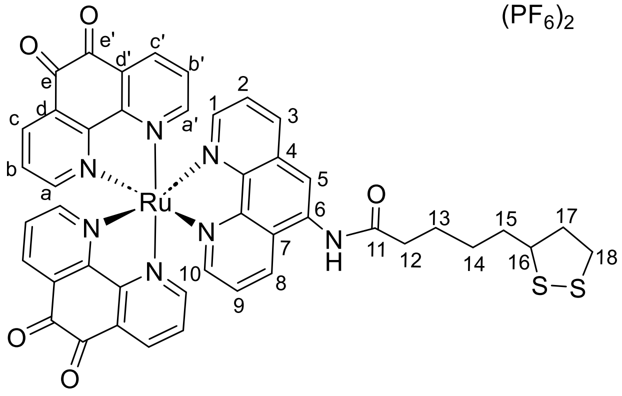

Synthesis provided by Maria Dalla Pozza: A mixture of Ru(phendione)$_2$Cl$_2$ (30 mg, 1 eq.) and L2 (23 mg, 1.2 eq) were mixed in 10 mL of EtOH:H$_2$O 1:1 and brought to reflux for 4 hours. After cooling down to room temperature, 10 mL of saturated NH$_4$PF$_6$ solution was added to precipitate the compound. Then, the brownish compound was filtered, washed with water and diethyl ether, and dried under vacuum. The product was purified by column chromatography eluting with 1-10% MeCN:H$_2$O (0.1 M KNO$_3$).The compound was synthesised adapting the reported procedure.[388] Yield: 61%

δ_H(400 MHz; CD$_3$CN): 8.88 (1H, s, NH), 8.78 (1H, dd, J= 1.2, 8.5, H-2), 8.65 (1H, d, J= 2.0, H-5?), 8.62 (1H, dd, J= 1.2, 8.5, H-9), 8.60-8.57 (2H, m, H-c), 8.48 (2H, ddd, J= 1.1, 2.4, 8.4, H-a'), 8.27 (1H, dd, J=1.2, 5.3, H-10), 8.24-8.18 (2H, m, H-c'), 8.15 (1H, dd, J=1.2, 5.3, H-1), 7.85-7.80 (4H, m, H-a,b), 7.77-7.67 (2H, m, H-3,8), 7.48 (2H, ddd, J= 2.0, 5.6, 7.8, H-b'), 3.67-3.59 (1H, dq, J= 6.2, 8.9, H-16), 3.22-3.07 (2H, m, H-18), 2.62 (2H, t, J= 7.4, H-12), 2.51-2.43 (1H, dtd, J=5.4, 6.5, 12.9, H-17), 1.91-1.89 (1H, d, J=7.1, H-14), 1.84-1.72 (2H, m, H-13), 1.61-1.52 (2H, m, H-15).

Synthesis of [Ru(dppz)$_2$(L2)](PF$_6$)$_2$

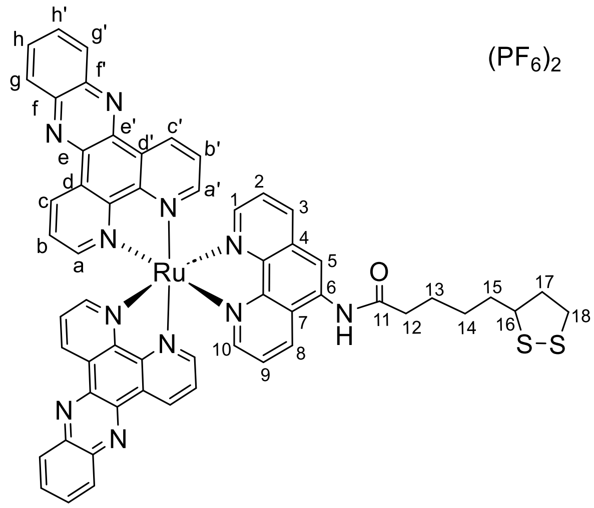

Synthesis provided by Maria Dalla Pozza: A mixture of [Ru(L2)(phendione)$_2$](PF$_6$) (28 mg, 1 equiv.) and phenylenediamine derivatives (13 mg, 4 equiv.) in 7 mL degassed CH$_3$CN/EtOH (1/3, v/v) was heated at 80 °C for 20 h under N$_2$ atmosphere. The reaction mixture was then cooled to room temperature. Addition of 5 mL of water followed by 5 mL of a saturated NH$_4$PF$_6$ solution resulted in the formation of a red/orange precipitate. The precipitate was collected using vacuum filtration, washed with distilled water, ice cold ethanol followed by ethanol and finally with diethyl ether. The precipitate was dried under reduced pressure to give the desired ruthenium (II) complex.

δ_H(400 MHz; CD$_3$CN): 9.65 (4H, dd, J=1.6, 8.2, H-c, c'), 8.87 (1H, s, H-NH), 8.73 (1H, dt, J= 1.5, 8.6, H-2), 8.65 (1H, d, J= 2.0, H-5), 8.57 (1H, dd, J= 1.5, 8.5, H-9), 8.50-8.43 (4H, m, H-g,g'), 8.31 (2H, td, J= 1.3, 5.8, H-a), 8.26 (1H, dd, J= 1.1, 5.3, H-1), 8.17-8-09 (6H, m, H-h,h',a',10), 7.86-7.77 (4H, m, H-b,b'), 7.72 (1H, dd, J= 5.3, 8.6, H-8), 7.64 (1H, dd, J= 5.3, 8.6, H-3), 3.67-3.59 (1H, dq, J= 6.2, 8.9, H-16), 3.22-3.07 (2H, m, H-18), 2.62 (2H, t, J= 7.4, H-12), 2.51-2.43 (1H, dtd, J=5.4, 6.5, 12.9, H-17), 1.91-1.89 (2H, d, J=7.1, H-14), 1.84-1.72 (2H, m, H-13), 1.61-1.52 (2H, m, H-15).

δ_C(100 MHz; CD_3CN): 173.81 (C-11), 155.37 (C-a), 154.03 (C-a'), 153.13 (C-h,h',1,10), 151.64 (C-e,e'), 149.10 (C-6), 146.40 (C-7), 143.59 (C-f,f'), 141.05 (C-d,d'), 137.50 (C-9), 135.07 (C-c), 134.60 (C-c'), 133.47 (C-2), 131.79 (C-4), 130.69 (C-g,g'), 128.35 (C-b,b'), 126.94 (C-3), 126.36 (C-8), 120.10 (C-5), 57.36 (C-18), 41.06 (C-16), 39.24 (C12), 37.26 (C-14), 35.34 (C-17), 29.48 (C-15), 25.85 (C-13).

MS(ESI^+) m/z: [M-PF_6]= 524.59

UV-Vis- [λ_{max} / nm (ε / M^{-1} cm^{-1})]: 450 (17324), 367 (22732), 278 (42303)

Synthesis of [Ru(dppz)$_2$(L2)]Cl$_2$ (RuDppzL2)

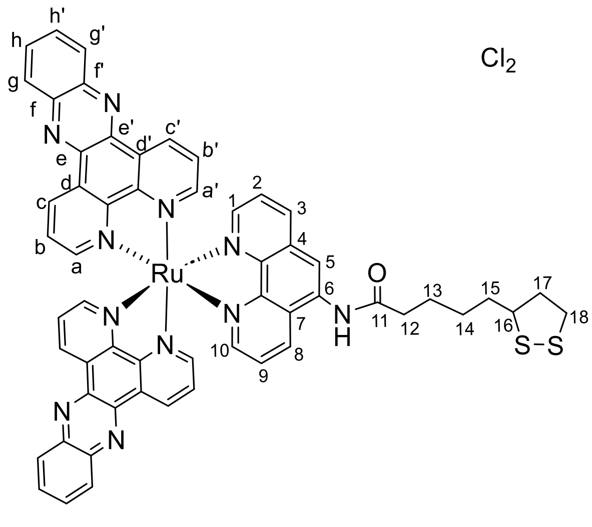

Synthesis provided by Maria Dalla Pozza: The PF_6^- counterion was exchanged by using Amberlite® IRA402 chloride form resin. The compound was dissolved in 1 mL of MeCN and 10 mL of MeOH was added. The resin was added and mixed by rotation for 5 hours.

After cotton filtration the chloride compound was dried under vacuum. Yield: 68% The counterion exchanged was proved by ^{31}P-NMR.

δ_H(400 MHz; MeOD): 9.81 (4H, dd, J= 1.7, 8.4, H-c,c'), 8.82 (1H, dd, J= 1.2, 8.6, H-2), 8.68 (1H, dd, J= 1.2, 8.6, H-9), 8.56-8.50 (5H, m, H-5, g,g'), 8.47-8.41 (1H, m, H-a), 8.45-8.37 (2H, m, H-1), 8.31 (1H, dd, J= 1.2, 5.3, H-10), 8.24 (2H, ddd, J= 1.3, 3.0, 5.5, H-a'), 8.15 (4H, dt, J= 3.5, 6.8, H-h,h'), 7.97-7.88 (4H, m, H-b,b'), 7.83 (1H, dd, J=5.3, 8.6, H-8), 7.76 (1H, dd, J= 5.3, 8.6, H-3), 3.58-3.47 (1H, dq, J= 6.2, 8.9, H-16), 3.22-3.07 (2H, m, H-18), 2.62 (2H, t, J= 7.4, H-12), 2.51-2.43 (1H, dtd, J=5.4, 6.5, 12.9, H-17), 2.33-2.15(2H, d, J=7.1, H-14), 1.97-1.40 (4H, m, H-13,15).

6.4 Methodology

6.4.1 Gold nanoparticles 13 nm (Au13) Synthesis

Monodispersed 13nm gold nanoparticles were synthesised using previously modified published methods.[246, 389, 390] A solution of sodium citrate (0.06 g), citric acid (0.013 g) and ethylenediaminetetraacetic acid (EDTA) (0,0013 g) were dissolved in Milli-Q water (100 mL). This solution was heated to 150 ºC at reflux. Meanwhile, in a separate bicker, 0.008 g of gold was weighted and dissolved in Milli-Q water (25mL) and heated at ~ 100 ºC. 5 minutes after the reflux started, the gold solution was added to the reflux and left it for 30 minutes. After that time, the reflux was turned off and left it stirring for 1 hour to make 125 mL of Au13. The synthesis and monodispersity of particles was confirmed by DLS.

6.4.2 Gold nanoparticles 25 nm (Au25) Synthesis

To increase the size of the gold nanoparticles, three fresh solutions were made up: A) HAuCl4 stock solution 49.25 mg (0.13 mmol) in 25mL of MilliQ water, B) 251 mg of ascorbic acid solution (57 mM) in 25 mL of MilliQ water, and C) 250 mg of trisodium citrate (34 mM) in 25 mL of MilliQ water. From these stock solutions, two seed solutions were made. 1) HAuCl4 stock (A) (4 mL) in 16 mL of MilliQ water and 2) 1 mL of ascorbic acid stock (B) , 0.5 mL of trisodium citrate stock (C) in 18.5 mL of MilliQ water. Then, 34mL of AuNP13 made previously, in 6 mL of MilliQ water were added to a 50 mL three neck round bottom flask. Solutions 1 and 2 were added at same time and dropwise in the centre of the flask, with constant stirring and at room temperature. When both solutions were added, the nanoparticles were brought to reflux for 30 minutes at 150 ºC. After that time, the reaction was allowed to cool down, maintaining the stirring, for 1 hour to finally make 60 mL of Au25. The synthesis and monodispersity of particles were confirmed by DLS.

6.4.3 Calculation of gold nanoparticles concentration

The concentration of the gold nanoparticles can be determined following three different methods. The first method involves an equation derived from the density of the gold, the quantity of gold used in the synthesis ($m_{I,Au}$), the diameter of the nanoparticles (D) obtained by TEM images and N which is the total number of gold atoms per nanoparticles with diameter D. (equation 4 and 5).[391, 392]

Method 1:

$$N = 30.89685812 \times D^3 \tag{4}$$

$$C = \frac{m_{i,Au}}{N \times V \times Mr} \tag{5}$$

Method 2:

The second method for the calculation of AuNPs concentration uses the absorption measured at 450 nm for citrate AuNPs or the absorption of the SPR for the coated AuNPs (due to ruthenium (II) complexes absorption), divided by the extinction coefficient at the same wavelength (equation 6).[393]

$$C = \frac{A_{450/SPR}}{\varepsilon_{450/SPR}} \tag{6}$$

Method 3:

The final method, that is usually the most accurate but also requires more experimental preparation, is Inductively Plasma Mass Spectrometry (ICP-MS). With this technique the concentration of gold is obtained in ppb and therefore the concentration of AuNPs in molarity is determined as demonstrated in equation 7, where [Au] is the concentration of gold, DF is the dilution factor and N_A the Avogadro number. The concentrations calculated by the different methods were within a less than 10 % error of each other.

$$\frac{[Au](ppb) \times 10^{-6} \times DF}{mAu \times N} \times \frac{1}{N_A} \tag{7}$$

To calculate the number of ruthenium atoms per AuNP can be obtained by equation 8, where [Ru] is the concentration of ruthenium in ppb and [Au] the concentration of gold in ppb.

$$\frac{Ru}{AuNP} = \frac{N \times [Ru]}{[Au]} \tag{8}$$

6.4.4 Coating of surfactants (Zonyl FSA, sPEG and LPEG) on Au13/25 nanoparticles

Gold nanoparticles solution (2mL) in each Eppendorf were centrifuged for 30 minutes at 13.3 G. The supernatant was discarded, and the particles resuspended in 1 mL Milli-Q water. Zonyl FSA of 0.05 M stock solution (10 µL), or sPEG/LPEG of 1 mM stock (10 µL / 5 µL, respectively) was added and the solution stirred for 10 minutes. The nanoparticles were centrifuged again for 25 minutes at 13 G. 2 Eppendorf's in 350 µL Milli-Q water and 1 in 300 µL were resuspended and combined into 3 Eppendorf's to give 1mL solution of gold nanoparticles coated with surfactant. All the particles were characterized by dynamic light scattering (DLS), transmission electron microscopy (TEM and specific surface plasmon resonance band (SPR) by UV-Vis.

6.4.5 Coating of ruthenium (II) complexes on Au13/25 nanoparticles

From the solution of AuNPs coated with surfactant, the maximum binding amount from a 1mM stock solution of the ruthenium (II) complexes, was added. To prevent aggregation of the AuNPs, the solution in methanol of ruthenium (II) complexes is added slowly, in 5 µL each time and stirring for 2 minutes between each addition until it reaches the total binding concentration. All the nanoparticles are purified by size exclusion chromatography by Sephadex-15.

All the AuNP.Ru were characterized by dynamic light scattering (DLS), transmission electron microscopy (TEM and specific surface plasmon resonance band (SPR) by UV-Vis.

6.4.6 Sample preparation for luminescence measurements

1 mL of the solutions were added to a cuvette. When gold nanoparticles were used, the solutions were stirred for 2 minutes before measurement. For the luminescence experiments, an FLS1000 Edinburgh instrument was used. The excitation used was 450 nm and emission of 610 nm, with a filter at 500 or 530 nm. For the luminescence lifetime measurement, a pulsed diode laser EPL-445 was used and a constant stirring inside the cuvette. To measure quantum yields, the instrument was fitted with an integrated sphere.

6.4.7 AuNPs samples preparation for Transmission Electron Microscopy (TEM)

1.5 µL of gold nanoparticles at a concentration of 2 nM were placed on EMResolution Formvar / Carbon film on Copper 200 mesh grids to be imaged using a Joel 1400 Bio Electron Micrsocope at the Centre for Electron Microscopy at the University of Birmingham.

6.4.8 Sample preparation for Inductively Coupled Mass Spectrometry (ICP-MS)

The gold nanoparticles samples were diluted to half of its concentration, 1.75 nM. Then, between 100 to 150 µL of pure aqua regia was added to digest the samples until solutions were colourless. The samples were then diluted to 5mL with 4% nitric acid in water to reduce the aqua regia content. A series of gold and ruthenium standards were used for calibration.

6.4.9 Preparation of Calf thymus ctDNA

A fragment of Calf thymus DNA sodium salt (Sigma Alrdich) was dissolved in Milli-Q water and washed using a 10 KDa MWCO centrifuge tube (Sartorius, Vivaspin, 10 mL). The solution obtained was then analysed by UV-Vis spectroscopy (Cary 60 spectrometer) and the concentration of DNA calculated by measuring ε (260 nm), to give a final solution of 28,000 mol^{-1} dm^3 cm^{-1} in DNA base pairs. This stock solution was kept in the freezer with fresh aliquots to be taken out for each experiment and dissolved in buffer.

6.4.10 Flow Linear Dichroism (LD)

Spectra were recorded on a Chirascan+ spectrometer with the LD accessory (Applied Photophysics limited). The samples were scanned between 600 and 200 nm with 3 repeats. The LD has an angular gap of 0.25 mm giving an overall path length of 0.5 mm. Samples volumes began at 150 µL and stopped at 250 µL. The cell was rotated at 24 revolutions per second to optimise the DNA signal. Titrations were carried out at a constant concentration of ctDNA (50 µM) by adding compensating solution of ctDNA in buffer of equal volume to the AuNPs solution addition. The concentration of AuNPs was increased stepwise by adding set volumes of a stock 3.5 nM AuNPs solution. The R value on the DNA/complexes titrations corresponds to the ratio of DNA base pairs to complex. However, due to the difference on concentration between DNA and AuNPs, presenting the results by ratio would be insignificant. Therefore, the concentration of AuNPs after each addition is described.

6.4.11 pBR322 plasmid linearization preparation

pBR322 plasmid DNA (MercK) linearization was achieved using the pst1-HF restriction endonuclease (new England biolabs). 50 µL of 0.5 µg/µL pBR-322 DNA solution was incubated with 50 µL Pst1-HF (20,000 units/mL), 250 µL of 10X cutsmart buffer and 50 µL Milli-Q water were incubated together at 37 °C for 15 minutes. This reaction mixture was then purified using QAIquick PCR purification columns and eluted with 50 µL of EB Buffer (10 mM Tris HCl, pH 8.5). Concentration in DNA base pairs (33 µM) was determined using a multichannel nanodrop 8000 spectrophotometer by using the absorbance at 260 nm and $\varepsilon 260 = 13{,}200 \text{ mol}^{-1} \text{ dm}^{-3} \text{ cm}^{-1}$ using the beer lambert law. Confirmation of linearization was performed by agarose gel electrophoresis by observing band shift and compare with 1 kb DNA ladder.

6.4.12 Agarose gel electrophoresis

Agarose gels were prepared by diluting 6 g of agarose in 400 mL 1x Tris-Boric acid buffer (890 mM each, pH 8.3), which was previously prepared in Milli-Q water. This solution was microwaved for 5 minutes until all the solid had dissolved. After leaving it to cool down, the transparent solution was cast into the agarose gel tray with a 15 lane comb. A 1 kb DNA ladder (from 250 bp to 25.000 bp) was used in the gel. 30 µM of the plasmid DNA in a 20 µL total per well was added to two different wells. The gel was run at 140 V for 2 hours in 1X TB buffer. The gel was then removed from the plate and stained with

SYBR TM Gold Nucleic Acid Gel Stain (Thermo fisher scientific) in 1X TB buffer for 45 minutes before imaging on a bio-rad ChemiDoc fluorescent imager with 305 nm excitation.

6.4.13 TEM/ STEM-EDX

To a solution of 3.5 nM AuNPs, a 16 µM solution of ctDNA/plasmid DNA previously prepared in water, was added and incubated for 3 minutes at 37 °C. Then, a 1.5 µL of that solution were placed on EMResolution Formvar / Carbon film on Copper 200 mesh grids to be imaged using a Joel 1400 Bio Electron Microscope at the Centre for Electron Microscopy at the University of Birmingham. For staining, the grids were subjected to a drop of 4% uranyl acetate in water for 15 minutes. Then, the grid was carefully dried using a paper filter around the edges to be imaged again. The same grids used for TEM were submitted to Theresa Morris from School of Metallurgy and Materials at University of Birmingham for STEM-EDX imaging.

6.4.14 UV-Vis titration with DNA

The spectra were recorded in a Cary 60 spectrometer. Titrations were carried out at a constant concentration of AuNPs (3.5 nM) by adding compensating solution of AuNPs of equal volume to the ctDNA solution addition. The concentration of ctDNA was increased stepwise by adding set volumes of a stock 50 µM ctDNA in buffer.

6.4.15 Fluorescence emission titration with DNA

For the luminescence experiments, an FLS1000 Edinburgh instrument was used. The excitation used was 450 nm and emission of 610 nm, with a filter at 500 or 530 nm. Titrations were caried out as stated previously for the UV-Vis experiment.

6.4.16 Cell Culture

A549 lung cancer cells were cultured at 37 °C in a humidified chamber with 5 % CO_2, 95 % air (MCO-15AC, Sanyo, Japan) in 75 cm^2 cell culture flasks (Greiner Bio-one, U.K.) containing 15 mL of cell media. Once the cells are confluent, the cells are sub-cultured after washed with calcium free phosphate buffered saline (10 mL) and detached from the flask by adding 2 mL of TrypLE Express enzyme. New fresh media was then added to the cells in a new cell culture flask and subsequently placed in a humidified chamber.

6.4.17 MTT assay

A549 cells were seeded at 6,500 cells per well in a 96-well plate in 100 µL of cell media and left overnight. Next day the media is changed and fresh media containing the appropriate concentration of test compounds (ruthenium (II) complexes or AuNPs samples) was added to the wells (100 µL per well). The plates were then incubated for 24 h. After treatment, the media + compounds were removed, and cells were washed with 200 µL of PBS and fresh media was added (200 µL) containing 3- (4,5-dimehtyl-2-thiazolyl)-2,5-diphenyl-2H-tetrazolium bromide (MTT) (0.5 mg/mL). Following incubation for 3 h at 37 °C, the medium is carefully removed and 100 µL of DMSO was added to solubilise the blue formazan product. At this point, the plates were gently rocked for 2 h at room temperature in the dark to help the solubilisation. After that time, the absorbance is determined at 590 nm using a Tecan Infinite 200 Pro plate reader. The MTT assay was carried out in biological duplicates.

6.4.18 Live cells- Confocal Microscopy

A549 cells were seeded at a density of 100,000 into a 35 mm dish with a 10 mm glass diameter insert and allowed to attach overnight. Next day, the cells were rinsed with PBS and treated with 3 mL of media containing 0.9 nM of Au13.SPEG, Au13.RuPhenL1, Au13.RuPhenL2, Au13.RuDppzL2 and 0.3 nM of Au25.RuPhenL1, Au25.RuPhenL2, Au25.RuDppzL, for 2, 4 and 12 h. At the end of each time point, spent media was removed and cells were washed three times with PBS followed by 30 minutes treatment with 2.5 µg/mL Hoechst 33258. Cells were finally rinsed three times with PBS and kept in DMEM media without phenol red. Confocal images and Z-stacks were collected on a Zeiss LSM900 inverted confocal microscope with Airyscan using a 63X oil immersion objective lens. All the images were processed with ImageJ.

6.4.19 Transmission electron Microscopy

The cells were seeded at a density of 100,000 into a 13 mm dimeter cover glass in a 6-well plate and allowed to attach overnight. Next day, the cells were rinsed with PBS and treated with 3 mL of media containing 0.9 nM of Au13.SPEG, Au13.RuPhenL1, Au13.RuPhenL2, Au13.RuDppzL2 and 0.3 nM of Au25.RuPhenL1, Au25.RuPhenL2, Au25.RuDppzL, for 4 and 12 h. At the end of each time point, spent media was removed and cells were washed three times with PBS followed by fixation with 2.5 % glutaraldehyde for 24 h at 4 °C. Samples were then taken for processing by Theresa Morris from School of Metallurgy and Materials, at University of Birmingham. Ultrathin sections of between 70-90 nm were cut parallel to cover-glass and mounted onto formvar-coated 200 mesh copper grids. Images were then acquired with Joel 1400 Bio Electron microscope and analysed by ImageJ software.

6.4.20 ICP-MS with cells

Cells were seeded at a density of 1 X 10^7 cells per 75 cm^2 flask and incubated for 7 days. Spent media was then removed and replaced with 3 mL of media containing 0.9 nM of Au13.SPEG, Au13.RuPhenL1, Au13.RuPhenL2, Au13.RuDppzL2 and 0.3 nM of Au25.RuPhenL1, Au25.RuPhenL2, Au25.RuDppzL and treated for 12 h. Spent media was then removed and cells rinsed three times with 1 mL PBS. Cells were detached by treating with 1 mL of TrypLE for 10 minutes. The cells are then added into fresh media, counted and transferred to sample vials. 300 µL of nitric acid ultrapure with 50 µL of aqua regia were then added to digest the cells overnight at room temperature. Next day, Honeywell ultrapure water was added to adjust the volume so that a final solution of 4 % nitric acid was prepared. The solutions were analysed by a Perkin Elmer 300X Nexion at the Department of Geography, Earth and Environmental Sciences at University of Birmingham and the data was acquired with Perkin Elmer Syngistix for ICP-MS version 3.1 software.

6.4.21 Phototoxicity with 535 nm (green light)

The cells were seeded at a 5,000 cells per well in a 96 well plate and were incubated at 37 °C for 24 h. The media was then replaced by fresh media containing 0.9 nM of Au13.RuPhenL1, Au13.RuPhenL2, Au13.RuDppzL2 and 0.3 nM for Au25.RuPhenL1, Au25.RuPhenL2, Au25.RuDppzL, for 24 h. After treatment, the media is removed and replaced by fresh DMEM media without phenol red (100 µL). The cells are then irradiated at 535 nm for 40 minutes with a GSW IP65 green lamp of 100 watts, with 20 mm between the lamp and the irradiated cells. During the irradiation time, the dark plate was removed from the incubator and placed in a dark fume hood, so that both plates were in the same conditions. Both dark and irradiated plates were incubated the rest of the time, up to 48 h. At the end of that time, media containing 3- (4,5-dimehtyl-2-thiazolyl)-2,5-diphenyl-2H-tetrazolium bromide (MTT) (0.5 mg/mL) was added to the cells. Following incubation for 3 h at 37 °C, the medium is carefully removed and 100 µL of DMSO was added to solubilise the blue formazan product. At this point, the plates were gently rocked for 2 h at room temperature in the dark to help the solubilisation. After that time, the absorbance is determined at 590 nm using a Tecan Infinite 200 Pro plate reader.

7. References

1. Thandra, K. C.; Barsouk, A.; Saginala, K.; Aluru, J. S.; Barsouk, A., Epidemiology of lung cancer. *Contemp Oncol (Pozn)* **2021,** *25* (1), 45-52.
2. Lemjabbar-Alaoui, H.; Hassan, O. U.; Yang, Y. W.; Buchanan, P., Lung cancer: Biology and treatment options. *Biochim Biophys Acta* **2015,** *1856* (2), 189-210.
3. Zappa, C.; Mousa, S. A., Non-small cell lung cancer: current treatment and future advances. *Transl Lung Cancer Res* **2016,** *5* (3), 288-300.
4. Dela Cruz, C. S.; Tanoue, L. T.; Matthay, R. A., Lung cancer: epidemiology, etiology, and prevention. *Clin Chest Med* **2011,** *32* (4), 605-44.
5. Zhang, C.; Xu, C.; Gao, X.; Yao, Q., Platinum-based drugs for cancer therapy and anti-tumor strategies. *Theranostics* **2022,** *12* (5), 2115-2132.
6. Antonarakis, E. S.; Emadi, A., Ruthenium-based chemotherapeutics: are they ready for prime time? *Cancer Chemother Pharmacol* **2010,** *66* (1), 1-9.
7. Kanaoujiya, R.; Meenakshi; Srivastava, S.; Singh, R.; Mustafa, G., Recent advances and application of ruthenium complexes in tumor malignancy. *Materials Today: Proceedings* **2023,** *72*, 2822-2827.
8. Lee, S. Y.; Kim, C. Y.; Nam, T. G., Ruthenium Complexes as Anticancer Agents: A Brief History and Perspectives. *Drug Des Devel Ther* **2020,** *14*, 5375-5392.
9. Mahmud, K. M.; Niloy, M. S.; Shakil, M. S.; Islam, M. A., Ruthenium Complexes: An Alternative to Platinum Drugs in Colorectal Cancer Treatment. *Pharmaceutics* **2021,** *13* (8).
10. Notaro, A.; Jakubaszek, M.; Rotthowe, N.; Maschietto, F.; Vinck, R.; Felder, P. S.; Goud, B.; Tharaud, M.; Ciofini, I.; Bedioui, F.; Winter, R. F.; Gasser, G., Increasing the Cytotoxicity of Ru(II) Polypyridyl Complexes by Tuning the Electronic Structure of Dioxo Ligands. *Journal of the American Chemical Society* **2020,** *142* (13), 6066-6084.
11. Lin, K.; Zhao, Z. Z.; Bo, H. B.; Hao, X. J.; Wang, J. Q., Applications of Ruthenium Complex in Tumor Diagnosis and Therapy. *Front Pharmacol* **2018,** *9*, 1323.
12. Das, S.; Powe, A. M.; Baker, G. A.; Valle, B.; El-Zahab, B.; Sintim, H. O.; Lowry, M.; Fakayode, S. O.; McCarroll, M. E.; Patonay, G.; Li, M.; Strongin, R. M.; Geng, M. L.; Warner, I. M., Molecular Fluorescence, Phosphorescence, and Chemiluminescence Spectrometry. *Analytical Chemistry* **2012,** *84* (2), 597-625.
13. Gill, M. R.; Garcia-Lara, J.; Foster, S. J.; Smythe, C.; Battaglia, G.; Thomas, J. A., A ruthenium(II) polypyridyl complex for direct imaging of DNA structure in living cells. *Nat Chem* **2009,** *1* (8), 662-7.
14. Liu, J.; Lai, H.; Xiong, Z.; Chen, B.; Chen, T., Functionalization and cancer-targeting design of ruthenium complexes for precise cancer therapy. *Chemical Communications* **2019,** *55* (67), 9904-9914.
15. Karges, J.; Kuang, S.; Maschietto, F.; Blacque, O.; Ciofini, I.; Chao, H.; Gasser, G., Rationally designed ruthenium complexes for 1- and 2-photon photodynamic therapy. *Nature Communications* **2020,** *11* (1), 3262.
16. Vidal, C.; Tomás-Gamasa, M.; Gutiérrez-González, A.; Mascareñas, J. L., Ruthenium-Catalyzed Redox Isomerizations inside Living Cells. *Journal of the American Chemical Society* **2019,** *141* (13), 5125-5129.
17. Shylin, S. I.; Pavliuk, Mariia V.; D'Amario, L.; Fritsky, I. O.; Berggren, G., Photoinduced hole transfer from tris(bipyridine)ruthenium dye to a high-valent iron-based water oxidation catalyst. *Faraday Discussions* **2019,** *215* (0), 162-174.
18. Grätzel, M., Solar energy conversion by dye-sensitized photovoltaic cells. *Inorg Chem* **2005,** *44* (20), 6841-51.

19. Lima, A. P.; Pereira, F. C.; Almeida, M. A.; Mello, F. M.; Pires, W. C.; Pinto, T. M.; Delella, F. K.; Felisbino, S. L.; Moreno, V.; Batista, A. A.; de Paula Silveira-Lacerda, E., Cytoxicity and apoptotic mechanism of ruthenium(II) amino acid complexes in sarcoma-180 tumor cells. *PloS one* **2014,** *9* (10), e105865.

20. Novakova, O.; Kasparkova, J.; Vrana, O.; van Vliet, P. M.; Reedijk, J.; Brabec, V., Correlation between Cytotoxicity and DNA Binding of Polypyridyl Ruthenium Complexes. *Biochemistry* **1995,** *34* (38), 12369-12378.

21. Lyon, R. F.; Southam, H. M.; Trevitt, C. R.; Liao, C.; El-Khamisy, S. F.; Poole, R. K.; Williamson, M. P., CORM-3 induces DNA damage through Ru(II) binding to DNA. *Biochemical Journal* **2022,** *479* (13), 1429-1439.

22. Alessio, E.; Messori, L., NAMI-A and KP1019/1339, Two Iconic Ruthenium Anticancer Drug Candidates Face-to-Face: A Case Story in Medicinal Inorganic Chemistry. *Molecules* **2019,** *24* (10).

23. Sava, G.; Bergamo, A.; Zorzet, S.; Gava, B.; Casarsa, C.; Cocchietto, M.; Furlani, A.; Scarcia, V.; Serli, B.; Iengo, E.; Alessio, E.; Mestroni, G., Influence of chemical stability on the activity of the antimetastasis ruthenium compound NAMI-A. *Eur J Cancer* **2002,** *38* (3), 427-35.

24. Kapitza, S.; Pongratz, M.; Jakupec, M. A.; Heffeter, P.; Berger, W.; Lackinger, L.; Keppler, B. K.; Marian, B., Heterocyclic complexes of ruthenium(III) induce apoptosis in colorectal carcinoma cells. *Journal of Cancer Research and Clinical Oncology* **2005,** *131* (2), 101-110.

25. Monro, S.; Colón, K. L.; Yin, H.; Roque, J., 3rd; Konda, P.; Gujar, S.; Thummel, R. P.; Lilge, L.; Cameron, C. G.; McFarland, S. A., Transition Metal Complexes and Photodynamic Therapy from a Tumor-Centered Approach: Challenges, Opportunities, and Highlights from the Development of TLD1433. *Chem Rev* **2019,** *119* (2), 797-828.

26. de Carvalho, N. C.; Neves, S. P.; Dias, R. B.; Valverde, L. F.; Sales, C. B. S.; Rocha, C. A. G.; Soares, M. B. P.; Dos Santos, E. R.; Oliveira, R. M. M.; Carlos, R. M.; Nogueira, P. C. L.; Bezerra, D. P., A novel ruthenium complex with xanthoxylin induces S-phase arrest and causes ERK1/2-mediated apoptosis in HepG2 cells through a p53-independent pathway. *Cell Death Dis* **2018,** *9* (2), 79.

27. McQuaid, K. T.; Takahashi, S.; Baumgaertner, L.; Cardin, D. J.; Paterson, N. G.; Hall, J. P.; Sugimoto, N.; Cardin, C. J., Ruthenium Polypyridyl Complex Bound to a Unimolecular Chair-Form G-Quadruplex. *Journal of the American Chemical Society* **2022,** *144* (13), 5956-5964.

28. Liao, G.; Chen, X.; Wu, J.; Qian, C.; Wang, Y.; Ji, L.; Chao, H., Ruthenium(ii) polypyridyl complexes as dual inhibitors of telomerase and topoisomerase. *Dalton Transactions* **2015,** *44* (34), 15145-15156.

29. Srinivas, U. S.; Tan, B. W. Q.; Vellayappan, B. A.; Jeyasekharan, A. D., ROS and the DNA damage response in cancer. *Redox Biology* **2019,** *25*, 101084.

30. Brabec, V.; Nováková, O., DNA binding mode of ruthenium complexes and relationship to tumor cell toxicity. *Drug Resist Updat* **2006,** *9* (3), 111-22.

31. Puckett, C. A.; Barton, J. K., Methods to Explore Cellular Uptake of Ruthenium Complexes. *Journal of the American Chemical Society* **2007,** *129* (1), 46-47.

32. Wang, J. Q.; Zhang, P. Y.; Qian, C.; Hou, X. J.; Ji, L. N.; Chao, H., Mitochondria are the primary target in the induction of apoptosis by chiral ruthenium(II) polypyridyl complexes in cancer cells. *J Biol Inorg Chem* **2014,** *19* (3), 335-48.

33. Wan, D.; Tang, B.; Wang, Y.-J.; Guo, B.-H.; Yin, H.; Yi, Q.-Y.; Liu, Y.-J., Synthesis and anticancer properties of ruthenium (II) complexes as potent apoptosis inducers through mitochondrial disruption. *European Journal of Medicinal Chemistry* **2017,** *139*, 180-190.

34. Sullivan, L. B.; Chandel, N. S., Mitochondrial reactive oxygen species and cancer. *Cancer Metab* **2014,** *2*, 17.

35. Sies, H.; Jones, D. P., Reactive oxygen species (ROS) as pleiotropic physiological signalling agents. *Nature Reviews Molecular Cell Biology* **2020,** *21* (7), 363-383.

36. Auten, R. L.; Davis, J. M., Oxygen Toxicity and Reactive Oxygen Species: The Devil Is in the Details. *Pediatric Research* **2009,** *66* (2), 121-127.
37. Klotz, L.-O.; Kröncke, K.-D.; Sies, H., Singlet oxygen-induced signaling effects in mammalian cells. *Photochemical & Photobiological Sciences* **2003,** *2* (2), 88-94.
38. Han, B.-J.; Jiang, G.-B.; Wang, J.; Li, W.; Huang, H.-L.; Liu, Y.-J., The studies on bioactivity in vitro of ruthenium(ii) polypyridyl complexes towards human lung carcinoma A549 cells. *RSC Advances* **2014,** *4* (77), 40899-40906.
39. Pan, N. L.; Liao, J. X.; Huang, M. Y.; Zhang, Y. Q.; Chen, J. X.; Zhang, Z. W.; Yang, Z. X.; Long, X. E.; Wu, X. T.; Sun, J., Lysosome-targeted ruthenium(II) complexes induce both apoptosis and autophagy in HeLa cells. *Journal of inorganic biochemistry* **2022,** *229*, 111729.
40. Gill, M. R.; Cecchin, D.; Walker, M. G.; Mulla, R. S.; Battaglia, G.; Smythe, C.; Thomas, J. A., Targeting the endoplasmic reticulum with a membrane-interactive luminescent ruthenium(ii) polypyridyl complex. *Chemical Science* **2013,** *4* (12), 4512-4519.
41. Deng, Z.; Gao, P.; Yu, L.; Ma, B.; You, Y.; Chan, L.; Mei, C.; Chen, T., Ruthenium complexes with phenylterpyridine derivatives target cell membrane and trigger death receptors-mediated apoptosis in cancer cells. *Biomaterials* **2017,** *129*, 111-126.
42. Qiu, K.; Wang, J.; Song, C.; Wang, L.; Zhu, H.; Huang, H.; Huang, J.; Wang, H.; Ji, L.; Chao, H., Crossfire for Two-Photon Photodynamic Therapy with Fluorinated Ruthenium (II) Photosensitizers. *ACS Applied Materials & Interfaces* **2017,** *9* (22), 18482-18492.
43. Martin, A.; Byrne, A.; Burke, C. S.; Forster, R. J.; Keyes, T. E., Peptide-Bridged Dinuclear Ru(II) Complex for Mitochondrial Targeted Monitoring of Dynamic Changes to Oxygen Concentration and ROS Generation in Live Mammalian Cells. *Journal of the American Chemical Society* **2014,** *136* (43), 15300-15309.
44. Gasser, G.; Sosniak, A. M.; Metzler-Nolte, N., Metal-containing peptide nucleic acid conjugates. *Dalton Transactions* **2011,** *40* (27), 7061-7076.
45. Pierroz, V.; Joshi, T.; Leonidova, A.; Mari, C.; Schur, J.; Ott, I.; Spiccia, L.; Ferrari, S.; Gasser, G., Molecular and cellular characterization of the biological effects of ruthenium(II) complexes incorporating 2-pyridyl-2-pyrimidine-4-carboxylic acid. *J Am Chem Soc* **2012,** *134* (50), 20376-87.
46. Yu, Q.; Liu, Y.; Xu, L.; Zheng, C.; Le, F.; Qin, X.; Liu, Y.; Liu, J., Ruthenium(II) polypyridyl complexes: cellular uptake, cell image and apoptosis of HeLa cancer cells induced by double targets. *Eur J Med Chem* **2014,** *82*, 82-95.
47. Balzani, V.; Juris, A.; Venturi, M.; Campagna, S.; Serroni, S., Luminescent and Redox-Active Polynuclear Transition Metal Complexes. *Chemical Reviews* **1996,** *96* (2), 759-834.
48. Juris, A.; Balzani, V.; Barigelletti, F.; Campagna, S.; Belser, P.; von Zelewsky, A., Ru(II) polypyridine complexes: photophysics, photochemistry, eletrochemistry, and chemiluminescence. *Coordination Chemistry Reviews* **1988,** *84*, 85-277.
49. Shee, N. K.; Drew, M. G. B.; Datta, D., Tuning of the lowest excited states in mixed ruthenium(ii) polypyridyl complexes having RuN6 cores by the conformation of the ancillary ligand. Emission from a 3ligand-to-ligand-charge-transfer state. *New Journal of Chemistry* **2016,** *40* (6), 5002-5009.
50. Heinemann, F.; Karges, J.; Gasser, G., Critical Overview of the Use of Ru(II) Polypyridyl Complexes as Photosensitizers in One-Photon and Two-Photon Photodynamic Therapy. *Accounts of Chemical Research* **2017,** *50* (11), 2727-2736.
51. Park, J.; Lee, Y. K.; Park, I. K.; Hwang, S. R., Current Limitations and Recent Progress in Nanomedicine for Clinically Available Photodynamic Therapy. *Biomedicines* **2021,** *9* (1).
52. Mari, C.; Pierroz, V.; Rubbiani, R.; Patra, M.; Hess, J.; Spingler, B.; Oehninger, L.; Schur, J.; Ott, I.; Salassa, L.; Ferrari, S.; Gasser, G., DNA intercalating Ru(II) polypyridyl complexes as effective photosensitizers in photodynamic therapy. *Chemistry* **2014,** *20* (44), 14421-36.
53. Monro, S.; Colón, K. L.; Yin, H.; Roque, J., III; Konda, P.; Gujar, S.; Thummel, R. P.; Lilge, L.; Cameron, C. G.; McFarland, S. A., Transition Metal Complexes and Photodynamic

Therapy from a Tumor-Centered Approach: Challenges, Opportunities, and Highlights from the Development of TLD1433. *Chemical Reviews* **2019,** *119* (2), 797-828.

54. Kulkarni, G.; Lilge, L.; Nesbitt, M.; Dumoulin-White, R.; Mandel, A.; Jewett, M., A Phase 1b Clinical Study of Intravesical Photodynamic Therapy in Patients with Bacillus Calmette-Guérin–unresponsive Non–muscle-invasive Bladder Cancer. *European Urology Open Science* **2022,** *41*, 105-111.

55. Lilge, L.; Roufaiel, M.; Lazic, S.; Kaspler, P.; Munegowda, M. A.; Nitz, M.; Bassan, J.; Mandel, A., Evaluation of a Ruthenium coordination complex as photosensitizer for PDT of bladder cancer: Cellular response, tissue selectivity and in vivo response. *Translational Biophotonics* **2020,** *2* (1-2), e201900032.

56. Li, J.; Chen, T., Transition metal complexes as photosensitizers for integrated cancer theranostic applications. *Coordination Chemistry Reviews* **2020,** *418*, 213355.

57. Pobłocki, K.; Drzeżdżon, J.; Kostrzewa, T.; Jacewicz, D. Coordination Complexes as a New Generation Photosensitizer for Photodynamic Anticancer Therapy *International journal of molecular sciences* [Online], 2021.

58. Smith, C. B.; Days, L. C.; Alajroush, D. R.; Faye, K.; Khodour, Y.; Beebe, S. J.; Holder, A. A., Photodynamic Therapy of Inorganic Complexes for the Treatment of Cancer. *Photochem Photobiol* **2022,** *98* (1), 17-41.

59. Conti, L.; Macedi, E.; Giorgi, C.; Valtancoli, B.; Fusi, V., Combination of light and Ru(II) polypyridyl complexes: Recent advances in the development of new anticancer drugs. *Coordination Chemistry Reviews* **2022,** *469*, 214656.

60. Bonnet, S., Ruthenium-Based Photoactivated Chemotherapy. *Journal of the American Chemical Society* **2023**.

61. Farrer, N. J.; Salassa, L.; Sadler, P. J., Photoactivated chemotherapy (PACT): the potential of excited-state d-block metals in medicine. *Dalton transactions (Cambridge, England : 2003)* **2009,** (48), 10690-10701.

62. Spiegel, M.; Adamo, C., Tuning the Photophysical Properties of Ru(II) Photosensitizers for PDT by Protonation and Metallation: A DFT Study. *The Journal of Physical Chemistry A* **2023,** *127* (16), 3625-3635.

63. Farrer, N. J.; Salassa, L.; Sadler, P. J., Photoactivated chemotherapy (PACT): the potential of excited-state d-block metals in medicine. *Dalton transactions (Cambridge, England : 2003)* **2009,** (48), 10690-701.

64. Bonnet, S., Why develop photoactivated chemotherapy? *Dalton Transactions* **2018,** *47* (31), 10330-10343.

65. Shi, H.; Sadler, P. J., How promising is phototherapy for cancer? *British Journal of Cancer* **2020,** *123* (6), 871-873.

66. Knoll, J. D.; Albani, B. A.; Turro, C., New Ru(II) Complexes for Dual Photoreactivity: Ligand Exchange and 1O2 Generation. *Accounts of Chemical Research* **2015,** *48* (8), 2280-2287.

67. Lameijer, L. N.; Ernst, D.; Hopkins, S. L.; Meijer, M. S.; Askes, S. H. C.; Le Dévédec, S. E.; Bonnet, S., A Red-Light-Activated Ruthenium-Caged NAMPT Inhibitor Remains Phototoxic in Hypoxic Cancer Cells. *Angewandte Chemie (International ed. in English)* **2017,** *56* (38), 11549-11553.

68. Meijer, M.; Saez Talens, V.; Hilbers, M.; Kieltyka, R.; Brouwer, A.; Natile, M.; Bonnet, S., NIR-Light-Driven Generation of Reactive Oxygen Species Using Ru(II)-Decorated Lipid-Encapsulated Upconverting Nanoparticles. *Langmuir* **2019,** *35*.

69. Siewert, B.; van Rixel, V. H. S.; van Rooden, E. J.; Hopkins, S. L.; Moester, M. J. B.; Ariese, F.; Siegler, M. A.; Bonnet, S., Chemical Swarming: Depending on Concentration, an Amphiphilic Ruthenium Polypyridyl Complex Induces Cell Death via Two Different Mechanisms. *Chemistry – A European Journal* **2016,** *22* (31), 10960-10968.

70. van Rixel, V. H. S.; Siewert, B.; Hopkins, S. L.; Askes, S. H. C.; Busemann, A.; Siegler, M. A.; Bonnet, S., Green light-induced apoptosis in cancer cells by a tetrapyridyl ruthenium prodrug offering two trans coordination sites. *Chem Sci* **2016,** *7* (8), 4922-4929.

71. Wei, J.; Renfrew, A. K., Photolabile ruthenium complexes to cage and release a highly cytotoxic anticancer agent. *Journal of inorganic biochemistry* **2018,** *179*, 146-153.

72. Albani, B. A.; Peña, B.; Leed, N. A.; de Paula, N. A. B. G.; Pavani, C.; Baptista, M. S.; Dunbar, K. R.; Turro, C., Marked Improvement in Photoinduced Cell Death by a New Tris-heteroleptic Complex with Dual Action: Singlet Oxygen Sensitization and Ligand Dissociation. *Journal of the American Chemical Society* **2014,** *136* (49), 17095-17101.

73. Rohrabaugh, T. N.; Collins, K. A.; Xue, C.; White, J. K.; Kodanko, J. J.; Turro, C., New Ru(ii) complex for dual photochemotherapy: release of cathepsin K inhibitor and 1O2 production. *Dalton Transactions* **2018,** *47* (34), 11851-11858.

74. Svozil, D.; Kalina, J.; Omelka, M.; Schneider, B., DNA conformations and their sequence preferences. *Nucleic Acids Research* **2008,** *36* (11), 3690-3706.

75. Sobell, H. M.; Jain, S. C., Stereochemistry of actinomycin binding to DNA. II. Detailed molecular model of actinomycin-DNA complex and its implications. *J Mol Biol* **1972,** *68* (1), 21-34.

76. Tsai, C. C.; Jain, S. C.; Sobell, H. M., Drug-nucleic acid interaction: X-ray crystallographic determination of an ethidium-dinucleoside monophosphate crystalline complex, ethidium: 5-iodouridylyl(3'-5')adenosine. *Philos Trans R Soc Lond B Biol Sci* **1975,** *272* (915), 137-46.

77. Watson, J. D.; Crick, F. H. C., Molecular Structure of Nucleic Acids: A Structure for Deoxyribose Nucleic Acid. *Nature* **1953,** *171* (4356), 737-738.

78. Almaqwashi, A. A.; Paramanathan, T.; Rouzina, I.; Williams, M. C., Mechanisms of small molecule-DNA interactions probed by single-molecule force spectroscopy. *Nucleic Acids Res* **2016,** *44* (9), 3971-88.

79. Dasari, S.; Tchounwou, P. B., Cisplatin in cancer therapy: molecular mechanisms of action. *Eur J Pharmacol* **2014,** *740*, 364-78.

80. Di Pietro, M. L.; La Ganga, G.; Nastasi, F.; Puntoriero, F. Ru(II)-Dppz Derivatives and Their Interactions with DNA: Thirty Years and Counting *Applied Sciences* [Online], 2021.

81. Eckel, R.; Ros, R.; Ros, A.; Wilking, S. D.; Sewald, N.; Anselmetti, D., Identification of binding mechanisms in single molecule-DNA complexes. *Biophys J* **2003,** *85* (3), 1968-73.

82. Mihailovic, A.; Vladescu, I.; McCauley, M.; Ly, E.; Williams, M. C.; Spain, E. M.; Nuñez, M. E., Exploring the interaction of ruthenium(II) polypyridyl complexes with DNA using single-molecule techniques. *Langmuir* **2006,** *22* (10), 4699-709.

83. Li, S.; Cooper, V.; Thonhauser, T.; Lundqvist, B.; Langreth, D., Stacking Interactions and DNA Intercalation. *The journal of physical chemistry. B* **2009,** *113*, 11166-72.

84. Kundu, S.; Maity, S.; Bhadra, R.; Ghosh, P., Trans-dichlorobis(N-p-tolylpyridin-2-amine)palladium(II): Synthesis, structure, fluorescence features and DNA binding. *Indian Journal of Chemistry - Section A Inorganic, Physical, Theoretical and Analytical Chemistry* **2011,** *50*.

85. Ju, C.-C.; Zhang, A.-G.; Yuan, C.-L.; Zhao, X.-L.; Wang, K.-Z., The interesting DNA-binding properties of three novel dinuclear Ru(II) complexes with varied lengths of flexible bridges. *Journal of inorganic biochemistry* **2011,** *105* (3), 435-443.

86. Chen, G.-J.; Qiao, X.; Gao, C.-Y.; Xu, G.-J.; Wang, Z.-L.; Tian, J.-L.; Xu, J.-Y.; Gu, W.; Liu, X.; Yan, S.-P., Synthesis, DNA binding, photo-induced DNA cleavage and cell cytotoxicity studies of a family of light rare earth complexes. *Journal of inorganic biochemistry* **2012,** *109*, 90-96.

87. Devi, C. S.; Thulasiram, B.; Satyanarayana, S.; Nagababu, P., Analytical Techniques Used to Detect DNA Binding Modes of Ruthenium(II) Complexes with Extended Phenanthroline Ring. *Journal of Fluorescence* **2017,** *27* (6), 2119-2130.

88. Nordén, B.; Kurucsev, T., Analysing DNA complexes by circular and linear dichroism. *J Mol Recognit* **1994,** *7* (2), 141-55.

89. Norden, B.; Kubista, M.; Kurucsev, T., Linear dichroism spectroscopy of nucleic acids. *Quarterly Reviews of Biophysics* **1992,** *25* (1), 51-170.

90. Rodger, A., How to study DNA and proteins by linear dichroism spectroscopy. *Sci Prog* **2008,** *91* (Pt 4), 377-96.

91. Kypr, J.; Kejnovská, I.; Renciuk, D.; Vorlícková, M., Circular dichroism and conformational polymorphism of DNA. *Nucleic Acids Res* **2009,** *37* (6), 1713-25.
92. Barai, H. R.; Lee, D. J.; Han, S. W.; Jang, Y. J. Interaction and Binding Modes of bis-Ruthenium(II) Complex to Synthetic DNAs *Metals* [Online], 2016.
93. Gilroy, E. L.; Hicks, M. R.; Smith, D. J.; Rodger, A., Viscosity of aqueous DNA solutions determined using dynamic light scattering. *Analyst* **2011,** *136* (20), 4159-4163.
94. Satyanarayana, S.; Dabrowiak, J. C.; Chaires, J. B., Neither .DELTA.- nor .LAMBDA.-tris(phenanthroline)ruthenium(II) binds to DNA by classical intercalation. *Biochemistry* **1992,** *31* (39), 9319-9324.
95. Barton, J. K.; Danishefsky, A.; Goldberg, J., Tris(phenanthroline)ruthenium(II): stereoselectivity in binding to DNA. *Journal of the American Chemical Society* **1984,** *106* (7), 2172-2176.
96. Satyanarayana, S.; Dabrowiak, J. C.; Chaires, J. B., Tris(phenanthroline)ruthenium(II) enantiomer interactions with DNA: Mode and specificity of binding. *Biochemistry* **1993,** *32* (10), 2573-2584.
97. Liu, Y.-J.; Chao, H.; Tan, L.-F.; Yuan, Y.-X.; Wei, W.; Ji, L.-N., Interaction of polypyridyl ruthenium (II) complex containing asymmetric ligand with DNA. *Journal of inorganic biochemistry* **2005,** *99* (2), 530-537.
98. Neyhart, G. A.; Grover, N.; Smith, S. R.; Kalsbeck, W. A.; Fairley, T. A.; Cory, M.; Thorp, H. H., Binding and kinetics studies of oxidation of DNA by oxoruthenium(IV). *Journal of the American Chemical Society* **1993,** *115* (11), 4423-4428.
99. Koenig, V. L.; Carrier, W. L.; Rahn, R. O., Viscosity studies on dna and the observation of double-stranded and single-stranded breaks in a 40% dmso-phosphate buffer system. *International Journal of Biochemistry* **1974,** *5* (7), 601-611.
100. Olmsted, J., III; Kearns, D. R., Mechanism of ethidium bromide fluorescence enhancement on binding to nucleic acids. *Biochemistry* **1977,** *16* (16), 3647-3654.
101. Lazić, D.; Arsenijević, A.; Puchta, R.; Bugarčić, Ž. D.; Rilak, A., DNA binding properties, histidine interaction and cytotoxicity studies of water soluble ruthenium(ii) terpyridine complexes. *Dalton Transactions* **2016,** *45* (11), 4633-4646.
102. Altammar, K. A., A review on nanoparticles: characteristics, synthesis, applications, and challenges. *Frontiers in Microbiology* **2023,** *14*.
103. Harish, V.; Tewari, D.; Gaur, M.; Yadav, A. B.; Swaroop, S.; Bechelany, M.; Barhoum, A., Review on Nanoparticles and Nanostructured Materials: Bioimaging, Biosensing, Drug Delivery, Tissue Engineering, Antimicrobial, and Agro-Food Applications. *Nanomaterials (Basel)* **2022,** *12* (3).
104. Khan, I.; Saeed, K.; Khan, I., Nanoparticles: Properties, applications and toxicities. *Arabian Journal of Chemistry* **2019,** *12* (7), 908-931.
105. Jiang, Y.; Liu, J.; Qin, J.; Lei, J.; Zhang, X.; Xu, Z.; Li, W.; Liu, X.; Wang, R.; Li, B.; Lu, X., Light-activated gold nanorods for effective therapy of venous malformation. *Materials Today Bio* **2022,** *16*, 100401.
106. Liu, Y.; Yuan, H.; Fales, A. M.; Register, J. K.; Vo-Dinh, T., Multifunctional gold nanostars for molecular imaging and cancer therapy. *Front Chem* **2015,** *3*, 51.
107. Bai, L.; Jiang, F.; Wang, R.; Lee, C.; Wang, H.; Zhang, W.; Jiang, W.; Li, D.; Ji, B.; Li, Z.; Gao, S.; Xie, J.; Ma, Q., Ultrathin gold nanowires to enhance radiation therapy. *J Nanobiotechnology* **2020,** *18* (1), 131.
108. Fu, Y.; Li, X.; Ren, Z.; Mao, C.; Han, G., Multifunctional Electrospun Nanofibers for Enhancing Localized Cancer Treatment. *Small* **2018**, e1801183.
109. Dirheimer, L.; Pons, T.; Marchal, F.; Bezdetnaya, L. Quantum Dots Mediated Imaging and Phototherapy in Cancer Spheroid Models: State of the Art and Perspectives *Pharmaceutics* [Online], 2022.
110. Jain, S.; Hirst, D. G.; O'Sullivan, J. M., Gold nanoparticles as novel agents for cancer therapy. *Br J Radiol* **2012,** *85* (1010), 101-13.

111. Gomes, H. I. O.; Martins, C. S. M.; Prior, J. A. V., Silver Nanoparticles as Carriers of Anticancer Drugs for Efficient Target Treatment of Cancer Cells. *Nanomaterials (Basel)* **2021,** *11* (4).

112. Samadi, A.; Klingberg, H.; Jauffred, L.; Kjær, A.; Bendix, P. M.; Oddershede, L. B., Platinum nanoparticles: a non-toxic, effective and thermally stable alternative plasmonic material for cancer therapy and bioengineering. *Nanoscale* **2018,** *10* (19), 9097-9107.

113. Yin, X.; Fan, T.; Zheng, N.; Yang, J.; Yan, L.; He, S.; Ai, F.; Hu, J., Palladium nanoparticle based smart hydrogels for NIR light-triggered photothermal/photodynamic therapy and drug release with wound healing capability. *Nanoscale Advances* **2023,** *5* (6), 1729-1739.

114. Shah, S.; Famta, P.; Bagasariya, D.; Charankumar, K.; Sikder, A.; Kashikar, R.; Kotha, A. K.; Chougule, M. B.; Khatri, D. K.; Asthana, A.; Raghuvanshi, R. S.; Singh, S. B.; Srivastava, S., Tuning Mesoporous Silica Nanoparticles in Novel Avenues of Cancer Therapy. *Molecular pharmaceutics* **2022,** *19* (12), 4428-4452.

115. Omurtag Ozgen, P. S.; Atasoy, S.; Zengin Kurt, B.; Durmus, Z.; Yigit, G.; Dag, A., Glycopolymer decorated multiwalled carbon nanotubes for dual targeted breast cancer therapy. *Journal of Materials Chemistry B* **2020,** *8* (15), 3123-3137.

116. Dristant, U.; Mukherjee, K.; Saha, S.; Maity, D., An Overview of Polymeric Nanoparticles-Based Drug Delivery System in Cancer Treatment. *Technol Cancer Res Treat* **2023,** *22*, 15330338231152083.

117. Friedman, A. D.; Claypool, S. E.; Liu, R., The smart targeting of nanoparticles. *Current pharmaceutical design* **2013,** *19* (35), 6315-29.

118. Rai, A.; Noor, S.; Ahmad, S. I.; Alajmi, M. F.; Hussain, A.; Abbas, H.; Hasan, G. M. Recent Advances and Implication of Bioengineered Nanomaterials in Cancer Theranostics *Medicina* [Online], 2021.

119. Doughty, A. C. V.; Hoover, A. R.; Layton, E.; Murray, C. K.; Howard, E. W.; Chen, W. R. Nanomaterial Applications in Photothermal Therapy for Cancer *Materials* [Online], 2019.

120. Quader, S.; Kataoka, K., Nanomaterial-Enabled Cancer Therapy. *Mol Ther* **2017,** *25* (7), 1501-1513.

121. Barenholz, Y., Doxil®--the first FDA-approved nano-drug: lessons learned. *J Control Release* **2012,** *160* (2), 117-34.

122. Ahmad, S.; Idris, R. A. M.; Wan Hanaffi, W. N.; Perumal, K.; Boer, J. C.; Plebanski, M.; Jaafar, J.; Lim, J. K.; Mohamud, R., Cancer Nanomedicine and Immune System—Interactions and Challenges. *Frontiers in Nanotechnology* **2021,** *3*.

123. Jia, Y.; Jiang, Y.; He, Y.; Zhang, W.; Zou, J.; Magar, K. T.; Boucetta, H.; Teng, C.; He, W. Approved Nanomedicine against Diseases *Pharmaceutics* [Online], 2023.

124. Polack, F. P.; Thomas, S. J.; Kitchin, N.; Absalon, J.; Gurtman, A.; Lockhart, S.; Perez, J. L.; Pérez Marc, G.; Moreira, E. D.; Zerbini, C.; Bailey, R.; Swanson, K. A.; Roychoudhury, S.; Koury, K.; Li, P.; Kalina, W. V.; Cooper, D.; Frenck, R. W., Jr.; Hammitt, L. L.; Türeci, Ö.; Nell, H.; Schaefer, A.; Ünal, S.; Tresnan, D. B.; Mather, S.; Dormitzer, P. R.; Şahin, U.; Jansen, K. U.; Gruber, W. C., Safety and Efficacy of the BNT162b2 mRNA Covid-19 Vaccine. *N Engl J Med* **2020,** *383* (27), 2603-2615.

125. Szebeni, J.; Kiss, B.; Bozó, T.; Turjeman, K.; Levi-Kalisman, Y.; Barenholz, Y.; Kellermayer, M., Insights into the Structure of Comirnaty Covid-19 Vaccine: A Theory on Soft, Partially Bilayer-Covered Nanoparticles with Hydrogen Bond-Stabilized mRNA-Lipid Complexes. *ACS Nano* **2023,** *17* (14), 13147-13157.

126. Jia, Y.; Jiang, Y.; He, Y.; Zhang, W.; Zou, J.; Magar, K. T.; Boucetta, H.; Teng, C.; He, W., Approved Nanomedicine against Diseases. *Pharmaceutics* **2023,** *15* (3).

127. Rodríguez, F.; Caruana, P.; De la Fuente, N.; Español, P.; Gámez, M.; Balart, J.; Llurba, E.; Rovira, R.; Ruiz, R.; Martín-Lorente, C.; Corchero, J. L.; Céspedes, M. V., Nano-Based Approved Pharmaceuticals for Cancer Treatment: Present and Future Challenges. *Biomolecules* **2022,** *12* (6).

128. Cucinotto, I.; Fiorillo, L.; Gualtieri, S.; Arbitrio, M.; Ciliberto, D.; Staropoli, N.; Grimaldi, A.; Luce, A.; Tassone, P.; Caraglia, M.; Tagliaferri, P., Nanoparticle albumin bound Paclitaxel in the treatment of human cancer: nanodelivery reaches prime-time? *J Drug Deliv* **2013,** *2013*, 905091.

129. Gerosa, C.; Crisponi, G.; Nurchi, V. M.; Saba, L.; Cappai, R.; Cau, F.; Faa, G.; Van Eyken, P.; Scartozzi, M.; Floris, G.; Fanni, D., Gold Nanoparticles: A New Golden Era in Oncology? *Pharmaceuticals (Basel)* **2020,** *13* (8).

130. Anik, M. I.; Mahmud, N.; Al Masud, A.; Hasan, M., Gold nanoparticles (GNPs) in biomedical and clinical applications: A review. *Nano Select* **2022,** *3* (4), 792-828.

131. Rad, A.; Abbasi, H.; Afzali, M., Gold Nanoparticles: Synthesising, Characterizing and Reviewing Novel Application in Recent Years. *Physics Procedia* **2011,** *22*, 203-208.

132. Yeh, Y.-C.; Creran, B.; Rotello, V. M., Gold nanoparticles: preparation, properties, and applications in bionanotechnology. *Nanoscale* **2012,** *4* (6), 1871-1880.

133. Dheyab, M. A.; Aziz, A. A.; Moradi Khaniabadi, P.; Jameel, M. S.; Oladzadabbasabadi, N.; Mohammed, S. A.; Abdullah, R. S.; Mehrdel, B., Monodisperse Gold Nanoparticles: A Review on Synthesis and Their Application in Modern Medicine. *International journal of molecular sciences* **2022,** *23* (13).

134. Amendola, V.; Pilot, R.; Frasconi, M.; Maragò, O. M.; Iatì, M. A., Surface plasmon resonance in gold nanoparticles: a review. *Journal of Physics: Condensed Matter* **2017,** *29* (20), 203002.

135. Mayer, K. M.; Hafner, J. H., Localized Surface Plasmon Resonance Sensors. *Chemical Reviews* **2011,** *111* (6), 3828-3857.

136. Hu, M.; Novo, C.; Funston, A.; Wang, H.; Staleva, H.; Zou, S.; Mulvaney, P.; Xia, Y.; Hartland, G. V., Dark-field microscopy studies of single metal nanoparticles: understanding the factors that influence the linewidth of the localized surface plasmon resonance. *J Mater Chem* **2008,** *18* (17), 1949-1960.

137. Li, W.; Chen, X., Gold nanoparticles for photoacoustic imaging. *Nanomedicine (Lond)* **2015,** *10* (2), 299-320.

138. Azubel, M.; Koivisto, J.; Malola, S.; Bushnell, D.; Hura, G. L.; Koh, A. L.; Tsunoyama, H.; Tsukuda, T.; Pettersson, M.; Häkkinen, H.; Kornberg, R. D., Nanoparticle imaging. Electron microscopy of gold nanoparticles at atomic resolution. *Science (New York, N.Y.)* **2014,** *345* (6199), 909-12.

139. Li, C.-H.; Chan, M.-H.; Chang, Y.-C.; Hsiao, M. Gold Nanoparticles as a Biosensor for Cancer Biomarker Determination *Molecules* [Online], 2023.

140. Lin, D.; Shen, L.; Luo, M.; Zhang, K.; Li, J.; Yang, Q.; Zhu, F.; Zhou, D.; Zheng, S.; Chen, Y.; Zhou, J., Circulating tumor cells: biology and clinical significance. *Signal Transduction and Targeted Therapy* **2021,** *6* (1), 404.

141. Huang, X.; O'Connor, R.; Kwizera, E. A., Gold Nanoparticle Based Platforms for Circulating Cancer Marker Detection. *Nanotheranostics* **2017,** *1* (1), 80-102.

142. Sheng, W.; Chen, T.; Tan, W.; Fan, Z. H., Multivalent DNA Nanospheres for Enhanced Capture of Cancer Cells in Microfluidic Devices. *ACS Nano* **2013,** *7* (8), 7067-7076.

143. Yang, Y.; Hong, H.; Zhang, Y.; Cai, W., Molecular Imaging of Proteases in Cancer. *Cancer Growth Metastasis* **2009,** *2*, 13-27.

144. Loynachan, C. N.; Soleimany, A. P.; Dudani, J. S.; Lin, Y.; Najer, A.; Bekdemir, A.; Chen, Q.; Bhatia, S. N.; Stevens, M. M., Renal clearable catalytic gold nanoclusters for in vivo disease monitoring. *Nat Nanotechnol* **2019,** *14* (9), 883-890.

145. Ma, X.; Song, S.; Kim, S.; Kwon, M.-s.; Lee, H.; Park, W.; Sim, S. J., Single gold-bridged nanoprobes for identification of single point DNA mutations. *Nature Communications* **2019,** *10* (1), 836.

146. Qiao, X.; Su, B.; Liu, C.; Song, Q.; Luo, D.; Mo, G.; Wang, T., Selective Surface Enhanced Raman Scattering for Quantitative Detection of Lung Cancer Biomarkers in Superparticle@MOF Structure. *Advanced Materials* **2018,** *30* (5), 1702275.

147. Huang, X.; El-Sayed, M. A., Gold nanoparticles: Optical properties and implementations in cancer diagnosis and photothermal therapy. *Journal of Advanced Research* **2010,** *1* (1), 13-28.
148. Dhada, K. S.; Hernandez, D. S.; Suggs, L. J., In Vivo Photoacoustic Tracking of Mesenchymal Stem Cell Viability. *ACS Nano* **2019,** *13* (7), 7791-7799.
149. Kwon, K. C.; Jo, E.; Kwon, Y. W.; Lee, B.; Ryu, J. H.; Lee, E. J.; Kim, K.; Lee, J., Superparamagnetic Gold Nanoparticles Synthesized on Protein Particle Scaffolds for Cancer Theragnosis. *Adv Mater* **2017,** *29* (38).
150. Kim, T.; Lee, N.; Arifin, D. R.; Shats, I.; Janowski, M.; Walczak, P.; Hyeon, T.; Bulte, J. W. M., In Vivo Micro-CT Imaging of Human Mesenchymal Stem Cells Labeled with Gold-Poly-L-Lysine Nanocomplexes. *Adv Funct Mater* **2017,** *27* (3).
151. Jia, X.; Xu, W.; Ye, Z.; Wang, Y.; Dong, Q.; Wang, E.; Li, D.; Wang, J., Functionalized Graphene@Gold Nanostar/Lipid for Pancreatic Cancer Gene and Photothermal Synergistic Therapy under Photoacoustic/Photothermal Imaging Dual-Modal Guidance. *Small* **2020,** *16* (39), e2003707.
152. Tian, F.; Conde, J.; Bao, C.; Chen, Y.; Curtin, J.; Cui, D., Gold nanostars for efficient in vitro and in vivo real-time SERS detection and drug delivery via plasmonic-tunable Raman/FTIR imaging. *Biomaterials* **2016,** *106*, 87-97.
153. Yahia-Ammar, A.; Sierra, D.; Mérola, F.; Hildebrandt, N.; Le Guével, X., Self-Assembled Gold Nanoclusters for Bright Fluorescence Imaging and Enhanced Drug Delivery. *ACS Nano* **2016,** *10* (2), 2591-2599.
154. García Calavia, P.; Bruce, G.; Pérez-García, L.; Russell, D. A., Photosensitiser-gold nanoparticle conjugates for photodynamic therapy of cancer. *Photochemical & Photobiological Sciences* **2018,** *17* (11), 1534-1552.
155. Guerrero-Florez, V.; Mendez-Sanchez, S. C.; Patrón-Soberano, O. A.; Rodríguez-González, V.; Blach, D.; Martínez O, F., Gold nanoparticle-mediated generation of reactive oxygen species during plasmonic photothermal therapy: a comparative study for different particle sizes, shapes, and surface conjugations. *Journal of Materials Chemistry B* **2020,** *8* (14), 2862-2875.
156. Lo, C.-Y.; Tsai, S.-W.; Niu, H.; Chen, F.-H.; Hwang, H.-C.; Chao, T.-C.; Hsiao, I.-T.; Liaw, J.-W., Gold-Nanoparticles-Enhanced Production of Reactive Oxygen Species in Cells at Spread-Out Bragg Peak under Proton Beam Radiation. *ACS Omega* **2023,** *8* (20), 17922-17931.
157. Gao, W.; Xu, K.; Ji, L.; Tang, B., Effect of gold nanoparticles on glutathione depletion-induced hydrogen peroxide generation and apoptosis in HL7702 cells. *Toxicology Letters* **2011,** *205* (1), 86-95.
158. Čapek, J.; Roušar, T., Detection of Oxidative Stress Induced by Nanomaterials in Cells-The Roles of Reactive Oxygen Species and Glutathione. *Molecules* **2021,** *26* (16).
159. He, W.; Zhou, Y.-T.; Wamer, W. G.; Hu, X.; Wu, X.; Zheng, Z.; Boudreau, M. D.; Yin, J.-J., Intrinsic catalytic activity of Au nanoparticles with respect to hydrogen peroxide decomposition and superoxide scavenging. *Biomaterials* **2013,** *34* (3), 765-773.
160. Zhang, R.; Kiessling, F.; Lammers, T.; Pallares, R. M., Clinical translation of gold nanoparticles. *Drug Delivery and Translational Research* **2023,** *13* (2), 378-385.
161. Lopez-Chaves, C.; Soto-Alvaredo, J.; Montes-Bayon, M.; Bettmer, J.; Llopis, J.; Sanchez-Gonzalez, C., Gold nanoparticles: Distribution, bioaccumulation and toxicity. In vitro and in vivo studies. *Nanomedicine* **2018,** *14* (1), 1-12.
162. Nilubol, N.; Oarr, D.; Tamarkin, L., Preclinical studies evaluate pivotal TNFα nanomedicine clinical trial design. *Journal of Clinical Oncology* **2019,** *37* (15_suppl), e14646-e14646.
163. Idriss, H. T.; Naismith, J. H., TNF alpha and the TNF receptor superfamily: structure-function relationship(s). *Microsc Res Tech* **2000,** *50* (3), 184-95.
164. Libutti, S. K.; Paciotti, G. F.; Byrnes, A. A.; Alexander, H. R., Jr.; Gannon, W. E.; Walker, M.; Seidel, G. D.; Yuldasheva, N.; Tamarkin, L., Phase I and pharmacokinetic studies of CYT-

6091, a novel PEGylated colloidal gold-rhTNF nanomedicine. *Clin Cancer Res* **2010,** *16* (24), 6139-49.

165. Dumas, E.; Miomandre, F.; Warmont, F.; Vigneron, J.; Pansu, R.; Etcheberry, A., Polypyridyl ruthenium complexes as coating agent for the formation of gold and silver nanocomposites in different media. Preliminary luminescence and electrochemical studies. *New Journal of Chemistry - NEW J CHEM* **2006,** *30*.

166. Zhang, P.; Wang, J.; Huang, H.; Chen, H.; Guan, R.; Chen, Y.; Ji, L.; Chao, H., RuNH2@AuNPs as two-photon luminescent probes for thiols in living cells and tissues. *Biomaterials* **2014,** *35* (32), 9003-9011.

167. Zhang, P.; Wang, J.; Huang, H.; Yu, B.; Qiu, K.; Huang, J.; Wang, S.; Jiang, L.; Gasser, G.; Ji, L.; Chao, H., Unexpected high photothemal conversion efficiency of gold nanospheres upon grafting with two-photon luminescent ruthenium(II) complexes: A way towards cancer therapy? *Biomaterials* **2015,** *63*, 102-114.

168. Han, H. S.; Choi, K. Y., Advances in Nanomaterial-Mediated Photothermal Cancer Therapies: Toward Clinical Applications. *Biomedicines* **2021,** *9* (3).

169. Thangavel, N.; Jayakumar, I.; Ravichandran, M.; Vaidyanathan Ganesan, V.; Nair, B. U., Photocrosslinking of collagen using Ru(II)-polypyridyl complex functionalized gold nanoparticles. *Spectrochimica Acta Part A: Molecular and Biomolecular Spectroscopy* **2019,** *215*, 196-202.

170. Gopalakrishnan, D.; Saravanan, S.; Merckx, R.; Madan Kumar, A.; Khamrang, T.; Velusamy, M.; Vasanth, K.; Sunitha, S.; Hoogenboom, R.; Maji, S.; Ganeshpandian, M., N,N-Ru(ii)-p-cymene-poly(N-vinylpyrrolidone) surface functionalized gold nanoparticles: from organoruthenium complex to nanomaterial for antiproliferative activity. *Dalton Transactions* **2021,** *50* (23), 8232-8242.

171. Guler, S.; Kayali, H. A.; Sadan, E. O.; Sen, B.; Subasi, E., Half-Sandwich Arene Ruthenium(II) Thiosemicarbazone Complexes: Evaluation of Anticancer Effect on Primary and Metastatic Ovarian Cancer Cell Lines. *Frontiers in Pharmacology* **2022,** *13*.

172. İnan, A.; Sünbül, A. B.; İkiz, M.; Tayhan, S. E.; Bilgin, S.; Elmastaş, M.; Sayın, K.; Ceyhan, G.; Köse, M.; İspir, E., Half-sandwich Ruthenium(II) arene complexes bearing the azo-azomethine ligands: Electrochemical, computational, antiproliferative and antioxidant properties. *Journal of Organometallic Chemistry* **2018,** *870*, 76-89.

173. Abrahamsson, M.; Wolpher, H.; Johansson, O.; Larsson, J.; Kritikos, M.; Eriksson, L.; Norrby, P.-O.; Bergquist, J.; Sun, L.; Åkermark, B.; Hammarström, L., A New Strategy for the Improvement of Photophysical Properties in Ruthenium(II) Polypyridyl Complexes. Synthesis and Photophysical and Electrochemical Characterization of Six Mononuclear Ruthenium(II) Bisterpyridine-Type Complexes. *Inorganic Chemistry* **2005,** *44* (9), 3215-3225.

174. Crosby, G. A.; Demas, J. N., Quantum efficiencies on transition metal complexes. II. Charge-transfer luminescence. *Journal of the American Chemical Society* **1971,** *93* (12), 2841-2847.

175. Cooke, M. M.; Doeven, E. H.; Hogan, C. F.; Adcock, J. L.; McDermott, G. P.; Conlan, X. A.; Barnett, N. W.; Pfeffer, F. M.; Francis, P. S., Comparison of homoleptic and heteroleptic 2,2′-bipyridine and 1,10-phenanthroline ruthenium complexes as chemiluminescence and electrochemiluminescence reagents in aqueous solution. *Analytica chimica acta* **2009,** *635* (1), 94-101.

176. Pyle, A. M.; Rehmann, J. P.; Meshoyrer, R.; Kumar, C. V.; Turro, N. J.; Barton, J. K., Mixed-ligand complexes of ruthenium(II): factors governing binding to DNA. *Journal of the American Chemical Society* **1989,** *111* (8), 3051-3058.

177. Bernhard, S.; Barron, J. A.; Houston, P. L.; Abruña, H. D.; Ruglovksy, J. L.; Gao, X.; Malliaras, G. G., Electroluminescence in Ruthenium(II) Complexes. *Journal of the American Chemical Society* **2002,** *124* (45), 13624-13628.

178. Nakamaru, K., Synthesis, Luminescence Quantum Yields, and Lifetimes of Trischelated Ruthenium(II) Mixed-ligand Complexes Including 3,3′-Dimethyl-2,2′-bipyridyl. *Bulletin of the Chemical Society of Japan* **1982,** *55* (9), 2697-2705.
179. Introduction. In *Molecular Fluorescence*, 2012; pp 1-30.
180. Absorption of Ultraviolet, Visible, and Near-Infrared Radiation. In *Molecular Fluorescence*, 2012; pp 31-51.
181. Characteristics of Fluorescence Emission. In *Molecular Fluorescence*, 2012; pp 53-74.
182. Izci, M.; Maksoudian, C.; Manshian, B. B.; Soenen, S. J., The Use of Alternative Strategies for Enhanced Nanoparticle Delivery to Solid Tumors. *Chem Rev* **2021,** *121* (3), 1746-1803.
183. Peckys, D. B.; de Jonge, N., Visualizing gold nanoparticle uptake in live cells with liquid scanning transmission electron microscopy. *Nano Lett* **2011,** *11* (4), 1733-8.
184. Katoozi, D.; Clayton, A. H. A.; Moss, D. J.; Chon, J. W. M., Uptake quantification of gold nanoparticles inside of cancer cells using high order image correlation spectroscopy. *Biomed Opt Express* **2021,** *12* (1), 539-552.
185. Kuznetsova, O. V.; Rubio, G.; Keppler, B. K.; Chin, J. M.; Reithofer, M. R.; Timerbaev, A. R., An ICP-MS-based assay for characterization of gold nanoparticles with potential biomedical use. *Anal Biochem* **2020,** *611*, 114003.
186. Noireaux, J.; Grall, R.; Hullo, M.; Chevillard, S.; Oster, C.; Brun, E.; Sicard-Roselli, C.; Loeschner, K.; Fisicaro, P. Gold Nanoparticle Uptake in Tumor Cells: Quantification and Size Distribution by sp-ICPMS *Separations* [Online], 2019.
187. Abdelrasoul, G. N.; Magrassi, R.; Dante, S.; d'Amora, M.; d'Abbusco, M. S.; Pellegrino, T.; Diaspro, A., PEGylated gold nanorods as optical trackers for biomedical applications: an in vivo and in vitro comparative study. *Nanotechnology* **2016,** *27* (25), 255101.
188. Kim, C. S.; Li, X.; Jiang, Y.; Yan, B.; Tonga, G. Y.; Ray, M.; Solfiell, D. J.; Rotello, V. M., Cellular imaging of endosome entrapped small gold nanoparticles. *MethodsX* **2015,** *2*, 306-15.
189. Li, M.-J.; Liu, X.; Nie, M.-J.; Wu, Z.-Z.; Yi, C.-Q.; Chen, G.-N., New Rhenium(I) Complexes: Synthesis, Photophysics, Cytotoxicity, and Functionalization of Gold Nanoparticles for Sensing of Esterase. *Organometallics* **2012,** *31* (12), 4459-4466.
190. Robson, J. A.; Gonzàlez de Rivera, F.; Jantan, K. A.; Wenzel, M. N.; White, A. J. P.; Rossell, O.; Wilton-Ely, J. D. E. T., Bifunctional Chalcogen Linkers for the Stepwise Generation of Multimetallic Assemblies and Functionalized Nanoparticles. *Inorganic Chemistry* **2016,** *55* (24), 12982-12996.
191. D'Souza, S.; Moeno, S.; Antunes, E.; Nyokong, T., Effects of gold nanoparticle shape on the aggregation and fluorescence behaviour of water soluble zinc phthalocyanines. *New Journal of Chemistry* **2013,** *37* (7), 1950-1958.
192. Blakey, I.; Schiller, T. L.; Merican, Z.; Fredericks, P. M., Interactions of phenyldithioesters with gold nanoparticles (AuNPs): implications for AuNP functionalization and molecular barcoding of AuNP assemblies. *Langmuir* **2010,** *26* (2), 692-701.
193. Chegel, V.; Rachkov, O.; Lopatynskyi, A.; Ishihara, S.; Yanchuk, I.; Nemoto, Y.; Hill, J. P.; Ariga, K., Gold Nanoparticles Aggregation: Drastic Effect of Cooperative Functionalities in a Single Molecular Conjugate. *The Journal of Physical Chemistry C* **2012,** *116* (4), 2683-2690.
194. Dosumu, A. N.; Claire, S.; Watson, L. S.; Girio, P. M.; Osborne, S. A. M.; Pikramenou, Z.; Hodges, N. J., Quantification by Luminescence Tracking of Red Emissive Gold Nanoparticles in Cells. *JACS Au* **2021,** *1* (2), 174-186.
195. Osborne, S. A. M.; Pikramenou, Z., Highly luminescent gold nanoparticles: effect of ruthenium distance for nanoprobes with enhanced lifetimes. *Faraday Discussions* **2015,** *185* (0), 219-231.
196. Rogers, N. J.; Claire, S.; Harris, R. M.; Farabi, S.; Zikeli, G.; Styles, I. B.; Hodges, N. J.; Pikramenou, Z., High coating of Ru(ii) complexes on gold nanoparticles for single particle luminescence imaging in cells. *Chemical Communications* **2014,** *50* (5), 617-619.

197. Dong, T.-Y.; Shih, H.-W.; Chang, L.-S., Synthesis and Redox Behavior of Biferrocenyl-Functionalized Ruthenium(II) Terpyridine Gold Clusters. *Langmuir* **2004,** *20* (21), 9340-9347.
198. Wang, S.; Sim, W. S., Au nanoparticles encapsulated in Ru carbonyl carboxylate shells. *Langmuir* **2006,** *22* (18), 7861-6.
199. Liu, F.; Nunzi, J.-M., Phosphorescent organic light emitting diode efficiency enhancement using functionalized silver nanoparticles. *Applied Physics Letters* **2011,** *99* (12), 123302.
200. Lakowicz, J. R., Radiative decay engineering: biophysical and biomedical applications. *Anal Biochem* **2001,** *298* (1), 1-24.
201. Eustis, S.; El-Sayed, M. A., Why gold nanoparticles are more precious than pretty gold: Noble metal surface plasmon resonance and its enhancement of the radiative and nonradiative properties of nanocrystals of different shapes. *Chemical Society reviews* **2006,** *35* (3), 209-217.
202. Kedem, O.; Wohlleben, W.; Rubinstein, I., Distance-dependent fluorescence of tris(bipyridine)ruthenium(ii) on supported plasmonic gold nanoparticle ensembles. *Nanoscale* **2014,** *6* (24), 15134-15143.
203. Estalayo-Adrián, S.; McManus, G. J.; Dalton, H. L.; Savyasachi, A. J.; Kelly, J. M.; Gunnlaugsson, T., Functionalisation of gold nanoparticles with ruthenium(ii) polypyridyl complexes for their application in cellular imaging. *Dalton Transactions* **2020,** *49* (40), 14158-14168.
204. Rotem, R.; Giustra, M.; Arrigoni, F.; Bertolini, J. A.; Garbujo, S.; Rizzuto, M. A.; Salvioni, L.; Barbieri, L.; Bertini, L.; De Gioia, L.; Colombo, M.; Prosperi, D., Conjugation of gold nanoparticles with multidentate surfactants for enhanced stability and biological properties. *Journal of Materials Chemistry B* **2023,** *11* (1), 61-71.
205. Shrestha, S.; Wang, B.; Dutta, P., Nanoparticle processing: Understanding and controlling aggregation. *Advances in Colloid and Interface Science* **2020,** *279*, 102162.
206. Jain, P.; El-Sayed, M., Plasmonic Coupling in Noble Metal Nanostructures. *Chemical Physics Letters* **2009,** *487*, 153-164.
207. Shipway, A. N.; Lahav, M.; Gabai, R.; Willner, I., Investigations into the Electrostatically Induced Aggregation of Au Nanoparticles. *Langmuir* **2000,** *16* (23), 8789-8795.
208. Blakey, I.; Merican, Z.; Thurecht, K. J., A Method for Controlling the Aggregation of Gold Nanoparticles: Tuning of Optical and Spectroscopic Properties. *Langmuir* **2013,** *29* (26), 8266-8274.
209. Alkilany, A. M.; Murphy, C. J., Toxicity and cellular uptake of gold nanoparticles: what we have learned so far? *J Nanopart Res* **2010,** *12* (7), 2313-2333.
210. Moore, T. L.; Rodriguez-Lorenzo, L.; Hirsch, V.; Balog, S.; Urban, D.; Jud, C.; Rothen-Rutishauser, B.; Lattuada, M.; Petri-Fink, A., Nanoparticle colloidal stability in cell culture media and impact on cellular interactions. *Chemical Society reviews* **2015,** *44* (17), 6287-6305.
211. Albanese, A.; Chan, W. C. W., Effect of Gold Nanoparticle Aggregation on Cell Uptake and Toxicity. *ACS Nano* **2011,** *5* (7), 5478-5489.
212. Yang, Y.; Matsubara, S.; Nogami, M.; Shi, J., Controlling the aggregation behavior of gold nanoparticles. *Materials Science and Engineering: B* **2007,** *140* (3), 172-176.
213. Reznickova, A.; Slavikova, N.; Kolska, Z.; Kolarova, K.; Belinova, T.; Hubalek Kalbacova, M.; Cieslar, M.; Svorcik, V., PEGylated gold nanoparticles: Stability, cytotoxicity and antibacterial activity. *Colloids and Surfaces A: Physicochemical and Engineering Aspects* **2019,** *560*, 26-34.
214. David, S.; Patel, D. Y.; Cardona, S. M.; Kirby, N.; Mayer, K. M., Cellular uptake and cytotoxicity of PEGylated gold nanoparticles in C33A cervical cancer cells. *Nano Express* **2022,** *3* (2), 025006.
215. Wang, Y.; Quinsaat, J. E. Q.; Ono, T.; Maeki, M.; Tokeshi, M.; Isono, T.; Tajima, K.; Satoh, T.; Sato, S.-i.; Miura, Y.; Yamamoto, T., Enhanced dispersion stability of gold nanoparticles by the physisorption of cyclic poly(ethylene glycol). *Nature Communications* **2020,** *11* (1), 6089.

216. Chen, T. Y.; Chen, M. R.; Liu, S. W.; Lin, J. Y.; Yang, Y. T.; Huang, H. Y.; Chen, J. K.; Yang, C. S.; Lin, K. M., Assessment of Polyethylene Glycol-Coated Gold Nanoparticle Toxicity and Inflammation In Vivo Using NF-κB Reporter Mice. *International journal of molecular sciences* **2020,** *21* (21).
217. Zhang, G.; Yang, Z.; Lu, W.; Zhang, R.; Huang, Q.; Tian, M.; Li, L.; Liang, D.; Li, C., Influence of anchoring ligands and particle size on the colloidal stability and in vivo biodistribution of polyethylene glycol-coated gold nanoparticles in tumor-xenografted mice. *Biomaterials* **2009,** *30* (10), 1928-1936.
218. Otsuka, H.; Nagasaki, Y.; Kataoka, K., PEGylated nanoparticles for biological and pharmaceutical applications. *Advanced Drug Delivery Reviews* **2003,** *55* (3), 403-419.
219. Clark, A. J.; Davis, M. E., Increased brain uptake of targeted nanoparticles by adding an acid-cleavable linkage between transferrin and the nanoparticle core. *Proceedings of the National Academy of Sciences* **2015,** *112* (40), 12486-12491.
220. Farokhzad, O. C.; Jon, S.; Khademhosseini, A.; Tran, T. N.; Lavan, D. A.; Langer, R., Nanoparticle-aptamer bioconjugates: a new approach for targeting prostate cancer cells. *Cancer Res* **2004,** *64* (21), 7668-72.
221. Siddique, S.; Chow, J. C. L. Gold Nanoparticles for Drug Delivery and Cancer Therapy *Applied Sciences* [Online], 2020.
222. Liu, J.; Cao, Z.; Lu, Y., Functional nucleic acid sensors. *Chem Rev* **2009,** *109* (5), 1948-98.
223. Li, D.; Song, S.; Fan, C., Target-responsive structural switching for nucleic acid-based sensors. *Acc Chem Res* **2010,** *43* (5), 631-41.
224. Zhang, X.; Huang, P.-J. J.; Servos, M. R.; Liu, J., Effects of Polyethylene Glycol on DNA Adsorption and Hybridization on Gold Nanoparticles and Graphene Oxide. *Langmuir* **2012,** *28* (40), 14330-14337.
225. Wei, M.-Z.; Deng, T.-S.; Zhang, Q.; Cheng, Z.; Li, S., Seed-Mediated Synthesis of Gold Nanorods at Low Concentrations of CTAB. *ACS Omega* **2021,** *6* (13), 9188-9195.
226. Kalipillai, P.; Raghuram, E.; Bandyopadhyay, S.; Mani, E., Self-assembly of a CTAB surfactant on gold nanoparticles: a united-atom molecular dynamics study. *Physical Chemistry Chemical Physics* **2022,** *24* (46), 28353-28361.
227. Mourdikoudis, S.; Menelaou, M.; Fiuza-Maneiro, N.; Zheng, G.; Wei, S.; Pérez-Juste, J.; Polavarapu, L.; Sofer, Z., Oleic acid/oleylamine ligand pair: a versatile combination in the synthesis of colloidal nanoparticles. *Nanoscale Horizons* **2022,** *7* (9), 941-1015.
228. Song, Y.; Huang, T.; Murray, R. W., Heterophase Ligand Exchange and Metal Transfer between Monolayer Protected Clusters. *Journal of the American Chemical Society* **2003,** *125* (38), 11694-11701.
229. Pan, L.-L.; Yang, Y.; Li, D.-L.; Geng, W.-C.; Jiang, Z.-L.; Song, G.-S.; Li, Y.-J., Linker-free Gold Nanoparticle Superstructure Coated with Poly(dopamine) by Site-Specific Polymerization for Amplifying Photothermal Cancer Therapy. *Chemistry – An Asian Journal* **2020,** *15* (17), 2742-2748.
230. Turkevich, J.; Stevenson, P. C.; Hillier, J., A study of the nucleation and growth processes in the synthesis of colloidal gold. *Discussions of the Faraday Society* **1951,** *11* (0), 55-75.
231. Murthy, V. S.; Cha, J. N.; Stucky, G. D.; Wong, M. S., Charge-Driven Flocculation of Poly(l-lysine)Gold Nanoparticle Assemblies Leading to Hollow Microspheres. *Journal of the American Chemical Society* **2004,** *126* (16), 5292-5299.
232. Peetla, C.; Labhasetwar, V., Biophysical Characterization of Nanoparticle−Endothelial Model Cell Membrane Interactions. *Molecular pharmaceutics* **2008,** *5* (3), 418-429.
233. Krafft, M. P.; Riess, J. G., Perfluorocarbons: Life sciences and biomedical uses Dedicated to the memory of Professor Guy Ourisson, a true RENAISSANCE man. *Journal of Polymer Science Part A: Polymer Chemistry* **2007,** *45* (7), 1185-1198.

234. Kalaycioglu, G. D.; Aydogan, N., Fluorocarbon/hydrocarbon hybrid surfactant decorated gold nanoparticles and their interaction with model cell membranes. *Journal of Molecular Liquids* **2021,** *326*, 115346.

235. Gerber, F.; Krafft, M. P.; Vandamme, T. F.; Goldmann, M.; Fontaine, P., Fluidization of a dipalmitoyl phosphatidylcholine monolayer by fluorocarbon gases: potential use in lung surfactant therapy. *Biophys J* **2006,** *90* (9), 3184-92.

236. Kondo, Y.; Miyazawa, H.; Sakai, H.; Abe, M.; Yoshino, N., First Anionic Micelle with Unusually Long Lifetime: Self-Assembly of Fluorocarbon−Hydrocarbon Hybrid Surfactant. *Journal of the American Chemical Society* **2002,** *124* (23), 6516-6517.

237. Elmes, R. B. P.; Orange, K. N.; Cloonan, S. M.; Williams, D. C.; Gunnlaugsson, T., Luminescent Ruthenium(II) Polypyridyl Functionalized Gold Nanoparticles; Their DNA Binding Abilities and Application As Cellular Imaging Agents. *Journal of the American Chemical Society* **2011,** *133* (40), 15862-15865.

238. Adams, S. J.; Lewis, D. J.; Preece, J. A.; Pikramenou, Z., Luminescent Gold Surfaces for Sensing and Imaging: Patterning of Transition Metal Probes. *ACS Applied Materials & Interfaces* **2014,** *6* (14), 11598-11608.

239. Tan, L.-F.; Chao, H.; Li, H.; Liu, Y.-J.; Sun, B.; Wei, W.; Ji, L.-N., Synthesis, characterization, DNA-binding and photocleavage studies of [Ru(bpy)2(PPIP)]2+ and [Ru(phen)2(PPIP)]2+. *Journal of inorganic biochemistry* **2005,** *99* (2), 513-520.

240. Balzani, V.; Ceroni, P.; Credi, A.; Venturi, M., Ruthenium tris(bipyridine) complexes: Interchange between photons and electrons in molecular-scale devices and machines. *Coordination Chemistry Reviews* **2021,** *433*, 213758.

241. Cocks, A. T.; Wright, R. D.; Seddon, K. R., Photophysical properties of mixed-ligand ruthenium(II) complexes [Ru(1,10-phenanthroline)n {2-(2-pyridyl)quinoline}3-n] 2+ (n = 0, 1, 2, or 3). *Chemical Physics Letters* **1982,** *85* (3), 369-373.

242. Crosby, G. A.; Perkins, W. G.; Klassen, D. M., Luminescence from Transition-Metal Complexes: Tris(2,2′-bipyridine)- and Tris(1,10-phenanthroline)Ruthenium(II). *The Journal of Chemical Physics* **2004,** *43* (5), 1498-1503.

243. Demas, J. N.; Addington, J. W., Luminescence quenching of the tris(2,2'-bipyridine)ruthenium(II) and tris(1,10-phenanthroline)ruthenium(II) cations. *Journal of the American Chemical Society* **1976,** *98* (19), 5800-5806.

244. Jang, H. J.; Hopkins, S. L.; Siegler, M. A.; Bonnet, S., Frontier orbitals of photosubstitutionally active ruthenium complexes: an experimental study of the spectator ligands' electronic properties influence on photoreactivity. *Dalton Transactions* **2017,** *46* (30), 9969-9980.

245. Maestri, M.; Armaroli, N.; Balzani, V.; Constable, E. C.; Thompson, A. M. W. C., Complexes of the Ruthenium(II)-2,2':6',2''-terpyridine Family. Effect of Electron-Accepting and -Donating Substituents on the Photophysical and Electrochemical Properties. *Inorganic Chemistry* **1995,** *34* (10), 2759-2767.

246. Schulz, F.; Homolka, T.; Bastús, N. G.; Puntes, V.; Weller, H.; Vossmeyer, T., Little Adjustments Significantly Improve the Turkevich Synthesis of Gold Nanoparticles. *Langmuir* **2014,** *30* (35), 10779-10784.

247. Tyagi, H.; Kushwaha, A.; Kumar, A.; Aslam, M., A Facile pH Controlled Citrate-Based Reduction Method for Gold Nanoparticle Synthesis at Room Temperature. *Nanoscale Res Lett* **2016,** *11* (1), 362.

248. Frens, G., Controlled Nucleation for the Regulation of the Particle Size in Monodisperse Gold Suspensions. *Nature Physical Science* **1973,** *241* (105), 20-22.

249. Maguire, C. M.; Rösslein, M.; Wick, P.; Prina-Mello, A., Characterisation of particles in solution - a perspective on light scattering and comparative technologies. *Sci Technol Adv Mater* **2018,** *19* (1), 732-745.

250. Owens, D. E.; Peppas, N. A., Opsonization, biodistribution, and pharmacokinetics of polymeric nanoparticles. *International Journal of Pharmaceutics* **2006,** *307* (1), 93-102.

251. Backmann, N.; Kappeler, N.; Braun, T.; Huber, F.; Lang, H.; Gerber, C.; Lim, R., Sensing surface PEGylation with microcantilevers. *Beilstein journal of nanotechnology* **2010,** *1*, 3-13.

252. Wang, C.; Zhao, H., Polymer brush-based nanostructures: from surface self-assembly to surface co-assembly. *Soft Matter* **2022,** *18* (28), 5138-5152.

253. de Gennes, P. G., Conformations of Polymers Attached to an Interface. *Macromolecules* **1980,** *13* (5), 1069-1075.

254. Sheng, J.; Gan, J.; Huang, Z., Structure-based DNA-targeting strategies with small molecule ligands for drug discovery. *Med Res Rev* **2013,** *33* (5), 1119-73.

255. Görner, H.; Tossi, A. B.; Stradowski, C.; Schulte-Frohlinde, D., Binding of Ru(bpy)3(2+) and Ru(phen)3(2+) to polynucleotides and DNA: effect to added salts on the absorption and luminescence properties. *J Photochem Photobiol B* **1988,** *2* (1), 67-89.

256. Kumar, C. V.; Barton, J. K.; Turro, N. J., Photophysics of ruthenium complexes bound to double helical DNA. *Journal of the American Chemical Society* **1985,** *107* (19), 5518-5523.

257. Lincoln, P.; Nordén, B., DNA Binding Geometries of Ruthenium(II) Complexes with 1,10-Phenanthroline and 2,2'-Bipyridine Ligands Studied with Linear Dichroism Spectroscopy. Borderline Cases of Intercalation. *The Journal of Physical Chemistry B* **1998,** *102* (47), 9583-9594.

258. Galindo-Murillo, R.; Cheatham, T. E., Ethidium bromide interactions with DNA: an exploration of a classic DNA-ligand complex with unbiased molecular dynamics simulations. *Nucleic Acids Res* **2021,** *49* (7), 3735-3747.

259. Soni, A.; Khurana, P.; Singh, T.; Jayaram, B., A DNA intercalation methodology for an efficient prediction of ligand binding pose and energetics. *Bioinformatics* **2017,** *33* (10), 1488-1496.

260. Hiort, C.; Lincoln, P.; Norden, B., DNA binding of .DELTA.- and .LAMBDA.-[Ru(phen)2DPPZ]2+. *Journal of the American Chemical Society* **1993,** *115* (9), 3448-3454.

261. Hiort, C.; Norden, B.; Rodger, A., Enantiopreferential DNA binding of [ruthenium(II)(1,10-phenanthroline)3]2+ studied with linear and circular dichroism. *Journal of the American Chemical Society* **1990,** *112* (5), 1971-1982.

262. Rehmann, J. P.; Barton, J. K., 1H NMR studies of tris(phenanthroline) metal complexes bound to oligonucleotides: characterization of binding modes. *Biochemistry* **1990,** *29* (7), 1701-9.

263. Mei, H. Y.; Barton, J. K., Chiral probe for A-form helixes of DNA and RNA: tris(tetramethylphenanthroline)ruthenium(II). *Journal of the American Chemical Society* **1986,** *108* (23), 7414-7416.

264. Boynton, A. N.; Marcélis, L.; McConnell, A. J.; Barton, J. K., A Ruthenium(II) Complex as a Luminescent Probe for DNA Mismatches and Abasic Sites. *Inorganic Chemistry* **2017,** *56* (14), 8381-8389.

265. Rüba, E.; Hart, J. R.; Barton, J. K., [Ru(bpy)2(L)]Cl2: Luminescent Metal Complexes That Bind DNA Base Mismatches. *Inorganic Chemistry* **2004,** *43* (15), 4570-4578.

266. Friedman, A. E.; Chambron, J. C.; Sauvage, J. P.; Turro, N. J.; Barton, J. K., A molecular light switch for DNA: Ru(bpy)2(dppz)2+. *Journal of the American Chemical Society* **1990,** *112* (12), 4960-4962.

267. Tuite, E.; Lincoln, P.; Nordén, B., Photophysical Evidence That Δ- and Λ-[Ru(phen)2(dppz)]2+ Intercalate DNA from the Minor Groove. *Journal of the American Chemical Society* **1997,** *119* (1), 239-240.

268. Mårtensson, A. K. F.; Abrahamsson, M.; Tuite, E. M.; Lincoln, P., Diastereomeric Crowding Effects in the Competitive DNA Intercalation of Ru(phenanthroline)2dipyridophenazine2+ Enantiomers. *Inorganic Chemistry* **2019,** *58* (14), 9452-9459.

269. Coates, C. G.; McGarvey, J. J.; Callaghan, P. L.; Coletti, M.; Hamilton, J. G., Probing the Interaction of [Ru(phen)2(dppz)]2+ with Single-Stranded DNAWhat Degree of Protection Is

Required for Operation of the “Light-Switch Effect”? *The Journal of Physical Chemistry B* **2001,** *105* (3), 730-735.

270. Olson, E. J. C.; Hu, D.; Hörmann, A.; Jonkman, A. M.; Arkin, M. R.; Stemp, E. D. A.; Barton, J. K.; Barbara, P. F., First Observation of the Key Intermediate in the “Light-Switch” Mechanism of [Ru(phen)2dppz]2+. *Journal of the American Chemical Society* **1997,** *119* (47), 11458-11467.

271. Önfelt, B.; Lincoln, P.; Nordén, B.; Baskin, J. S.; Zewail, A. H., Femtosecond linear dichroism of DNA-intercalating chromophores: Solvation and charge separation dynamics of [Ru(phen)2dppz]2+ systems. *Proceedings of the National Academy of Sciences* **2000,** *97* (11), 5708-5713.

272. Brennaman, M. K.; Meyer, T. J.; Papanikolas, J. M., [Ru(bpy)2dppz]2+ Light-Switch Mechanism in Protic Solvents as Studied through Temperature-Dependent Lifetime Measurements. *The Journal of Physical Chemistry A* **2004,** *108* (45), 9938-9944.

273. Poynton, F. E.; Hall, J. P.; Keane, P. M.; Schwarz, C.; Sazanovich, I. V.; Towrie, M.; Gunnlaugsson, T.; Cardin, C. J.; Cardin, D. J.; Quinn, S. J.; Long, C.; Kelly, J. M., Direct observation by time-resolved infrared spectroscopy of the bright and the dark excited states of the [Ru(phen)2(dppz)]2+ light-switch compound in solution and when bound to DNA. *Chemical Science* **2016,** *7* (5), 3075-3084.

274. Metcalfe, C.; Thomas, J. A., Kinetically inert transition metal complexes that reversibly bind to DNA. *Chemical Society reviews* **2003,** *32* (4), 215-224.

275. Zeglis, B. M.; Pierre, V. C.; Barton, J. K., Metallo-intercalators and metallo-insertors. *Chemical Communications* **2007,** (44), 4565-4579.

276. Gill, M. R.; Thomas, J. A., Ruthenium(ii) polypyridyl complexes and DNA—from structural probes to cellular imaging and therapeutics. *Chemical Society reviews* **2012,** *41* (8), 3179-3192.

277. Wachter, E.; Moyá, D.; Parkin, S.; Glazer, E. C., Ruthenium Complex "Light Switches" that are Selective for Different G-Quadruplex Structures. *Chemistry* **2016,** *22* (2), 550-9.

278. Elgar, C. E.; Yusoh, N. A.; Tiley, P. R.; Kolozsvári, N.; Bennett, L. G.; Gamble, A.; Péan, E. V.; Davies, M. L.; Staples, C. J.; Ahmad, H.; Gill, M. R., Ruthenium(II) Polypyridyl Complexes as FRET Donors: Structure- and Sequence-Selective DNA-Binding and Anticancer Properties. *Journal of the American Chemical Society* **2023,** *145* (2), 1236-1246.

279. Hess, J.; Huang, H.; Kaiser, A.; Pierroz, V.; Blacque, O.; Chao, H.; Gasser, G., Evaluation of the Medicinal Potential of Two Ruthenium(II) Polypyridine Complexes as One- and Two-Photon Photodynamic Therapy Photosensitizers. *Chemistry – A European Journal* **2017,** *23* (41), 9888-9896.

280. Pierroz, V.; Rubbiani, R.; Gentili, C.; Patra, M.; Mari, C.; Gasser, G.; Ferrari, S., Dual mode of cell death upon the photo-irradiation of a RuII polypyridyl complex in interphase or mitosis. *Chemical Science* **2016,** *7* (9), 6115-6124.

281. Gill, M. R.; Harun, S. N.; Halder, S.; Boghozian, R. A.; Ramadan, K.; Ahmad, H.; Vallis, K. A., A ruthenium polypyridyl intercalator stalls DNA replication forks, radiosensitizes human cancer cells and is enhanced by Chk1 inhibition. *Scientific Reports* **2016,** *6* (1), 31973.

282. Yusoh, N. A.; Leong, S. W.; Chia, S. L.; Harun, S. N.; Rahman, M. B. A.; Vallis, K. A.; Gill, M. R.; Ahmad, H., Metallointercalator [Ru(dppz)2(PIP)]2+ Renders BRCA Wild-Type Triple-Negative Breast Cancer Cells Hypersensitive to PARP Inhibition. *ACS Chemical Biology* **2020,** *15* (2), 378-387.

283. Harun, S. N.; Ahmad, H.; Lim, H.; Chia, S. L.; Gill, M., Synthesis and Optimization of Mesoporous Silica Nanoparticles for Ruthenium Polypyridyl Drug Delivery. *Pharmaceutics* **2021,** *13*, 150.

284. Caballero, A. B.; Cardo, L.; Claire, S.; Craig, J. S.; Hodges, N. J.; Vladyka, A.; Albrecht, T.; Rochford, L. A.; Pikramenou, Z.; Hannon, M. J., Assisted delivery of anti-tumour platinum drugs using DNA-coiling gold nanoparticles bearing lumophores and intercalators: towards a

new generation of multimodal nanocarriers with enhanced action. *Chemical Science* **2019,** *10* (40), 9244-9256.

285. Kang, B.; Mackey, M. A.; El-Sayed, M. A., Nuclear Targeting of Gold Nanoparticles in Cancer Cells Induces DNA Damage, Causing Cytokinesis Arrest and Apoptosis. *Journal of the American Chemical Society* **2010,** *132* (5), 1517-1519.

286. Vorobjev, P.; Epanchintseva, A.; Lomzov, A.; Tupikin, A.; Kabilov, M.; Pyshnaya, I.; Pyshnyi, D., DNA Binding to Gold Nanoparticles through the Prism of Molecular Selection: Sequence–Affinity Relation. *Langmuir* **2019,** *35* (24), 7916-7928.

287. Chen, X.; Wang, Y.; Dai, X.; Ding, L.; Chen, J.; Yao, G.; Liu, X.; Luo, S.; Shi, J.; Wang, L.; Nechushtai, R.; Pikarsky, E.; Willner, I.; Fan, C.; Li, J., Single-Stranded DNA-Encoded Gold Nanoparticle Clusters as Programmable Enzyme Equivalents. *Journal of the American Chemical Society* **2022,** *144* (14), 6311-6320.

288. Li, F.; Zhang, H.; Dever, B.; Li, X.-F.; Le, X. C., Thermal Stability of DNA Functionalized Gold Nanoparticles. *Bioconjugate Chemistry* **2013,** *24* (11), 1790-1797.

289. Deka, J.; Mojumdar, A.; Parisse, P.; Onesti, S.; Casalis, L., DNA-conjugated gold nanoparticles based colorimetric assay to assess helicase activity: a novel route to screen potential helicase inhibitors. *Scientific Reports* **2017,** *7* (1), 44358.

290. Mirau, P. A.; Smith, J. E.; Chávez, J. L.; Hagen, J. A.; Kelley-Loughnane, N.; Naik, R., Structured DNA Aptamer Interactions with Gold Nanoparticles. *Langmuir* **2018,** *34* (5), 2139-2146.

291. Mirkin, C. A.; Letsinger, R. L.; Mucic, R. C.; Storhoff, J. J., A DNA-based method for rationally assembling nanoparticles into macroscopic materials. *Nature* **1996,** *382* (6592), 607-609.

292. Alivisatos, A. P.; Johnsson, K. P.; Peng, X.; Wilson, T. E.; Loweth, C. J.; Bruchez, M. P.; Schultz, P. G., Organization of 'nanocrystal molecules' using DNA. *Nature* **1996,** *382* (6592), 609-611.

293. Saeed, A. A.; Sánchez, J. L. A.; O'Sullivan, C. K.; Abbas, M. N., DNA biosensors based on gold nanoparticles-modified graphene oxide for the detection of breast cancer biomarkers for early diagnosis. *Bioelectrochemistry* **2017,** *118*, 91-99.

294. Zhang, K.; Lv, S.; Lin, Z.; Li, M.; Tang, D., Bio-bar-code-based photoelectrochemical immunoassay for sensitive detection of prostate-specific antigen using rolling circle amplification and enzymatic biocatalytic precipitation. *Biosensors and Bioelectronics* **2018,** *101*, 159-166.

295. Tu, Y.; Wu, P.; Zhang, H.; Cai, C., Fluorescence quenching of gold nanoparticles integrating with a conformation-switched hairpin oligonucleotide probe for microRNA detection. *Chemical Communications* **2012,** *48* (87), 10718-10720.

296. Rouge, J. L.; Hao, L.; Wu, X. A.; Briley, W. E.; Mirkin, C. A., Spherical Nucleic Acids as a Divergent Platform for Synthesizing RNA–Nanoparticle Conjugates through Enzymatic Ligation. *ACS Nano* **2014,** *8* (9), 8837-8843.

297. Latorre, A.; Posch, C.; Garcimartín, Y.; Celli, A.; Sanlorenzo, M.; Vujic, I.; Ma, J.; Zekhtser, M.; Rappersberger, K.; Ortiz-Urda, S.; Somoza, Á., DNA and aptamer stabilized gold nanoparticles for targeted delivery of anticancer therapeutics. *Nanoscale* **2014,** *6* (13), 7436-7442.

298. Zhang, Y.; Chen, Y.; Han, D.; Ocsoy, I.; Tan, W., Aptamers selected by cell-SELEX for application in cancer studies. *Bioanalysis* **2010,** *2* (5), 907-18.

299. Luo, Y.-L.; Shiao, Y.-S.; Huang, Y.-F., Release of Photoactivatable Drugs from Plasmonic Nanoparticles for Targeted Cancer Therapy. *ACS Nano* **2011,** *5* (10), 7796-7804.

300. Yang, Y.; Han, Y.; Sun, Q.; Cheng, J.; Yue, C.; Liu, Y.; Song, J.; Jin, W.; Ding, X.; de la Fuente, J. M.; Ni, J.; Wang, X.; Cui, D., Au-siRNA@ aptamer nanocages as a high-efficiency drug and gene delivery system for targeted lung cancer therapy. *Journal of Nanobiotechnology* **2021,** *19* (1), 54.

301. Vidal, A.; Calligaro, R.; Gasser, G.; Alberto, R.; Balducci, G.; Alessio, E., Cis-Locked Ru(II)-DMSO Precursors for the Microwave-Assisted Synthesis of Bis-Heteroleptic Polypyridyl Compounds. *Inorganic chemistry* **2021,** *XXXX*.

302. Notaro, A.; Gasser, G.; Castonguay, A., Note of Caution for the Aqueous Behaviour of Metal-Based Drug Candidates. *ChemMedChem* **2020,** *15* (4), 345-348.

303. Vinck, R.; Gandioso, A.; Burckel, P.; Saubaméa, B.; Cariou, K.; Gasser, G., Red-Absorbing Ru(II) Polypyridyl Complexes with Biotin Targeting Spontaneously Assemble into Nanoparticles in Biological Media. *Inorganic Chemistry* **2022,** *61* (34), 13576-13585.

304. Alam, P.; Climent, C.; Alemany, P.; Laskar, I. R., "Aggregation-induced emission" of transition metal compounds: Design, mechanistic insights, and applications. *Journal of Photochemistry and Photobiology C: Photochemistry Reviews* **2019,** *41*, 100317.

305. Huang, M.; Yu, R.; Xu, K.; Ye, S.; Kuang, S.; Zhu, X.; Wan, Y., An arch-bridge-type fluorophore for bridging the gap between aggregation-caused quenching (ACQ) and aggregation-induced emission (AIE). *Chemical Science* **2016,** *7* (7), 4485-4491.

306. Li, H.; Luo, J.; Zhang, Z.-Y.; Wei, R.-J.; Xie, M.; Huang, Y.-L.; Ning, G.-H.; Li, D., Cyclic Trinuclear Copper(I) Complex Exhibiting Aggregation-Induced Emission: A Novel Fluorescent Probe for the Selective Detection of Gold(III) Ions. *Inorganic Chemistry* **2022,** *61* (1), 414-421.

307. Chambron, J.-C.; Sauvage, J.-P., Ru (bipy)2dppz2+ : a highly sensitive luminescent probe for micellar sodium dodecyl sulfate solutions. *Chemical Physics Letters* **1991,** *182* (6), 603-607.

308. Fu, Y.; Zhang, J.; Lakowicz, J. R., Plasmonic enhancement of single-molecule fluorescence near a silver nanoparticle. *J Fluoresc* **2007,** *17* (6), 811-6.

309. Li, J.-F.; Li, C.-Y.; Aroca, R. F., Plasmon-enhanced fluorescence spectroscopy. *Chemical Society reviews* **2017,** *46* (13), 3962-3979.

310. Wang, W.; Ding, X.; Xu, Q.; Wang, J.; Wang, L.; Lou, X., Zeta-potential data reliability of gold nanoparticle biomolecular conjugates and its application in sensitive quantification of surface absorbed protein. *Colloids and Surfaces B: Biointerfaces* **2016,** *148*, 541-548.

311. Zhang, C.-Y.; Zhang, N.-H. Mechanical Constraint Effect on DNA Persistence Length *Molecules* [Online], 2022.

312. Carnerero, J. M.; Masuoka, S.; Baba, H.; Yoshikawa, Y.; Prado-Gotor, R.; Yoshikawa, K., Decorating a single giant DNA with gold nanoparticles. *RSC Advances* **2018,** *8* (47), 26571-26579.

313. Chiaramoni, N. S.; Baccarini, L. C.; Taira, M. C.; Alonso Sdel, V., Liposome/DNA systems: correlation between hydrophobicity and DNA conformational changes. *J Biol Phys* **2008,** *34* (1-2), 179-88.

314. Li, L.; Pa, Q.; Xu, Z.; Song, G., Study on the Aggregation of Fluorinated Surfactant FC-134 on the Surface of DNA. *Physics Procedia* **2012,** *25*, 388-393.

315. Waga, S.; Bauer, G.; Stillman, B., Reconstitution of complete SV40 DNA replication with purified replication factors. *J Biol Chem* **1994,** *269* (14), 10923-34.

316. Kriegstein, H. J.; Hogness, D. S., Mechanism of DNA replication in Drosophila chromosomes: structure of replication forks and evidence for bidirectionality. *Proceedings of the National Academy of Sciences of the United States of America* **1974,** *71* (1), 135-9.

317. Bawendi, M.; Steigerwald, M.; Brus, L., The Quantum Mechanics of Larger Semiconductor Clusters ("Quantum Dots"). *Annual Review of Physical Chemistry* **2003,** *41*, 477-496.

318. Hartl, C.; Frank, K.; Amenitsch, H.; Fischer, S.; Liedl, T.; Nickel, B., Position Accuracy of Gold Nanoparticles on DNA Origami Structures Studied with Small-Angle X-ray Scattering. *Nano Letters* **2018,** *18* (4), 2609-2615.

319. Mirkin, C. A.; Letsinger, R. L.; Mucic, R. C.; Storhoff, J. J., A DNA-based method for rationally assembling nanoparticles into macroscopic materials. *Nature* **1996,** *382* (6592), 607-9.

320. Creighton, J. A.; Blatchford, C. G.; Albrecht, M. G., Plasma resonance enhancement of Raman scattering by pyridine adsorbed on silver or gold sol particles of size comparable to the

excitation wavelength. *Journal of the Chemical Society, Faraday Transactions 2: Molecular and Chemical Physics* **1979,** *75* (0), 790-798.

321. Jiang, Q.; Shi, Y.; Zhang, Q.; Li, N.; Zhan, P.; Song, L.; Dai, L.; Tian, J.; Du, Y.; Cheng, Z.; Ding, B., A Self-Assembled DNA Origami-Gold Nanorod Complex for Cancer Theranostics. *Small* **2015,** *11* (38), 5134-41.

322. Kumar, N.; Kaushal, R.; Awasthi, P., Non-covalent binding studies of transition metal complexes with DNA: A review. *Journal of Molecular Structure* **2023,** *1288*, 135751.

323. Very, T.; Despax, S.; Hébraud, P.; Monari, A.; Assfeld, X., Spectral properties of polypyridyl ruthenium complexes intercalated in DNA: theoretical insights into the surrounding effects of [Ru(dppz)(bpy)2]2+. *Physical Chemistry Chemical Physics* **2012,** *14* (36), 12496-12504.

324. Shahabadi, N.; Kashanian, S.; Fatahi, A., Identification of Binding Mode of a Platinum (II) Complex, PtCl(2)(DIP), and Calf Thymus DNA. *Bioinorg Chem Appl* **2011,** *2011*, 687571.

325. Shahabadi, N.; Kashanian, S.; Mahdavi, M.; Sourinejad, N., DNA Interaction and DNA Cleavage Studies of a New Platinum(II) Complex Containing Aliphatic and Aromatic Dinitrogen Ligands. *Bioinorg Chem Appl* **2011,** *2011*, 525794.

326. Yun, B. H.; Jin, B.; Lee, B. W.; Lincoln, P.; Nordén, B.; Kim, J.-M.; Kim, S., Simultaneous Binding of Ruthenium(II) [(1,10-Phenanthroline) 2dipyridophenazine]2+ and Minor Groove Binder 4′,6-Diamidino-2-Phenylindole to Poly[d(A-T)2] at High Binding Densities: Observation of Fluorescence Resonance Energy Trasfer Across the DNA Stem. *Journal of Physical Chemistry B - J PHYS CHEM B* **2003,** *107*.

327. Choi, S. D.; Kim, M. S.; Kim, S. K.; Lincoln, P.; Tuite, E.; Nordén, B., Binding mode of [ruthenium(II) (1,10-phenanthroline)2L]2+ with poly (dT*dA-dT) triplex. Ligand size effect on third-strand stabilization. *Biochemistry* **1997,** *36* (1), 214-23.

328. Quintana, C.; Cifuentes, M. P.; Humphrey, M. G., Transition metal complex/gold nanoparticle hybrid materials. *Chemical Society reviews* **2020,** *49* (8), 2316-2341.

329. Leung, F. C.-M.; Tam, A. Y.-Y.; Au, V. K.-M.; Li, M.-J.; Yam, V. W.-W., Förster Resonance Energy Transfer Studies of Luminescent Gold Nanoparticles Functionalized with Ruthenium(II) and Rhenium(I) Complexes: Modulation via Esterase Hydrolysis. *ACS Applied Materials & Interfaces* **2014,** *6* (9), 6644-6653.

330. Martínez-Calvo, M.; Orange, K. N.; Elmes, R. B. P.; la Cour Poulsen, B.; Williams, D. C.; Gunnlaugsson, T., Ru(ii)-polypyridyl surface functionalised gold nanoparticles as DNA targeting supramolecular structures and luminescent cellular imaging agents. *Nanoscale* **2016,** *8* (1), 563-574.

331. Cosgrave, L.; Devocelle, M.; Forster, R. J.; Keyes, T. E., Multimodal cell imaging by ruthenium polypyridyl labelled cell penetrating peptides. *Chemical communications (Cambridge, England)* **2010,** *46* (1), 103-5.

332. Lau, C. T.-S.; Chan, C.; Zhang, K. Y.; Roy, V. A. L.; Lo, K. K.-W., Photophysical, Cellular-Uptake, and Bioimaging Studies of Luminescent Ruthenium(II)–Polypyridine Complexes Containing a d-Fructose Pendant. *European Journal of Inorganic Chemistry* **2017,** *2017* (44), 5288-5294.

333. Lo, K. K.-W.; Lee, T. K.-M.; Lau, J. S.-Y.; Poon, W.-L.; Cheng, S.-H., Luminescent Biological Probes Derived from Ruthenium(II) Estradiol Polypyridine Complexes. *Inorganic Chemistry* **2008,** *47* (1), 200-208.

334. Wang, P.; Wang, X.; Wang, L.; Hou, X.; Liu, W.; Chen, C., Interaction of gold nanoparticles with proteins and cells. *Sci Technol Adv Mater* **2015,** *16* (3), 034610.

335. Chithrani, B. D.; Chan, W. C. W., Elucidating the Mechanism of Cellular Uptake and Removal of Protein-Coated Gold Nanoparticles of Different Sizes and Shapes. *Nano Letters* **2007,** *7* (6), 1542-1550.

336. Chithrani, B. D.; Ghazani, A. A.; Chan, W. C. W., Determining the Size and Shape Dependence of Gold Nanoparticle Uptake into Mammalian Cells. *Nano Letters* **2006,** *6* (4), 662-668.

337. Mayle, K. M.; Le, A. M.; Kamei, D. T., The intracellular trafficking pathway of transferrin. *Biochim Biophys Acta* **2012,** *1820* (3), 264-81.

338. Yang, N. J.; Hinner, M. J., Getting across the cell membrane: an overview for small molecules, peptides, and proteins. *Methods Mol Biol* **2015,** *1266*, 29-53.

339. Sousa de Almeida, M.; Susnik, E.; Drasler, B.; Taladriz-Blanco, P.; Petri-Fink, A.; Rothen-Rutishauser, B., Understanding nanoparticle endocytosis to improve targeting strategies in nanomedicine. *Chemical Society reviews* **2021,** *50* (9), 5397-5434.

340. Walkey, C. D.; Olsen, J. B.; Guo, H.; Emili, A.; Chan, W. C. W., Nanoparticle Size and Surface Chemistry Determine Serum Protein Adsorption and Macrophage Uptake. *Journal of the American Chemical Society* **2012,** *134* (4), 2139-2147.

341. Kaksonen, M.; Roux, A., Mechanisms of clathrin-mediated endocytosis. *Nature Reviews Molecular Cell Biology* **2018,** *19* (5), 313-326.

342. Dey, A. K.; Gonon, A.; Pécheur, E. I.; Pezet, M.; Villiers, C.; Marche, P. N., Impact of Gold Nanoparticles on the Functions of Macrophages and Dendritic Cells. *Cells* **2021,** *10* (1).

343. Augustine, R.; Hasan, A.; Primavera, R.; Wilson, R. J.; Thakor, A. S.; Kevadiya, B. D., Cellular uptake and retention of nanoparticles: Insights on particle properties and interaction with cellular components. *Materials Today Communications* **2020,** *25*, 101692.

344. Shukla, R.; Bansal, V.; Chaudhary, M.; Basu, A.; Bhonde, R. R.; Sastry, M., Biocompatibility of Gold Nanoparticles and Their Endocytotic Fate Inside the Cellular Compartment: A Microscopic Overview. *Langmuir* **2005,** *21* (23), 10644-10654.

345. Zhao, F.; Zhao, Y.; Liu, Y.; Chang, X.; Chen, C.; Zhao, Y., Cellular uptake, intracellular trafficking, and cytotoxicity of nanomaterials. *Small* **2011,** *7* (10), 1322-37.

346. Kapara, A.; Brunton, V.; Graham, D.; Faulds, K., Investigation of cellular uptake mechanism of functionalised gold nanoparticles into breast cancer using SERS. *Chemical Science* **2020,** *11* (22), 5819-5829.

347. Xie, X.; Liao, J.; Shao, X.; Li, Q.; Lin, Y., The Effect of shape on Cellular Uptake of Gold Nanoparticles in the forms of Stars, Rods, and Triangles. *Scientific Reports* **2017,** *7* (1), 3827.

348. Kay, R. R., Macropinocytosis: Biology and mechanisms. *Cells & Development* **2021,** *168*, 203713.

349. Huo, S.; Jin, S.; Ma, X.; Xue, X.; Yang, K.; Kumar, A.; Wang, P. C.; Zhang, J.; Hu, Z.; Liang, X.-J., Ultrasmall Gold Nanoparticles as Carriers for Nucleus-Based Gene Therapy Due to Size-Dependent Nuclear Entry. *ACS Nano* **2014,** *8* (6), 5852-5862.

350. Paine, P. L.; Moore, L. C.; Horowitz, S. B., Nuclear envelope permeability. *Nature* **1975,** *254* (5496), 109-14.

351. Dwivedi, P.; Nayak, V.; Kowshik, M., Role of gold nanoparticles as drug delivery vehicles for chondroitin sulfate in the treatment of osteoarthritis. *Biotechnol Prog* **2015,** *31* (5), 1416-22.

352. Campos, W. N.; Marangoni, V.; Sonego, D. A.; Andrade, M. A.; Colodel, E.; Souza, R., Synthesis and characterization of gold nanoparticles combined with curcumin and its effect on experimental osteoarthritis in mice. *Osteoarthritis and Cartilage* **2015,** *23*, A397.

353. Kong, F. Y.; Zhang, J. W.; Li, R. F.; Wang, Z. X.; Wang, W. J.; Wang, W., Unique Roles of Gold Nanoparticles in Drug Delivery, Targeting and Imaging Applications. *Molecules* **2017,** *22* (9).

354. Huang, H.; Quan, Y. Y.; Wang, X. P.; Chen, T. S., Gold Nanoparticles of Diameter 13 nm Induce Apoptosis in Rabbit Articular Chondrocytes. *Nanoscale Res Lett* **2016,** *11* (1), 249.

355. Khaing Oo, M. K.; Yang, Y.; Hu, Y.; Gomez, M.; Du, H.; Wang, H., Gold Nanoparticle-Enhanced and Size-Dependent Generation of Reactive Oxygen Species from Protoporphyrin IX. *ACS Nano* **2012,** *6* (3), 1939-1947.

356. Mari, C.; Rubbiani, R.; Gasser, G., Biological evaluation of nitrile containing Ru(II) polypyridyl complexes as potential photodynamic therapy agents. *Inorganica Chimica Acta* **2017,** *454*, 21-26.

357. Chen, L.; Huang, J.; Li, X.; Huang, M.; Zeng, S.; Zheng, J.; Peng, S.; Li, S., Progress of Nanomaterials in Photodynamic Therapy Against Tumor. *Front Bioeng Biotechnol* **2022,** *10*, 920162.

358. Ostańska, E.; Aebisher, D.; Bartusik-Aebisher, D., The potential of photodynamic therapy in current breast cancer treatment methodologies. *Biomedicine & Pharmacotherapy* **2021,** *137*, 111302.

359. Kobayashi, H.; Watanabe, R.; Choyke, P. L., Improving conventional enhanced permeability and retention (EPR) effects; what is the appropriate target? *Theranostics* **2013,** *4* (1), 81-9.

360. Yang, C.; Fu, Y.; Huang, C.; Hu, D.; Zhou, K.; Hao, Y.; Chu, B.; Yang, Y.; Qian, Z., Chlorin e6 and CRISPR-Cas9 dual-loading system with deep penetration for a synergistic tumoral photodynamic-immunotherapy. *Biomaterials* **2020,** *255*, 120194.

361. Chung, C. H.; Lu, K. Y.; Lee, W. C.; Hsu, W. J.; Lee, W. F.; Dai, J. Z.; Shueng, P. W.; Lin, C. W.; Mi, F. L., Fucoidan-based, tumor-activated nanoplatform for overcoming hypoxia and enhancing photodynamic therapy and antitumor immunity. *Biomaterials* **2020,** *257*, 120227.

362. Sheng, S.; Liu, F.; Lin, L.; Yan, N.; Wang, Y.; Xu, C.; Tian, H.; Chen, X., Nanozyme-mediated cascade reaction based on metal-organic framework for synergetic chemo-photodynamic tumor therapy. *J Control Release* **2020,** *328*, 631-639.

363. Kim, Y.; Uthaman, S.; Pillarisetti, S.; Noh, K.; Huh, K. M.; Park, I. K., Bioactivatable reactive oxygen species-sensitive nanoparticulate system for chemo-photodynamic therapy. *Acta Biomater* **2020,** *108*, 273-284.

364. Riley, R. S.; Day, E. S., Gold nanoparticle-mediated photothermal therapy: applications and opportunities for multimodal cancer treatment. *Wiley Interdiscip Rev Nanomed Nanobiotechnol* **2017,** *9* (4).

365. Maehara, Y.; Anai, H.; Tamada, R.; Sugimachi, K., The ATP assay is more sensitive than the succinate dehydrogenase inhibition test for predicting cell viability. *European Journal of Cancer and Clinical Oncology* **1987,** *23* (3), 273-276.

366. Slater, T. F.; Sawyer, B.; Sträuli, U., Studies on succinate-tetrazolium reductase systems: III. Points of coupling of four different tetrazolium salts III. Points of coupling of four different tetrazolium salts. *Biochimica et Biophysica Acta* **1963,** *77*, 383-393.

367. López-García, J.; Lehocký, M.; Humpolíček, P.; Sáha, P., HaCaT Keratinocytes Response on Antimicrobial Atelocollagen Substrates: Extent of Cytotoxicity, Cell Viability and Proliferation. *J Funct Biomater* **2014,** *5* (2), 43-57.

368. Yang, Y.; Zheng, X.; Chen, L.; Gong, X.; Yang, H.; Duan, X.; Zhu, Y., Multifunctional Gold Nanoparticles in Cancer Diagnosis and Treatment. *Int J Nanomedicine* **2022,** *17*, 2041-2067.

369. Komor, A. C.; Barton, J. K., The path for metal complexes to a DNA target. *Chemical Communications* **2013,** *49* (35), 3617-3630.

370. Andrian, T.; Muela, Y.; Delgado, L.; Albertazzi, L.; Pujals, S., A super-resolution and transmission electron microscopy correlative approach to study intracellular trafficking of nanoparticles. *Nanoscale* **2023,** *15* (35), 14615-14627.

371. O'Sullivan, M. J.; Lindsay, A. J., The Endosomal Recycling Pathway-At the Crossroads of the Cell. *International journal of molecular sciences* **2020,** *21* (17).

372. Donahue, N. D.; Acar, H.; Wilhelm, S., Concepts of nanoparticle cellular uptake, intracellular trafficking, and kinetics in nanomedicine. *Advanced Drug Delivery Reviews* **2019,** *143*, 68-96.

373. Panté, N.; Kann, M., Nuclear pore complex is able to transport macromolecules with diameters of about 39 nm. *Mol Biol Cell* **2002,** *13* (2), 425-34.

374. Gasiorowski, J. Z.; Dean, D. A., Mechanisms of nuclear transport and interventions. *Advanced Drug Delivery Reviews* **2003,** *55* (6), 703-716.

375. Leslie, D. M.; Zhang, W.; Timney, B. L.; Chait, B. T.; Rout, M. P.; Wozniak, R. W.; Aitchison, J. D., Characterization of karyopherin cargoes reveals unique mechanisms of Kap121p-mediated nuclear import. *Mol Cell Biol* **2004,** *24* (19), 8487-503.
376. Jans, D. A.; Briggs, L. J.; Gustin, S. E.; Jans, P.; Ford, S.; Young, I. G., The cytokine interleukin-5 (IL-5) effects cotransport of its receptor subunits to the nucleus in vitro. *FEBS Lett* **1997,** *410* (2-3), 368-72.
377. Zhang, S.; Li, J.; Lykotrafitis, G.; Bao, G.; Suresh, S., Size-Dependent Endocytosis of Nanoparticles. *Advanced Materials* **2009,** *21* (4), 419-424.
378. Mehanna, S.; Mansour, N.; Audi, H.; Bodman-Smith, K.; Mroueh, M. A.; Taleb, R. I.; Daher, C. F.; Khnayzer, R. S., Enhanced cellular uptake and photochemotherapeutic potential of a lipophilic strained Ru(ii) polypyridyl complex. *RSC Advances* **2019,** *9* (30), 17254-17265.
379. Puckett, C. A.; Ernst, R. J.; Barton, J. K., Exploring the cellular accumulation of metal complexes. *Dalton Transactions* **2010,** *39* (5), 1159-1170.
380. Ghezzi, A.; Aceto, M.; Cassino, C.; Gabano, E.; Osella, D., Uptake of antitumor platinum(II)-complexes by cancer cells, assayed by inductively coupled plasma mass spectrometry (ICP-MS). *Journal of inorganic biochemistry* **2004,** *98* (1), 73-78.
381. Parray, Z. A.; Hassan, M. I.; Ahmad, F.; Islam, A., Amphiphilic nature of polyethylene glycols and their role in medical research. *Polymer Testing* **2020,** *82*, 106316.
382. Piksa, M.; Lian, C.; Samuel, I. C.; Pawlik, K. J.; Samuel, I. D. W.; Matczyszyn, K., The role of the light source in antimicrobial photodynamic therapy. *Chemical Society reviews* **2023,** *52* (5), 1697-1722.
383. Kim, M. M.; Darafsheh, A., Light Sources and Dosimetry Techniques for Photodynamic Therapy. *Photochemistry and Photobiology* **2020,** *96* (2), 280-294.
384. Sullivan, B. P.; Salmon, D. J.; Meyer, T. J., Mixed phosphine 2,2'-bipyridine complexes of ruthenium. *Inorganic Chemistry* **1978,** *17* (12), 3334-3341.
385. Shreeve, J. M., *Inorganic syntheses: Volume 24*. 2007; p 1-308.
386. Alessio, E.; Mestroni, G.; Nardin, G.; Attia, W. M.; Calligaris, M.; Sava, G.; Zorzet, S., Cis- and trans-dihalotetrakis(dimethyl sulfoxide)ruthenium(II) complexes (RuX2(DMSO)4; X = Cl, Br): synthesis, structure, and antitumor activity. *Inorganic Chemistry* **1988,** *27* (23), 4099-4106.
387. Pinczewska, A.; Sosna, M.; Bloodworth, S.; Kilburn, J. D.; Bartlett, P. N., High-Throughput Synthesis and Electrochemical Screening of a Library of Modified Electrodes for NADH Oxidation. *Journal of the American Chemical Society* **2012,** *134* (43), 18022-18033.
388. Younts T., P. J. C., Ruthenium coordination chemistry: Implications for directed carbon nanotube assembly. *Journal of Undergraduate Materials Research* **2008,** *33*, 44-49.
389. Ziegler, C.; Eychmüller, A., Seeded Growth Synthesis of Uniform Gold Nanoparticles with Diameters of 15−300 nm. *The Journal of Physical Chemistry C* **2011,** *115* (11), 4502-4506.
390. Grabar, K. C.; Freeman, R. G.; Hommer, M. B.; Natan, M. J., Preparation and Characterization of Au Colloid Monolayers. *Analytical Chemistry* **1995,** *67* (4), 735-743.
391. Carney, R. P.; Kim, J. Y.; Qian, H.; Jin, R.; Mehenni, H.; Stellacci, F.; Bakr, O. M., Determination of nanoparticle size distribution together with density or molecular weight by 2D analytical ultracentrifugation. *Nature Communications* **2011,** *2* (1), 335.
392. Shang, J.; Gao, X., Nanoparticle counting: towards accurate determination of the molar concentration. *Chemical Society reviews* **2014,** *43* (21), 7267-7278.
393. Haiss, W.; Thanh, N. T. K.; Aveyard, J.; Fernig, D. G., Determination of Size and Concentration of Gold Nanoparticles from UV−Vis Spectra. *Analytical Chemistry* **2007,** *79* (11), 4215-4221.